

**Naval Research Laboratory**

Washington, DC 20375-5000



**NRL Report 9028**

# **ELF/VLF/LF Propagation and System Design**

**FRANCIS J. KELLY**

*Ionospheric Effects Branch  
Space Science Division*

June 23, 1987

REPORT DOCUMENTATION PAGE				
1a. REPORT SECURITY CLASSIFICATION <b>UNCLASSIFIED</b>		1b. RESTRICTIVE MARKINGS		
2a. SECURITY CLASSIFICATION AUTHORITY		3. DISTRIBUTION/AVAILABILITY OF REPORT		
2b. DECLASSIFICATION/DOWNGRADING SCHEDULE		Approved for public release, distribution unlimited.		
4. PERFORMING ORGANIZATION REPORT NUMBER(S) NRL Report 9028		5. MONITORING ORGANIZATION REPORT NUMBER(S)		
6a. NAME OF PERFORMING ORGANIZATION Naval Research Laboratory	6b. OFFICE SYMBOL (If applicable) Code 4183	7a. NAME OF MONITORING ORGANIZATION		
6c. ADDRESS (City, State, and ZIP Code) Washington, DC 20375-5000		7b. ADDRESS (City, State, and ZIP Code)		
8a. NAME OF FUNDING/SPONSORING ORGANIZATION Defense Communication Agency	8b. OFFICE SYMBOL (If applicable)	9. PROCUREMENT INSTRUMENT IDENTIFICATION NUMBER		
8c. ADDRESS (City, State, and ZIP Code) Arlington, VA 22212-5410		10. SOURCE OF FUNDING NUMBERS		
		PROGRAM ELEMENT NO.	PROJECT NO.	TASK NO.
				WORK UNIT ACCESSION NO. DN280-098
11. TITLE (Include Security Classification) ELF/VLF/LF Propagation and System Design				
12. PERSONAL AUTHOR(S) Kelly, Francis J.				
13a. TYPE OF REPORT Interim	13b. TIME COVERED FROM _____ TO _____	14. DATE OF REPORT (Year, Month, Day) 1987 June 23	15. PAGE COUNT 127	
16. SUPPLEMENTARY NOTATION				
17. COSATI CODES		18. SUBJECT TERMS (Continue on reverse if necessary and identify by block number)		
FIELD	GROUP	SUB-GROUP		
		VLF Propagation Dispersion		
		LF Minimum shift keying Earth-ionosphere waveguide		
		ELF TACAMO		
19. ABSTRACT (Continue on reverse if necessary and identify by block number)				
<p>The effects of propagation conditions in the ELF/VLF/LF frequency band on the design and performance of digital communications systems are described in this report. Also, discussed in this report is the communications channel from a ground-based or airborne transmitting antenna through the earth-ionosphere waveguide to the receiver. Questions about coverage, noise, dispersion, time variance, and propagation disturbances are also summarized here.</p>				
20. DISTRIBUTION/AVAILABILITY OF ABSTRACT <input checked="" type="checkbox"/> UNCLASSIFIED/UNLIMITED <input type="checkbox"/> SAME AS RPT <input type="checkbox"/> DTIC USERS		21. ABSTRACT SECURITY CLASSIFICATION <b>UNCLASSIFIED</b>		
22a. NAME OF RESPONSIBLE INDIVIDUAL F. J. Kelly		22b. TELEPHONE (Include Area Code) (202) 767-2941/2891	22c. OFFICE SYMBOL Code 4183	



## CONTENTS

INTRODUCTION .....	1
ANTENNAS .....	1
PROPAGATION .....	8
Summary .....	8
The Ionosphere and Reflection Coefficients .....	9
Field Strength Calculations Using Waveguide Modes .....	10
Wavehop Coverage Predictions .....	40
Future Needs for Coverage Predictions .....	43
Dispersion and Multipath .....	45
MODULATION TECHNIQUES FOR LONGWAVE SYSTEMS .....	52
Elementary Signal Theory .....	52
Modulation Methods .....	55
MSK Signals .....	55
The MSK Correlation Receiver .....	56
Two Propagation Modes and a Stationary Transmitter .....	59
LONGWAVE FIELD-STRENGTH VARIATIONS FROM AN AIRBORNE ANTENNA [57] .....	59
Theory .....	59
Calculations and Results .....	62
Discussion and Results .....	63
ANTENNA MOTION EFFECTS ON MODULATION SYSTEMS [58] .....	67
Diagrammatic Representations .....	68
Numerical Calculations .....	75
DISTURBANCES .....	104
Solar Flares—Sudden Ionospheric Disturbances .....	105
Polar Cap Absorption Events .....	105
Transition Fading .....	106
Electron Precipitation-Induced Perturbations .....	109
ELF Nighttime and PCA Disturbances .....	110
C-Layer Disturbance .....	110
Ground Conductivity and Weather Effects in Low-Frequency Radio Propagation .....	110
NOISE .....	110
Noise Mitigation .....	113
SYSTEM PERFORMANCE CALCULATION .....	113
ACKNOWLEDGMENTS .....	113
REFERENCES .....	116
APPENDIX — The Importance of the ELF/VLF/LF Band .....	123

1  
2  
3  
4  
5  
6  
7  
8  
9  
10  
11  
12  
13  
14  
15  
16  
17  
18  
19  
20  
21  
22  
23  
24  
25

## ELF/VLF/LF PROPAGATION AND SYSTEM DESIGN

### INTRODUCTION

The utilization of the longwave channel (5 Hz to 300 kHz) for digital radio transmission has greatly increased during the past 20 years. Several large VLF ground based transmitting antennas have been rebuilt, and new facilities have been constructed. The ELF band has been opened up for use. Squadrons of longwave broadcasting aircraft have been procured and operated. A widespread use of new modulation techniques and receivers has been verified. The importance of systems using the longwave band is not widely appreciated, but the statement by Donald C. Latham, Assistant Secretary of Defense for Command, Control, Communication and Intelligence in the Appendix [1], is abundantly clear. It is impossible to present a comprehensive picture of the long wavelength situation today without producing a book as large as A. D. Watt's monumental treatise [2]. However, because many students and readers are unfamiliar with the longwave area, we present a brief introductory discussion of the total longwave communications system including transmitting antennas and radio receivers before discussing in detail the impact of propagation on system design and performance.

### ANTENNAS

The longwave channel antennas are an important component of the overall propagation medium because they provide a basic restriction on types of signals that can be launched. The longwave channel is characterized by the fact that efficient radiation from conventional size man-made structures is difficult to achieve. Great ingenuity has been employed to produce adequately large antenna configurations and to obtain the greatest possible efficiency from antenna systems that are necessarily small in comparison to a wavelength. Figure 1 shows the types of longwave antenna commonly used.

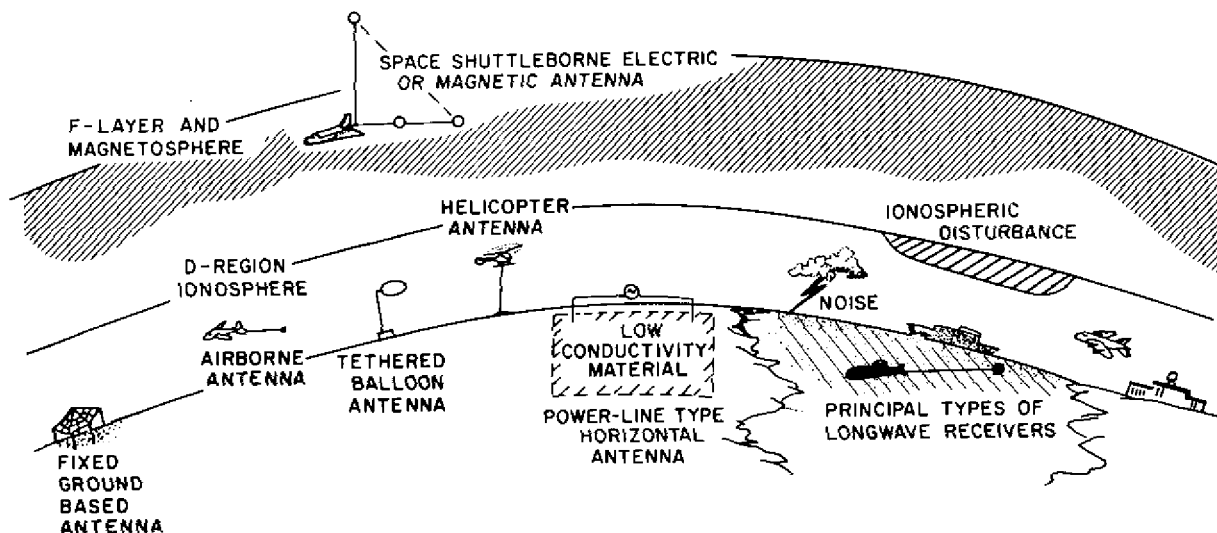


Fig. 1 — Longwave broadcast systems

Many of the fixed/ground based vertical monopole antennas are of the "small antenna" variety characterized by a very small radiation resistance (less than  $1 \Omega$ ). Consequently, these antennas are quite inefficient unless special precautions are taken to reduce utterly all unnecessary losses. One common technique is the construction of a large ground plane to suppress losses in the earth near the antenna. A second feature is the deployment of an elaborate "top hat" consisting of cables connected together and suspended from towers to provide additional antenna capacity to increase wirease the antenna's ability to carry current for a given voltage. In this way the losses are reduced to a minimum and a higher efficiency is achieved. However, a high "Q" antenna system with a consequent low bandwidth results from these procedures. The design considerations for such antennas are summarized in Refs. 1 through 3. Figures 2 through 5 [3] show the four principal ground based antenna types: Triatic, Goliath, Trideco, and valley span. Figures 6 through 11 illustrate the designs of U.S. Navy VLF fixed ground-based antennas.

The suspension of a long conducting cable from an aircraft or other lifting vehicle is an alternative method for making an efficient radiator at long wavelengths. Thus a half wave dipole antenna is achieved with a large radiation resistance and high radiation efficiency without the high "Q" and limited bandwidth of the ground-based tower antennas. This technology is the basis of the TACAMO and airborne command post longwave communication capability as presented in Refs. 5, 6, and 7. The airborne facilities are illustrated in Fig. 12, [5].

An horizontal electric antenna can be used at long waves. This antenna is utilized for the ELF communication system [8,9]. In this system, a powerful current is driven along horizontal wires that like power lines are stretched over the earth's surface and grounded at each end. When the conductivity of the underlying earth is low, it is as if the antenna is suspended at a modest height above the "electrical" earth. The effective image currents flow from one terminal to the other at a depth proportional to the electromagnetic skin depth of the underlying material. This mechanism permits the horizontal antennas to operate with modest efficiency.

In the near future, it will be feasible to deploy a large longwave antenna from an earth orbiting satellite. Italy and the United States (NASA) in a joint program are developing a 60 km conducting tether system for use in space. One of the applications of this tether is the generation of long radio waves [10].

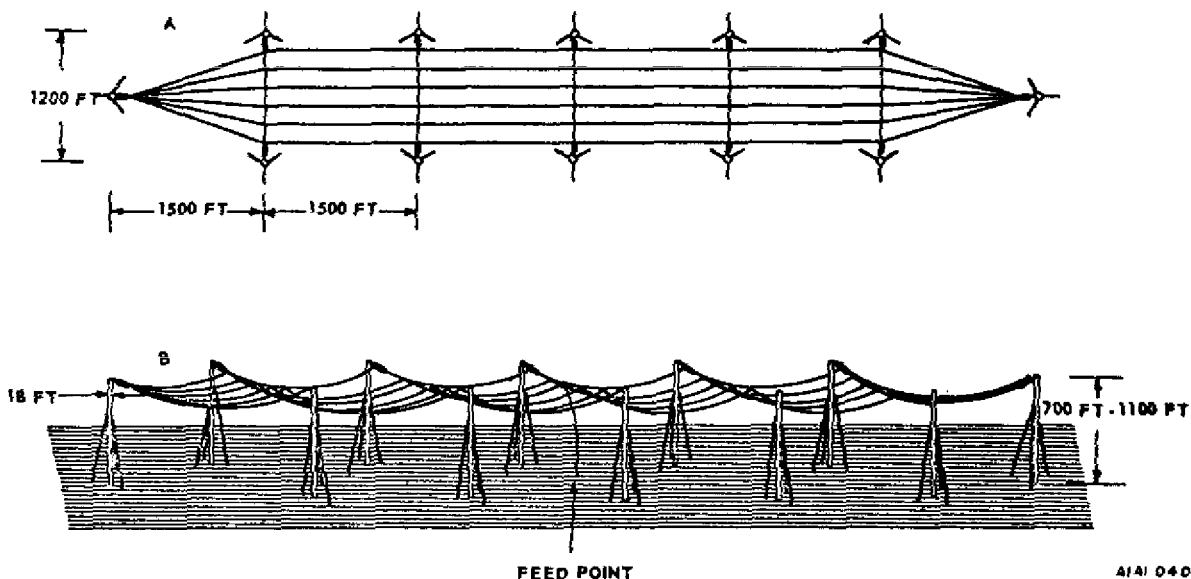


Fig. 2 — Triatic type antenna

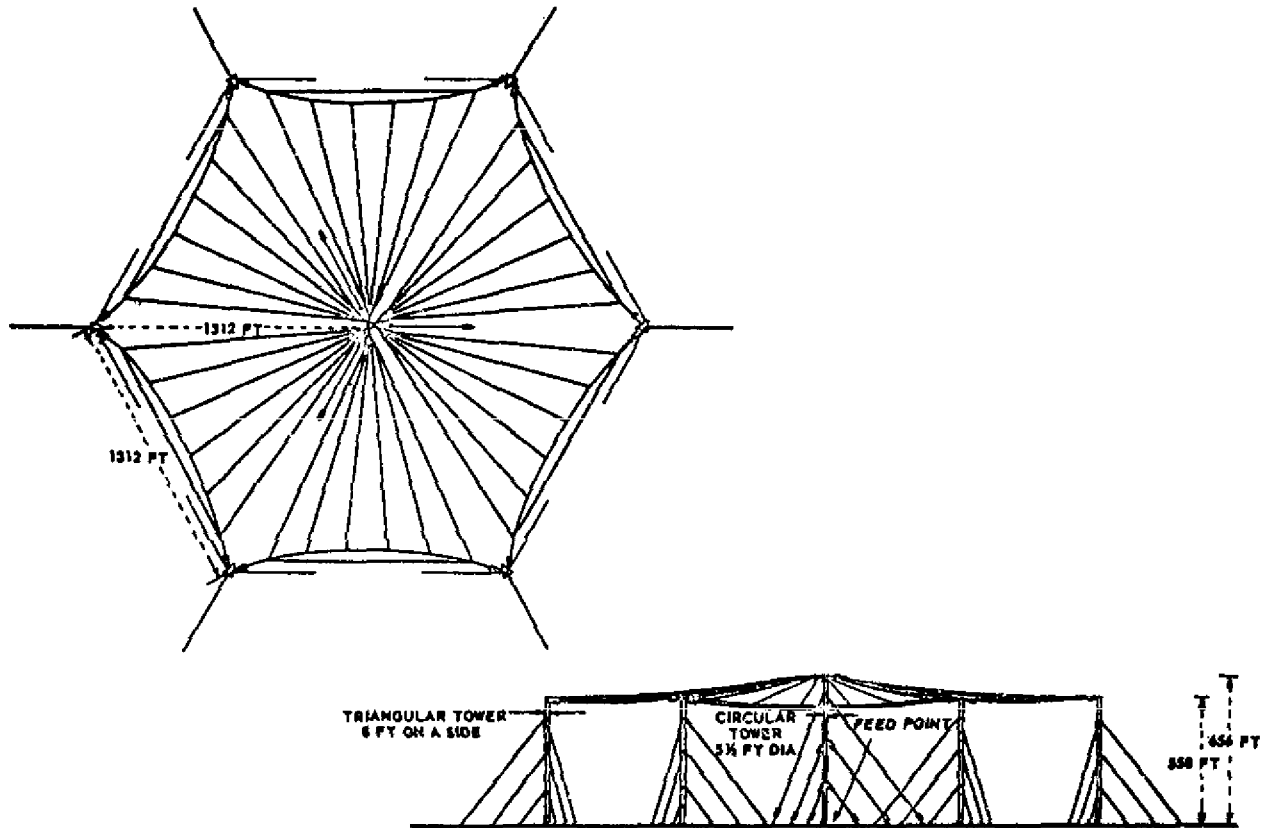


Fig. 3 — Goliath type antenna

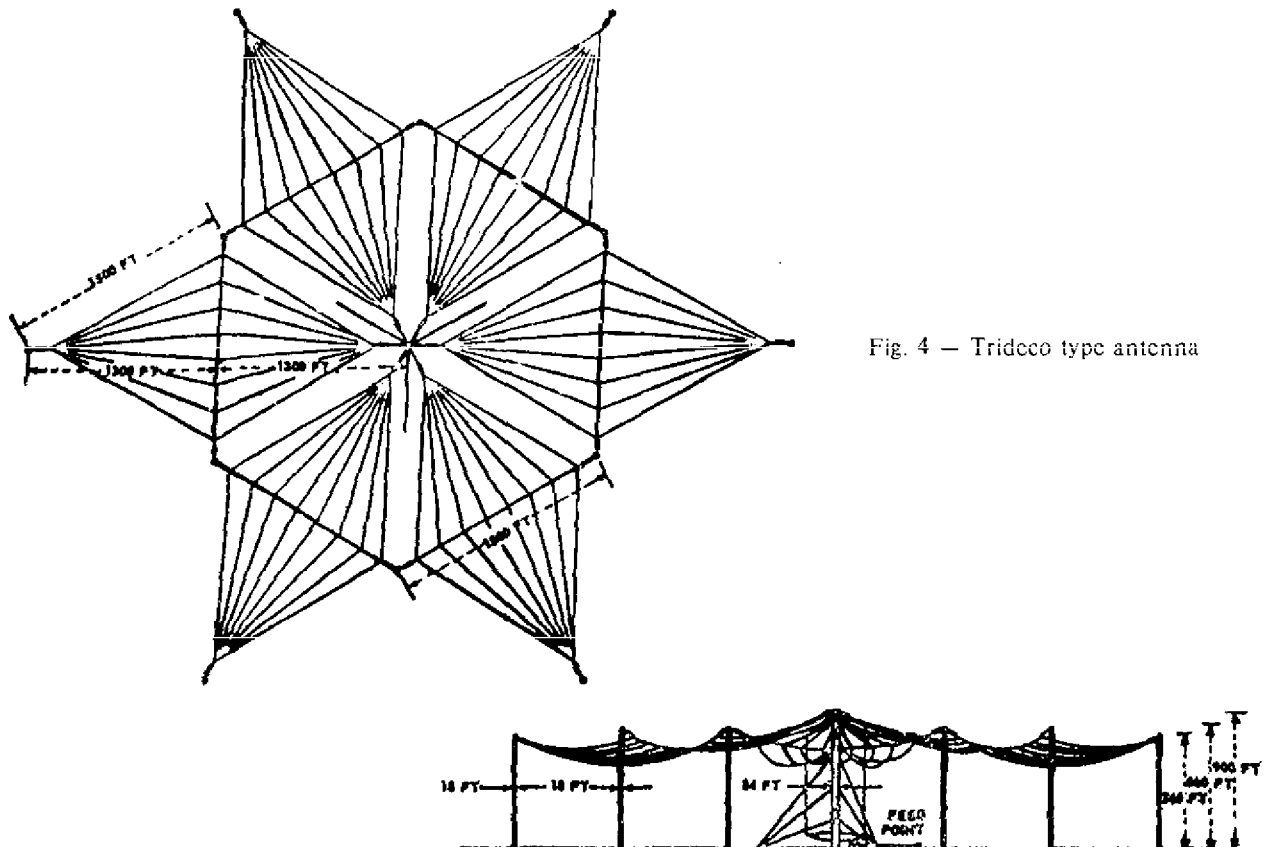


Fig. 4 — Tridcco type antenna



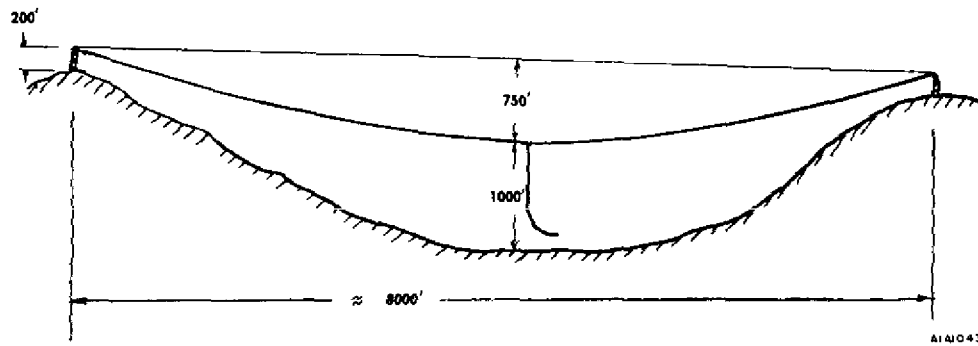


Fig. 5 — Natural valley-span antenna

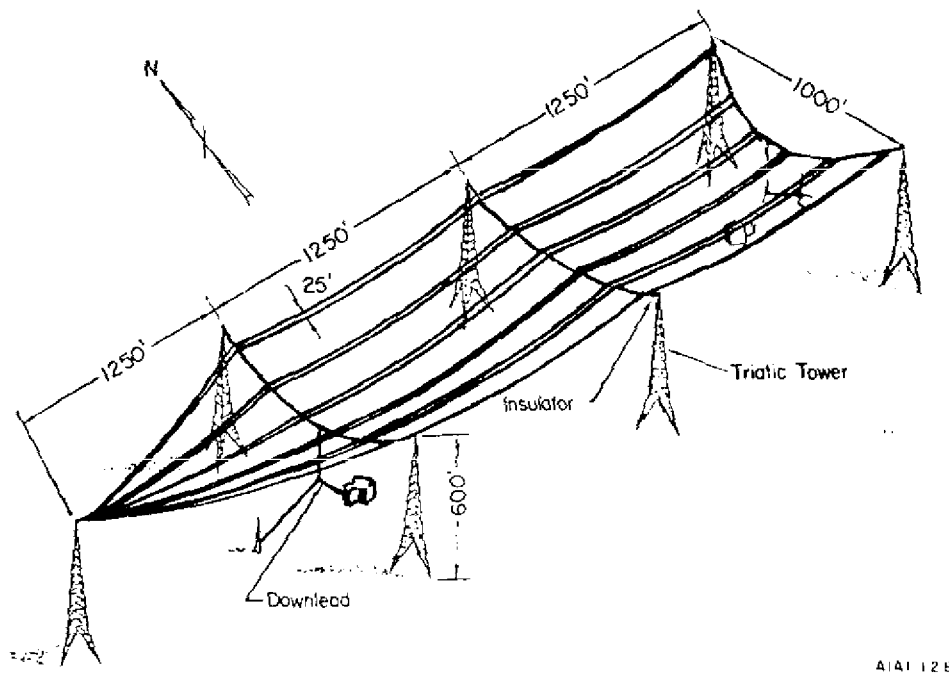


Fig. 6 — Old Luaualei antenna, pictorial view

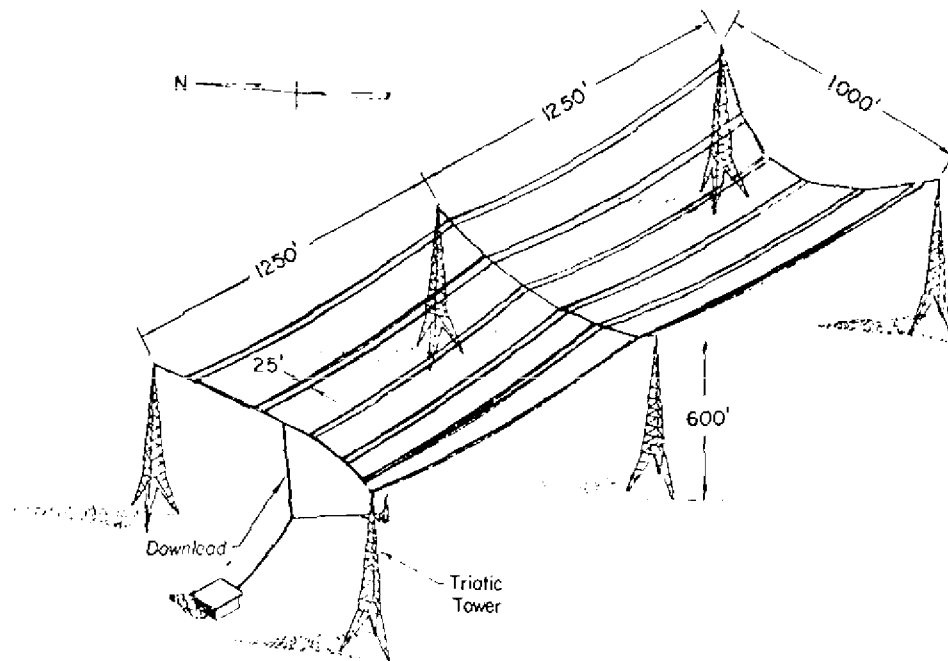


Fig. 7 — Balboa (Summit) antenna, pictorial view

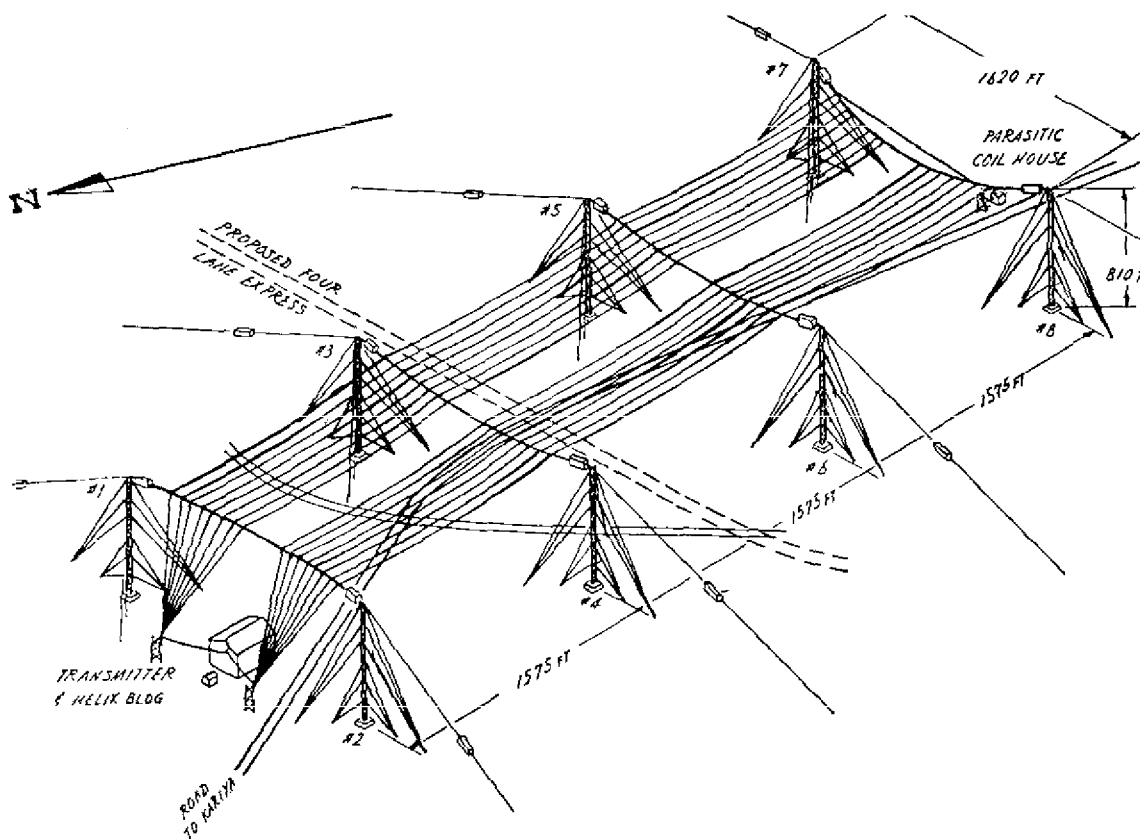


Fig. 8 — Yosami, Japan antenna, pictorial view

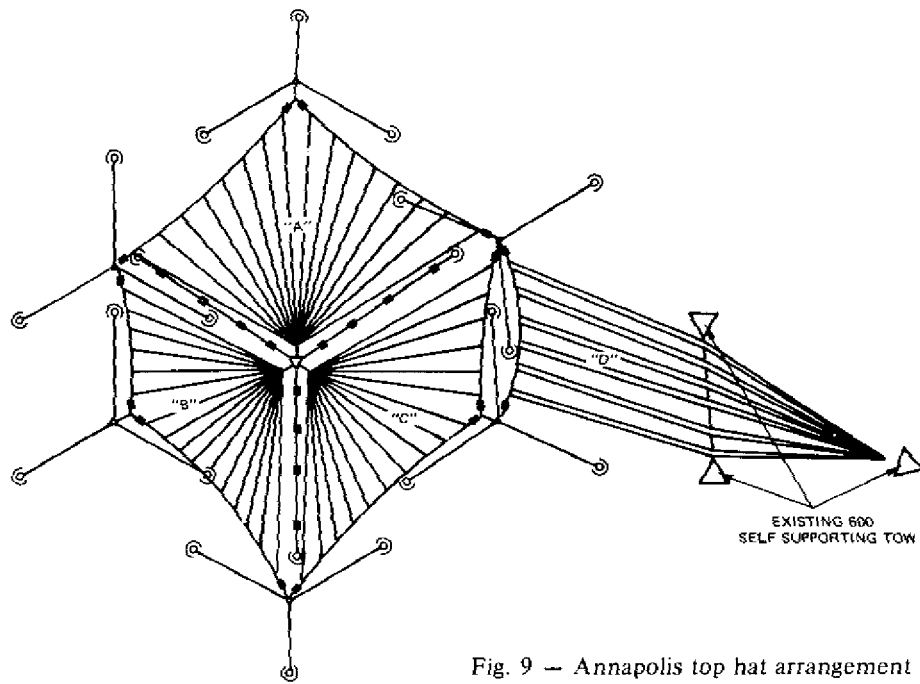


Fig. 9 — Annapolis top hat arrangement

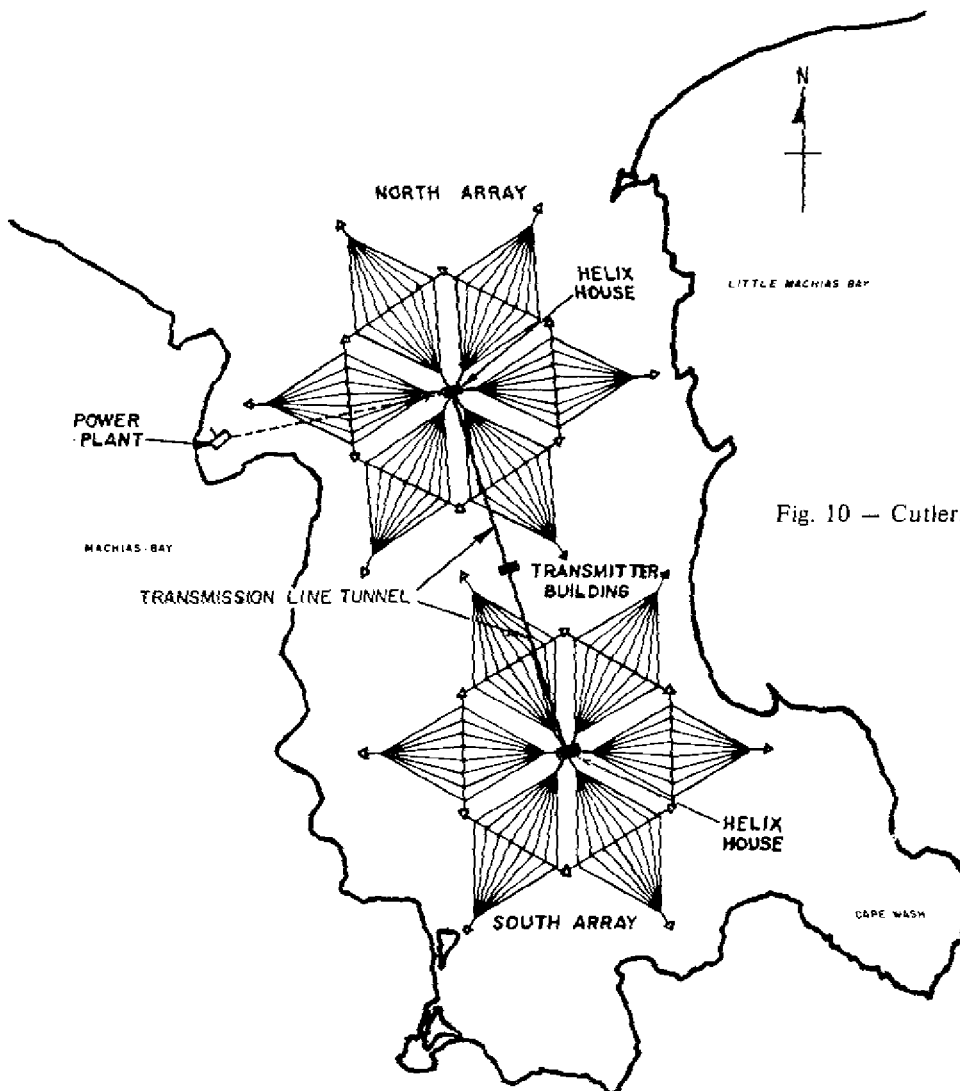


Fig. 10 — Cutler, Maine antenna-installation, plan view

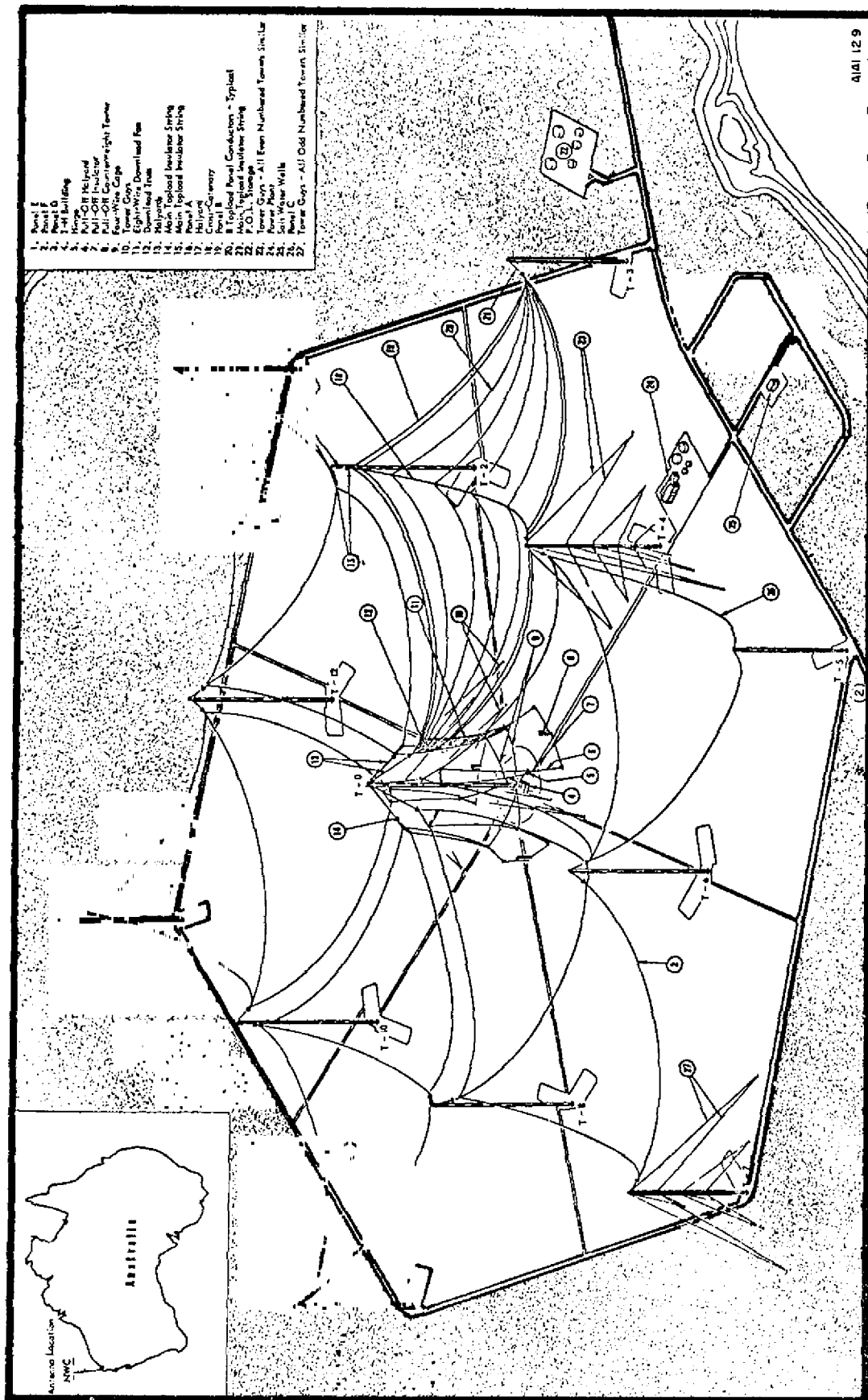


Fig. 11 - NWC Australia antenna

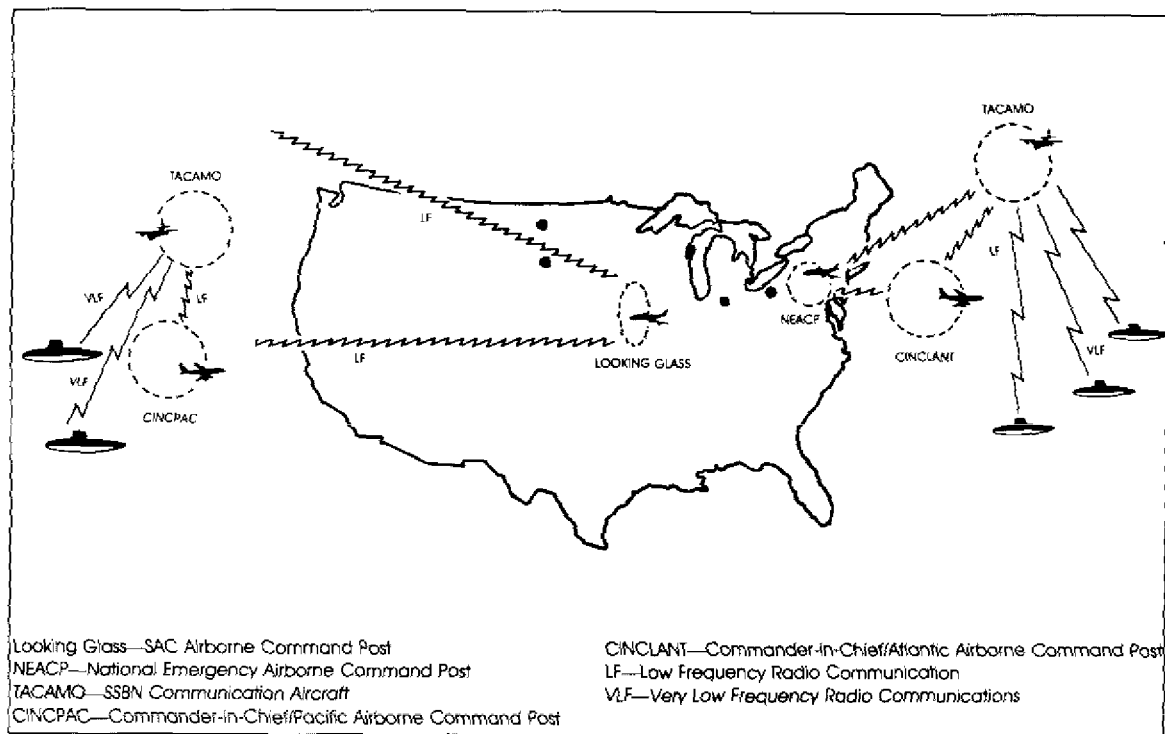


Fig. 12 — Airborne submarine communications. (Figure 3 on p. 28, Vol. 39, No. 7, entitled "Strategic Command and Control and National Security," by Dr. Bruce G. Blair from *Signal*, published by The Armed Forces Communications and Electronics Association Copyright (c) 1985, used by permission.)

## PROPAGATION

### Summary

The first transatlantic radio propagation experiments of Marconi were conducted in the long-wavelength band [2]. In comparison to the short-wave band, the long-wavelength band is highly reliable. Long-distance propagation of a long radio wave relies on a reflection from the lower ionosphere to bring the radio wave back to earth. On the other hand, short-waves are gradually bent back to earth because of a refraction process that depends on the detailed horizontal and vertical gradients of an upper-ionosphere F-layer. A VLF wave spends most of its journey in the free space between the earth's surface and the lower ionosphere. A short-wave propagates mostly through the ionosphere between 70 and 300 km height, between the D-layer and the F-layer. This is probably the basic reason that long-wavelength waves show greater stability of reception. The disadvantages of long waves (which were deadly from an ordinary economic point of view) are:

- (a) Large antenna structure
- (b) Narrow bandwidths
- (c) Limited total spectrum
- (d) High powers required to overcome noise.

The advantages of long waves are:

- (a) Great propagation range (even to the antipodes)
- (b) High phase stability
- (c) Significant ability to penetrate earth and seawater.

The long propagation range and phase stability for long wavelength waves make their use for navigation feasible (Omega, Decca, and Loran). Their penetration into the earth makes the waves useful to prospectors looking for ore-bodies or other deposits beneath the earth.

### The Ionosphere and Reflection Coefficients

The layers ascribed to the ionosphere and atmosphere are illustrated in Fig. 13 [11]. The ionospheric reflection coefficients are defined as the ratio of downcoming electric field to the upgoing field. Because there are two orthogonal upgoing and downcoming field components, four complex reflection coefficients characterize the process at any given angle of incidence. The matrix form is as follows:

$$\begin{pmatrix} E_{\parallel}^d \\ E_{\perp}^d \end{pmatrix} = \begin{pmatrix} R_{\parallel\parallel} & R_{\perp\parallel} \\ R_{\parallel\perp} & R_{\perp\perp} \end{pmatrix} \begin{pmatrix} E_{\parallel}^u \\ E_{\perp}^u \end{pmatrix} \quad (1)$$

where

- $E_{\parallel}^u$  is the upgoing electric field in the plane of incidence;
- $E_{\perp}^u$  is the upgoing electric field perpendicular to the plane of incidence (i.e., the horizontal electric field);
- $E_{\parallel}^d$  is the downcoming electric field in the plane of incidence;
- $E_{\perp}^d$  is the downcoming electric field perpendicular to the plane of incidence.

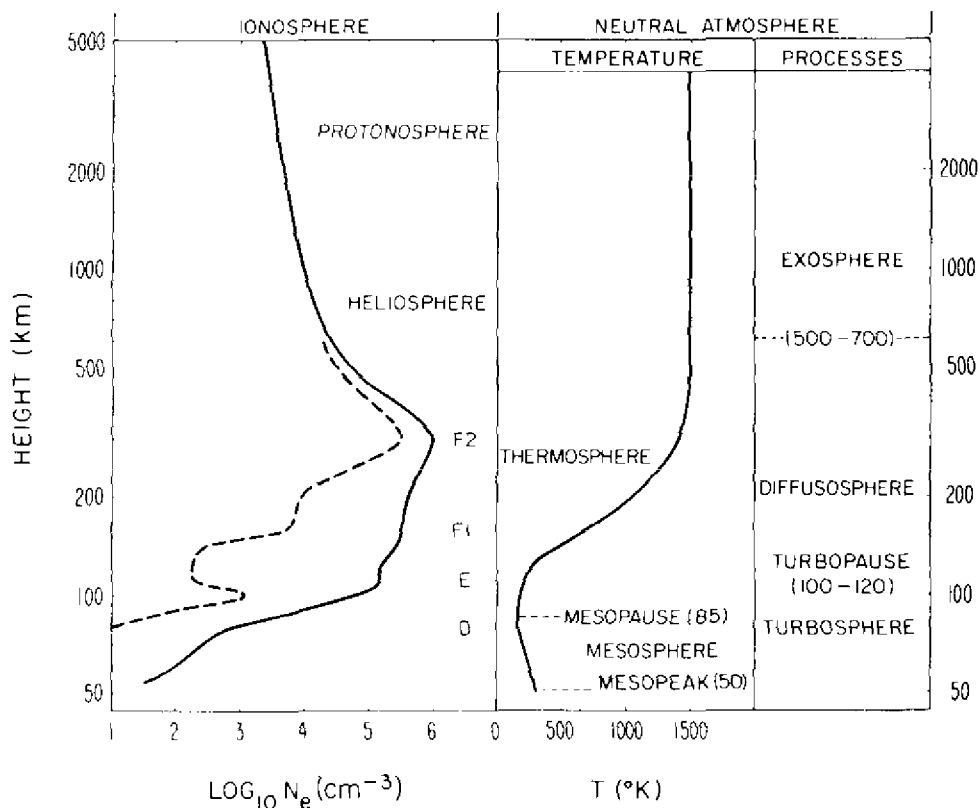


Fig. 13 — Atmospheric layers and nomenclature

The reflection coefficients are functions of the electron and ion density profiles of the ionosphere. The collision frequency profiles, geomagnetic field and angle of incidence must also be specified. Several full-wave techniques can be used to calculate the reflection coefficient matrix. It is beyond the range of this lecture to describe these methods in depth. Figures 14 through 16 show sample calculations of reflection coefficients versus incidence angle at 3 kHz for a geomagnetic dip angle of  $60^\circ$ . (Ref. 12) Figure 17 shows two reflection coefficients as a function of frequency for fixed incidence angle of approximately  $30^\circ$ . (Ref. 13) The ionospheric profile used for each calculation is shown in Fig. 18. Notice that the calculated reflection coefficients above about 30 kHz are strongly varying with frequency. They seem to reflect the detailed structure of the ionosphere. The smooth approximation by Allcock and Belrose (Ref. 14) seems adequate for a first approximation; but it lacks the oscillations noted in the fullwave results. During nighttime long radio waves are transmitted through the lower ionosphere with small loss. Space-borne receivers can readily hear ground-based transmitters. Likewise receivers on the ground can sense many curious electrical noises that are generated and stimulated in the ionosphere and magnetosphere. For these ground-to-space and space-to-ground paths the lower ionosphere transmission coefficient is significant in forming a signal power budget. This transmission coefficient can be calculated using Pitteway's full wave method. (Ref. 15). Sample transmission coefficient results for a 3 kHz case are shown in Figs. 19 and 20.

### Field Strength Calculations using Waveguide Modes

For long range propagation calculations it is customary [16] to treat the space between the earth and the ionosphere as a waveguide and to calculate the field strengths from a transmitter as a summation of waveguide modes. A popular method for achieving this is by using the WAVEGUIDE computer program.

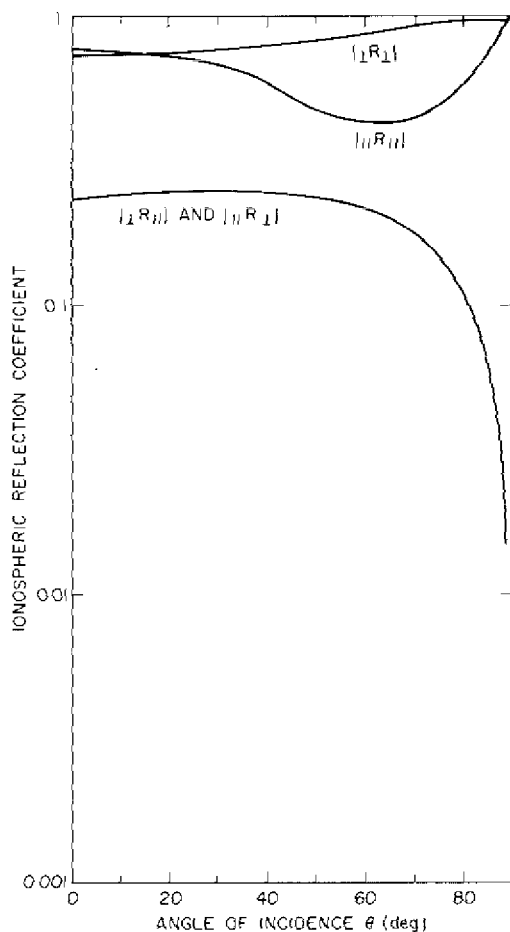


Fig. 14 — 3 kHz nighttime ionospheric reflection coefficients, west-to-east propagation

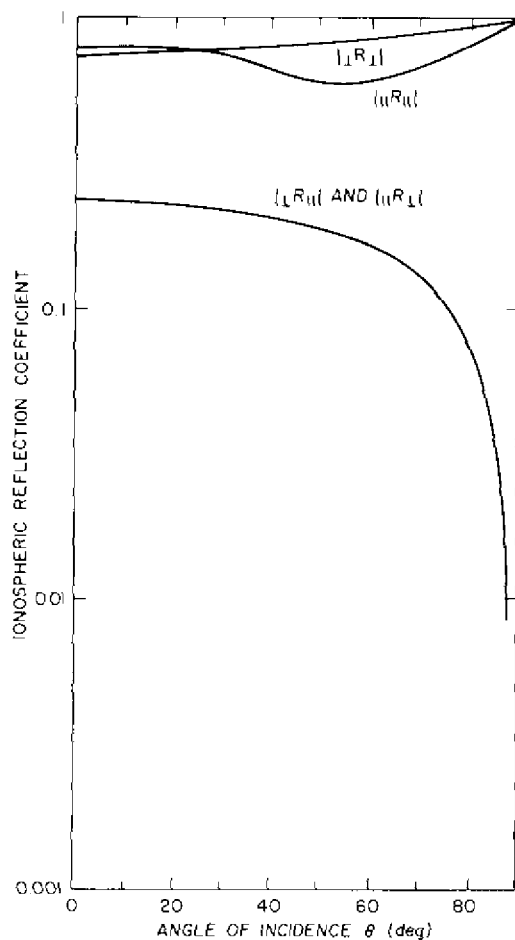
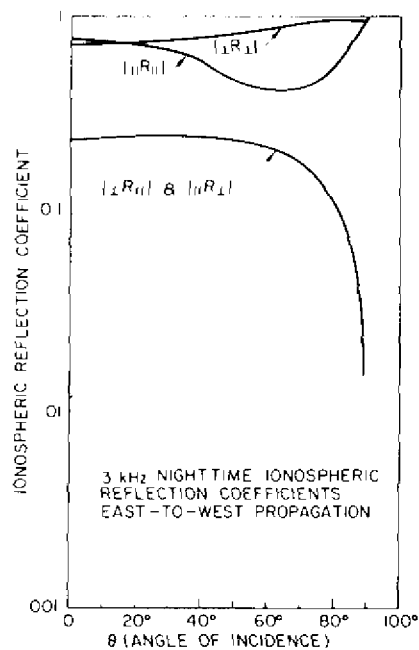


Fig. 15 — 3 kHz nighttime ionospheric reflection coefficients, south-to-north propagation

Fig. 16 — 3 kHz nighttime ionospheric reflection coefficients, east-to-west propagation





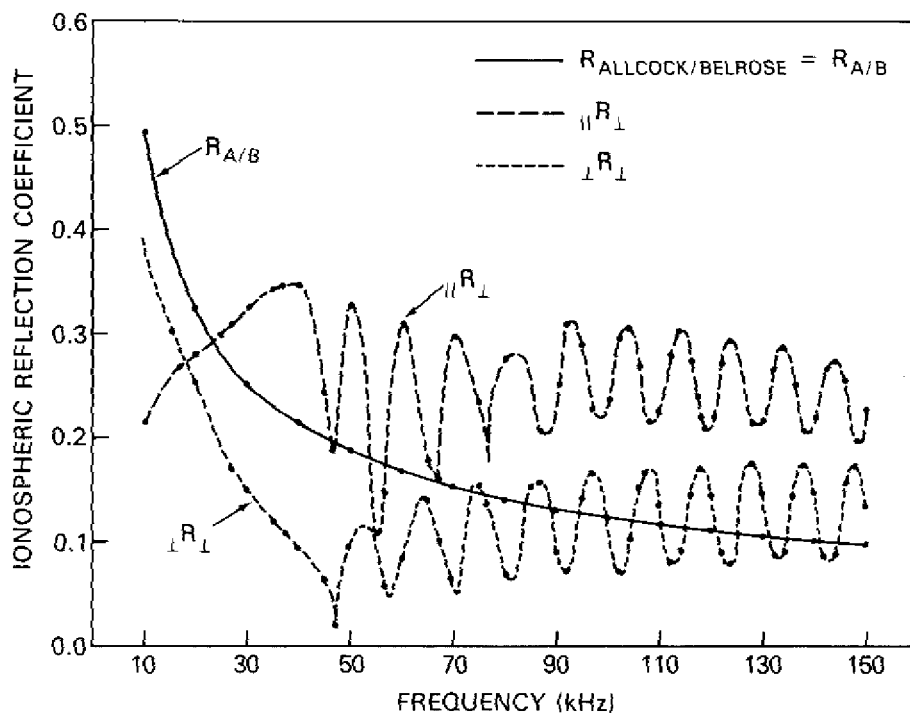


Fig. 17 — Reflection coefficients vs frequency. The  $R_{A/B}$  curve is a plot of an empirical reflection coefficient approximation given by Belrose [14] using an equivalent frequency concept of Allcock. The  $||R_{\perp}$  and  $\perp R_{\perp}$  reflection coefficients follow the convention of Ref. 15.

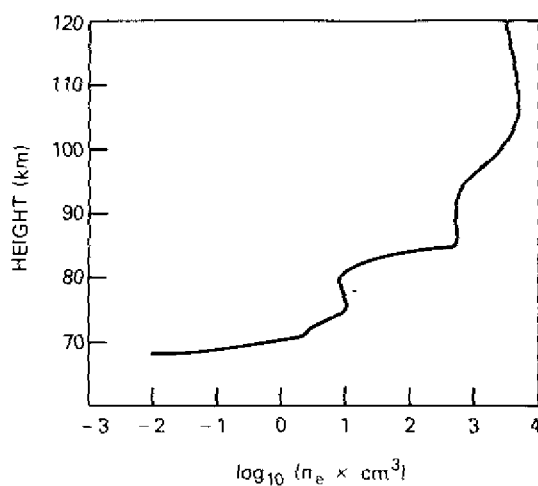


Fig. 18 — Electron density profile for nighttime calculations

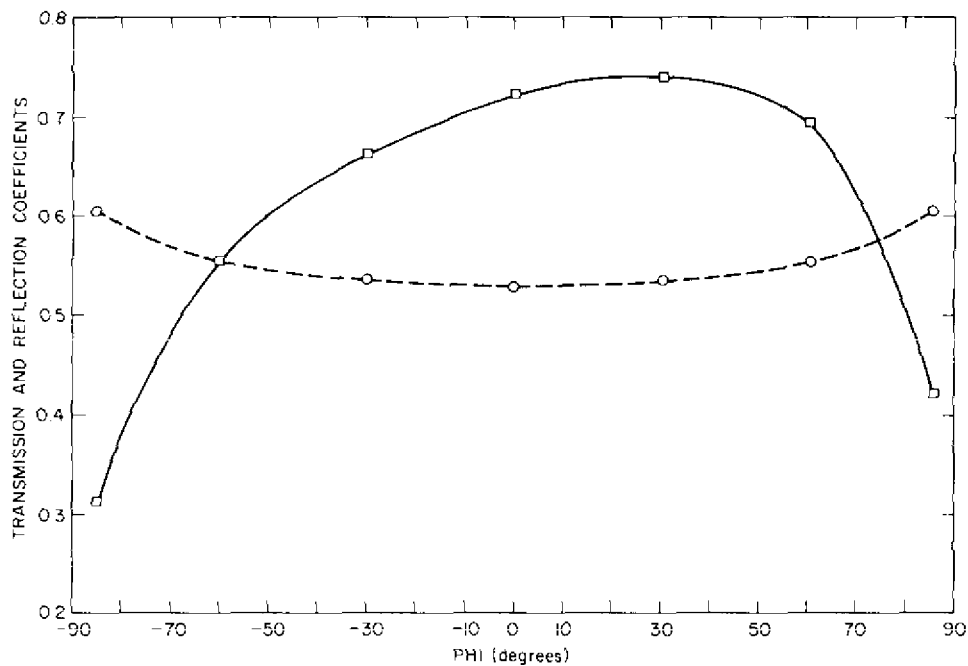


Fig. 19 — Transmission coefficient (solid line) and reflection coefficient (dashed line) vs angle of incidence from vertical (PHI) for frequency of 3 kHz, dip angle =  $60^\circ$ , and azimuth =  $0^\circ$  (measured from magnetic north)

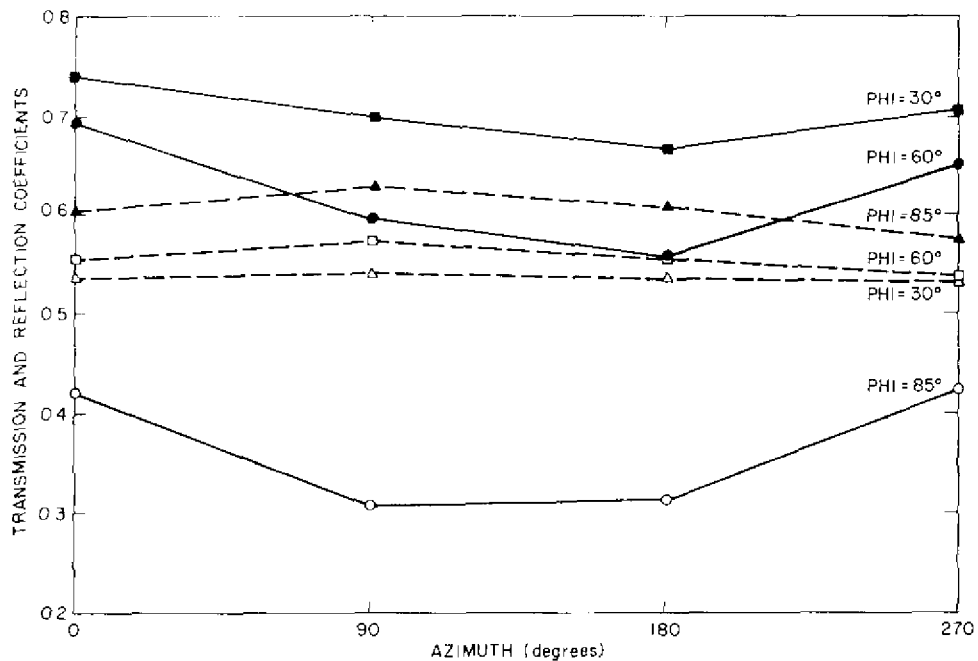


Fig. 20 — Transmission coefficients (solid lines) and reflection coefficients (dashed lines) vs azimuth (measured from magnetic north) for frequency of 3 kHz, dip angle =  $60^\circ$ , and angle of incidence from vertical (PHI) =  $30^\circ$ ,  $60^\circ$ , and  $85^\circ$

## Description of WAVEGUIDE

The WAVEGUIDE computer program originally was developed at the Naval Electronics Laboratory Center to predict the vertical electric field received at a point on the earth's surface and produced by a vertical electric transmitting antenna at another point on the earth's surface. Later it was extended to give the crosspolarized (horizontal) components of the field at any height in the earth-ionosphere waveguide and even in the ionosphere [17-19]. The basic formulation of the equations for the fields is given in Ref. 20. The net resultant vertical electric field at the earth's surface is represented as a summation of waveguide-mode fields:

$$E_z(0) = \frac{i\sqrt{\mu_0/\epsilon_0}}{\sqrt{d\lambda h}} Ids \sqrt{\frac{d/a}{\sin(d/a)}} \sum_n [\sin^{3/2} \theta_n \Lambda_n \exp(i\pi/4 + ik_0 d \sin \theta_n)], \quad (2)$$

where

- $\theta_n$  is the eigenangle of the  $n$ th waveguide mode,
- $Ids$  is the dipole moment (ampere-meter) of the vertical antenna located on the earth's surface,
- $\Lambda_n$  is the excitation factor of the  $n$ th waveguide mode,
- $a$  is the radius of the earth,
- $d$  is the great-circle distance between the transmitter and the receiver,
- $h$  is the reference height of the ionosphere (used in the definition of  $\Lambda_n$ ),
- $k_0$  ( $= \omega/c$ ) is the free-space propagation constant of the wave,
- $\lambda$  is the wavelength of the wave,

and

$\mu_0$  and  $\epsilon_0$  are the magnetic permeability and dielectric constant of free space.

Each waveguide mode is characterized by its own value of attenuation rate  $\alpha_n$  and phase velocity  $v_p^n$ , which are related to the eigenangle of the  $n$ th waveguide mode  $\theta_n$  according to

$$\alpha_n = 0.02895 \omega \operatorname{Im}(\sin \theta_n) \quad (3)$$

and

$$v_p^n = \frac{c}{\operatorname{Re}(\sin \theta_n)}, \quad (4)$$

where  $\alpha_n$  is measured in decibels per 1000 km (dB/Mm) and  $c$  is the speed of light.

The values of the waveguide-mode eigenangles depend on the reflection coefficients of the ground and the ionosphere. Because of its anisotropy, the ionosphere has four reflection coefficients  $_{||}R_{||}(\theta_n)$ ,  $_{\perp}R_{\perp}(\theta_n)$ ,  $_{||}R_{\perp}(\theta_n)$ , and  $_{\perp}R_{||}(\theta_n)$  for a given angle of incidence  $\theta_n$ . The ground is assumed to be isotropic and to have reflection coefficients  $_{||}\bar{R}_{||}(\theta_n)$  and  $_{\perp}\bar{R}_{\perp}(\theta_n)$ , that are calculable from the eigenangle, ground conductivity, and dielectric constant. The WAVEGUIDE program uses a procedure for calculating the ground and ionospheric reflection coefficients referenced to any height  $z$  in the waveguide. References 26, 27, and 28 discuss the reflection coefficients further. The eigenangle  $\theta_n$  for a given waveguide mode is obtained by satisfying the mode equation

$$0 = \begin{bmatrix} _{||}R_{||}(\theta_n) & _{\perp}R_{||}(\theta_n) \\ _{||}R_{\perp}(\theta_n) & _{\perp}R_{\perp}(\theta_n) \end{bmatrix} \begin{bmatrix} _{||}\bar{R}_{||}(\theta_n) & 0 \\ 0 & _{\perp}\bar{R}_{\perp}(\theta_n) \end{bmatrix} - \begin{bmatrix} 1 & 0 \\ 0 & 1 \end{bmatrix}. \quad (5)$$

This matrix equation is simply rewritten

$$F(\theta_n) = (_{||}R_{||} _{||}\bar{R}_{||} - 1) (_{\perp}R_{\perp} _{\perp}\bar{R}_{\perp} - 1) - _{\perp}R_{||} _{\perp}\bar{R}_{\perp} _{||}R_{\perp} _{||}\bar{R}_{||} = 0, \quad (6)$$

where the dependence of the reflection coefficient on  $\theta_n$  has been suppressed to simplify the notation. The new variable  $F(\theta_n)$  is also defined. Each value of  $\theta_n$  which satisfies Eq. (6) is the eigenangle of the  $n$ th waveguide mode. The excitation factor  $\Lambda_n$  for the  $n$ th waveguide mode is obtained from

$$\Lambda_n = -i \frac{kh}{2} \sin \theta_n \frac{(1 + {}_{\parallel}\bar{R}_{\parallel})^2 (1 - {}_{\perp}\bar{R}_{\perp} \bar{R}_{\perp})}{{}_{\parallel}\bar{R}_{\parallel} \left. \frac{\partial F(\theta)}{\partial \theta} \right|_{\theta=\theta_n}}, \quad (7)$$

where the variable  $F(\theta)$  is as defined in Eq. (6). In addition to the vertical electric field  $E_z$  for a given waveguide mode having eigenangle  $\theta_n$ , in general, there exist five other nonzero field components  $E_x$ ,  $E_y$ ,  $H_x$ ,  $H_y$ , and  $H_z$  within the waveguide for each mode.

These extra fields arise because the ionosphere is anisotropic because of the earth's magnetic field. Propagation through and reflection from such an anisotropic medium rotates the plane of polarization of the incident wave to generate crosspolarized reflected fields. Alternatively one could consider the linearly polarized wave transmitted from the vertical electric dipole antenna to be a linear superposition of right-handed and left-handed circularly polarized waves, each reflected with a different amplitude at the ionosphere. The ionospheric reflection causes a mixture of wave polarizations at a reception point on or above the earth's surface. The fields at height  $z$  are related to the vertical electric fields at the earth's surface  $E_z(0)$  in a given waveguide mode by the following functions of reflection coefficients and Hankel functions:

$$E_z(z)/E_z(0) = f_{\parallel}(z), \quad (8)$$

$$E_x(z)/E_z(0) = g(z)/S, \quad (9)$$

$$E_y(z)/E_z(0) = \frac{{}_{\parallel}R_{\perp} (1 + {}_{\perp}\bar{R}_{\perp}) f_{\perp}(z)}{S(1 + {}_{\parallel}\bar{R}_{\parallel}) (1 - {}_{\perp}\bar{R}_{\perp} R_{\perp})}, \quad (10)$$

$$H_z(z)/E_z(0) = - \frac{{}_{\parallel}R_{\perp} (1 + {}_{\perp}\bar{R}_{\perp}) f_{\perp}(z)}{\eta(1 + {}_{\parallel}\bar{R}_{\parallel}) (1 - {}_{\perp}\bar{R}_{\perp} R_{\perp})}, \quad (11)$$

$$H_y(z)/E_z(0) = \frac{f_{\parallel}(z)}{\eta S}, \quad (12)$$

and

$$H_x(z)/E_z(0) = \frac{{}_{\parallel}R_{\perp} (1 + {}_{\perp}\bar{R}_{\perp})}{i \eta k S (1 + {}_{\parallel}\bar{R}_{\parallel}) (1 - {}_{\perp}\bar{R}_{\perp} R_{\perp})} \frac{df_{\perp}(z)}{dz}, \quad (13)$$

where

$$f_{\parallel}(z) = \exp\left\{\frac{z-D}{a}\right\} \frac{F_1 h_1(q) + F_2 h_2(q)}{F_1 h_1(q_d) + F_2 h_2(q_d)}, \quad (14)$$

$$f_{\perp}(z) = \frac{F_3 h_1(q) + F_4 h_2(q)}{F_3 h_1(q_d) + F_4 h_2(q_d)}, \quad (15)$$

and

$$g(z) = \frac{1}{ik} \frac{d}{dz} [f_{\parallel}(z)], \quad (16)$$

in which

$$F_1 = - \left\{ H_2(q_0) - i \frac{n_0^2}{N_g^2} \left( \frac{ak}{2} \right)^{1/3} (N_g^2 - S^2)^{1/2} h_2(q_0) \right\}, \quad (17)$$

$$F_2 = H_1(q_0) - i \frac{n_0^2}{N_g^2} \left( \frac{ak}{2} \right)^{1/3} (N_g^2 - S^2)^{1/2} h_1(q_0), \quad (18)$$

$$F_3 = - \left\{ h'_2(q_0) - i \left( \frac{ak}{2} \right)^{1/3} (N_g^2 - S^2)^{1/2} h_2(q_0) \right\}, \quad (19)$$

$$F_4 = h'_1(q_0) - i \left( \frac{ak}{2} \right)^{1/3} (N_g^2 - S^2)^{1/2} h_1(q_0), \quad (20)$$

$$q = \left( \frac{2}{ak} \right)^{-2/3} \left[ C^2 - \frac{2}{a}(h - z) \right], \quad (21)$$

and

$$q_d = \left( \frac{2}{ak} \right)^{-2/3} \left[ C^2 - \frac{2}{a}(h - D) \right], \quad (22)$$

with

$$q_0 = \left( \frac{2}{ak} \right)^{-2/3} \left[ C^2 - \frac{2h}{a} \right], \quad (23)$$

$$H_j(q) = h'_j(q) + \frac{1}{2} \left( \frac{2}{ak} \right)^{2/3} h_j(q), \quad j = 1, 2, \quad (24)$$

$$n^2 = 1 - \frac{2}{a}(h - z), \quad (25)$$

$$n_0^2 = 1 - \frac{2}{a} h, \quad (26)$$

and

$$N_g^2 = \epsilon/\epsilon_0 - j \frac{\sigma}{\omega\epsilon}. \quad (27)$$

In Equation 27  $\sigma$  and  $\epsilon$  refer to the conductivity and dielectric constant of the earth.

#### Typical Waveguide Mode Parameters

Using the WAVEGUIDE program, one can calculate the propagation parameters of the various modes. Figures 21 through 23 [21] give the excitation factors and attenuation rates for the three lowest order waveguide modes in the ELF band and lower VLF band. Figures 24 through 26 show the behavior of the magnetic fields vs height in the waveguide and inside the lower ionosphere. The nighttime ionosphere as shown in Fig. 18 was used. The direction of propagation is toward magnetic north for a dip angle of 60°. Using these propagation parameters and Eqs. (7-27), one can estimate the field strength produced by a transmitter. Additional equations and sample parameters for this task are given in Ref. 16.

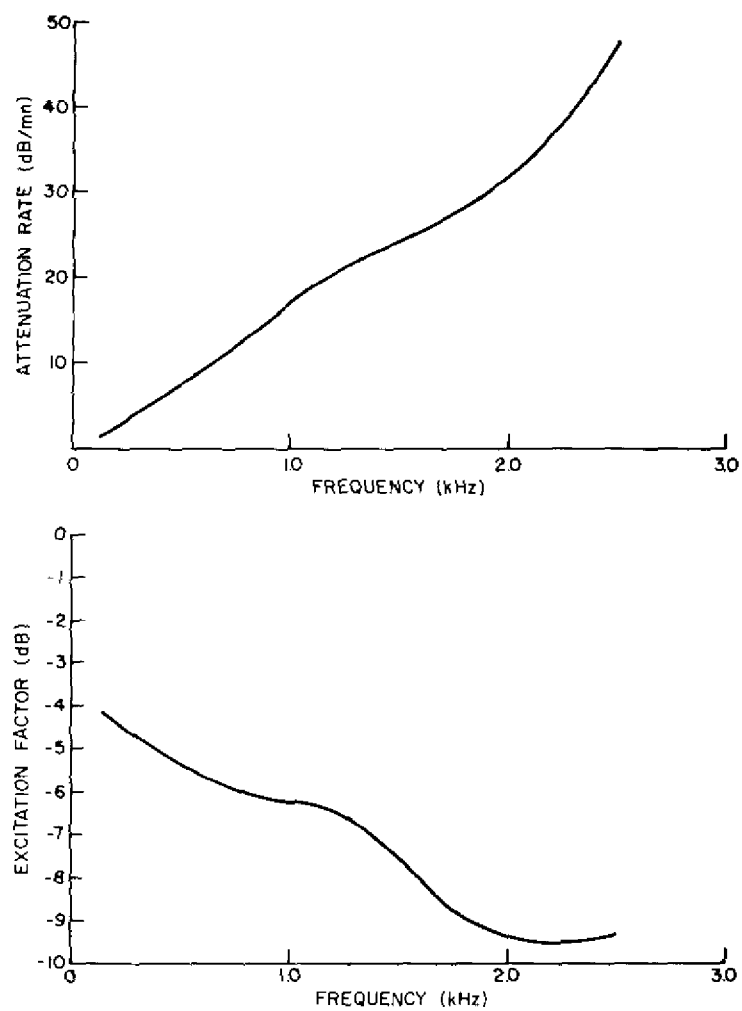


Fig. 21 — Lowest order TEM mode propagation parameters vs frequency

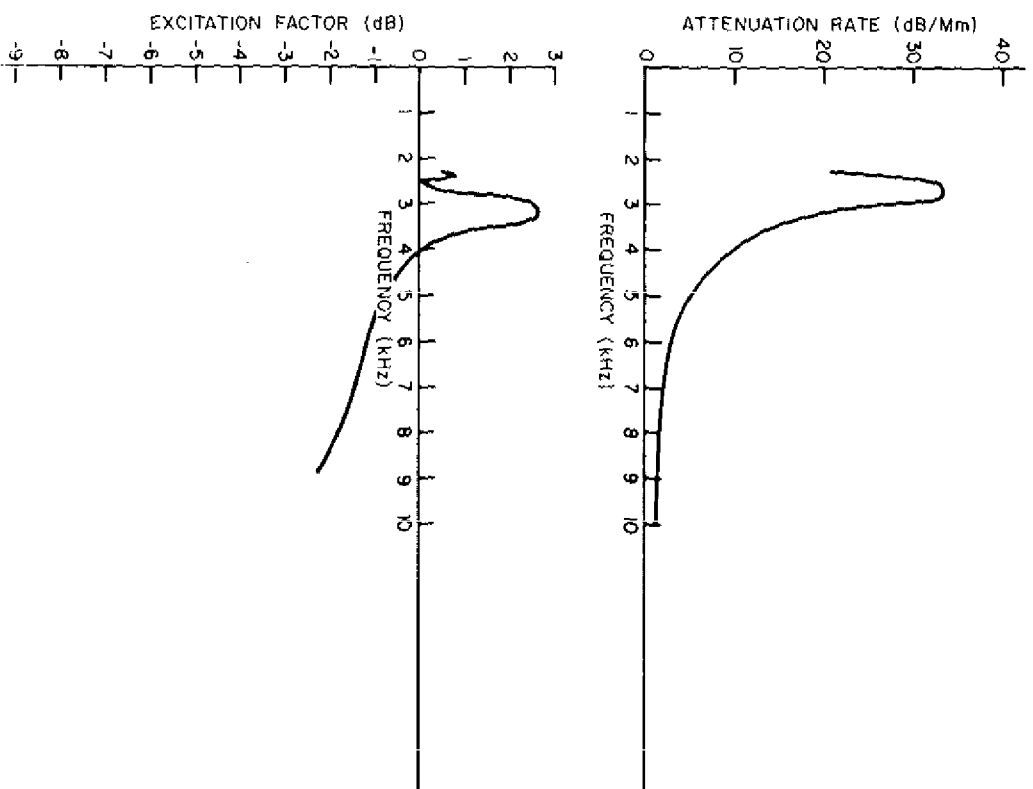


Fig. 22 — First-order TM mode propagation parameters vs frequency

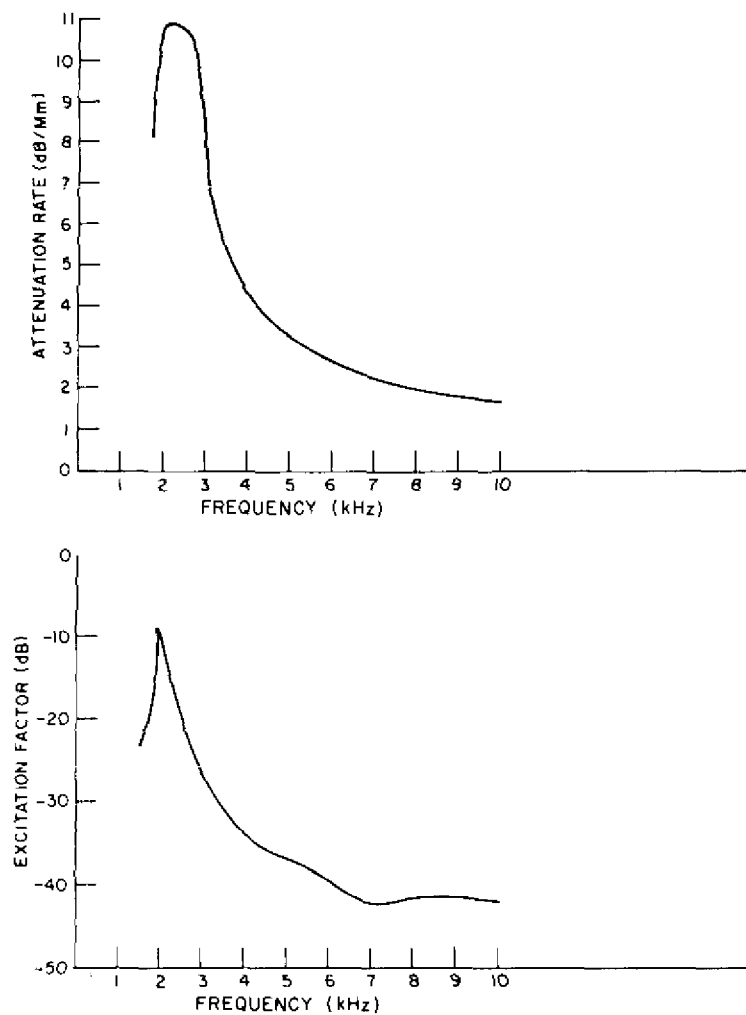


Fig. 23 — First-order TE mode propagation parameters vs. frequency



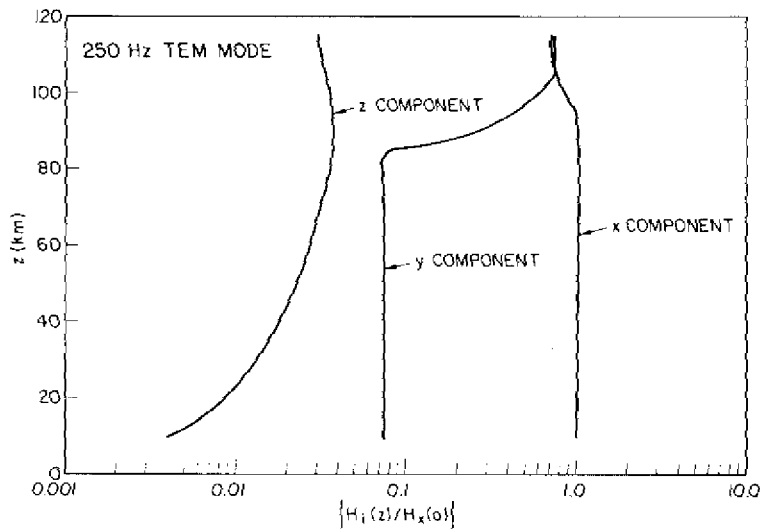


Fig. 24 — Relative excitation efficiencies vs height of the zero-order TEM mode at 0.25 kHz

Fig. 25 — Relative excitation efficiency vs height of the first-order TE mode at 6.0 kHz

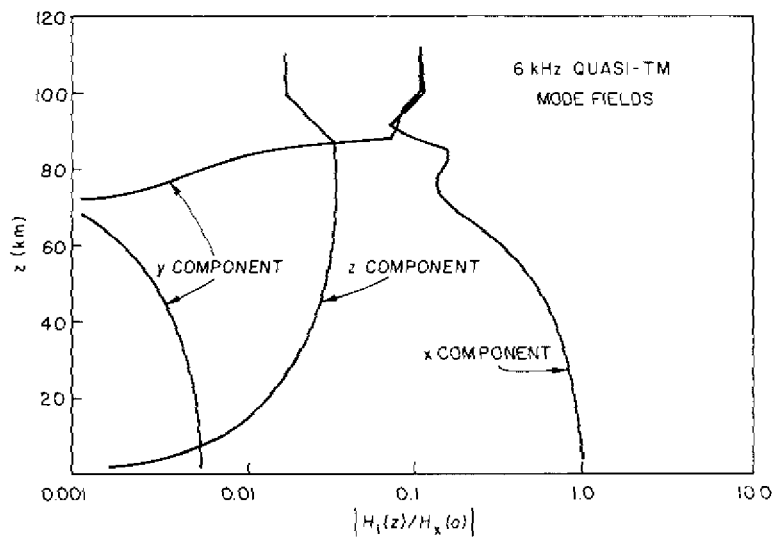
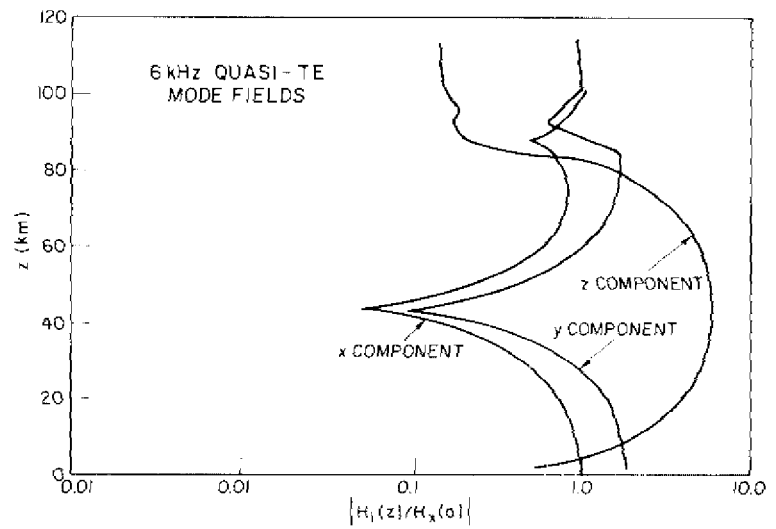


Fig. 26 — Relative excitation efficiency vs height of the first-order TM mode at 6.0 kHz

Figures 27 through 35 give propagation parameters for the first three waveguide modes calculated for a typical daytime isotropic ionosphere and used in the noise prediction computer program described in Ref. 22. These are similar to but more comprehensive than the parameters given in Ref. 23.

### Field Strength Calculations and Measurements

As shown in Ref. 24, field strength vs distance curves are calculated from these parameters. Figures 36 through 41 [25] illustrate the pattern of field strength vs distance for 1 kW radiated power transmitter propagating over sea water at 24.0 kHz. The very sharp predicted interference null at 2.4 Mm is noted in Fig. 36. Using the parameters given in Ref. 23, a statistical prediction of field strength vs distance was made by a Monte Carlo technique. A Gaussian distribution of height  $h$  and conductivity gradient  $\beta$  was assumed to have an average  $h = 70$  km and average  $\beta = .5 \text{ km}^{-1}$ . The standard deviation of  $h$  was 1 km and of  $\beta$  was  $.05 \text{ km}^{-1}$ . This method predicted the greatest variability of signal level to occur near the interference nulls at 2.4 and 3.8 Mm. Experimental data were taken for a period during summer 1970 near the 2.4 Mm null produced by the NBA, Balboa transmitter that was operating on 24.0 kHz [26]. The measured standard deviation was much smaller than that predicted from the model. It was also smaller than that observed with long-term data-taking. From this data, it was concluded that during the short period of this experiment the ionosphere was highly repeatable, even though it showed greater variability over longer durations.

### DCA Recommended Ionospheres

From an analysis of field strength vs distance data similar to those shown in Figs. 42 and 43, the U.S. Defense Communications Agency [27] recommended the ionosphere profiles shown in Table 1. Graphs showing these ionosphere parameters are shown in Figs. 44 and 45, [27]. The electron density  $N(z)$  vs height  $z$  in kilometers for a particular  $\beta$  and  $h$  is given by Eq. (28).

$$N(z) = \left\{ 1.43 \cdot 10^7 \frac{e1}{\text{cm}^3} \cdot \exp(-0.15 h) \right\} \left\{ \exp[(\beta - 0.15)(z - h)] \right\}. \quad (28)$$

Table 1 — DCA [27] Recommended Profiles to Use in WAVEGUIDE OR WAVEHOP Propagation Programs

	DAYTIME		NIGHTTIME	
	Summer	Winter	Summer	Winter
High Latitude	$\beta = 0.3, h' = 72$	$\beta = 0.3, h' = 72$	$\beta = 0.5,$	$h' = 87$
Low Latitude	$\beta = 0.5, h' = 70$	$\beta = 0.3, h' = 72$		

The collision frequency vs height is given by Eq. (29).

$$\nu(z) = \nu_o \exp(-\alpha z) \quad (29)$$

where

$$\nu_o = 1.82 \times 10^{11} \text{ collision/s} \quad \alpha = 0.15 \text{ km}^{-1}$$

From an analysis of multifrequency midlatitude day and nighttime data [28] that was conducted later during flights from Hawaii to California, recommendations were derived which are given in Table 2. It is significant that for nighttime the laterally homogeneous ionospheric profile must be assumed to changes with broadcast frequency. This unphysical situation reflects our current lack of understanding of the nighttime lower ionosphere.

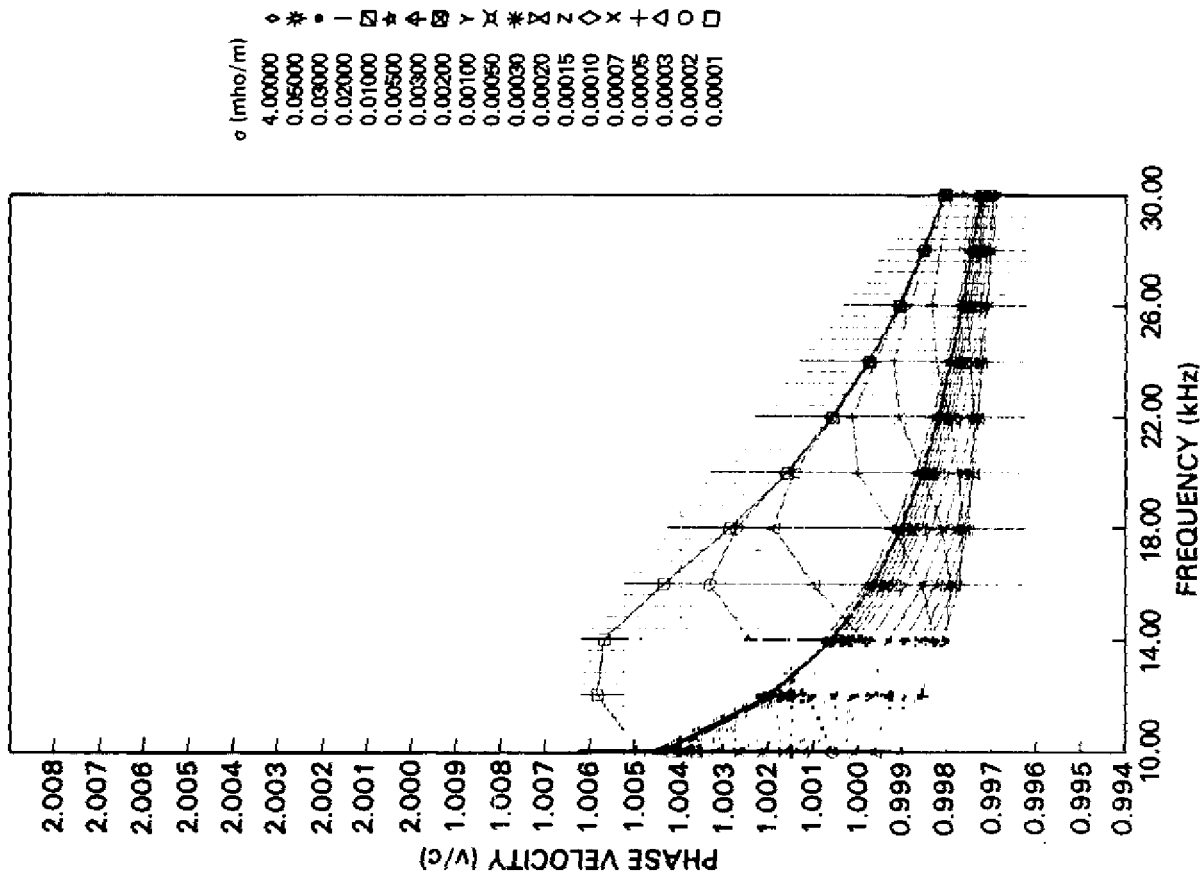


Fig. 27 — Attenuation rate for the first-order TM mode vs frequency and ground conductivity for an isotropic daytime ionosphere

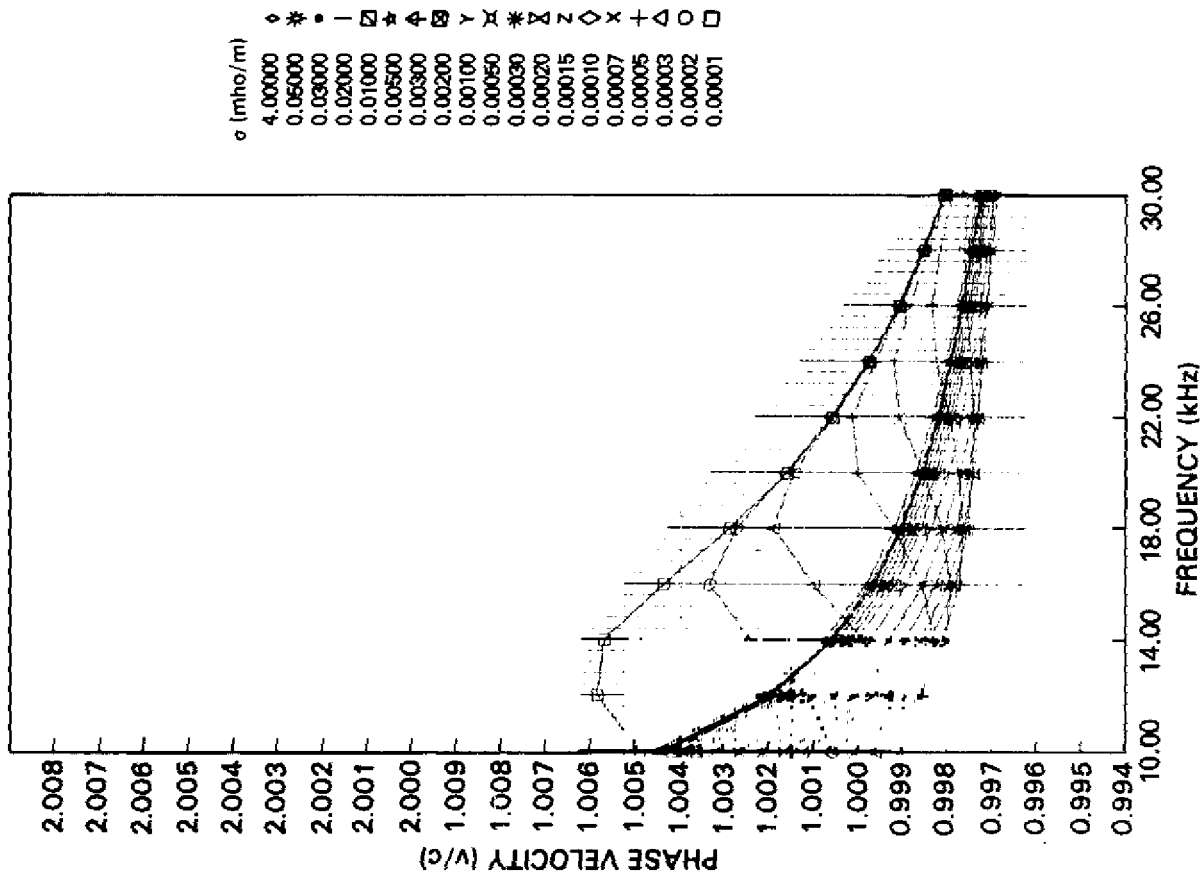


Fig. 28 — Phase velocity for the first-order TM mode vs frequency and ground conductivity from isotropic daytime ionosphere

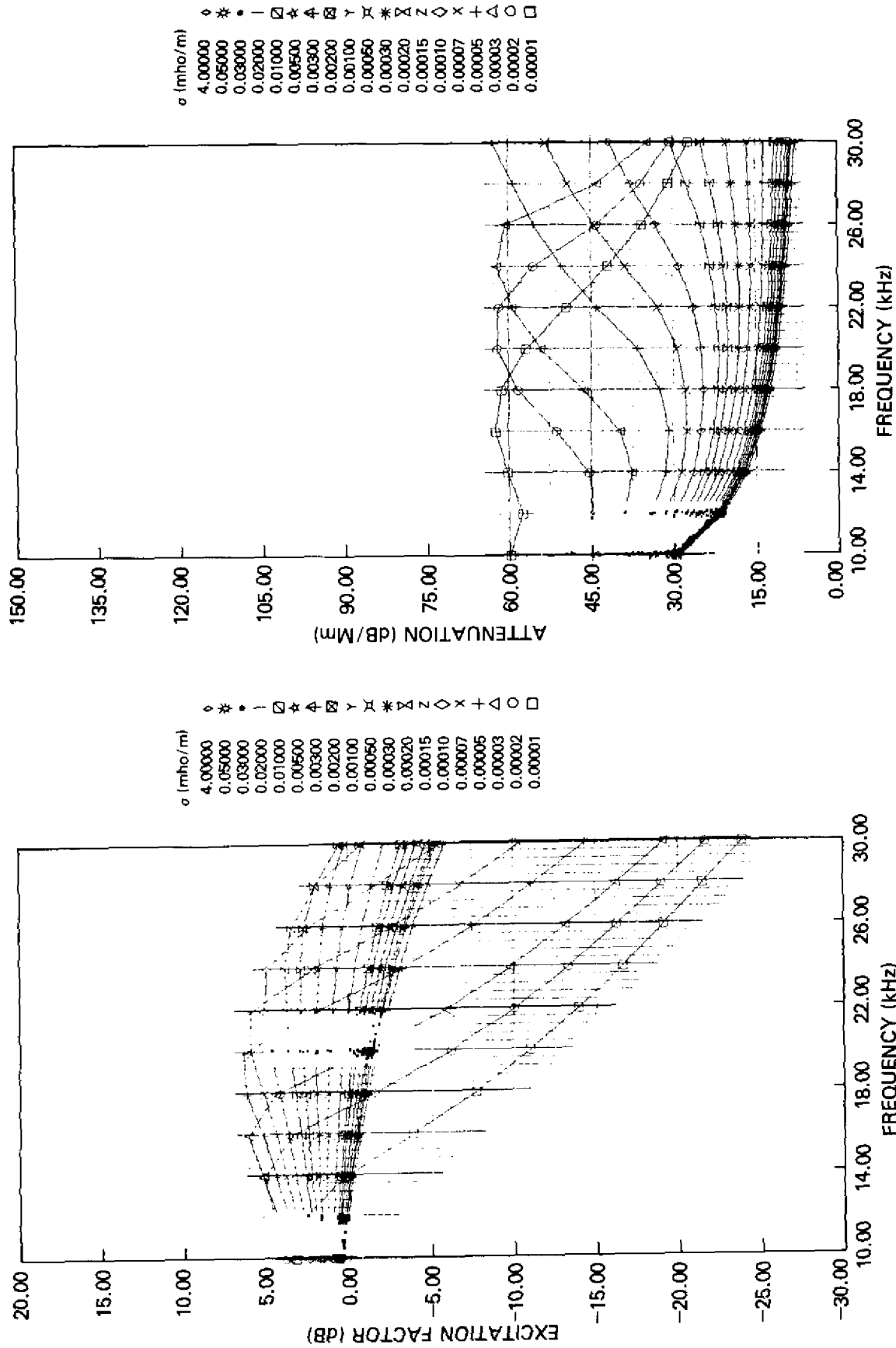


Fig. 29 — Excitation factor for the first-order TM mode vs frequency and ground conductivity from isotropic daytime ionosphere

Fig. 30 — Attenuation rate for the second-order TM mode vs frequency and ground conductivity for an isotropic daytime ionosphere

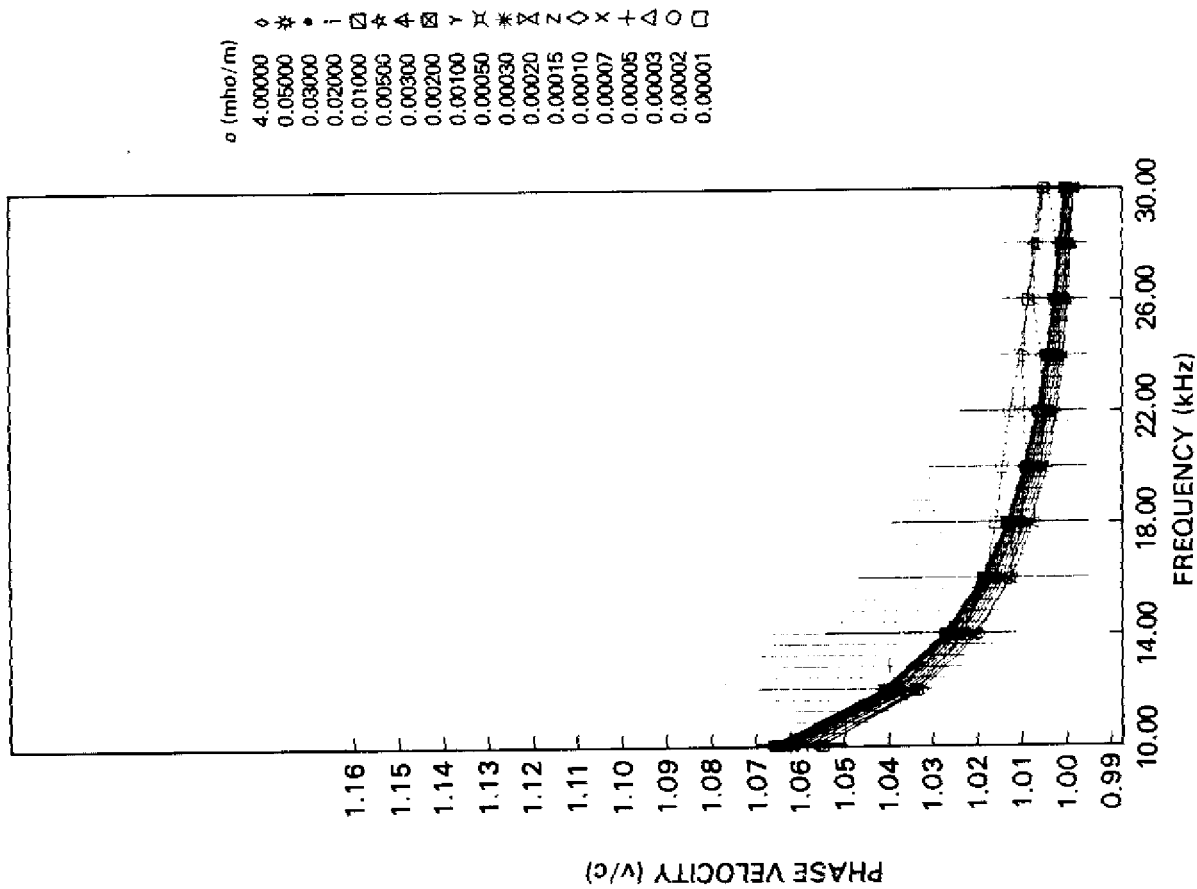


Fig. 31 — Phase velocity for the second-order TM mode vs frequency and ground conductivity for an isotropic daytime ionosphere

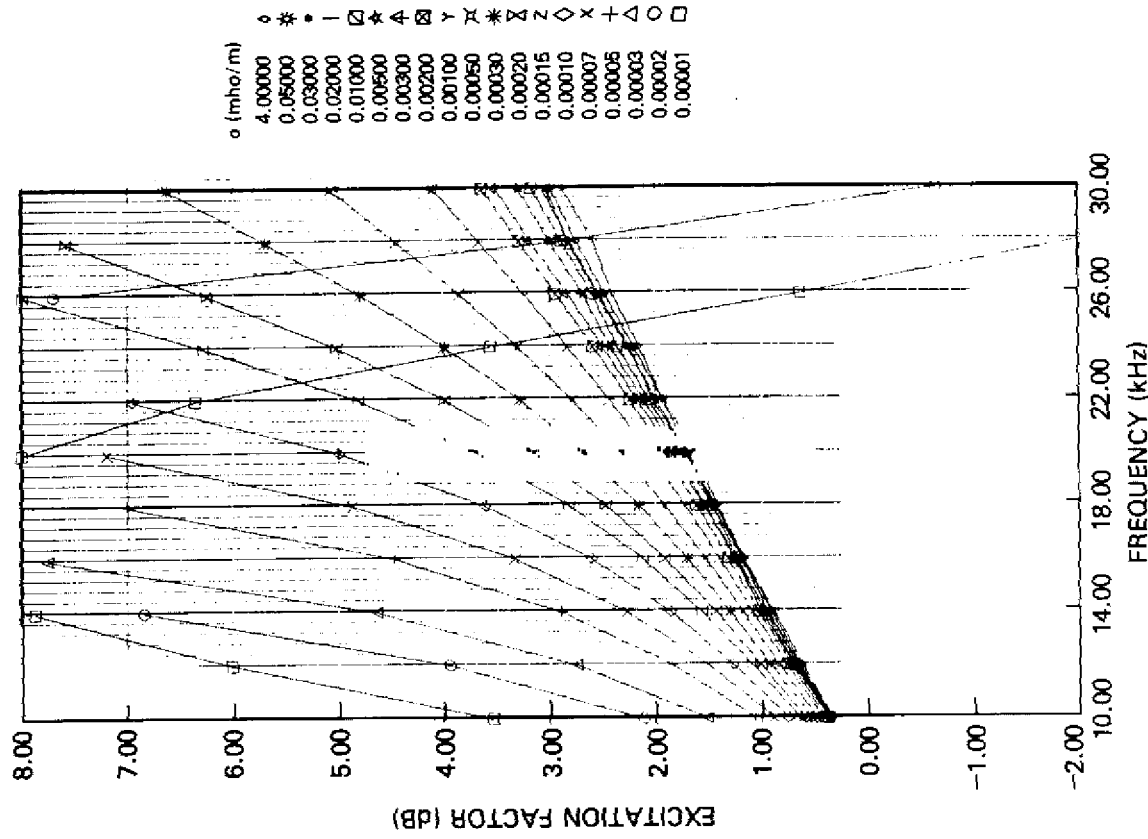


Fig. 32 — Excitation factor for the second-order TM mode vs frequency and ground conductivity for an isotropic daytime ionosphere

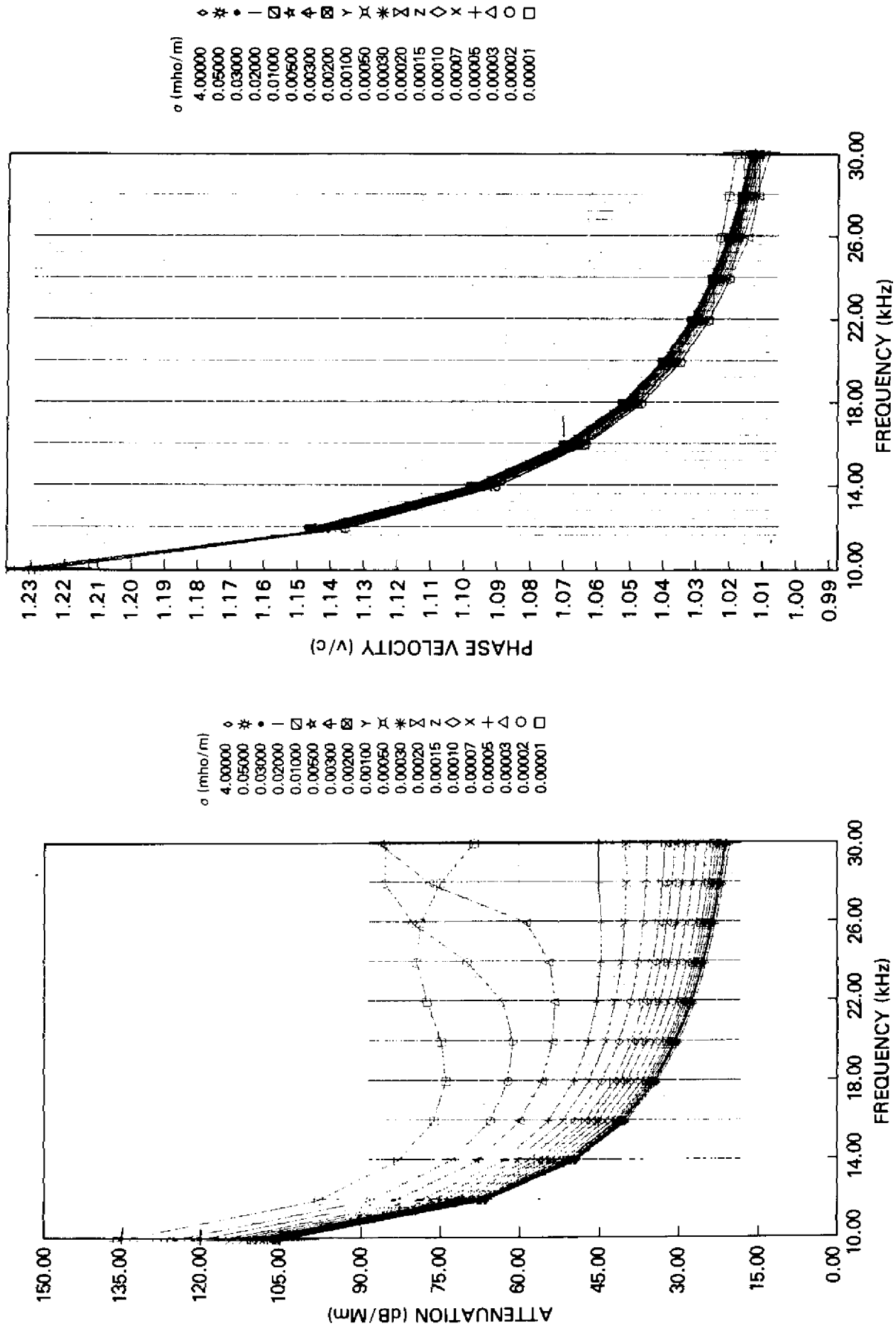


Fig. 34 — Phase velocity for the third-order TM mode vs frequency and ground conductivity from isotropic daytime ionosphere

Fig. 33 — Attenuation rate for the third-order TM mode vs frequency and ground conductivity for an isotropic daytime ionosphere

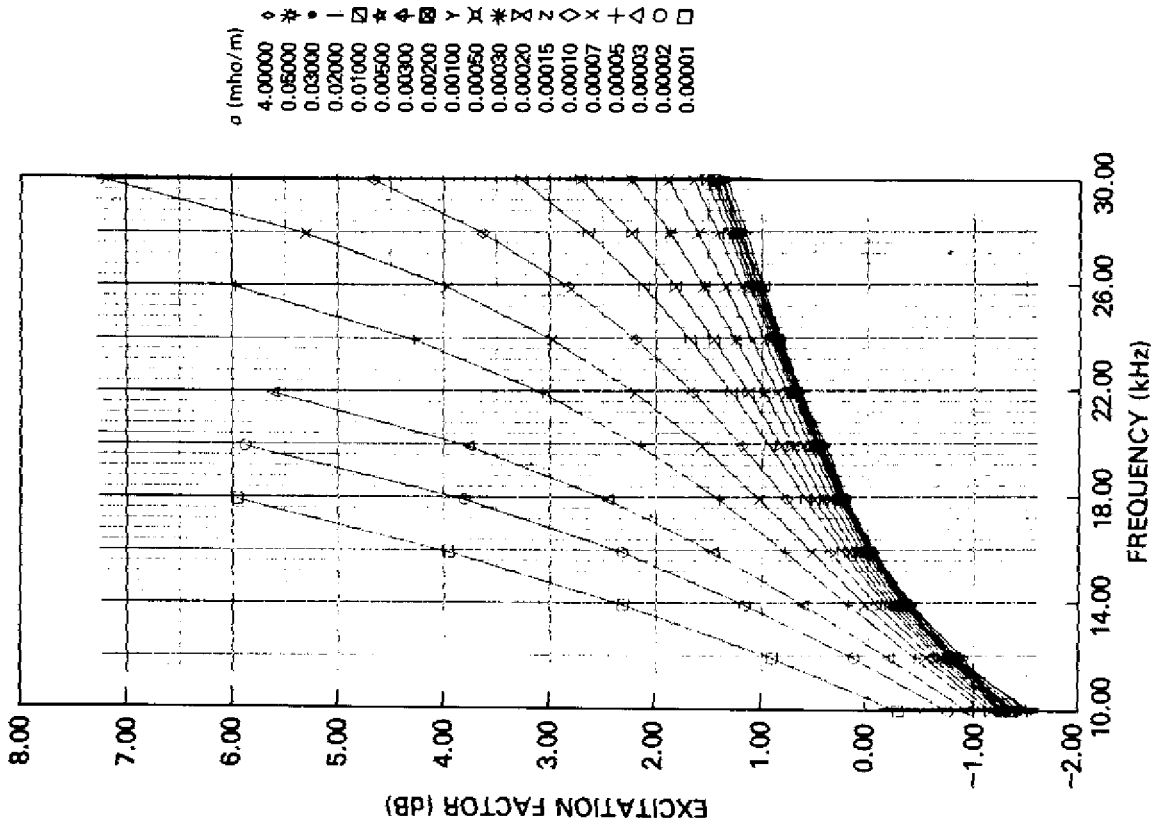


Fig. 35 — Excitation factor for the third-order TM mode vs frequency and ground conductivity for an isotropic daytime ionosphere

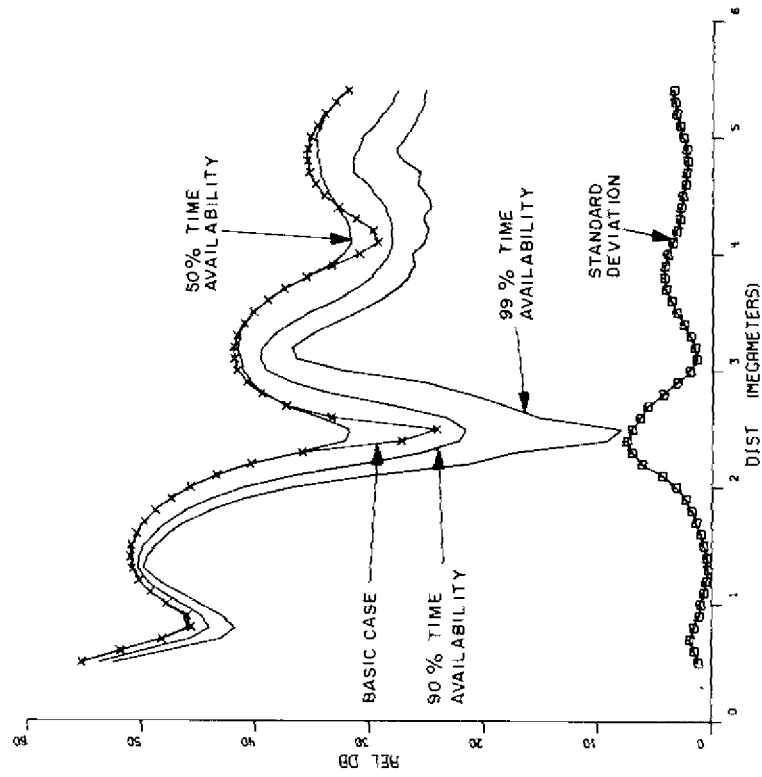


Fig. 36 — Plot of field strengths having 99%, 90%, and 50% time availabilities versus distance. Plot of standard deviation of field strength versus distance. Plot of basic multimode field strength ( $\beta = 0.5 \text{ km}^{-1} h \approx 70 \text{ km}$ ) case.

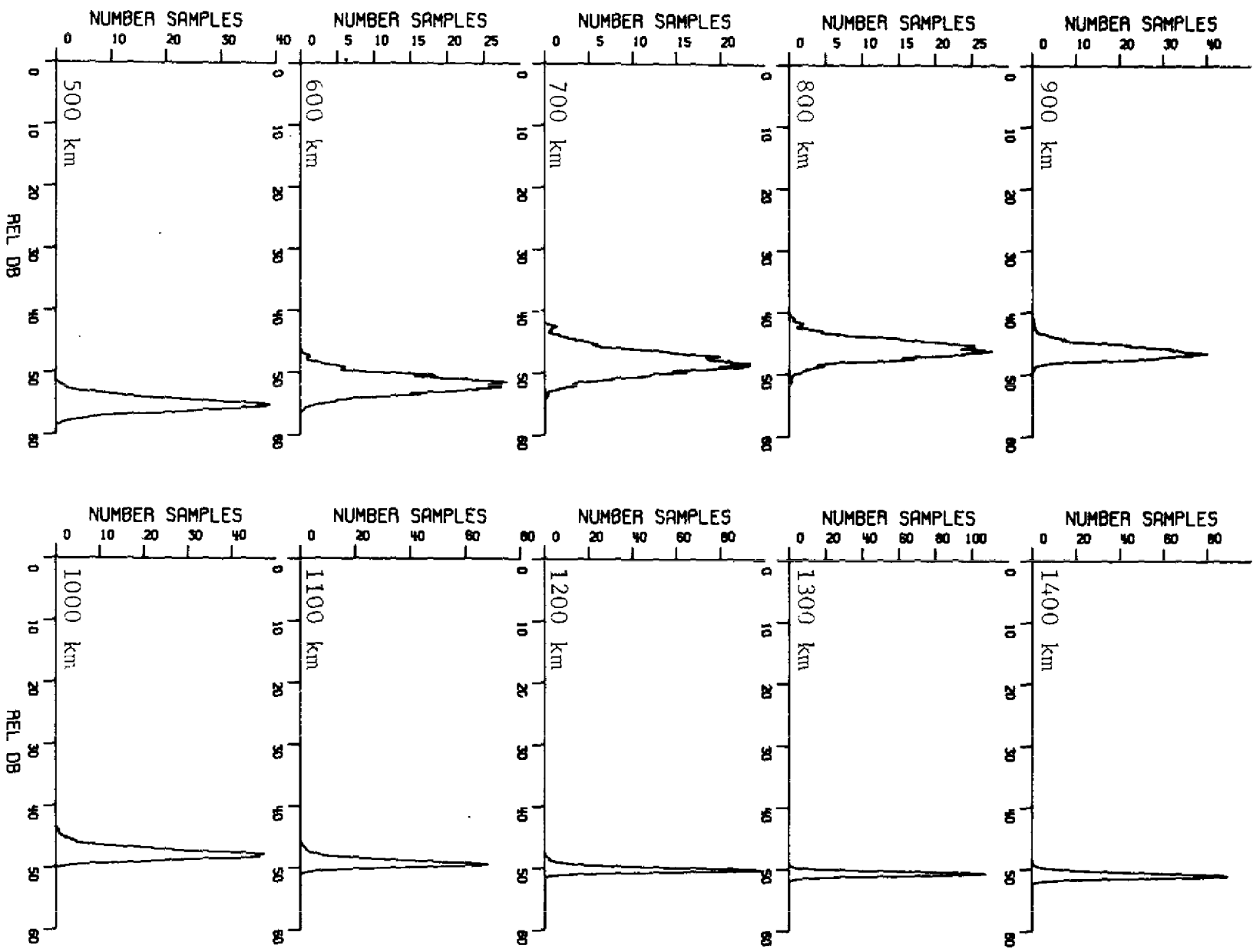


Fig. 37 — Histograms of calculated field strengths



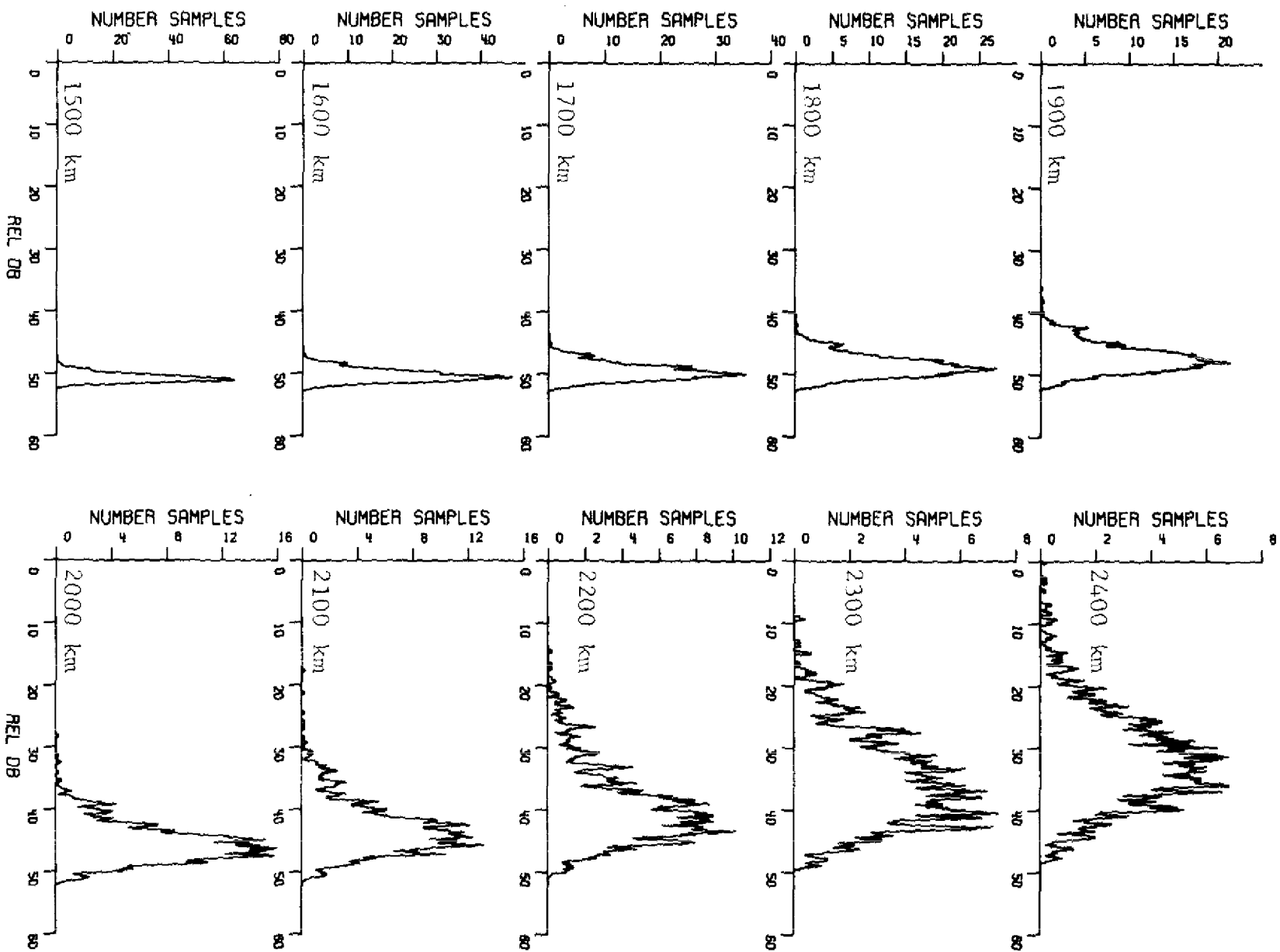


Fig. 38 — Histograms of calculated field strengths

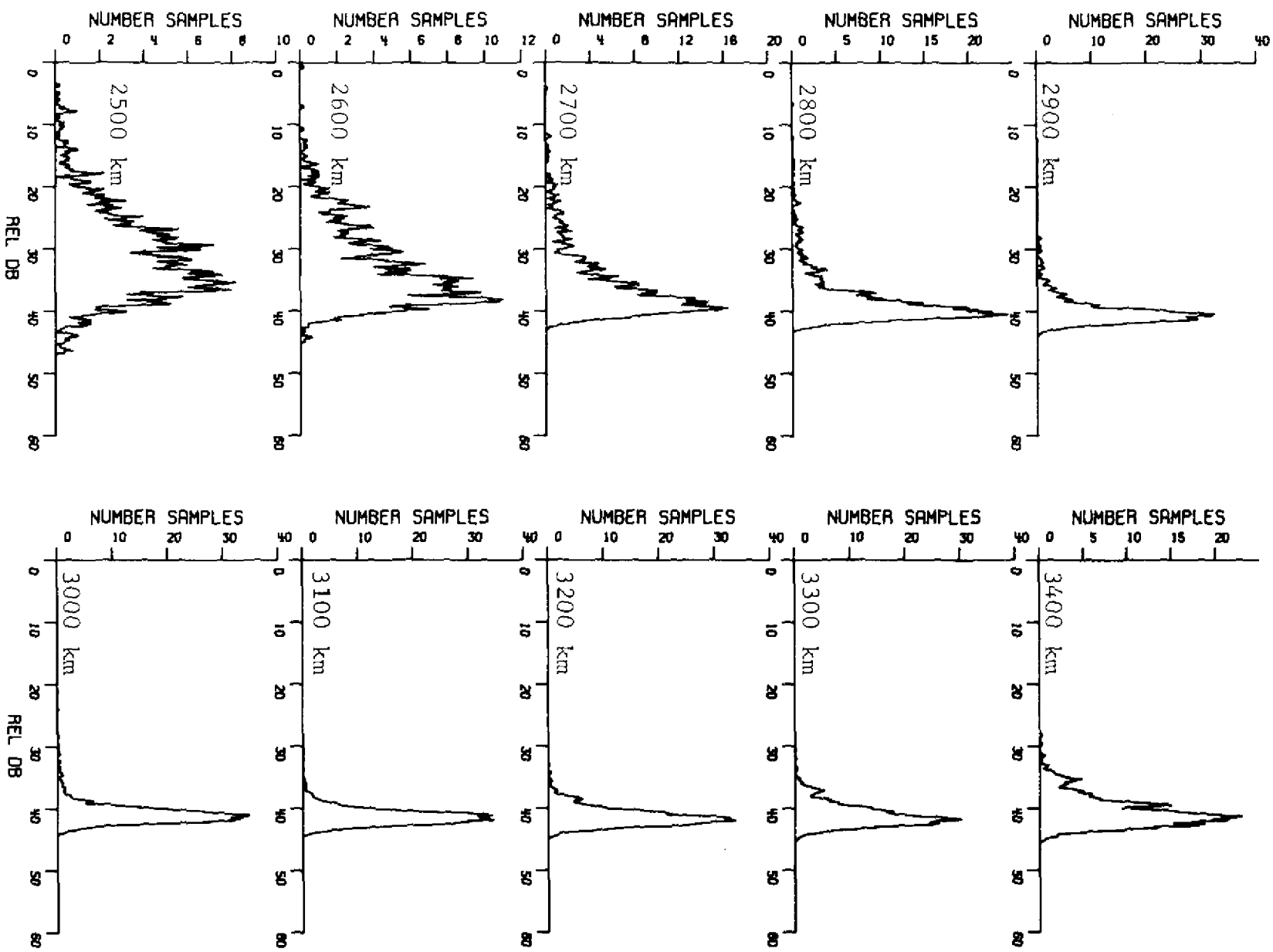


Fig. 39 — Histograms of calculated field strengths

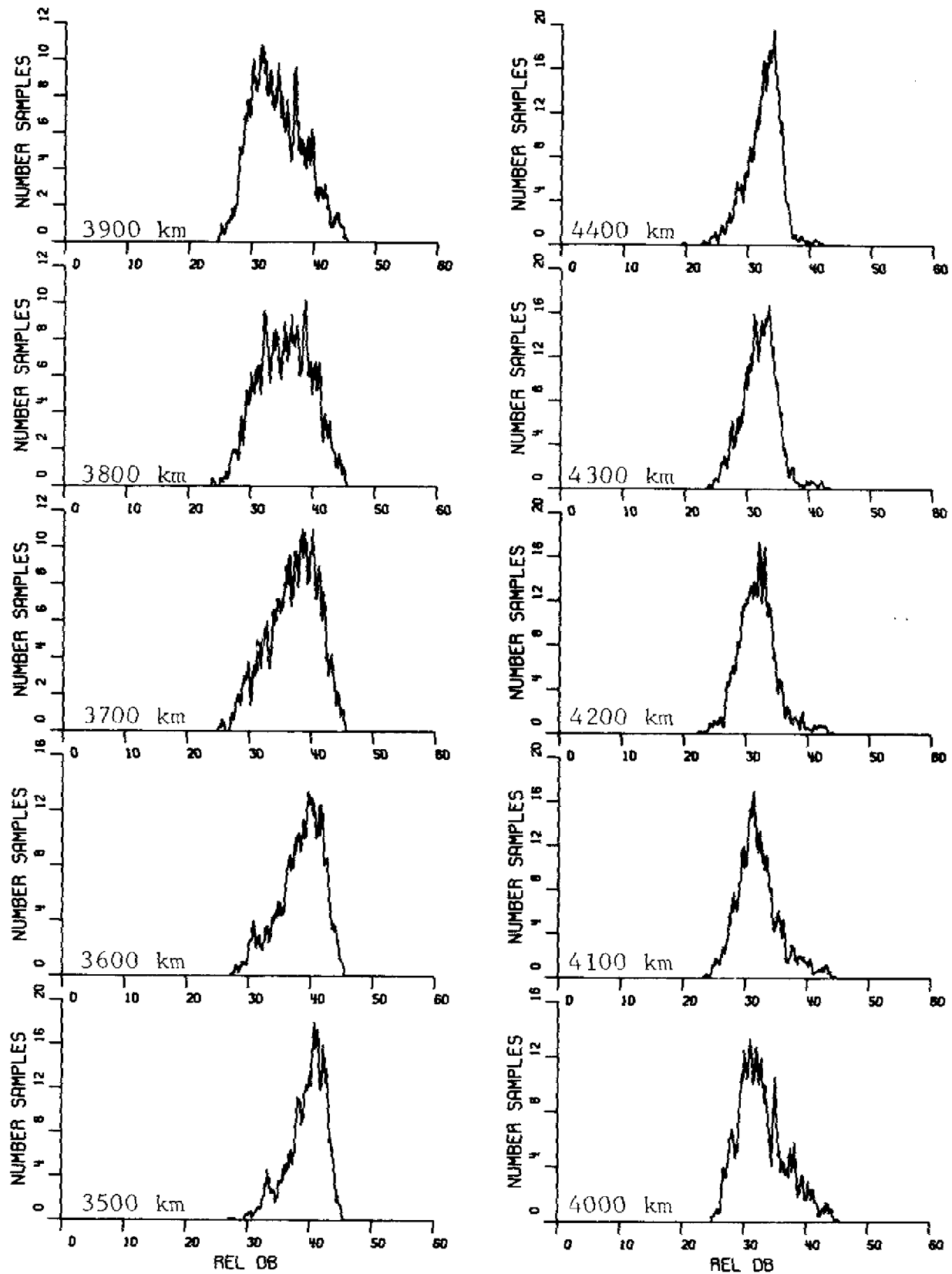


Fig. 40 — Histograms of calculated field strengths

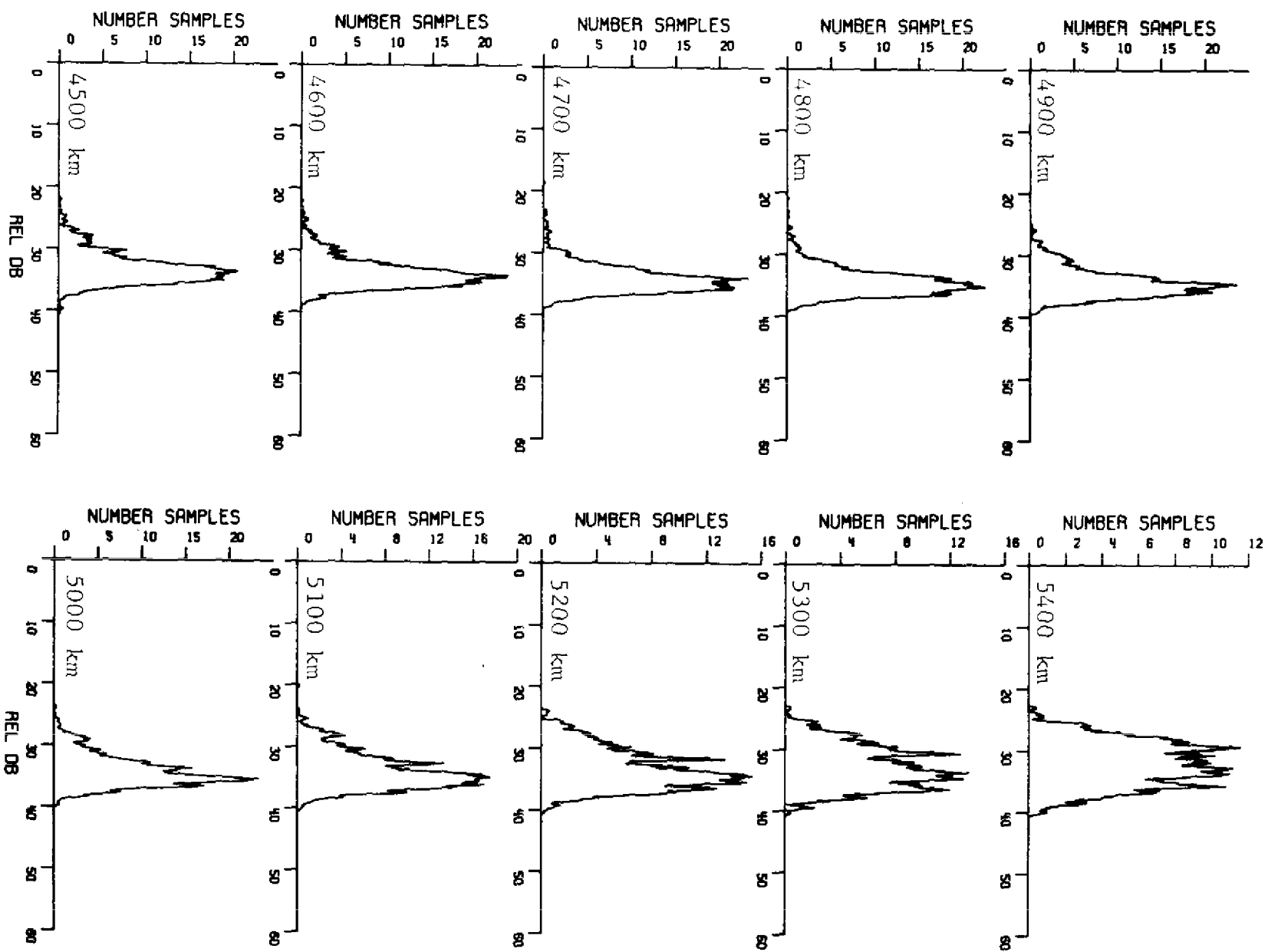


Fig. 41 — Histograms of calculated field strengths

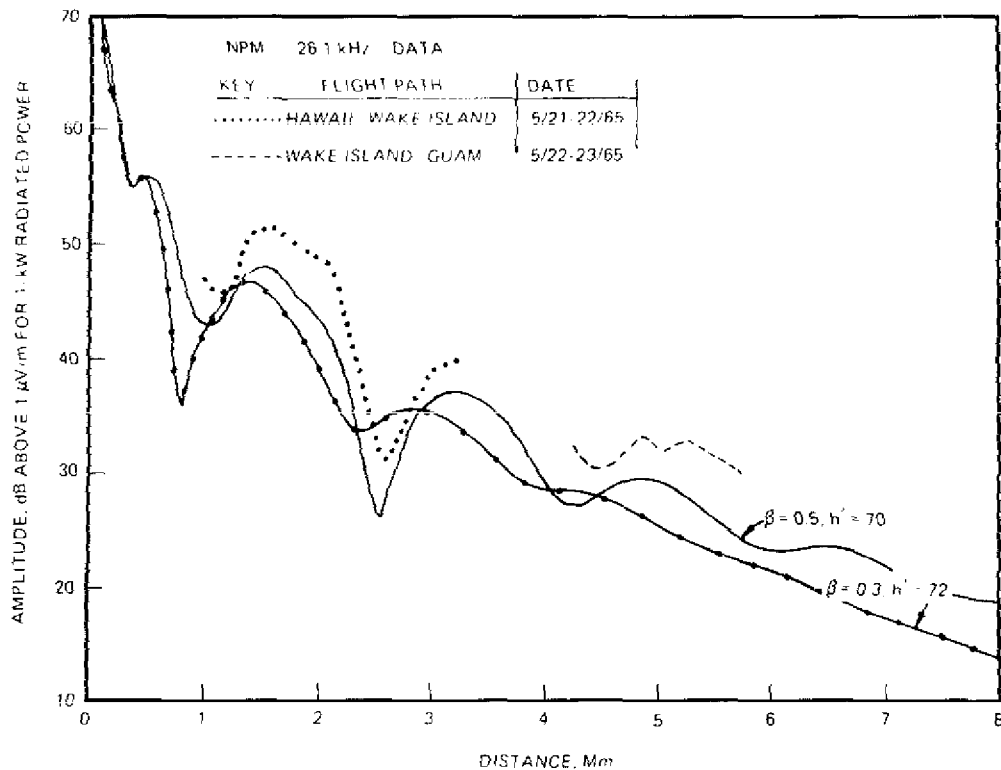


Fig. 42 — Propagation over the Pacific Ocean (daytime, summer) (26.1 kHz)

Flight Path: Hawaii to Wake Island to Guam (daytime)

Ground Conductivity: Seawater

Transmitter: NPM, Hawaii at 26.1 kHz

Date: June 1965

Electron Density Profiles:  $\beta = 0.5 \text{ km}^{-1}$ ,  $h' = 70 \text{ km}$  with base of the ionosphere at 50 km, and,  
 $\beta = 0.3 \text{ km}^{-1}$ ,  $h' = 72 \text{ km}$  with base of the ionosphere at 30 km.

Method of Computation: Horizontally homogeneous waveguide

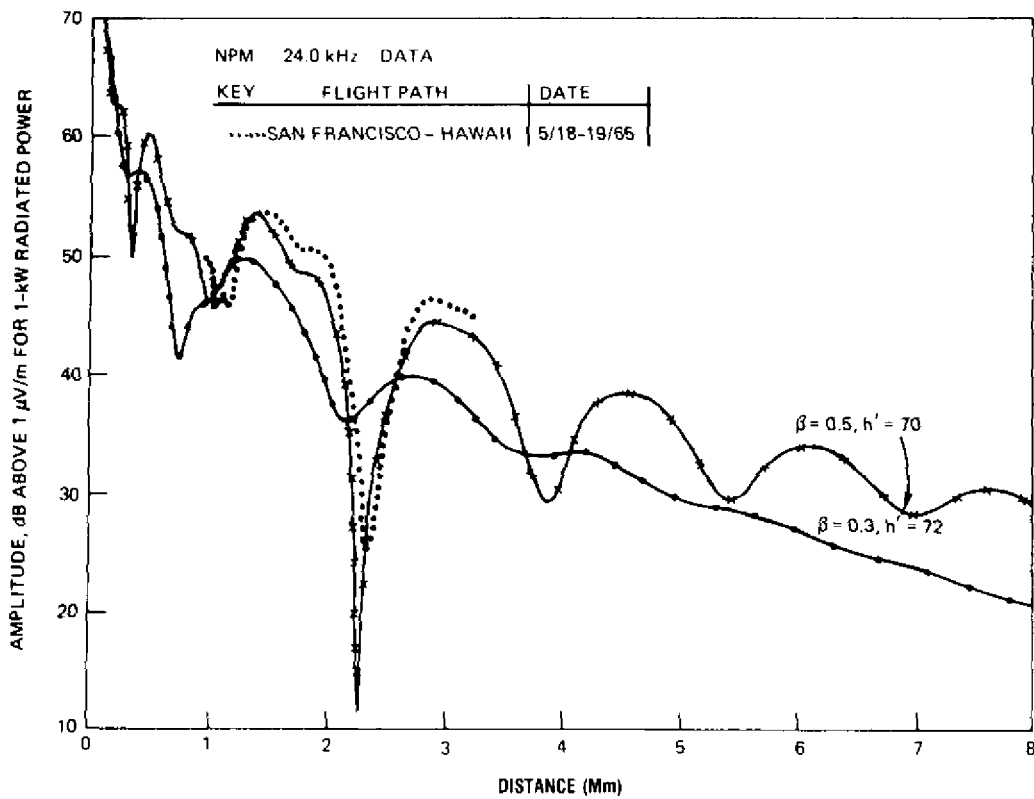


Fig. 43 — Propagation over the Pacific Ocean (daytime, summer) (24 kHz)

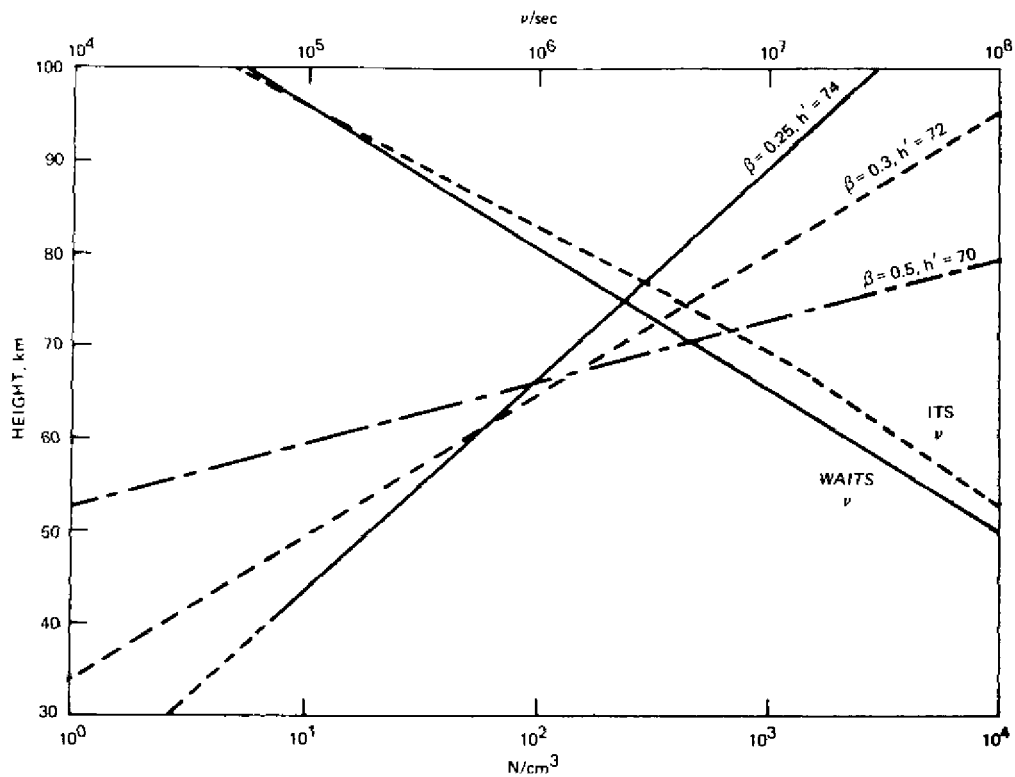


Fig. 44 — Daytime Electron Density Profiles and Collision Frequency Profiles

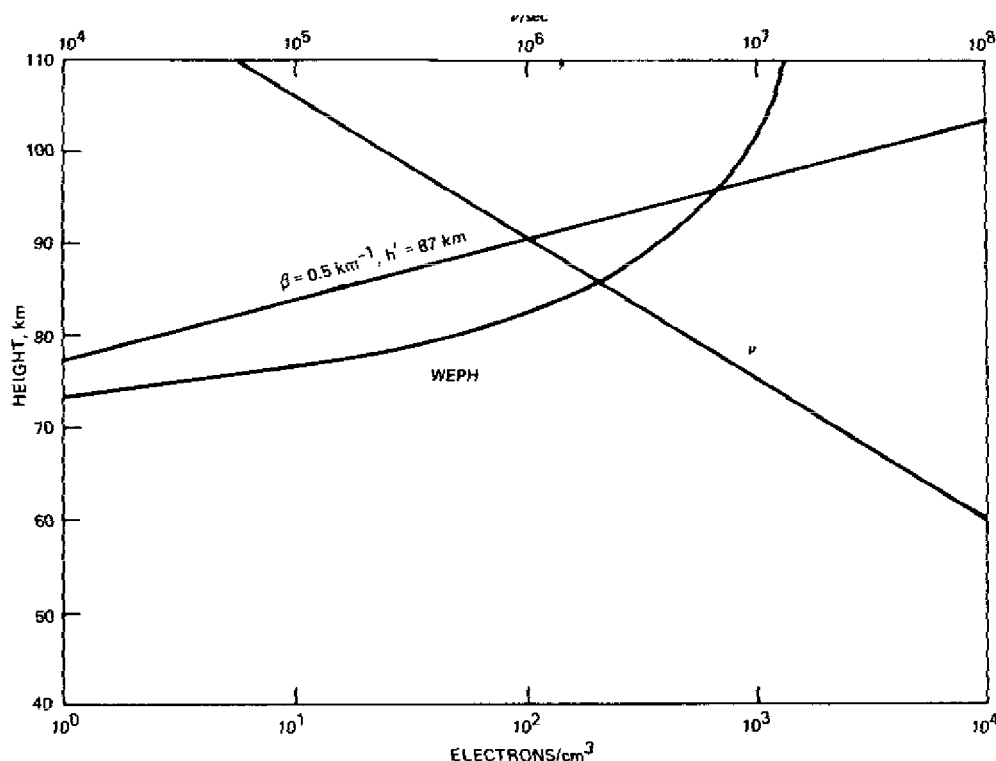


Fig. 45 — Nighttime Electron Density Profiles and Collision Frequency Profile

Table 2 — DCA [28] Recommended Electron Density Profiles for Use in Propagation Predictions (midlatitude)

DAYTIME		NIGHTTIME	
Winter		Winter	
Frequency (kHz)	Profile $\beta$ ( $\text{km}^{-1}$ ), $H'$ (km)	Frequency (kHz)	Profile $\beta$ ( $\text{km}^{-1}$ ), $H'$ (km)
9-60	$\beta = 0.3$ , $H' = 74$	below 10	$\beta = 0.3$ , $H' = 87$
		10 - 15	$\beta = 0.4$ , $H' = 87$
		15 - 25	$\beta = 0.5$ , $H' = 87$
		25 - 30	$\beta = 0.6$ , $H' = 88$
		30 - 40	$\beta = 0.7$ , $H' = 88$
		40 - 60	$\beta = 0.8$ , $H' = 88$

#### Coverage Prediction Programs for Inhomogeneous Paths

Up to this point we have discussed prediction methods for homogeneous paths only. However, the earth's surface, earth's magnetic field, and the ionosphere typically vary with distance along a propagation path. References 32 and 33 represent early efforts to apply mode theory to these inhomogeneous paths. References 34 through 37 describe further developments and elaboration of the waveguide mode propagation picture using mode-matching and the WKB approximation to propagate the waves through spatially varying portions of the path.

Reference 38 describes a Very Low Frequency Automatic Computation Method (VLFACM) computer model. It is approximate but it is inexpensive to run [39]. It makes predictions with built in easily-computed values for the attenuation and excitation of the signal. VLFACM only computes a single dominant waveguide mode and operates best from 15 to 30 kHz. The model parameters were

selected by comparing the program predictions with a great many propagation paths. VLFACM contains expressions that permit it to give a complete diurnal prediction taking solar zenith angle, geomagnetic azimuth, and ground conductivity into account.

#### *DCA Arctic Propagation Recommendation and Recent Experiments*

The DCA recommendations (Ref. 27) for Arctic or high-latitude propagation conditions were based on the comparisons shown in Figs. 46 through 53. Notice that in all cases the field strength predictions are noticeably higher than the measured values for waves propagating across the Greenland Ice Cap and that the conductivity of the ice cap is assumed to be  $10^{-5} \Omega/\text{meter}$  in conformity with references 29 and 30. However at 25 kHz reference 31 gives the measured conductivity of an antarctic glacier as  $5.0$  to  $6.1 \times 10^{-5} \Omega/\text{m}$  with a relative dielectric constant of approximately 11. Referring to Figure 27 we see that this conductivity change could raise the attenuation rate over Greenland at 24 hKz from 9dB for  $\sigma = 10^{-5} \Omega/\text{m}$  to between 13 and 15 dB/Mm for the larger values of  $\sigma$  given by Ref. 31. Recent measurements of the 24.0 kHz signal from NAA indicate an attenuation rate over Greenland in better agreement with the higher attenuation rate, suggesting that the conductivity and dielectric constant of the Greenland Ice Cap may need modification.

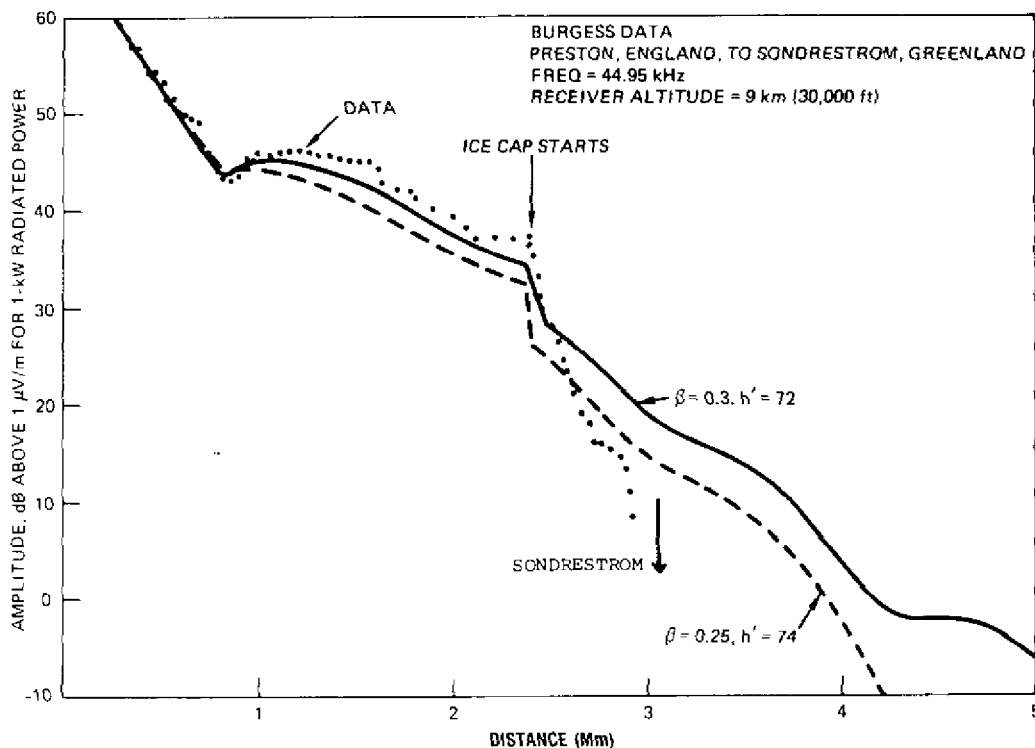


Fig. 46 — High-Latitude Propagation

Flight Path: England to Sondrestrom, Greenland (daytime)  
Ground conductivity: Seawater,  $4 \Omega/\text{m}$ ; Greenland ice cap,  
 $10^{-5} \Omega/\text{m}$

Transmitter: GYN Preston, England (45 kHz)

Date: July 1970

Electron Density Profiles:  $\beta = 0.3 \text{ km}^{-1}$ ,  $h' = 72 \text{ km}$  with the  
base of the ionosphere at 30 km and,  
 $\beta = 0.25 \text{ km}^{-1}$ ,  $h' = 74 \text{ km}$  with the  
base of the ionosphere at 40 km

Method of Computation: WKB approximation



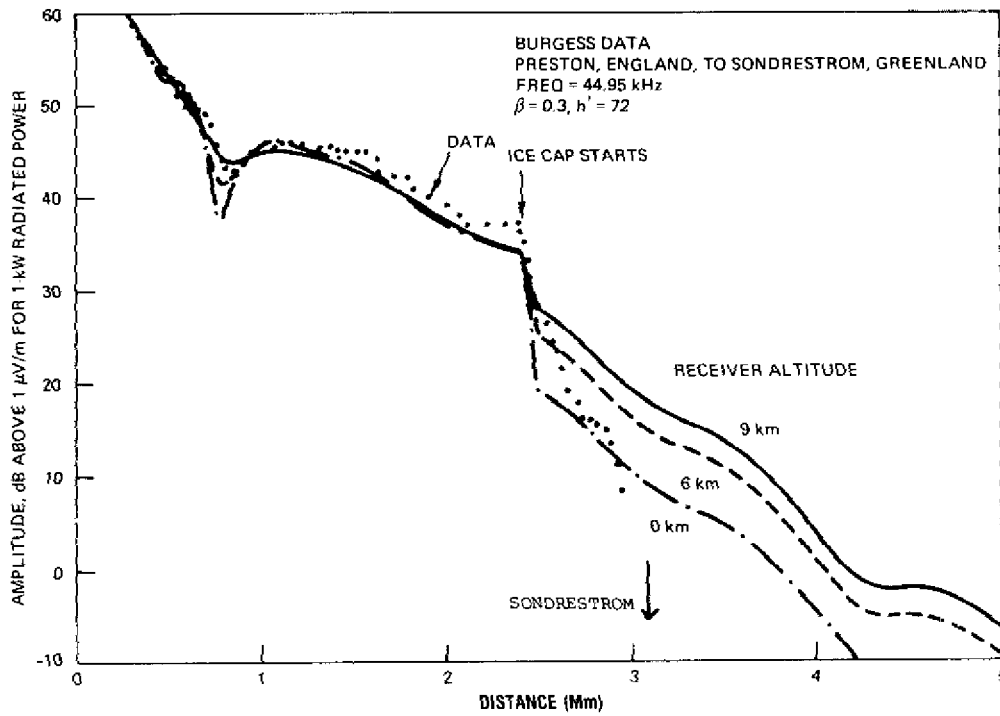


Fig. 47 — High-Latitude Propagation

Propagation parameters are the same as those in Fig. 46 except that only the  $\beta = 0.3 \text{ km}^{-1}$ ,  $h' = 72 \text{ km}$  profile are shown. Field strengths are computed for receiver altitudes (RALT) of 0, 6, and 9 km.

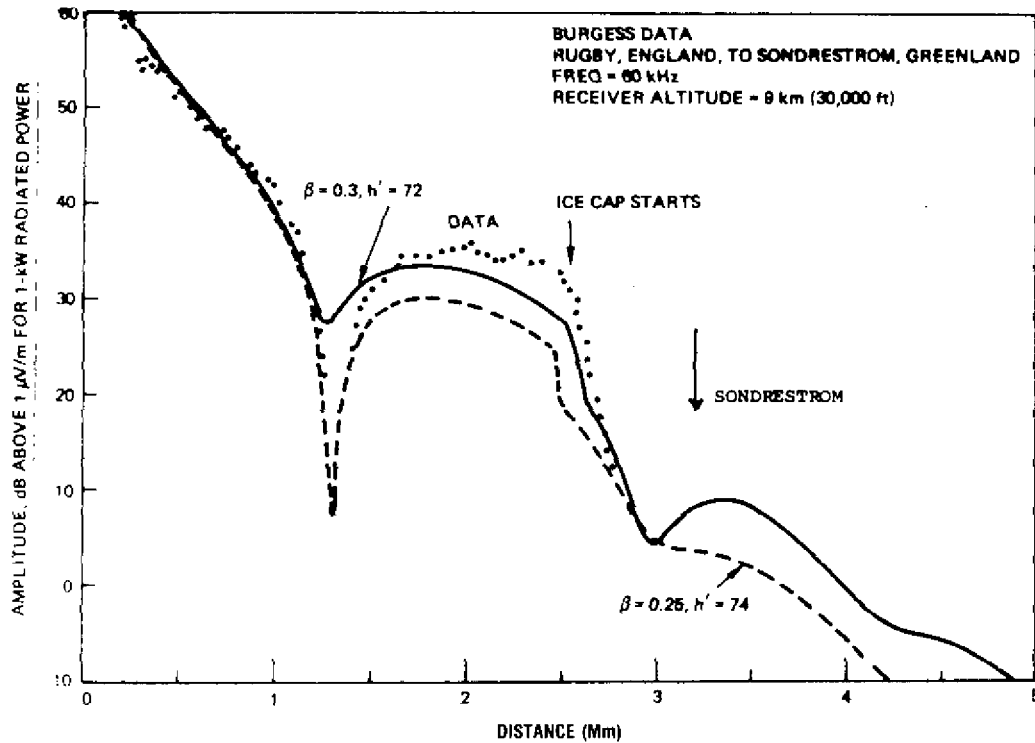


Fig. 48 — High-Latitude Propagation

Flight Path: England to Sondrestrom, Greenland (daytime)

Ground conductivity: Seawater,  $4 \Omega/\text{m}$ ; Greenland ice cap,  $10^{-5} \Omega/\text{m}$

Transmitter: MSF Rugby, England (60 kHz)

Date: July 1970

Electron Density Profiles:  $\beta = 0.3 \text{ km}^{-1}$ ,  $h' = 72 \text{ km}$  with the base of the ionosphere at 30 km and,  $\beta = 0.25 \text{ km}^{-1}$ ,  $h' = 74 \text{ km}$  with the base of the ionosphere at 40 km

Method of Computation: WKB approximation

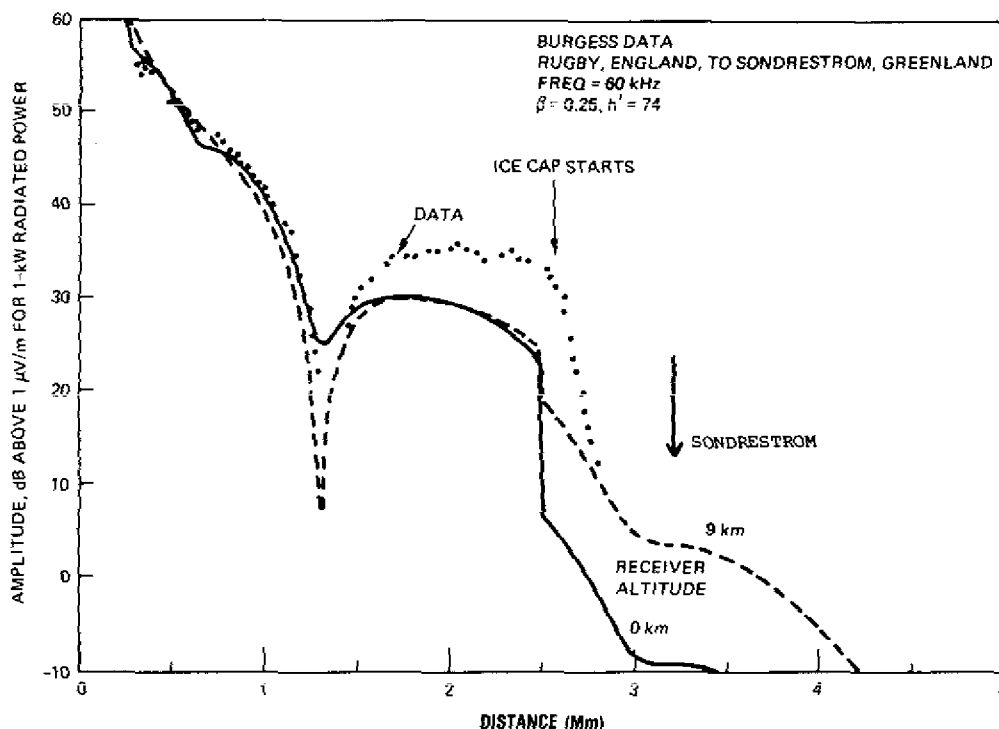


Fig. 49 — High-Latitude Propagation

Propagation parameters are the same as those in Fig. 48 except that only the  $\beta = 0.25 \text{ km}^{-1}$ ,  $h' = 74 \text{ km}$  profile is shown. Field strengths are computed for receiver altitudes (RALT) of 0 and 9 km.

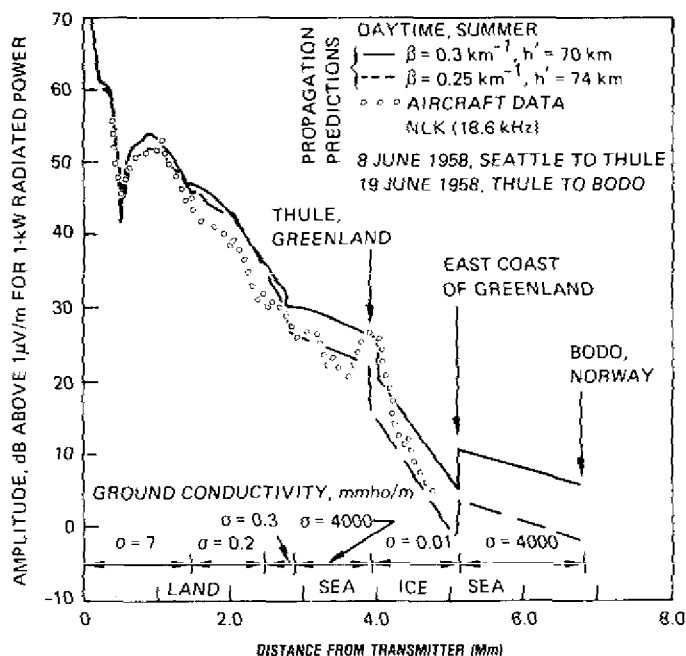


Fig. 50 — High-Latitude Propagation

Flight Path: Seattle, Washington across Canada and over the Greenland ice cap

ground conductivity:

Various values of land, sea, and ice along the path  
Transmitter: NLK, Seattle, Washington (18.6 kHz)  
Date: June 1958

Electron Density Profiles:

$\beta = 0.3 \text{ km}^{-1}$ ,  $h' = 72 \text{ km}$  with the base of the ionosphere at 30 km and,  
 $\beta = 0.25 \text{ km}^{-1}$ ,  $h' = 74 \text{ km}$  with the base of the ionosphere at 40 km

Method of Computation: WKB approximation

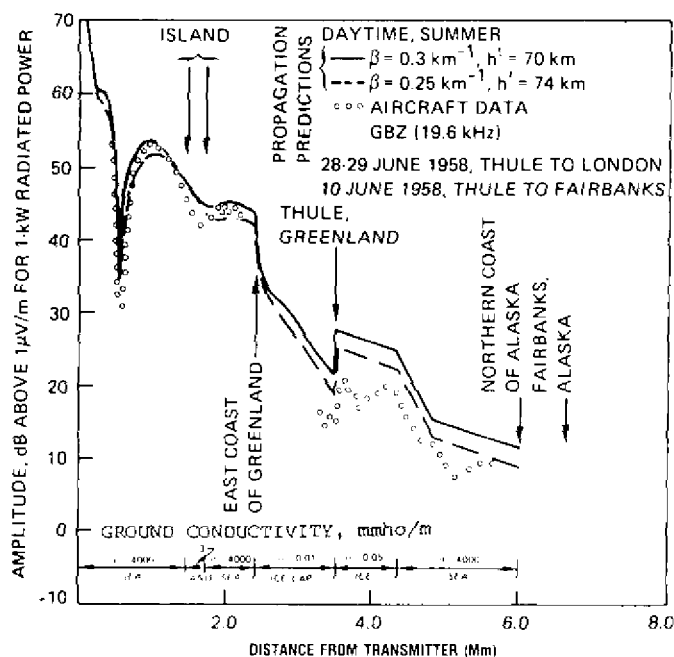


Fig. 51 — High-Latitude Propagation

Flight Path: Thule, Greenland across the ice cap to London, England and Thule to Fairbanks, Alaska

Ground conductivity:

Various values of land, sea, and ice along the path

Transmitter: NLK, Seattle, Washington (18.6 kHz)

Date: June 1958

Electron Density Profiles:

$\beta = 0.3 \text{ km}^{-1}$ ,  $h' = 72 \text{ km}$  with the base of the ionosphere at 30 km and,  
 $\beta = 0.25 \text{ km}^{-1}$ ,  $h' = 74 \text{ km}$  with the base of the ionosphere at 40 km

Method of Computation: WKB approximation

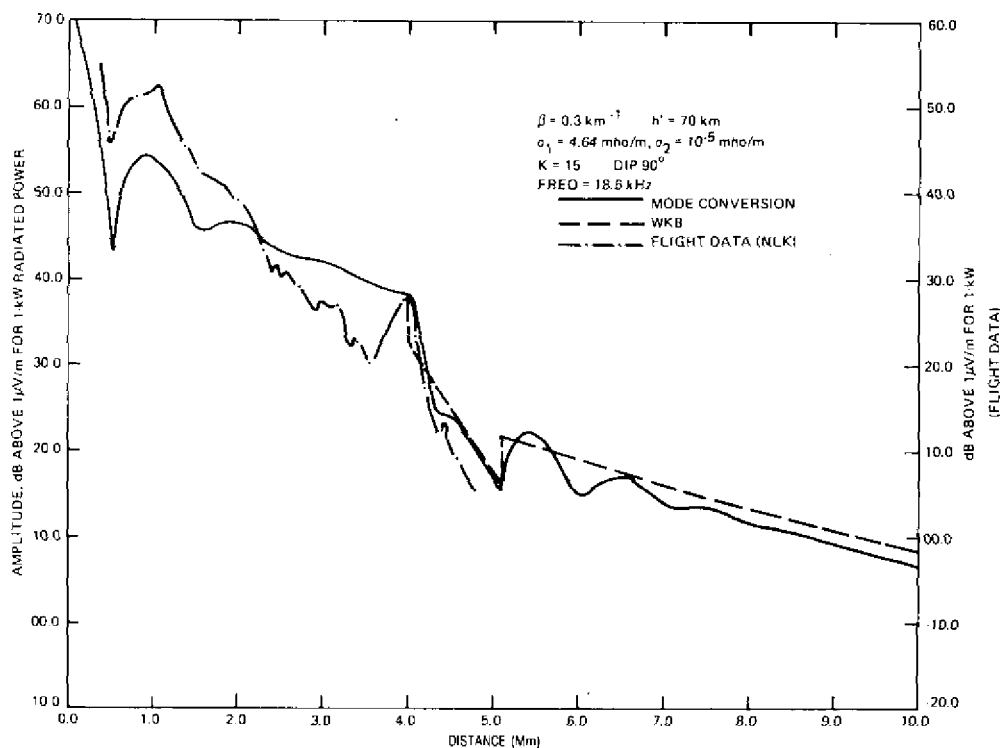


Fig. 52 — High-Latitude Propagation

The propagation parameters are the same as those of Fig. 50 except that the earth's conductivities are taken as only seawater,  $\sigma = 4.64 \text{ } \Omega/\text{m}$  and Greenland ice,  $\sigma = 10^{-5} \text{ } \Omega/\text{m}$ . The computations are made using the mode-conversion procedures.

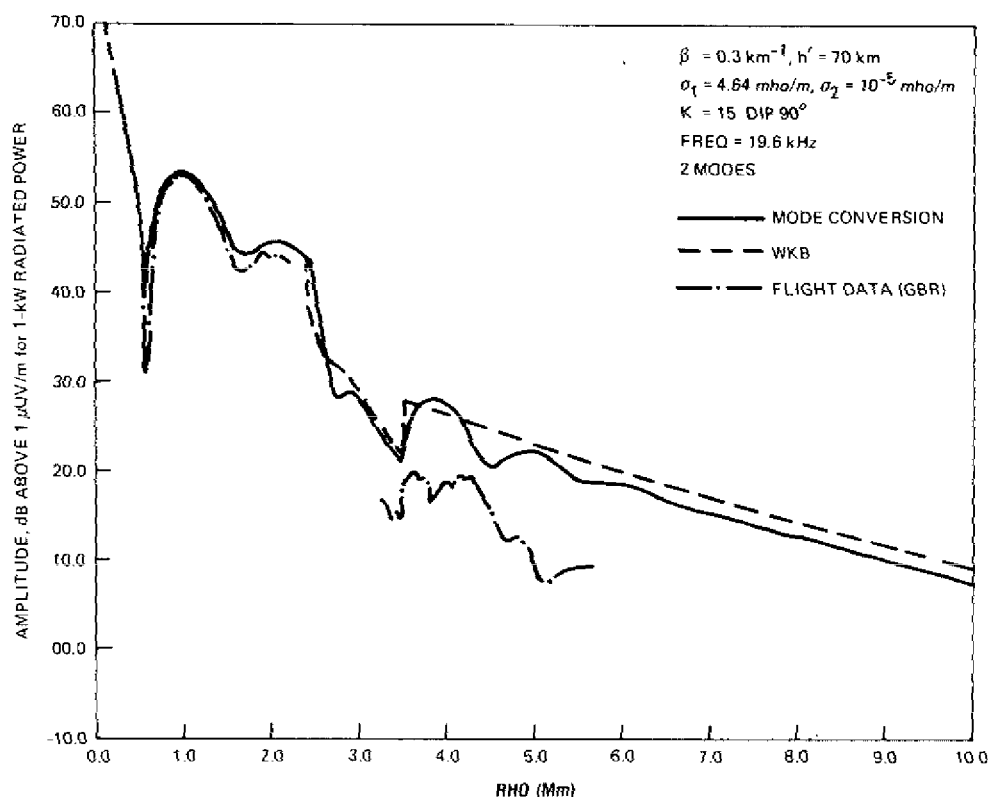


Fig. 53 — High-Latitude Propagation

The propagation parameters are the same as those of Fig. 51 except that the earth's conductivities are taken as only seawater, ( $\sigma = 4.64 \Omega/m$ ) and Greenland ice, ( $\sigma = 10^{-5} \Omega/m$ ). The computations are made using the mode-conversion procedures.

### Coverage Problems

The question of the actual coverage of longwave systems is currently in a status of reevaluation and flux. Because of the meager amount of airborne propagation data available and the tendency of the ionosphere not to stand still, we find that our coverage prediction techniques are unable to achieve the accuracy that will readily satisfy a system designer. Significantly large sums of money are involved in the purchase of aircraft squadrons or in the building of a huge ground based transmitters, therefore greater emphasis and resources should be and are being allocated to longwave coverage research.

### Wavehop Coverage Predictions

The solution of the Helmholtz equation for the Hertz vector between concentric spherical shells [40] is given by a summation of products of spherical harmonics functions (Eq. 30).

$$u \sim \frac{\bar{ikC}}{4\pi} \sum_{q=0}^{\infty} (2q+1) h_q^{(2)}(kb) h_q^{(1)}(kr) P_q(\cos\Theta) \frac{F_q}{D_q}. \quad (30)$$

Watson [41] discovered a technique for transforming this slowly converging series into an integral in the complex plane and reexpressing the integral as a summation over residues.

$$u = -i \int_L \frac{(\nu+1/2)}{\sin \nu \pi} f(\nu) P_\nu[\cos \pi - \Theta] d\nu. \quad (31)$$

In this expression the sum of spherical harmonic Legendre polynomial  $P_q(\cos \Theta)$  functions, which utilize integral values of  $q$ , are reexpressed as an integral over complex contour in the variable  $\nu$  using a Legendre function  $P_\nu[\cos(\pi - \Theta)]$  that utilizes a complex value of the subscript  $\nu$ . The function  $P_\nu[\cos(\pi - \Theta)]$  behaves like a propagating and exponentially decaying wave in the  $\Theta$  direction; i.e.,

along the surface of the earth. In the waveguide mode theory the integral in Eq. (31) is evaluated by the method of residues at residue points  $\nu_i$ . Each value of  $\nu_i$  is referred to as a waveguide mode root and is a solution of Eq. (32).

$$D_\nu = 0 = 1 - R_g^{(\nu)} R_i^{(\nu)} \frac{h_\nu^{(1)}(ka) h_\nu^{(2)}(kc)}{h_\nu^{(2)}(ka) h_\nu^{(1)}(kc)}. \quad (32)$$

The wave-hop formulation for the propagation of long radio waves originated at a very early time after Marconi's original transatlantic transmissions. An early paper by Hollingworth [42] is particularly noteworthy in that Hollingworth experimentally determined that the field strength vs distance of a long wavelength station truly behaves in an undulatory manner, thereby exhibiting the effect of groundwave and skywave interference at ranges governed by geometry and wavelength. The hop approach was adopted by most workers in the field during the 1930s and 1940s—as exemplified by Bremmer's textbook [43].

J. R. Wait [40,44] opened up a new line for theoretical advance when he pointed out that the Watson integral expression for the fields, (Eq. 31), that leads to the waveguide mode formulation, can also be expressed in terms of a geometric series in the reflection coefficients. The first term in the geometric series corresponds to the ground wave. The second term to a one-hop skywave. The third term describes a two-hop skywave, etc. This concept was extended by L. Berry, J.R. Johler, and others [45-49] to produce a method for expressing the fields utilizing the anisotropic ionospheric reflection coefficients in a realistic way. These methods were developed during the 1960s and culminated in computer programs produced by Berry, Herman, and Gonzales, and by Lewis in the early 1970s. The wave hop method has been shown by Jones et al. [50] and Morfitt and Halley [51] to compare well with the waveguide mode methods of calculation.

The wavehop programs have been directly applied to making field strength prediction maps. The wavehop method possesses the great virtue that after inserting the parameters of a propagation path, the results are produced directly after a straightforward calculation that requires no human intervention to complete. Results are automatically mapped to provide signal to noise coverage charts, Figs. 54 through 57.

LONG WAVE PROPAGATION CENTER PHIL119 (SUMMER)

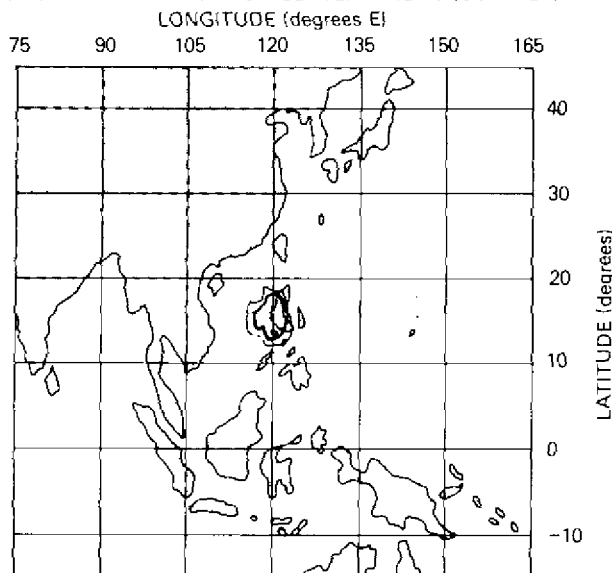


Fig. 54 — Coverage chart showing signal to noise contours (3 dB, heavy line; 0 dB light line) for a naval broadcast station at Tarlac, Philippines on 119.85 kHz for 99% time availability for all hours of the month of July. Assumed transmitter power is 2.5 kW, and noise bandwidth is 1 kHz.

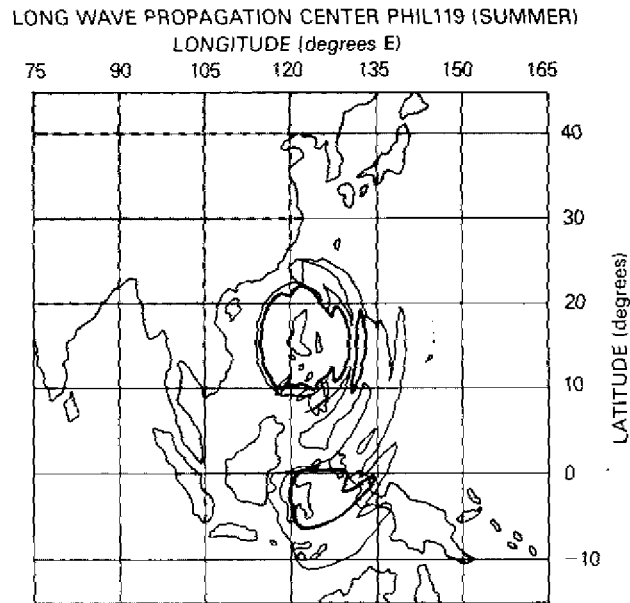


Fig. 55 — Coverage chart for some conditions as those in the previous figure, except time availability is reduced to 90%

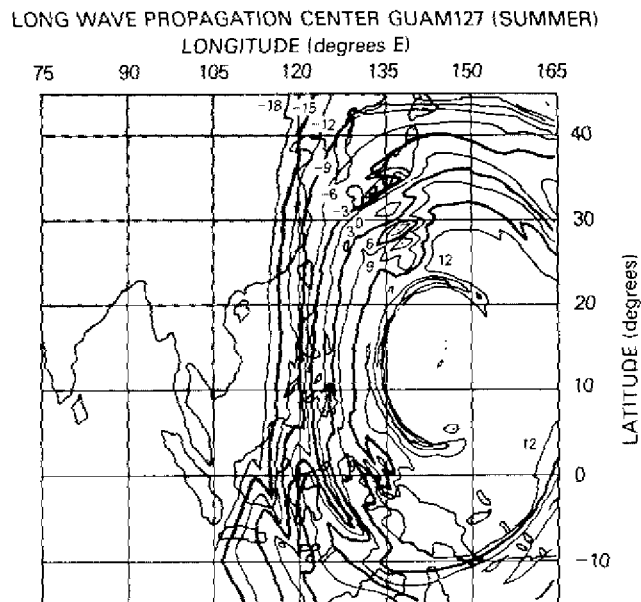


Fig. 56 — Coverage chart showing signal to noise contours for a broadcast station at Guam on 127.5 kHz for 90% time availability for all hours of July. Assumed transmitter power is 23 kW, and noise bandwidth is 1 kHz.

**SIGNAL TO NOISE RATIO CONTOUR MAP**  
**GUAM 143 kHz, JULY**  
**99% TIME AVAILABILITY 1 kHz BANDWIDTH**

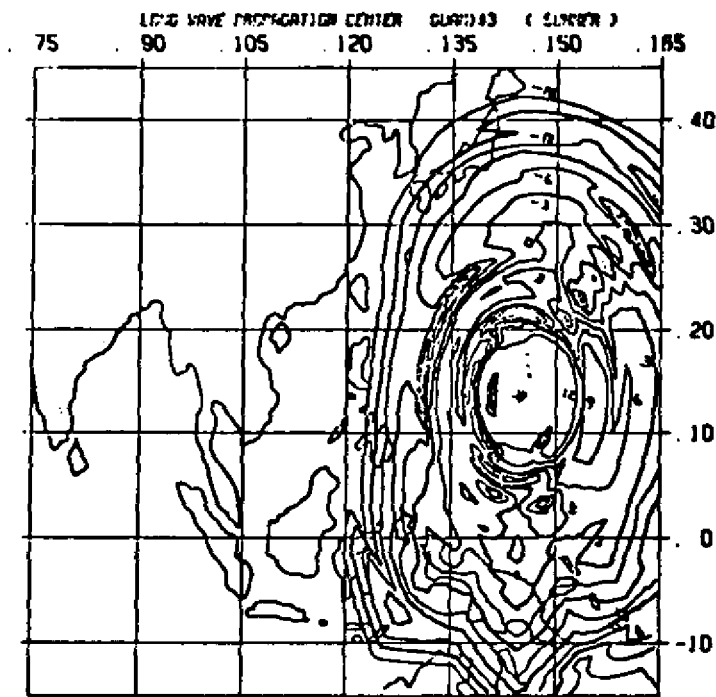


Fig. 57 — Coverage chart for same conditions as those in the previous figure, except time availability is increased to 99%

#### *Recent Developments in Wave Hop*

Recently we have implemented some of the initial ideas of Johler to make the wavehop program amenable to the treatment of inhomogeneous paths in a realistic way. To do this, one must calculate ionospheric reflection coefficients along the propagation path at a variety of angles of incidence and utilize these values in evaluating the fields via interpolation techniques. Thus, greater realism should be introduced into the programs at the cost of increased complexity and bookkeeping problems. Some calculations utilizing this technique are compared with the original Berry and Herman method in Figs. 58 and 59. We see that for long daytime paths the two programs give similar predictions, but for passage through the day-night terminator there are obvious differences.

Because both the multimode and multihop methods have complimentary advantages when applied to longwave propagation predictions, both methods should be applied to problems whenever either one is doubtful.

#### **Future Needs for Coverage Predictions**

Progress in the accurate prediction of long wave radio fields is strongly tied to our ability to monitor and model the lower ionospheric D-region and to accurately map ground conductivity of the earth as a function of frequency. A medium-sized campaign of aircraft flights and long term ground based receivers could reduce our uncertainties in many areas.



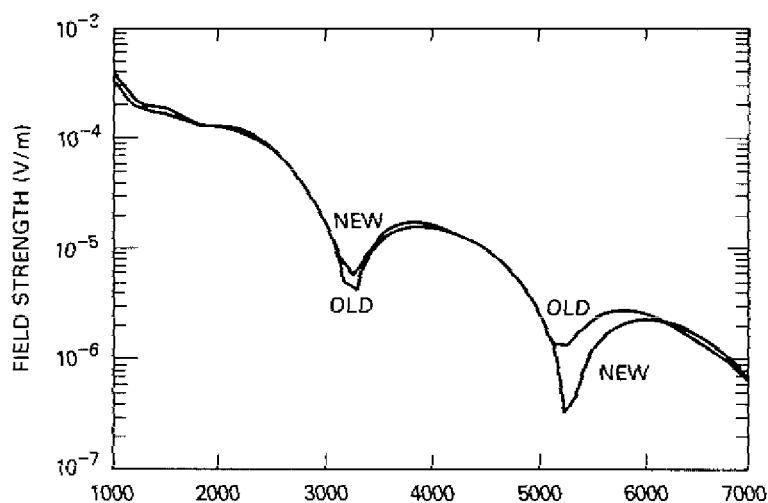


Fig. 58 — Field strength vs distance predictions for Naval LF Broadcast Station Greece on 59 kHz for July, 3.5 kW radiated power, due north at 0000 UT. Solar zenith angle at midpoints (3500 km) is  $62^\circ$ . Path is quite homogeneous daytime, so old and new methods of prediction give similar results.

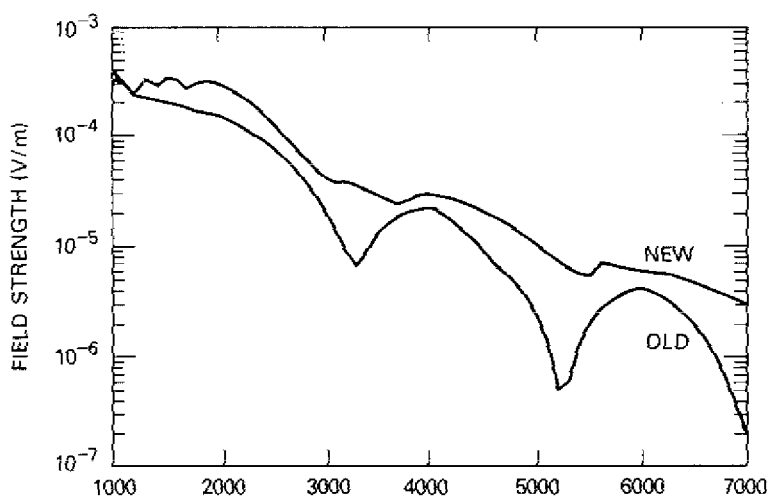


Fig. 59 — Field strength vs distance predictions for Naval LF Broadcast Station Greece on 59 kHz for July, 3.6 kW radiated power, due north at 0000 UT. Solar zenith angle at midpoint (3500 km) is  $87^\circ$  or daytime condition; at 2500 km the solar zenith angle is  $96^\circ$  or nighttime condition. The old method interprets the path as all daylight; the new method has reduced attenuation for the nighttime portion of the path and appropriate daytime attenuation for the daytime portion.

The possibility for making a worldwide D-region sensing and monitoring system is very appealing. Numerous systems can produce D-region ionospheric information, and special systems can be readily designed and implemented to serve this purpose. For example, the auroral photographs currently available from the DMSP satellite can be correlated with actual propagation calculations and measurements to get a model of the aurora-dominated situation. Data from DMSP type sensors working in various spectral bands could detect regions of high electron precipitation to provide real-time feedback to communications traffic managers to permit efficient mode, transmitter location and frequency selection. Numerous inexpensive ground systems can be implemented to provide auxiliary data. A prime example of a ground based D-region ionosphere sensor would be the large Arecibo Thomson Scatter Radar. It gives local electron density profile information from 60 km up to 1000 km. Performing a series of experiments with this facility tied in with OTH HF radar, partial reflection sensors, riometers, and microwave and airglow monitors should greatly enhance our knowledge of the D-region and of its properties relevant to long wavelength propagation prediction. A second series of experiments are the auroral zone using the University of Tromsø's Partial Reflection Experiments and EISCAT Thompson Scatter Radar facility at Tromsø, Norway, would give additional validity to the polar ionospheric models and help with the validation of a polar imaging system. The data from the HILAT satellite discussed by Huffman et. al., [52] are another example of valuable satellite produced information.

### Dispersion and Multipath

Because wide bandwidth or short pulse-length modulation can be used for VLF communication systems, it is important to consider how multimode propagation and dispersion tend to distort short signal pulses. References 53 and 54 present various methods for treating transient signals in a dispersive channel.

Reference 55 considers VLF pulse stretching from the point of view of the waveguide-mode theory of VLF propagation to show the predictions that this theory makes about short-pulse transmission.

When short pulses are propagated in a waveguide, the received pulse shape is altered by both multimode (or equivalent multipath) propagation and by dispersion of the pulses propagating by individual modes. Multimode distortion arises when a pulse leaves a transmitting antenna and travels down the waveguide in several modes. The different modes have different phase and group velocities, so the pulses arrive at the receiver displaced from one another in time. Depending on how much displacement has occurred, the pulse can look like one long pulse or like a series of two or more pulses. Such multimode distortion is identical, in effect, to the classical multipath distortion that always arises when a signal can take more than one path to a receiver.

Dispersive distortion is independent of the multimode problem. A short pulse is composed of a spread of frequencies around a carrier frequency and thus occupies a certain bandwidth  $\Delta f$  that is roughly given by the reciprocal of the length of the pulse  $\tau_0$ ; i.e.,  $\Delta f = 1/\tau_0$ . Since the group velocities of the components on different frequencies are not the same, the components arrive at the receiver displaced in time. This leads to pulse smearing due to propagation even on a single mode.

It is important to remember that multimode distortion and dispersive distortion are distinct and independent phenomena. Thus, propagation channels that have a great deal of multimode distortion but little dispersion and vice versa, could exist.

The equations that describe pulse stretching due to multimode propagation in the waveguide are straightforward. The index of refraction for the  $n$ th mode  $n_n$  is given by the ratio of the speed of light to the phase velocity (we use the letter  $n$  both for the index of refraction and as a mode index).

$$n_n = c/v_{ph, n} \quad (33)$$

The group velocity  $v_{g,n}$  of a signal on the  $n$ th mode is obtained from the index of refraction and its derivative as follows:

$$v_{g,n}/c = (n_n + f \, dn_n/df)^{-1}. \quad (34)$$

The time delay  $\Delta T_{mn}$  between pulses arriving on different modes (the  $m$ th and  $n$ th modes) is simply given by:

$$\Delta T_{mn} = a\Theta \left\{ \frac{1}{v_{g,m}} - \frac{1}{v_{g,n}} \right\}. \quad (35)$$

Here  $a\Theta$  ( $=d$ ) is the distance between the transmitter and receiver. The equations that describe the dispersion spread are also obtained very straightforwardly [56]. The difference in arrival times  $\Delta\tau_{\text{disp}}$  between the components on the different frequencies on a single mode are calculated for a frequency difference  $\Delta f$ :

$$\Delta\tau_{\text{disp}} = a\Theta \left\{ \frac{1}{v_g(f)} - \frac{1}{v_g(f+\Delta f)} \right\} \quad (36)$$

Collecting terms and introducing the initial pulse length  $\tau_0 = 1/\Delta f$ , we obtain

$$\Delta\tau_{\text{disp}} = \frac{a\Theta \Delta f}{v_g^2} \left\{ \frac{v_g(f+\Delta f) - v_g(f)}{\Delta f} \right\} = \frac{a\Theta}{\tau_0 v_g^2} \frac{dv_g}{df}. \quad (37)$$

The fractional dispersive spreading is given by

$$\frac{\Delta\tau_{\text{disp}}}{\tau_0} = \frac{a\Theta}{\tau_0^2 v_g^2} \frac{dv_g}{df} \quad (38)$$

There is a further type of dispersive distortion that cannot be treated by these simple concepts. This type of spreading occurs because of the frequency variation of the excitation factors and of the attenuation coefficients on the various modes. The amplitudes of different frequency components of a pulse are excited differently and attenuated differently. A pulse that was initially composed of frequencies over an initial effective bandwidth will appear to be shifted in frequency or to occupy a smaller bandwidth because of the greater absorption of the frequency components at one side or the other of the occupied band. This type of distortion could be very significant, but it appears that it can only be treated by considering various pulse shapes and performing Fourier transforms. The procedure for numerically studying this type of dispersion is well known. A pulse shape  $v_i(t)$  at the transmitting antenna is given by some modulation function  $A(t)$  times a basic sine wave  $\exp i\omega_0 t$  on the frequency  $\omega_0$ :

$$v_i(t) = A(t) \exp i\omega_0 t. \quad (39)$$

This pulse can be Fourier analyzed:

$$v_i(\omega) = \frac{1}{(2\pi)^{1/2}} \int_{-\infty}^{+\infty} A(t) \exp i\omega_0 t \exp -i\omega t \, dt. \quad (40)$$

The received pulse  $v_{r,n}(\omega)$  on the  $n$ th mode will be given by:

$$v_{r,n}(\omega) = v_i(\omega) \frac{e^{-ika\Theta}}{a(\Theta \sin \Theta)^{1/2}} V_n \quad (41)$$

where  $V_n$  is the  $n$ th term in the summation of (2); i.e.,

$$V_n = \sin^{3/2} \theta_n \Lambda_n \exp (i\pi/4 + ik_o d \sin \theta_n). \quad (42)$$

The received pulse must then be transformed back to the time domain to obtain the pulse shape as a function of time:

$$v_{r,n}(t) = \frac{1}{(2\pi)^{1/2}} \int_{-\infty}^{+\infty} e^{i\omega t} v_{r,n}(\omega) d\omega. \quad (43)$$

If we desire the total received pulse shape, we merely sum the pulses on the various modes:

$$v_r(t) = \sum_{n=1}^{\infty} v_{r,n}(t). \quad (44)$$

We could just as well obtain  $v_r(t)$  by performing the summation over the  $V_n$  before the integration over  $\omega$ . We would then have obtained:

$$v_r(t) = \frac{1}{(2\pi)^{1/2}} \int_{-\infty}^{+\infty} e^{i\omega t} \frac{v_r(\omega) e^{ika\Theta}}{a(\Theta \sin \Theta)^{1/2}} \left\{ \sum_{n=1}^{\infty} V_n \right\} d\omega. \quad (45)$$

The equivalence of (44) and (45) indicates that it makes no difference whether we consider the pulses as carried by different modes or whether we just consider the existence of the complicated complex transfer function:

$$H(\omega) = \frac{e^{-ika\Theta}}{a(\Theta \sin \Theta)^{1/2}} \left[ \sum_{n=1}^{\infty} V_n \right]. \quad (46)$$

It is easier to think of pulses traveling by different modes or hops, so we prefer to use this separate mode approach rather than the transfer function approach.

#### Dispersion Calculation

The isotropic exponential ionosphere model with a  $\beta = 0.5$  and heights of 70 and 90 km may be used to represent daytime and nighttime ionospheric conditions. From data given in Ref. 23, one may calculate the index of refraction (Fig. 60) assuming an infinite ground conductivity. The derivative of the index of refraction can be determined numerically (Fig. 61); and thus the group velocity as a function of frequency is obtained (Fig. 62). Using these group velocities, the delays between pulses on various modes were calculated. The multimode interference will normally have the greatest observable effect when two or more modes are approximately of equal strength. The region of frequency-range space in which two or more modes are within 4 dB of each other was determined by studying the graphs of signal strength vs distance given by Ref. 24, which are based on the parameters given by Ref. 23. The group delays, the time of arrival between pulses on the first and second modes, and between pulses on the second and third modes were then computed. These delay times are shown in Tables 3 and 4, and two time delays are given for most frequencies. The upper time delay is between the first and second-mode pulses; the lower time delay is between the second- and third-mode pulses. For some frequencies, Ref. 23 gives the phase velocity for only two modes; and for these cases only one delay time is presented. Delay time values are given only for the region for which two or more modes have amplitudes within 4 dB of each other. Delay time values at other ranges can be easily calculated by proportionality. In the regions given, two pulses may be separated by the time delay given on the upper line, or, if the two dominant pulses are arranged so as to cancel out to a great extent, the pulse remnant of the cancellation of the first two pulses would be followed by a pulse traveling on another mode.

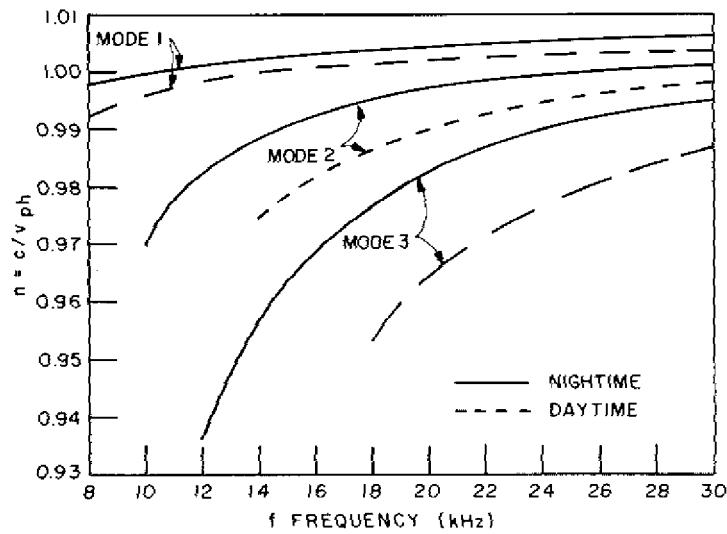


Fig. 60 — Index of refraction vs frequency calculated by Wait and Spies [1964] for three modes ( $\beta = 0.5$ ,  $h = 70$  km, and 90 km). Solid line, nighttime; dashed line, daytime.

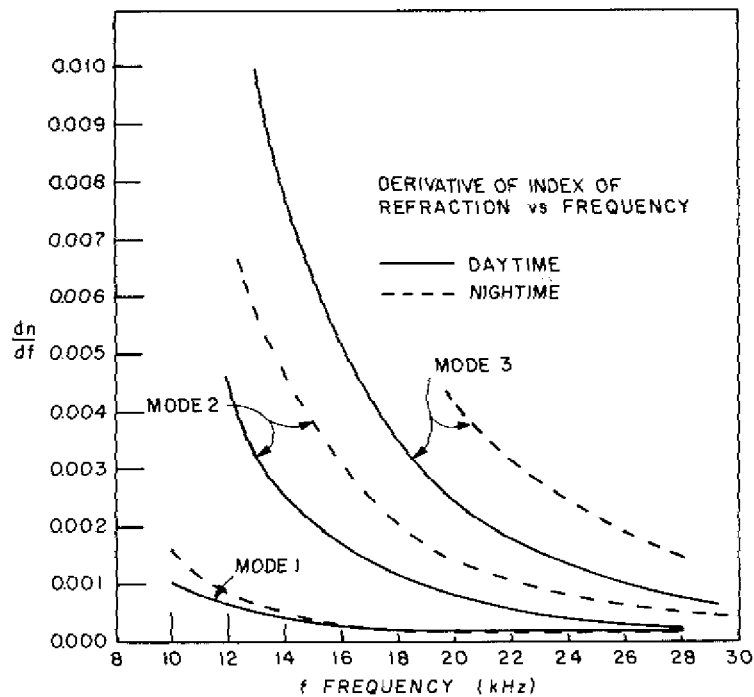


Fig. 61 — Derivative of the index of refraction vs frequency. Solid line, daytime; dashed line, nighttime.

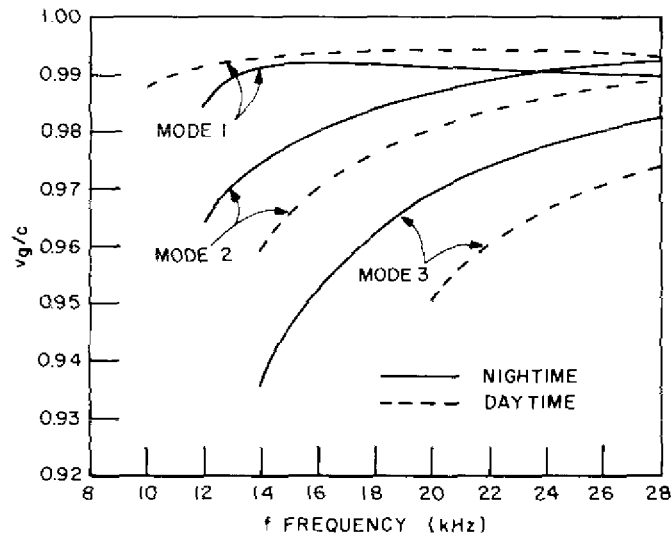


Fig. 62 — Group velocity as a function of frequency.  
Solid line, nighttime; dashed line, daytime.

Table 3 — Daytime multipath time delays in milliseconds  
( $\beta = 0.5, h = 70\text{km}$ )

Frequency, kHz	Range, Mm					
	0.5	1.0	1.5	2.0	4.0	6.0
16	0.039					
18	0.031	0.061				
20	0.024	0.047	0.071			
	0.052	0.104	0.156			
22	0.018	0.036	0.054	0.073		
	0.042	0.084	0.126	0.168		
24	0.014		0.042	0.056		
	0.036		0.107	0.142		
26	0.009			0.038	0.076	
	0.031			0.123	0.246	
28	0.008				0.066	0.101
	0.025				0.202	0.302

Note: Where two values of delay are given, the upper value is the delay between pulses on the first- and second-order modes, and the lower is the delay between pulses on the second- and third-order modes.

Table 4 — Nighttime multipath time delays in milliseconds  
( $\beta = 0.5$ ,  $h = 90$  km)

Frequency kHz	Range, Mm									
	0.5	1.0	1.5	2.0	4.0	6.0	8.0	10.0	12.0	14.0
12	0.048	0.097								
14	0.030	0.061	0.091	0.121						
	0.065	0.130	0.195	0.261						
16	0.020		0.061	0.082	0.164					
	0.057		0.152	0.203	0.406					
18	0.0132				0.106	0.158				
	0.0383				0.312	0.467				
20	0.0076					0.091	0.121	0.151	0.182	
	0.0315					0.378	0.404	0.530	0.756	
22	0.0034									0.095
	0.0262									0.734
24	$8 \times 10^{-10}$	$1.6 \times 10^{-9}$								
	0.022	0.045								
26	$2.5 \times 10^{-4}$	$5 \times 10^{-5}$	$7.5 \times 10^{-5}$							
	0.019	0.038	0.057							
28	$4.1 \times 10^{-5}$	$0.83 \times 10^{-4}$	$1.24 \times 10^{-4}$	$1.6 \times 10^{-4}$						
	0.017	0.034	0.051	0.068						

Note: Where two values of delay are given, the upper value is the delay between pulses on the first- and second-order modes, and the lower is the delay between pulses on the second- and third-order modes.

The dispersive time delay fraction  $\Delta\tau/\tau_0$  from Eq. (38) was also calculated for an initial pulse length of 2 ms received at 6000 km from the transmitter. The results are given in Figs. 63 and 64. We see that the spreading is small, typically only a few percent.

#### Results of Dispersion Calculations

One observes that the time delays between the second- and third-order mode pulses are usually greater than the delay between the first- and second-order mode pulses. During the daytime the greatest delay between the first- and second-mode pulses in the interference region is approximately 0.1 ms at 28 kHz and 6-Mm range. The greatest delay between the second- and third-mode pulse is approximately 0.3 ms at the same frequency and range. At nighttime the interference region is shifted to lower frequency. The greatest time delay between pulses on the first and second modes is approximately 0.18 ms at a frequency of 20 kHz and 12-Mm range. The time delay between the second- and third-mode pulses is approximately 0.76 ms at the same frequency and range.

#### Dispersion Conclusions

Theoretical estimates were obtained of the severity of multimode and dispersive distortion in the VLF propagation channel. It appears that multimode propagation will cause greater pulse distortion than dispersion will. Even at long distance at night, the multimode propagation introduces appreciable pulse distortion on some frequencies for pulse lengths shorter than  $\sim 1$  or 2 ms, since the maximum delay time is of the order of 0.7 ms. During the daytime, however, the delays are smaller, only about 0.3 ms, and the pulse stretching is also smaller. From the present calculation, it would appear that a communicator can choose an optimum frequency for transmission to avoid the regions of frequency-range space given in Tables 3 and 4 and thereby avoid both problems of multimode reception time delays and of modal interference nulls.

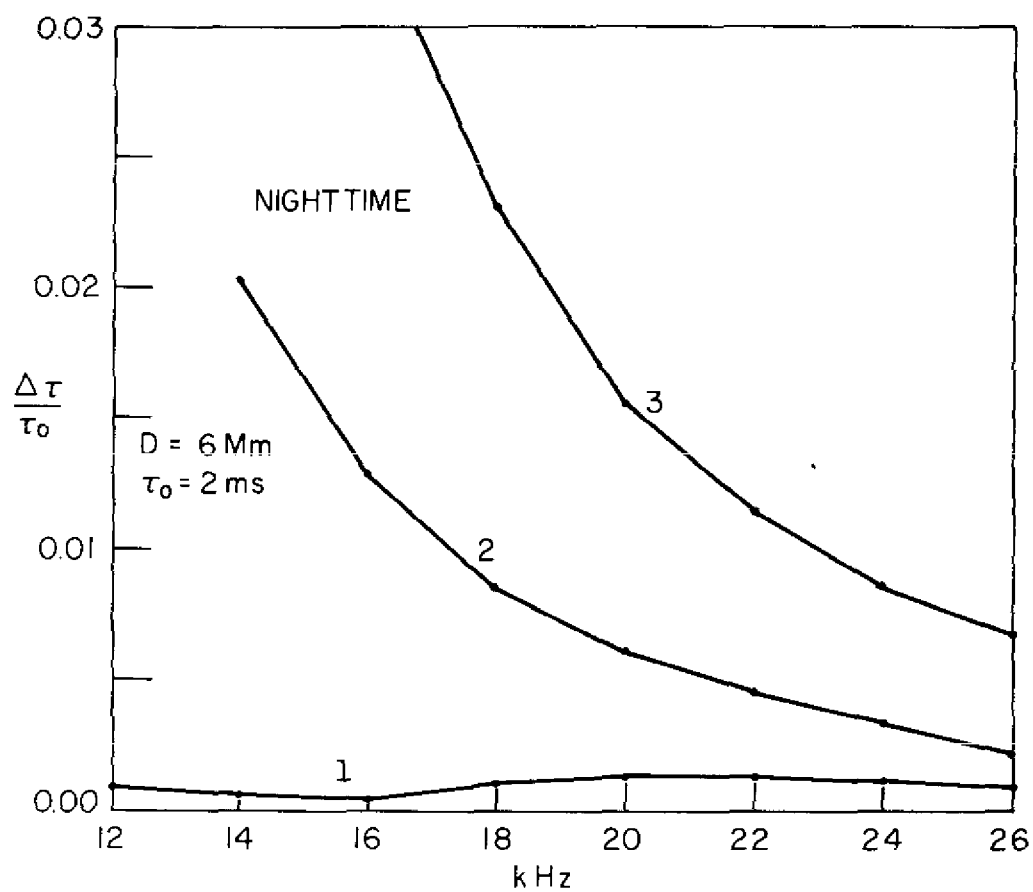


Fig. 63 — Fractional time delay dispersion vs frequency for three modes for a distance  $D = a\theta$  of 6 Mm for nighttime ( $\beta = 0.5$ ,  $h = 90 \text{ km}$ )



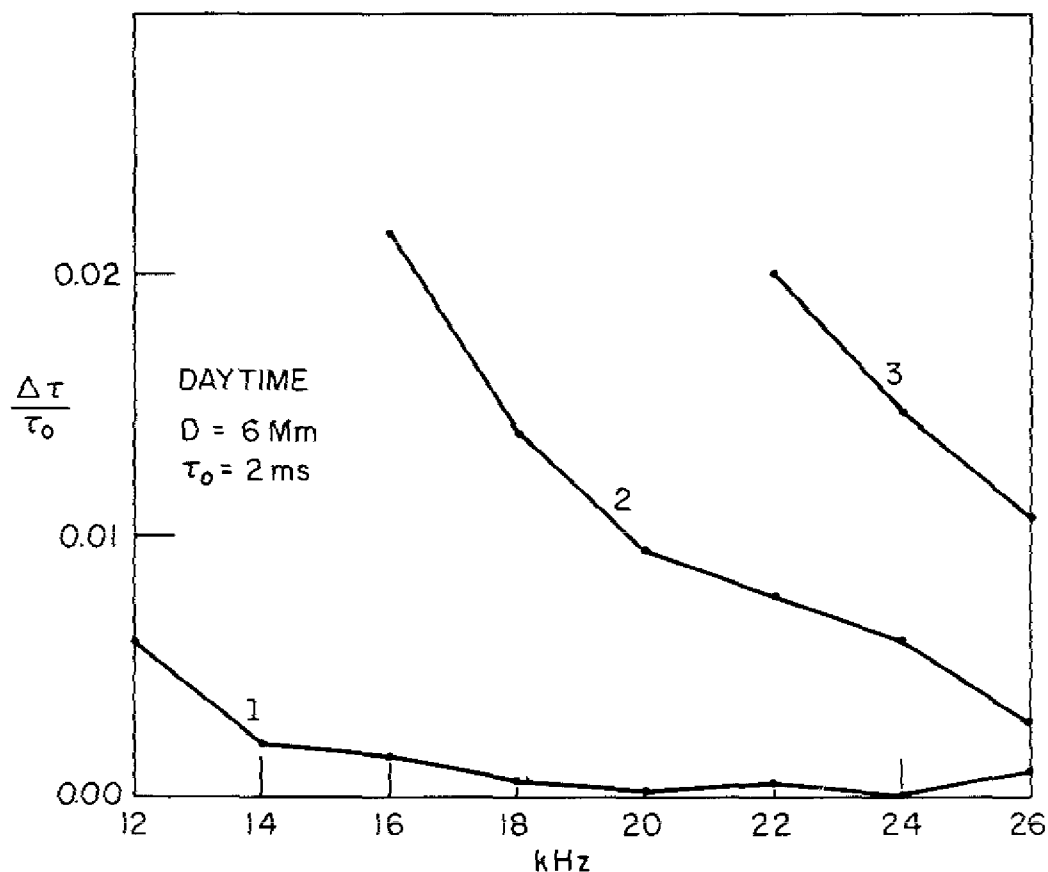


Fig. 64 — Fractional time delay dispersion vs frequency for three modes for a distance  $D = a\theta$  of 6 Mm for daytime ( $\beta = 0.5$ ,  $h = 70$  km)

## MODULATION TECHNIQUES FOR LONGWAVE SYSTEMS

Most of the time, the longwave communication channel was dominated by on-off keyed (OOK) systems transmitting Morse code. Frequency-shift keyed (FSK) systems were introduced to provide data transfer at higher speed. The performance of these systems is summarized in Ref. 2. Recently, minimum shift keying (MSK) systems have been introduced to provide still more efficient use of the limited frequency spans of each longwave communications channel. The following mathematical development is intended to provide an understanding of the newer MSK systems.

### Elementary Signal Theory

Figure 65 shows schematically the outlines of a long-wavelength communication system. Figure 66 shows a conceptual version of a receiver and demodulation portion of Fig. 65. The operation of the integrator portion of the equipment in Fig. 66 is to sample the received waveforms  $h(t)$  and to multiply them by the desired waveform  $h_1(t)$  and  $h_2(t)$  and to integrate over a time equal to a bit-keying-element period  $T_B$ , centered about the time  $t_i$  the midpoint of the  $i$ th expected bit interval. The transmitted waveform is constructed as a linear superposition of  $h_1(t)$  and  $h_2(t)$  according to:

$$h(t) = X_i h_1(t) + Y_i h_2(t). \quad (47)$$

The outputs of the integrators yield the values of  $X_i$  and  $Y_i$  that contain the transmitted information,

$$X_i = (T_B)^{-1} \int_{t_i - T_B/2}^{t_i + T_B/2} h_1(t) h(t) dt \quad (48)$$

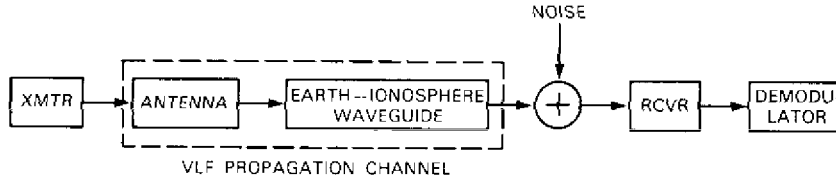


Fig. 65 - Model of the communication system

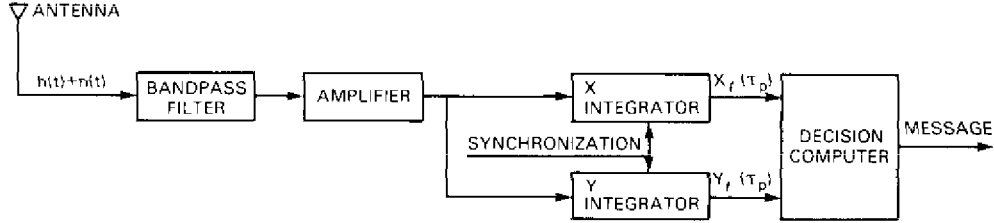


Fig. 66 - Model of the receiver-demodulator

and

$$Y_i = (T_B)^{-1} \int_{t_i - T_B/2}^{t_i + T_B/2} h_2(t) h(t) dt, \quad (49)$$

as long as  $h_1(t)$  and  $h_2(t)$  are orthonormal to each other:

$$(T_B)^{-1} \int_{t_i - T_B/2}^{t_i + T_B/2} h_i(t) h_j(t) dt = \delta_{ij}. \quad (50)$$

Here  $\delta_{ij}$  is the Kronecker delta function, equal to zero for  $i \neq j$  and equal to 1 for  $i = j$ .

#### Correlation of Orthogonal Waveforms

A set of orthogonal wideband waveforms  $h_1(t)$  and  $h_2(t)$  can be generated by using a baseband waveform  $h_B(t)$  to modulate both a cosinusoidal and sinusoidal wave:

$$h_1(t) = h_B(t) \cos \omega_0 t, \quad (51)$$

$$h_2(t) = h_B(t) \sin \omega_0 t, \quad (52)$$

$$h(t) = h_B(t) (X_i \cos \omega_0 t + Y_i \sin \omega_0 t). \quad (53)$$

The values of  $X_i$  and  $Y_i$  give the strength of the cosinusoidal and sinusoidal components. A correlation receiver can then be made to extract the value of  $X_i$  and  $Y_i$ :

$$X_i = 2(T_B)^{-1} \int_{t_i - T_B/2}^{t_i + T_B/2} h_B(t) (X_i \cos \omega_0 t + Y_i \sin \omega_0 t) h_B(t) \cos \omega_0 t dt \quad (54)$$

and

$$Y_i = 2(T_B)^{-1} \int_{t_i - T_B/2}^{t_i + T_B/2} h_B(t) (X_i \cos \omega_0 t + Y_i \sin \omega_0 t) h_B(t) \sin \omega_0 t dt. \quad (55)$$

A propagation delay time of  $\tau_p$  modifies the correlator outputs to give new ones that we call  $X_i(\tau_p)$  and  $Y_i(\tau_p)$ :

$$X_i(\tau_p) = 2(T_B)^{-1} \int_{t_i - T_B/2}^{t_i + T_B/2} h_B(t + \tau_p) [X_i \cos \omega_0(t + \tau_p) + Y_i \sin \omega_0(t + \tau_p)] \times h_B(t) \cos \omega_0 t dt \quad (56)$$

and

$$Y_i(\tau_p) = 2(T_B)^{-1} \int_{t_i - T_B/2}^{t_i + T_B/2} h_B(t + \tau_p) [X_i \cos \omega_0(t + \tau_p) + Y_i \sin \omega_0(t + \tau_p)] \times h_B(t) \sin \omega_0 t dt. \quad (57)$$

We find that the vector  $\mathbf{R}_l(\tau_p) = (X_l(\tau_p), Y_l(\tau_p))$  is approximately the phase-rotated version of  $\mathbf{R}_l = (X_l, Y_l)$ . We have

$$X_l(\tau_p) = T_B^{-1} (X_l \cos \omega_0 \tau_p + Y_l \sin \omega_0 \tau_p) \int_{t_l - T_B/2}^{t_l + T_B/2} h_B(t) h_B(t + \tau_p) dt \quad (58)$$

and

$$Y_l(\tau_p) = T_B^{-1} (-X_l \sin \omega_0 \tau_p + Y_l \cos \omega_0 \tau_p) \int_{t_l - T_B/2}^{t_l + T_B/2} h_B(t) h_B(t + \tau_p) dt. \quad (59)$$

Thus we can write this equation in vector form if  $\mathbf{R}_l = (X_l, Y_l)$ :

$$\mathbf{R}_l(\tau_p) = T_B^{-1} \left[ \int_{t_l - T_B/2}^{t_l + T_B/2} h_B(t) h_B(t + \tau_p) dt \right] \begin{bmatrix} \cos \omega_0 \tau_p & \sin \omega_0 \tau_p \\ -\sin \omega_0 \tau_p & \cos \omega_0 \tau_p \end{bmatrix} \mathbf{R}_l. \quad (60)$$

The magnitude of the vector  $\mathbf{R}_l(\tau_p) = [X_l(\tau_p)^2 + Y_l(\tau_p)^2]^{1/2}$  is given by

$$|\mathbf{R}_l(\tau_p)| = T_B^{-1} |\bar{R}_l| \int_{t_l - T_B/2}^{t_l + T_B/2} h_B(t) h_B(t + \tau_p) dt. \quad (61)$$

The phase of the vector  $\mathbf{R}_l(\tau_p)$  is given by

$$\phi_l(\tau_p) = \arg(X_l(\tau_p) + iY_l(\tau_p)) = \arg(X_l + iY_l) + \omega_0 \tau_p. \quad (62)$$

Thus the magnitude of the  $\mathbf{R}_l(\tau_p)$  vector varies slowly with  $\tau_p$ , and the phase  $\phi_l(\tau_p)$  changes rapidly.

#### Correlation of Other Orthogonal Waveforms

A more complicated set of orthogonal waveforms can be generated by using two orthogonal baseband waveforms  $h_{B1}(t)$  and  $h_{B2}(t)$  such that for  $i, j = 1, 2$

$$(T_B)^{-1} \int_{t_l - T_B/2}^{t_l + T_B/2} h_{B1}(t) h_{Bj}(t) dt = \delta_{ij}, \quad (63)$$

where  $\delta_{ij}$  is the Kronecker delta function. The transmitted waveform  $h(t)$  is given by

$$h(t) = X_l h_{B1}(t) \cos \omega_0 t + Y_l h_{B2}(t) \sin \omega_0 t. \quad (64)$$

To extract the value of  $X_l$  and  $Y_l$  from this waveform, we need a correlator receiver that does the following integrations:

$$X_l = 2(T_B)^{-1} \int_{t_l - T_B/2}^{t_l + T_B/2} [X_l h_{B1}(t) \cos \omega_0 t + Y_l h_{B2}(t) \sin \omega_0 t] [h_{B1}(t) + h_{B2}(t)] \cos \omega_0 t dt \quad (65)$$

and

$$Y_l = 2(T_B)^{-1} \int_{t_l - T_B/2}^{t_l + T_B/2} [X_l h_{B1}(t) \cos \omega_0 t + Y_l h_{B2}(t) \sin \omega_0 t] [h_{B1}(t) + h_{B2}(t)] \sin \omega_0 t dt. \quad (66)$$

When the time of arrival is changed to  $t = t + \tau_p$ , we have

$$\begin{aligned} X_l(\tau_p) &= 2(T_B)^{-1} \int_{t_l - T_B/2}^{t_l + T_B/2} [X_l h_{B1}(t + \tau_p) \cos \omega_0(t + \tau_p) + Y_l h_{B2}(t + \tau_p) \sin \omega_0(t + \tau_p)] \\ &\quad \times [h_{B1}(t) + h_{B2}(t)] \cos \omega_0 t dt \end{aligned} \quad (67)$$

and

$$\begin{aligned} Y_l(\tau_p) &= 2(T_B)^{-1} \int_{t_l - T_B/2}^{t_l + T_B/2} [X_l h_{B1}(t + \tau_p) \cos \omega_0(t + \tau_p) + Y_l h_{B2}(t + \tau_p) \sin \omega_0(t + \tau_p)] \\ &\quad \times [h_{B1}(t) + h_{B2}(t)] \sin \omega_0 t dt. \end{aligned} \quad (68)$$

This gives

$$X_I(\tau_p) = X_I \cos \omega_0 \tau_p T_B^{-1} \int h_{B1}(t + \tau_p) [h_{B1}(t) + h_{B2}(t)] dt \\ + Y_I \sin \omega_0 \tau_p T_B^{-1} \int h_{B2}(t + \tau_p) [h_{B1}(t) + h_{B2}(t)] dt \quad (69)$$

and

$$Y_I(\tau_p) = -X_I \sin \omega_0 \tau_p T_B^{-1} \int_{t_i - T_B/2}^{t_i + T_B/2} h_{B1}(t + \tau_p) [h_{B1}(t) + h_{B2}(t)] dt \\ + Y_I \cos \omega_0 \tau_p T_B^{-1} \int_{t_i - T_B/2}^{t_i + T_B/2} h_{B2}(t + \tau_p) [h_{B1}(t) + h_{B2}(t)] dt. \quad (70)$$

If the two baseband modulation functions are sufficiently orthogonal that

$$T_B^{-1} \int_{t_i - T_B/2}^{t_i + T_B/2} h_{B1}(t + \tau_p) h_{B2}(t) dt \approx 0 \quad (71)$$

and sufficiently similar that

$$T_B^{-1} \int_{t_i - T_B/2}^{t_i + T_B/2} h_{B1}(t + \tau_p) h_{B1}(t) dt = T_B^{-1} \int_{t_i - T_B/2}^{t_i + T_B/2} h_{B2}(t + \tau_p) h_{B2}(t) dt, \quad (72)$$

we again obtain

$$X_I(\tau_p) = (X_I \cos \omega_0 \tau_p + Y_I \sin \omega_0 \tau_p) T_B^{-1} \int_{t_i - T_B/2}^{t_i + T_B/2} h_{B1}(t + \tau_p) h_{B1}(t) dt \quad (73)$$

and

$$Y_I(\tau_p) = (-X_I \sin \omega_0 \tau_p + Y_I \cos \omega_0 \tau_p) T_B^{-1} \int_{t_i - T_B/2}^{t_i + T_B/2} h_{B1}(t + \tau_p) h_{B1}(t) dt. \quad (74)$$

When the more complicated correlators of Eqs. (65) and (66) are used, and the orthogonal waveforms satisfy the conditions of Eqs. (71) and (72), the type of waveform of Eq. (64) gives a behavior similar to that of Eq. (53).

## Modulation Methods

The values of  $\bar{R}_I$  can be modified at the transmitter to initiate the communication of information. In amplitude modulation the magnitude of  $\mathbf{R}_I$  is varied. In phase-shift keying the phase angle  $\phi_I$  is modulated. Thus, in general, information may be transmitted by changing the transmitted vector  $\mathbf{R}_I$  in some prescribed way. The stability of the received vector  $\mathbf{R}_I(\tau_p)$  in amplitude and phase is important in the performance of communication systems. In the realistic communication channel the values of  $\mathbf{R}_I(\tau_p)$  will also depend on the noise present. In this study we neglect noise and simply study the effects of propagation on  $\mathbf{R}_I(\tau_p)$ .

## MSK Signals

In the field of VLF communications, minimum shift keying (MSK) is a commonly used type of spread-spectrum modulation. MSK is mathematically described in terms of a transmitted waveform  $s(t)$ , a baseband modulation  $u(t)$ , and a chip waveform  $p(t)$ , as follows:

$$s(t) = \text{Re} \left[ u(t) e^{i\omega_0 t} \right], \quad (75)$$

$$u(t) = \sum_{n=0}^{N/2-1} \left[ X_I I_n p(t - nT) - i Y_I Q_n p(t - T/2 - nT) \right], \quad (76)$$

$$p(t) = \begin{cases} \sqrt{\frac{2}{T}} \left[ \cos \left[ \frac{\pi t}{T} \right] \right] & -T/2 \leq t \leq T/2, \\ 0, & |t| > T/2. \end{cases} \quad (77)$$

This is a specific version of the signal described in general by Eq. (64), where the orthogonal baseband waveforms  $h_{B1}(t)$  and  $h_{B2}(t)$  are given by

$$h_{B1}(t) = \sqrt{T} \sum_{n=0}^{\frac{N}{2}-1} I_n p(t - nT) \quad (78)$$

and

$$h_{B2}(t) = \sqrt{T} \sum_{n=0}^{\frac{N}{2}-1} Q_n p(t - T/2 - nT). \quad (79)$$

In Eqs. (76), (78), and (79)  $I_n$  and  $Q_n$  are pseudorandomly chosen integers of value  $+1$  or  $-1$ . It is assumed that both the transmitter and receiver possess synchronized pseudorandom-number-sequence generators that provide the  $I_n$  and  $Q_n$  sequences. The frequency  $\omega_0$  is the carrier frequency of the broadcast. The time interval  $T$  is the duration of a chip. Since two chips are transmitted during each chip duration, the chip length  $\tau_c$  is  $T/2$ . The MSK modulation method gives rise to a constant-amplitude waveform with continuous phase as long as  $X_i$  and  $Y_i$  are equal to  $\pm 1$ . The bandwidth of the transmitted signal is inversely related to the chip period. The value of the waveform  $s(t)$  depends on one value of  $I_n$  and one value of  $Q_n$  simultaneously except at the instant when a transition is being made from one value of  $I_n$  or  $Q_n$  to the next. At the transition time the amplitude of the waveform undergoing transition is zero, because the  $p(t)$  function goes smoothly to zero at the beginning and end of its range. At that instant the value of  $s(t)$  depends only on the other integer  $Q_n$  or  $I_n$ . Considering the autocorrelation function  $B(\tau)$  for the MSK waveform  $s(t)$ :

$$B(\tau) = \lim_{T' \rightarrow \infty} \frac{1}{T'} \int_0^{T'} s(t) s(t + \tau) dt. \quad (80)$$

The use of  $s(t)$  from Eq. (75) makes  $B(\tau)$  nonzero as long as  $|\tau| < T$ . When  $|\tau| > T$ , all the contributions to  $B(\tau)$  are from terms that have the products  $Q_n I_m$ ,  $Q_n Q_m$ , and  $I_n I_m$  with  $n \neq m$ . These terms are as often  $+1$  as they are  $-1$  for an orthogonal or uncorrelated set of  $\{Q_n\}$  and  $\{I_n\}$ ; therefore a summation based on these values should remain small. A large value for the autocorrelation function occurs only for  $|\tau| < T$ , when  $I_n^2$  and  $Q_n^2$  terms contribute. Since  $I_n^2 = Q_n^2 = 1$ , these terms are easily evaluated. The correlation vector  $\mathbf{R}_l(\tau_p)$  is closely related to the autocorrelation function  $B(\tau)$ . At very low frequencies the electromagnetic waves may be considered to propagate by distinct waveguide modes or hops. The time delays between dominant modes and hops are small—less than 1 ms [55]—producing the coherent overlap of one chip with its time-delayed image. At some receiver locations the interference of the two waves with each other results in “selective” fading. Such fading is called “selective” because it occurs only for frequencies for which the interference condition is satisfied. At other nearby receiver locations or frequencies the time delays will be such as to produce two pulses that reinforce each other. The propagation channel can be simulated by a multipath model in which  $h_T(t)$  is the transmitted wave, and the received wave is

$$h_R(t) = \sum_{i=1}^N A_i h_T(t - \tau_i), \quad (81)$$

where  $\tau_i$  is the propagation time for the  $i$ th mode or hop and  $A_i$  is the amplitude for the  $i$ th mode or hop. In the case of earth-ionosphere waveguide propagation, sometimes the waves have distinctly different group and phase velocities. Therefore we must consider both the phase and group delay times  $\tau_p^{(i)}$  and  $\tau_g^{(i)}$ . The phase delay of the baseband modulation is governed by  $\tau_p^{(i)}$ , and the group delay is governed by  $\tau_g^{(i)}$ .

### The MSK Correlation Receiver

The performance of a correlation receiver for MSK modulation and the coherent detection of signal reception on a single-path propagation channel are readily evaluated. The correlation vector  $\mathbf{R}_l(\tau_p)$  obtained when one uses MSK modulation is explicitly calculated by substituting the expression for  $h_{B1}(t)$  from Eq. (78) into Eqs. (73) and (74). The integral  $I_B(\tau_p)$ , defined as

$$\begin{aligned}
I_B(\tau_p) &= T_B^{-1} \int_{t_l - T_B/2}^{t_l + T_B/2} h_{B1}(t + \tau_p) h_{B1}(t) dt \\
&= T_B^{-1} \sum_{\substack{n=0 \\ n'=0}}^{\frac{N}{2}-1} I_n I_{n'} \int_{t_l - T_B/2}^{t_l + T_B/2} p(t - nT) p(t + \tau_p - n'T) dt,
\end{aligned} \quad (82)$$

is readily evaluated. The limits of integration in this equation extend far beyond the region of variable  $t$ , for which the integrand is nonzero. We can change the integration variable to

$$t' = t - nT. \quad (83)$$

The limits of integration are thereby changed to  $t_l + T_B/2 - nT$  and  $t_l - T_B/2 - nT$ :

$$I_B(\tau_p) = T_B^{-1} \sum_{\substack{n=0 \\ n'=0}}^{\frac{N}{2}-1} I_n I_{n'} \int_{t_l - T_B/2 - nT}^{t_l + T_B/2 - nT} p(t') p(t' + nT + \tau_p - n'T) dt. \quad (84)$$

Since  $p(t') = 0$ , for  $|t'| > T/2$ , we need to integrate only between  $-T/2 \leq t \leq T/2$ . We obtain

$$I_B(\tau_p) = T_B^{-1} \sum_{\substack{n=0 \\ n'=0}}^{\frac{N}{2}-1} I_n I_{n'} \int_{-T/2}^{+T/2} p(t') p[t' + \tau_p + (n - n')T] dt. \quad (85)$$

From this formulation we see that the integral depends only on the difference between  $n$  and  $n'$  and not on the individual values of  $n$  and  $n'$  separately. Let us define

$$C_k(\tau_p) = \int_{-T/2}^{T/2} p(t') p(t' + \tau_p + kT) dt. \quad (86)$$

Since  $k = n - n'$ , Eq. (85) becomes

$$\begin{aligned}
I_B(\tau_p) &= T_B^{-1} \sum_{\substack{n=0 \\ n'=0}}^{\frac{N}{2}-1} I_n I_{n'} C_{n-n'}(\tau_p) \\
&= T_B^{-1} \sum_{n=0}^{\frac{N}{2}-1} \sum_{k=n}^{n+1-\frac{N}{2}} I_n I_{n-k} C_k(\tau_p) \\
&= T_B^{-1} \sum_{n=0}^{\frac{N}{2}-1} \sum_{k=-\left\{\frac{N}{2}-1\right\}}^{\frac{N}{2}-1} I_n I_{n-k} C_k(\tau_p) U_{n-k},
\end{aligned} \quad (87)$$

where

$$\begin{aligned}
U_{n-k} &= 1, \text{ if } 0 \leq n - k \leq \frac{N}{2} - 1, \\
&= 0, \text{ if } n - k < 0 \text{ or } n - k > \frac{N}{2} - 1.
\end{aligned}$$

We then interchange the order of summation in Eq. (87) to get

$$I_B(\tau_p) = T_B^{-1} \sum_{k=-\left\{\frac{N}{2}-1\right\}}^{\frac{N}{2}-1} C_k(\tau_p) \sum_{n=0}^{\frac{N}{2}-1} I_n I_{n-k} U_{n-k}. \quad (88)$$

Because of the orthogonality of the set  $\{I_n\}$  with any sequentially shifted copy of itself, we can write

$$\sum_{n=0}^{\frac{N}{2}-1} I_n I_{n-k} U_{n-k} = \frac{N}{2} \delta_{k,0}. \quad (89)$$

This assumes that the binary sequence  $\{I_n\}$  has been generated by a method that has "good" autocorrelation properties for the pseudo-noise-coding application. We obtain

$$I_B(\tau_p) = \frac{NT_B^{-1}}{2} C_0(\tau_p). \quad (90)$$

To calculate  $C_0(\tau_p)$ , we substitute into Eq. (86)

$$C_0(\tau_p) = \int_{-T/2}^{T/2} p(t')p(t' + \tau_p) dt'. \quad (91)$$

The value of  $C_0(\tau_p)$  is symmetric with respect to  $\tau_p$  and can be obtained by using elementary integration methods:

$$\begin{aligned} C_0(\tau_p) &= \frac{4}{T} \int_{-\frac{T}{2}}^{T/2-\tau_p} p(t')p(t' + \tau_p) dt', \quad \text{if } \tau_p \geq 0, \\ &= \frac{4}{T} \int_{-\frac{T}{2}}^{T/2-\tau_p} \cos\left\{\frac{\pi t'}{T}\right\} \cos\left\{\pi \left[\frac{t' + \tau_p}{T}\right]\right\} dt' \\ &= \frac{4}{T} \left[ \left[1 - \frac{|\tau_p|}{T}\right] \cos \frac{\pi \tau_p}{T} + \frac{1}{\pi} \sin \frac{|\tau_p|}{T} \right]. \end{aligned} \quad (92)$$

Equations (73) and (74) become

$$X_I(\tau_p) = (X_I \cos \omega_0 \tau_p + Y_I \sin \omega_0 \tau_p) NT_B^{-1} C_0(\tau_p) \quad (93)$$

and

$$Y_I(\tau_p) = (-X_I \sin \omega_0 \tau_p + Y_I \cos \omega_0 \tau_p) NT_B^{-1} C_0(\tau_p). \quad (94)$$

In matrix form we have

$$\mathbf{R}_I(\tau_p) = NT_B^{-1} T^{-1} \begin{Bmatrix} \cos \omega_0 \tau_p & \sin \omega_0 \tau_p \\ -\sin \omega_0 \tau_p & \cos \omega_0 \tau_p \end{Bmatrix} \mathbf{R}_I C_0(\tau_p). \quad (95)$$

A receiver can be adaptively synchronized to the incoming signal by introducing a variable delay  $\tau_R$  into the stream of baseband keying elements to generate a family of ideal baseband keying elements  $h_{B1}$  and  $h_{B2}$ . Mathematically this means that the variable  $t + \tau_R$  is introduced into the expression for  $h_{B1}$  in Eqs. (68) and (69) in place of  $t$ . The selection of the synchronization time  $\tau_R$  can greatly affect the receiver performance when the actual propagation delay time  $\tau_p$  is unknown (or equivalently the clocks that generate the chip streams are not in perfect initial synchronism). Therefore we rewrite Eq. (95) to exhibit the dependence of the system performance on  $\tau_R$ . We obtain the following expression for  $\mathbf{R}_I(\tau_p, \tau_R)$ :

$$\mathbf{R}_I(\tau_p, \tau_R) = NT_B^{-1} \begin{Bmatrix} \cos \omega_0 \tau_p & \sin \omega_0 \tau_p \\ -\sin \omega_0 \tau_p & \cos \omega_0 \tau_p \end{Bmatrix} \mathbf{R}_I C_0(\tau_p - \tau_R). \quad (96)$$

The magnitude of the components of  $\mathbf{R}_I(\tau_p, \tau_R)$  is proportional to the in-phase and quadrature components of the received radio-frequency carrier wave because of the multipliers  $\cos \omega_0 \tau_p$  and  $\sin \omega_0 \tau_p$  in the matrix. However, the magnitude of  $\mathbf{R}_I(\tau_p, \tau_R)$  depends on the propagation delay time  $\tau_p$  and on the receiver time  $\tau_R$  by the factor  $\tau_p = \tau_R$ . If the receiver is out of synchronization, the factor can be zero or can be very small. If the receiver is employing phase-shift keying, any change in the propagation time  $\tau_p$ , even after the receiver is perfectly synchronized on the chip ( $0 \approx |\tau_p - \tau_R| \ll T$ ), will induce a corresponding phase change in the phase of the vector  $\mathbf{R}_I = (\tau_p, \tau_R)$ ; that is, the doppler phase variation of the radio-frequency carrier induces an equal doppler shift on the phase angle  $\phi_R$ . These types of doppler-signal phase variations are often seen when a mobile transmitter or receiver is used. In such a circumstance we cannot assume that  $\tau_p(t)$  will be constant at each instant within a bit period to permit the factorization shown in Eqs. (67) and (68). However, the other manipulations that we performed on the expression for  $\mathbf{R}$  are all valid up to this point. To obtain the resultant correlation vector  $\mathbf{R}_I(\tau_p, \tau_R)$  if the delay time is slowly changing within a bit period, we must average the instantaneous values of  $\mathbf{R}_I[\tau_p(t), \tau_p]$  over an entire bit period:

$$\mathbf{R}_i(\tau_p, \tau_R) = NT_b^{-1} T^{-1} \int_{t_1 - T_{B/2}}^{t_1 + T_{B/2}} \begin{pmatrix} \cos \omega_0 \tau_p(t) & \sin \omega_0 \tau_p(t) \\ -\sin \omega_0 \tau_p(t) & \cos \omega_0 \tau_p(t) \end{pmatrix} \mathbf{R}_i C_0[\tau_p(t) - \tau_R] dt. \quad (97)$$

From this expression one can approximately evaluate the effect on the  $\mathbf{R}_i(\tau_p(t), \tau_R)$  vector for various conditions of  $\tau_p(t)$  and synchronization conditions for a single path propagation.

We have reviewed the elementary cases of a stationary and moving transmitter that has a single path of propagation, since this is the simplest case. Linear superposition holds for the waves and correlation procedures; thus a result from a case that has several propagation paths can be obtained by adding the terms from single-path cases.

### Two Propagation Modes and a Stationary Transmitter

When a stationary transmitter produces a signal at a receiver, the signal comes from two propagation paths, there are two propagation delay times  $\tau_{p1}$  and  $\tau_{p2}$  and two (real-valued) amplitudes of the two modes  $A_1$  and  $A_2$ . Alternatively, we may say that each mode is described by a complex amplitude, and the magnitude of each complex amplitude is the real amplitude and the phase is related to the propagation time. The voltage impressed on the receiving antenna by the received signal represents a waveform that is the sum of two time-delayed replicas of the initial waveform. The subscript  $i$  denotes the mode index. The result is shown in the following expression for the total correlation vector  $\mathbf{R}^T(\tau_R)$ :

$$\begin{aligned} \mathbf{R}_i^T(\tau_R) &= \sum_{i=1}^2 \mathbf{R}_i(\tau_{p,i}, \tau_R) \\ &= NT_b^{-1} T^{-1} \sum_{i=1}^2 A_i \begin{pmatrix} \cos \omega_0 \tau_{p,i} & \sin \omega_0 \tau_{p,i} \\ -\sin \omega_0 \tau_{p,i} & \cos \omega_0 \tau_{p,i} \end{pmatrix} \begin{pmatrix} X_i \\ Y_i \end{pmatrix} C_0(\tau_{p,i} - \tau_R). \end{aligned} \quad (98)$$

The behavior of  $\mathbf{R}_i^T(\tau_R)$  as a function of the receiver chip synchronization time  $\tau_R$  can be quite different from the behavior when there is only a single path. A splitting of the correlation peak can occur, and instead of the correlation being best when  $\tau_{p,i} = \tau_R$ , it could be bad at this time. Numerical examples given later exhibit this circumstance.

### LONGWAVE FIELD-STRENGTH VARIATIONS FROM AN AIRBORNE ANTENNA [57]

Consider the fields generated by an inclined, elevated transmitting antenna as the antenna moves in a circular path (orbit). This antenna is an idealization of a trailing-wire antenna carried by an aircraft circling at a constant altitude.

As the antenna goes around a circular path, the VLF waveguide modes generated by the vertical and horizontal components of this inclined antenna cause periodic variations in field strength. The magnitude of these orbit-produced periodic variations is a function of the distance from the transmitter. The sense of the variation (i.e., increasing or decreasing at a given time) can be opposite at points that are relatively close together on the same radial from the transmitter. Either one or two maximum values of received signal strength per orbit can be observed. When the antenna undergoes a periodic change of verticality caused by a gradient in wind velocity at the altitudes through which the antenna passes or droops, the magnitude of the periodic variation in received field strength depends on the direction of the receiver from the transmitter.

### Theory

Reference 16 gives the equations with which the electric and magnetic fields can be calculated from a vertical and horizontal antenna in the waveguide mode theory. First we consider only expressions for the vertical electric field strength, that use the earth-ionosphere waveguide model in which there is no conversion of horizontal electric fields to vertical fields at the ionospheric level.



$$E_r^{ve}(r, \theta) = i(\mu_0/\epsilon_0)^{1/2} I ds^{ve} \sum_n S_n^{1.5} F_n \quad (99)$$

$$E_r^{he}(r, \theta) = i(\mu_0/\epsilon_0)^{1/2} I ds^{he} \cos\phi \sum_n \Delta_n(z_s) S_n^{0.5} F_n \quad (100)$$

where

$$F_n = \frac{1}{(D\lambda h)^{1/2}} \left\{ \frac{D/a}{\sin(D/a)} \right\}^{1/2} G_n(z) G_n(z_s) \Lambda_n \exp(i\pi/4 + ik_0 D S_n) \quad (101)$$

Here,

$E_r^{ve}(r, \theta)$ ,  $E_r^{he}(r, \theta)$  indicate the vertical electric field strength at the point  $r, \theta$  received from a vertical or a horizontal electric dipole transmitting antenna, respectively (Fig. 67).

$(\mu_0/\epsilon_0)^{1/2}$  is the impedance of free space

$I$  is the transmitting antenna current

$ds^{he}$ ,  $ds^{ve}$  indicate the length of the horizontal or vertical transmitting antenna

$S_n$  is the sine of the complex eigenangle for the  $n$ th TM mode

$\Delta_n(z_s)$  is the impedance of the  $n$ th TM mode at the height  $z_s$  of the transmitter

$\phi$  is the angle between the great-circle path to the receiver and the end-fire direction of the horizontal antenna

$\lambda$  is the free-space wavelength of the electromagnetic wave

$D$  is the great-circle distance between the transmitter and the receiver

$a$  is the radius of the earth

$G_n(z)$  is the height-gain function of the  $n$ th mode

$\Lambda_n$  is the excitation factor of the  $n$ th mode

$k_0 = 2\pi/\lambda$

The total field  $E_r(r, \theta)$  from an inclined antenna is the sum of the fields from the horizontal and vertical components of the inclined antenna when the inclined antenna's length  $ds$  is broken up into its horizontal and vertical components  $ds^{he}$  and  $ds^{ve}$ ; they are inserted in Eqs. (99) and (100):

$$E_r(r, \theta) = E_r^{ve}(r, \theta) + E_r^{he}(r, \theta). \quad (102)$$

To simulate mathematically the effect of the motion of an antenna trailing behind a circling aircraft, we construct a Cartesian coordinate system with its origin on the earth's surface below the center of the circle. The  $z$  axis is normal to the earth's surface and the  $y$  axis points in the direction of the receiver. In these  $(x, y, z)$  coordinates we locate the antenna originally at the point  $(r_0, 0, z_s)$ , where  $r_0$  is the radius of the orbit and  $z_s$  is the height of the antenna above the ground. The receiver is located at the point  $(0, d, 0)$ , i.e., on the  $y$  axis on the surface of the earth a great-circle distance  $d$  from the origin. A diagram of this arrangement is shown in Fig. 68. The antenna is a short straight-line element centered at  $(r_0, 0, z_s)$  and inclined at the angle  $\gamma$  from the normal. Therefore,  $ds^{he} = ds \sin \gamma$  and  $ds^{ve} = ds \cos \gamma$ . The horizontal projection of the antenna points along the  $y$  axis. We define  $\zeta$  as the angle between the  $x$  axis and the projection in the  $x$ - $y$  plane of the line from the origin of the coordinate system to the center of the antenna. Since  $d \gg r$ , we use the approximation  $\phi \approx \zeta$ , which states that,

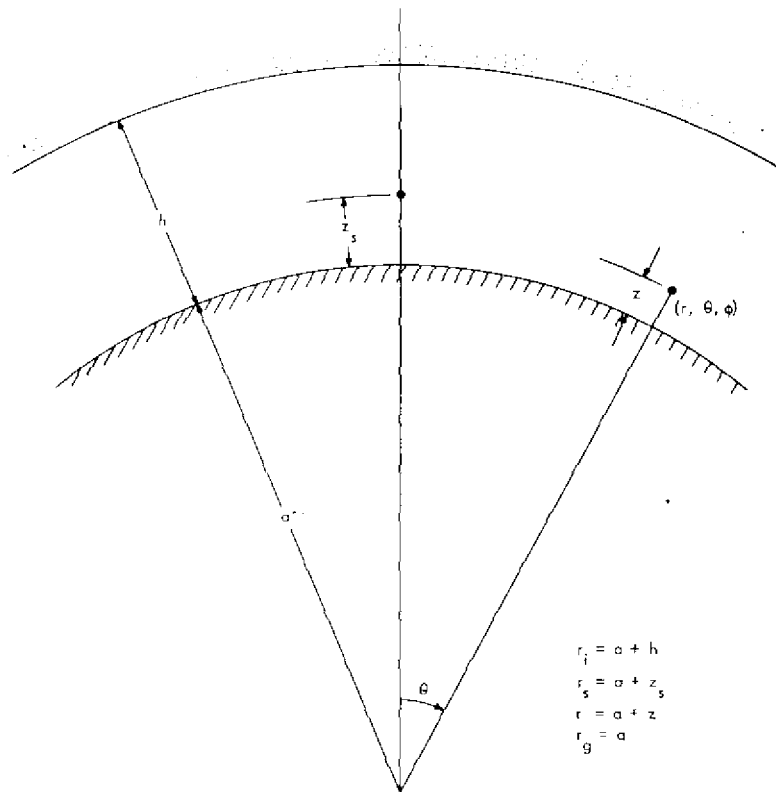


Fig. 67 — Diagram of sender and receiver locations

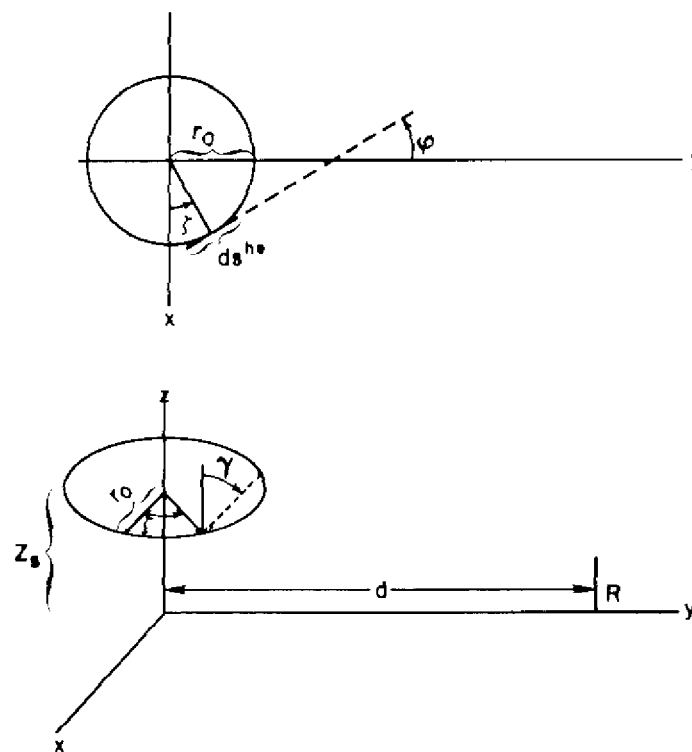


Fig. 68 — Diagram defining various angles.  
Upper diagram shows orbit from above.

when the horizontal projection of the antenna is parallel to the  $y$  axis, this horizontal projection points directly at the receiver. There is a small error in this approximation, but in this calculation it is at most of the order of  $r_0/d \approx 0.01$  radian. The great circle path  $D$  from the antenna to the receiver is calculated according to

$$D = (d^2 + r_0^2)^{1/2}, \quad (103)$$

which is exact for a flat earth and is a good approximation for the spherical earth. With these values we then calculate  $E_r(r, \theta)$  at the receiver. Next we carry the antenna smoothly about a circle, therefore we choose some incremental angle  $\Delta\zeta$  and move the antenna to the new coordinates  $(x_s', y_s', z_s')$  from the old coordinates  $(x_s, y_s, z_s)$  that were  $(r_0, 0, z_s)$  according to the transformation

$$x_s' = x_s \cos \Delta\zeta - y_s \sin \Delta\zeta \quad (104a)$$

$$y_s' = x_s \sin \Delta\zeta + y_s \cos \Delta\zeta \quad (104b)$$

$$z_s' = z_s, \quad (104c)$$

which is a rotation of the antenna location by an angle  $\Delta\zeta$  about the  $z$  axis. The previous angles  $\zeta$  and  $\phi$ , were zero but now are changed to  $\zeta'$  and  $\phi'$  angles according to

$$\phi' = \phi + \Delta\zeta = \zeta' = \zeta + \Delta\zeta. \quad (105)$$

A new great-circle distance  $D'$  between the transmitting antenna and the receiver is calculated according to

$$D' = ((x_s')^2 + (d - y_s')^2)^{1/2}. \quad (106)$$

When we consider a static inclined antenna that is being carried in a circle, the angle  $\gamma$  of the antenna from the vertical is unchanged. Because of the changes in the antenna direction and in the winds at different altitudes, we must consider that the antenna could undergo a periodic change in inclination as it traverses a circle. We can take this yo-yo motion into account by letting the angle  $\gamma$  oscillate about some average angle  $\gamma_0$  as the antenna goes about an orbit by setting

$$\gamma = \gamma_0 + \Delta\gamma \sin(\zeta + \zeta_0) \quad (107)$$

where  $\zeta_0$  is a phase angle that relates the orbital variation of the end-fire angle  $\phi$  with the variation of the inclination angle  $\gamma$ . Static conditions exist when  $\Delta\gamma = 0$ . The vertical electric field for the new antenna location is calculated according to Eqs. (99) through (102). Then the antenna is moved through a further  $\Delta\zeta$  rotation, and the process is repeated. From the results of these calculations, we determine the variations of amplitude and phase as the antenna proceeds about a circle.

## Calculations and Results

For our sample calculations, we chose the mode parameters of Galejs for 20 kHz transmissions. The numerical values that we used are given in Table 5.

Table 5 — Constants Used in the Calculations

$\Lambda_1 = 0.4$	$G_1(z) = 1$
$\Lambda_2 = 1.2$	$G_2(z) = 1$
$S_1 = 1.002 + 0.000689i$	$\Delta_1(z_s) = -0.02i$
$S_2 = 0.993 + 0.00138i$	$\Delta_2(z_s) = 0.05i$
$z = 0$ km	$r_0 = 4$ km
$G_1(z_s) = 0.965 + 0.259i$	$z_s = 10$ km
$G_2(z_s) = 0.95$	Radiated power = 1 kw

After each complete rotation we moved the receiver 100 km farther from the transmitter over a distance range of 500 to 5500 km. The topmost curve of Fig. 69 shows the vertical electric field strength obtained by considering the first- and second-order modes from a vertical antenna as a function of distance. The fourth curve from the top of Fig. 69 shows the maximum field strength as a function of distance from an elevated horizontal antenna. Note that the modal interference pattern for the horizontal antenna is quite different from that of the vertical antenna. Since we consider an isotropic model here, these results do not include the effects of polarization changes on reflection from the ionosphere.

The second and third curves from the top of Fig. 69 show field strength as a function of distance for antennas inclined with  $\gamma = 45^\circ$  and  $\gamma = 80^\circ$ , respectively, for  $\Delta\gamma = 0^\circ$ . The error bars represent the maximum and minimum values obtained as the antenna follows an orbit. The lower portion of Fig. 69 shows the relative phase of the fields from the vertical and horizontal antennas.

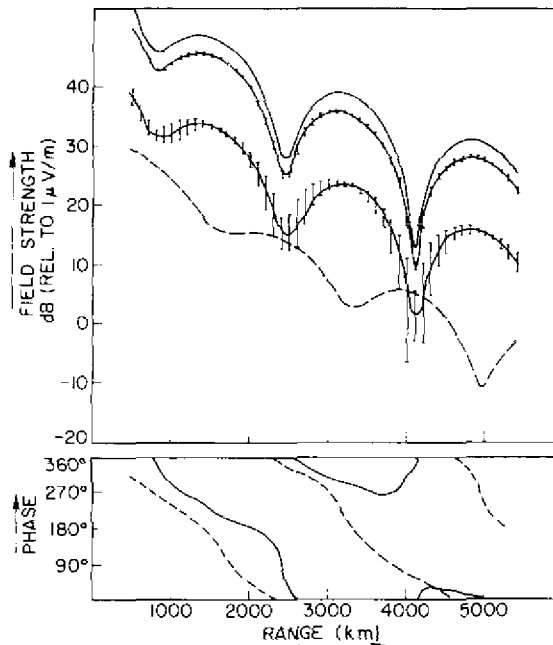


Fig. 69 — Amplitude and relative phase plots of fields generated by vertical, inclined, and horizontal antennas.

Figure 70 shows in more detail the variation of amplitude and phase for an inclined antenna ( $\gamma = 80^\circ$ ) at several ranges. Figure 71 shows the field strength variations with distance for the values of  $\gamma_0 = 60^\circ$ ,  $\Delta\gamma = 11^\circ$ , and  $\zeta_0 = 0^\circ$ .

## Discussion and Results

Figure 69 indicates that the amplitude of the orbit-produced, periodic variations of the received field strength is a function of the distance from the transmitter. In Fig. 70 we see a complete reversal of the sense of the oscillation between 4000 and 4200 km. At 4100 km the field strength has two relative maxima per orbit. This behavior seems very puzzling, although it has a natural explanation. Figure 72 shows a complex phasor representation of the sum contained in Eq. (102). The total vertical electric field strength is the phasor sum of the field strengths generated by the vertical and horizontal components of the antenna,  $E_r^V$  and  $E_r^H$ . (These are the same as  $E_r^{ve}$  and  $E_r^{he}$ , respectively.)

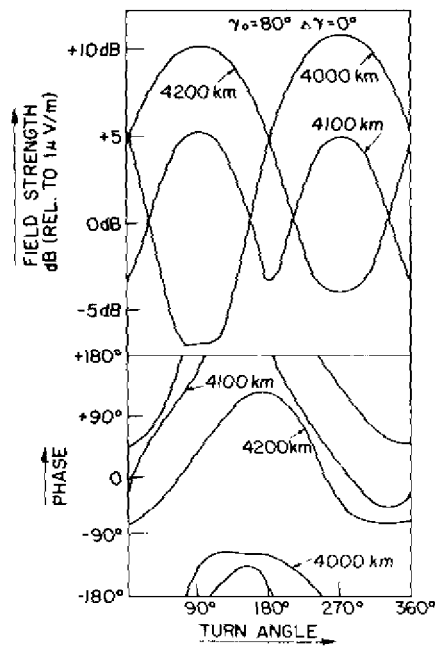


Fig. 70 — Amplitude and phase plots of fields as a function of the turn angle  $\zeta$  of the antenna

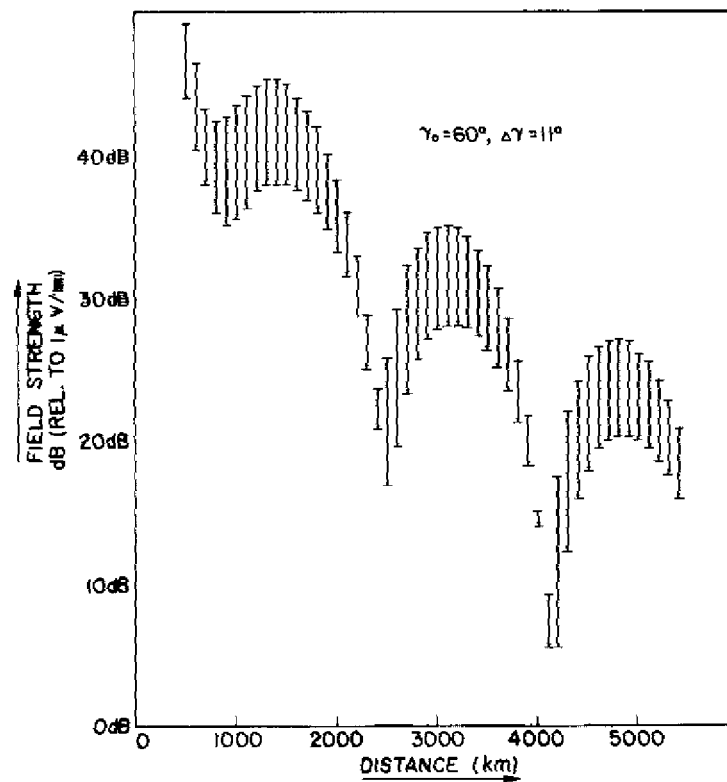


Fig. 71 — Amplitude plot of field generated by an orbiting, yo-yoing antenna

Generally, these phasors may have any angle with respect to one another; the angle may vary with distance. The  $E_r^V$  phasor represents an omnidirectional radiation pattern that does not change with orbit (as long as  $\gamma$  is fixed). The  $E_r^H$  phasor is not omnidirectional, however, and varies as the  $\cos \phi$  (see expression 100); therefore, it is modulated by a factor that changes from  $+1$  to  $-1$  with the orbit. In Fig. 72 this is represented by  $\pm E_r^H$ . The resultant field strength is represented by a phasor, one end of which is fixed at the origin; the other end slides along the  $E_r^H$  phasor. The sense of the variation of the resultant phasor is indicated by the curved trace on the right-hand side of the figure. The field strength, therefore, goes first through a maximum and then to a minimum as the antenna orbits. The middle diagram of Fig. 72 shows the  $E_r^H$  phasor at  $90^\circ$  to the  $E_r^V$  phasor; this relation causes two relative maxima in field strength per orbit. When the angle between phasors rotates farther, as shown on the bottom of Fig. 72, the case of a single maximum per orbit is reestablished, but now the variation is in the opposite sense to that shown in the top diagram of Fig. 72.

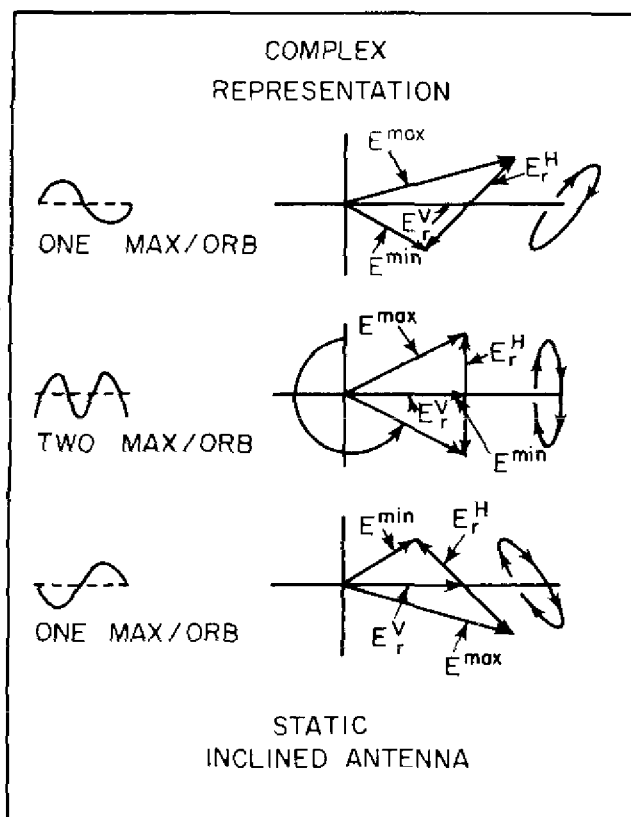


Fig. 72 — The number of maximum field strength values per orbit may change with the distance from the transmitter

From Fig. 69 we see a gradual change in the size of the periodic variations with distance. We also see that quite different modal interference patterns are set up by horizontal and vertical antennas. (The difference is caused by the presence of the impedance  $\Delta_n(z_s)$  in Eq. (100) and by its absence in Eq. (99)). The ratio of  $E_r^H$  to  $E_r^V$  changes with distance, and the nulls of the two interference patterns occur at different ranges. This effect is diagramed in Fig. 73. The lower portion shows two horizontally generated phasors from two modes that combine to give a resultant phasor. Two different  $E_r^H$  phasors are shown to illustrate the relative rotation of the horizontally generated phasors of the first and second modes as the distance from the transmitter changes. In the upper portion, two vertically generated phasors also combine to give a resultant. Here two different  $E_r^V$  phasors are shown to illustrate the relative rotation of the vertically generated phasors of the first and second modes as the distance from the transmitter changes. The vertically generated resultant is then added to the horizontally generated resultant. The horizontally generated resultant is modulated by a  $\cos \phi$  term; therefore the

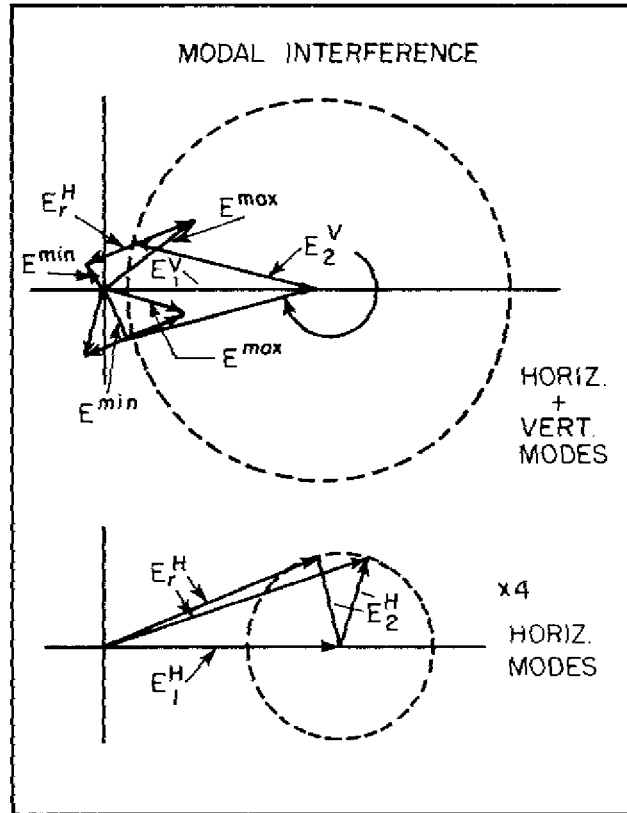


Fig. 73 — Changes in modal interference with range can change the received amplitude pattern

final resultant phasor may have one or two maxima per orbit, as we mentioned previously. As illustrated in the upper diagram of Fig. 73, the relative rotation of the mode phasors can cause the condition to change from a single maximum per orbit at one distance to two relative maxima per orbit at another distance. With the help of diagrams shown in Figs. 72 and 73, the behavior shown in Figs. 69 and 70 can be understood.

When the angle  $\gamma$  changes with the orbit angle, as in Eq. (107), we find an additional periodic variation that enhances or reduces the received field strength variation caused by purely orbital motion. This is illustrated in Fig. 71, where a large, abrupt change in the field strength variation is predicted between 4000 and 4200 km and between 2400 and 2500 km. For these cases, the purely orbital variation changes its sense of direction, whereas the yo-yo variation does not change appreciable in size or sense. On the near side of the null at 2400 km, the two fluctuations are out of phase and tend to cancel each other (1.3 dB oscillation). On the far side of the null at 2500 km, however, the fluctuations are in phase and reinforce to give a 12 dB oscillation. If we had chosen  $\zeta_0$  to be  $180^\circ$  instead of  $0^\circ$ , the situation would be reversed. Thus the variations are dependent on bearing as well as on range. The reference direction for determining the bearing dependence is provided by the wind-shear direction.

For the cases considered, we have assumed an homogeneous isotropic ionosphere, i.e., no earth's magnetic-field effects. For this isotropic condition, the vertical electric field  $E_r$  comes from the transverse magnetic (TM) modes. The transverse electric (TE) modes from the horizontal component are generated with a  $\sin \phi$  variation, but they do not carry any  $E_r$  field. When the earth's magnetic field is taken into account, however, we find that the TE modes become quasi-TE and have an appreciable  $E_r$  field that is due to polarization conversion at the ionosphere. This will create an additional complication, that is illustrated in Fig. 74. Here, the  $E_r^{ve}$  phasor is fixed in magnitude, but the  $E_r^{he}$  (TM) and  $E_r^{he}$  (TE) phasors are modulated by  $\cos \phi$  and  $\sin \phi$ , respectively, as the antenna goes around an orbit. These three phasors must be added to give the resultant observed field:

$$E_r = E_r^{ve} + E_r^{he}(\text{TM}) + E_r^{he}(\text{TE}). \quad (108)$$

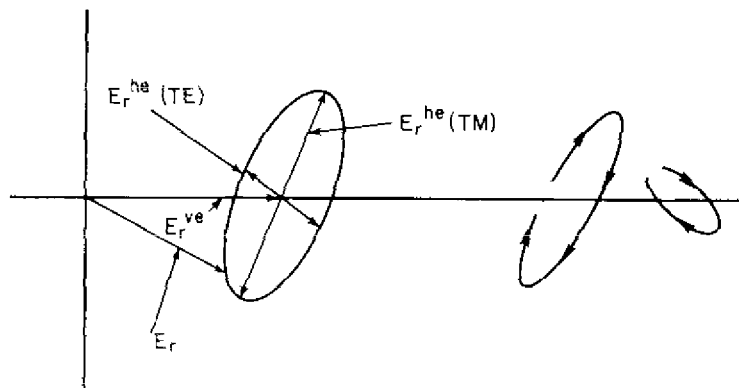


Fig. 74 — The additional complication that the quasi-TE modes may make in the received field variation

Actually, there will be  $E_r^{ve}$  (TE) and  $E_r^{ve}$  (TM) fields, but they are combined to form a constant  $E_r^{ve}$  field. The  $E_r^{he}$  (TE) phasor has a sinusoidal variation. The variation is shifted by just  $90^\circ$  in  $\phi$  angle from the  $E_r^{he}$  (TM) phasor. Instead of the end of the resultant phasor  $E_r$  following the line traced out by the  $E_r^{he}$  (TM) phasor, it will now follow around an ellipse as  $\phi$  goes from  $0^\circ$  to  $360^\circ$ , as shown in Fig. 74. As  $E_r^{he}$  (TM) goes through zero,  $E_r^{he}$  (TE) reaches its maximum and vice versa. It is possible, of course, for the ellipse to become either a straight line or a circle, depending on the relative magnitudes and directions of  $E_r^{he}$  (TM) and  $E_r^{he}$  (TE) on the phasor plane.

For an orbiting horizontal antenna, the homogeneous, isotropic ionosphere model predicts that the field strength will be zero for  $\phi = 90^\circ$ . However, the introduction of the earth's magnetic field changes this prediction; the contribution from the quasi-TE modes has a maximum at  $\phi = 90^\circ$ . Since the quasi-TE and quasi-TM modes generate different modal interference patterns, there should exist some combination of range, frequency, and bearing at which the ellipse of Fig. 74 is a circle. In this case, an horizontal orbiting antenna would cause no amplitude variation at the receiver. This special case is not likely to be experienced often, but this possibility shows the diversity of the results that may be obtained from an orbiting antenna.

We see that the variation of the signal received from an orbiting antenna is quite complicated, even though the antenna itself is a simple short dipole. The magnitude of the variation is a function of the range and bearing of the receiver. Large changes in the size of the variations can occur with small changes in range.

#### ANTENNA MOTION EFFECTS ON MODULATION SYSTEMS [58]

With the previous development of the mathematics it is easy to show the effects of rotation by an inclined elevated antenna. The horizontal component of the inclined antenna generates TE and TM modes; the horizontally generated fields have phases and amplitudes different from those generated by the vertical antenna components. The waveguide modal interference pattern for an elevated horizontal antenna differs from that of a vertical antenna. This effect is illustrated in Fig. 69. It shows the fields generated by various inclined antennas at 20 kHz. The amplitudes of the horizontally generated fields vary as the cosine of the angle between the horizontal antenna component and the direction of propagation.

In simulating the effect of this variation on the receiver output vector, we use Eq. (98) for the received correlation vectors, we also use four amplitudes  $\{A_i\}$ , four phase time delays  $\{\tau_i^p\}$ , and four group time delays  $\{\tau_i^g\}$ . Two of the amplitudes represent two vertically generated mode fields and vary as  $\sin \gamma$ . The other two represent horizontally generated TM mode fields and vary as the product  $\cos \zeta \cos \gamma$ . The resultant expression for the correlator output is the same as Eq. (98) except that in this case the correlation output is the summation of the outputs for the four individual modes.



Denoting the  $X_l^{(i)}(\tau_R)$  from the vertically electrically generated modes as  $X_l^{(i)ve}(\tau_R)$  and the  $X_l^{(i)}(\tau_R)$  from the horizontally electrically generated modes as  $X_l^{(i)he}(\tau_R)$ , we can write

$$X_l^T(\tau_R) = \cos \gamma \sum_{i=1}^{N'} X_l^{(i)ve}(\tau_R) + \cos \zeta \sin \gamma \sum_{i=1}^{N'} X_l^{(i)he}(\tau_R). \quad (109a)$$

Parallel definitions can be made for  $Y_l^T(\tau_R)$ ,  $Y_l^{(i)ve}(\tau_R)$  and  $Y_l^{(i)he}(\tau_R)$ , and we obtain

$$Y_l^T(\tau_R) = \cos \gamma \sum_{i=1}^{N'} Y_l^{(i)ve}(\tau_R) + \cos \zeta \sin \gamma \sum_{i=1}^{N'} Y_l^{(i)he}(\tau_R). \quad (109b)$$

The vector  $\mathbf{R}_l^T(\tau_R)$  is a sum of two vectors  $\mathbf{R}_l^{ve}(\tau_R)$  and  $\mathbf{R}_l^{he}(\tau_R)$ :

$$\mathbf{R}_l^T(\tau_R) = \cos \gamma \mathbf{R}_l^{ve}(\tau_R) + \cos \zeta \sin \gamma \mathbf{R}_l^{he}(\tau_R). \quad (110)$$

The vectors  $\mathbf{R}_l^{ve}(\tau_R)$  and  $\mathbf{R}_l^{he}(\tau_R)$  can be parallel, perpendicular, or opposed to each other, depending on circumstances and the value of  $\tau_R$ . The resultant  $\mathbf{R}_l^T(\tau_R)$  vector can change quite dramatically during a complete orbit. For example, if  $\mathbf{R}_l^{ve}(\tau_R)$  and  $\mathbf{R}_l^{he}(\tau_R)$  are of the same magnitude and phase, there would be one large oscillation of  $|\mathbf{R}_l^T(\tau_R)|$  per orbit (provided  $\gamma = 45^\circ$ ). If  $\mathbf{R}_l^{ve}(\tau_R)$  and  $\mathbf{R}_l^{he}(\tau_R)$  are perpendicular to each other, there would be two oscillations of  $|\mathbf{R}_l^T(\tau_R)|$  with one cycle  $\zeta$ . There is a mathematical isomorphism between the phasor  $E_r(D)$  and the vector  $\mathbf{R}_l^T(\tau_R)$ , since the composition of various phasors that form the complex phasor sum  $E_r(D)$  is isomorphic to the composition of various correlation vectors that form the two-dimensional correlation vector sum  $\mathbf{R}_l^T(\tau_R)$ . When both TE and TM waveguide mode propagation from an airborne transmitting facility are taken into account, we obtain the following relation.

$$\mathbf{R}_l^T(\tau_R) = \mathbf{R}_l^{ve}(\tau_R) \cos \gamma + \sin \gamma [\cos \zeta \mathbf{R}_l^{he}(TM, \tau_R) + \sin \zeta \mathbf{R}_l^{he}(TE, \tau_R)]. \quad (111)$$

The total vector  $\mathbf{R}_l^T(\tau_R)$  is the sum of independently propagated vertical endfire- and broadside-generated components. These components are sums of components that are propagated by different waveguide modes.

### Diagrammatic Representations

It is instructive to view diagrams that illustrate the behavior of the various  $\mathbf{R}_l$  vectors as  $\tau_R$  and  $\zeta$  vary. The following example illustrates what can happen in a particularly severe case of modal interference. Figure 75 depicts the variation of a single-mode correlation output  $\mathbf{R}_l^{(1)ve}(\tau_R)$  from a stationary vertical electric transmitter. Figure 76 shows an output function  $\mathbf{R}_l^{(2)ve}(\tau_R)$  for a signal coming slightly later on a second-order mode and  $180^\circ$  out of phase with the first. Figure 77 gives the resultant  $\mathbf{R}_l^{ve}(\tau_R)$ , that is the sum of the correlation outputs of the first and second modes. Figure 78 shows the phase of the vector  $\mathbf{R}_l^{ve}(\tau_R)$  as a function of  $\tau_R$ .

Figure 79 shows the results  $\mathbf{R}_l^T(\tau_R) = \cos \gamma \mathbf{R}_l^{ve}(\tau_R) + \sin \gamma \cos \zeta \mathbf{R}_l^{he}(\tau_R)$ , where  $\zeta$  is the angle between the direction of propagation and the endfire direction of the antenna. The angle  $\gamma$  is the inclination angle of the antenna; we take  $\gamma = 45^\circ$  and  $\zeta = 0$  for this example. Figure 80 shows the same results except for the condition  $\zeta = 180^\circ$ . The conditions for  $\zeta = 90^\circ$  and  $\zeta = 270^\circ$  are both shown by the pattern of Fig. 77, since  $\mathbf{R}_l^T(\tau_R)$  is composed solely of the vertically generated modes in these cases. These figures give a picture of  $\mathbf{R}_l^T(\tau_R)$  at the four cardinal points of an orbit.

In Fig. 80 four sample synchronization times, designated  $\tau_{R1}$ ,  $\tau_{R2}$ ,  $\tau_{R3}$ , and  $\tau_{R4}$ , represent possible correlation times that might occur within a receiver. We look at the variation of the correlation vector magnitude  $|\mathbf{R}_l^T(\tau_{Ri})|$  and phase  $\phi_l^T(\tau_{Ri})$  during a complete orbit for these times. Figures 81 and 82 show the phase and magnitude of  $\mathbf{R}_l^T(\tau_{R1})$ . The phase is constant in this case, because  $\mathbf{R}_l^{ve}(\tau_{R1})$  is greater than and parallel to  $\mathbf{R}_l^{he}(\tau_{R1})$ . The magnitude varies in a mild way. In Figs. 83 and 84 showing the phase and amplitude for the time  $\tau_{R2}$ , the phase makes two quick successive  $180^\circ$  changes in the

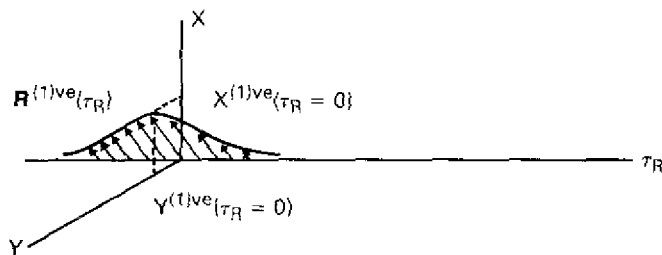


Fig. 75 —  $R_i^{(1)ve}(\tau_R)$  vs  $\tau_R$  for a stationary vertical electric-dipole transmitter

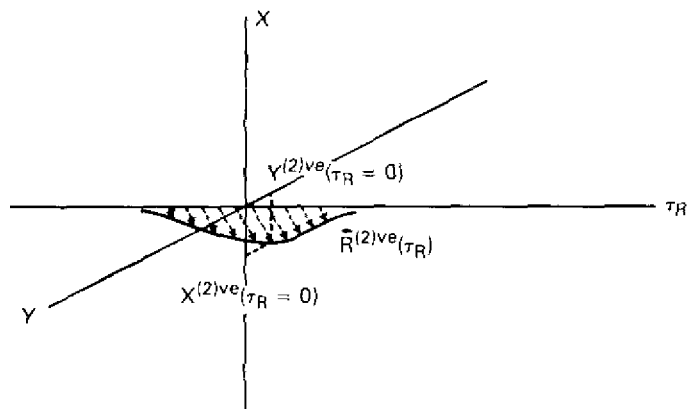


Fig. 76 —  $R_i^{(2)ve}(\tau_R)$  vs  $\tau_R$  for a stationary vertical electric dipole transmitter. The phase of this wave is  $180^\circ$  opposite to that illustrated in Fig. 75. The maximum value of  $|R_i^{(2)ve}(\tau_R)|$  occurs at slightly greater  $\tau_R$  values than does the maximum value of  $|R_i^{(1)ve}(\tau_R)|$  shown in Fig. 75.

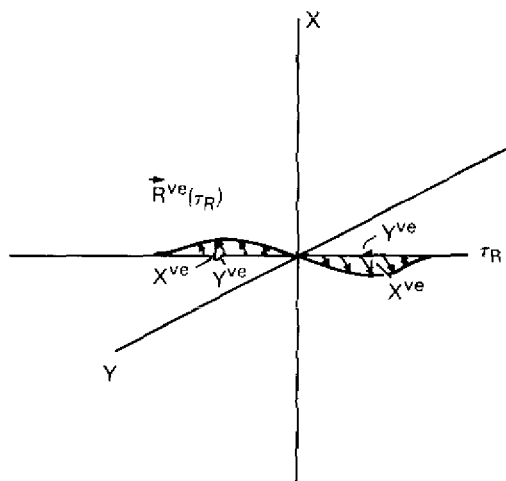


Fig. 77 —  $R_i^{ve}(\tau_R) = R_i^{(1)ve}(\tau_R) + R_i^{(2)ve}(\tau_R)$  shows an abrupt change of phase at  $\tau_R = 0$  and a large shift in the value of  $\tau_R$  for which  $|R_i^{ve}(\tau_R)|$  is greatest

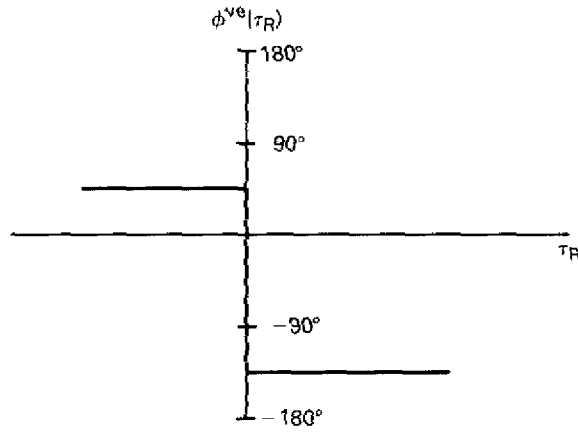


Fig. 78 —  $\phi_j^{ve}(\tau_R)$ , the angle of the  $\mathbf{R}_j^{ve}(\tau_R)$  vector with the x axis in Fig. 77 shows an abrupt shift of phase at  $\tau_R = 0$

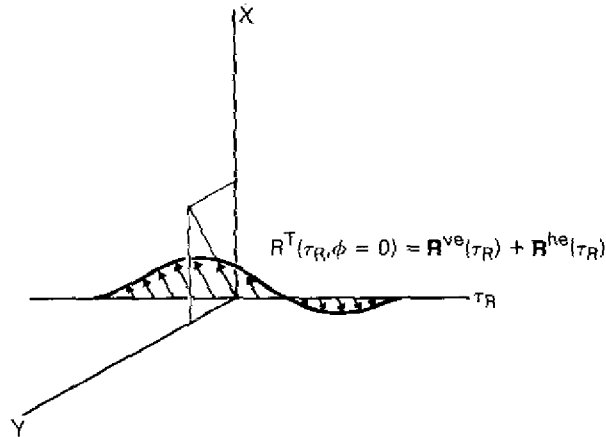


Fig. 79 —  $\mathbf{R}_j^T(\tau_R)$  for an endfire case ( $\cos \zeta = +1$ ) illustrates the change in the value of  $\tau_R$  for which  $|\mathbf{R}_j^T(\tau_R)| = 0$  and the variation in the size of the peak values of  $|\mathbf{R}_j^T(\tau_R)|$  on opposite sides of  $\tau_R = 0$ . Here a relatively small value of  $|\mathbf{R}_j^{ve}(\tau_R)|$  is assumed.

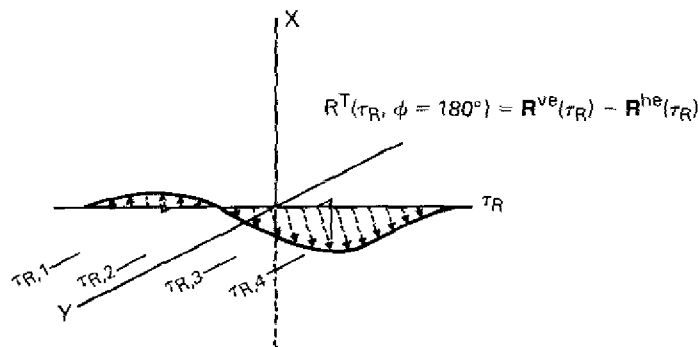


Fig. 80 —  $\mathbf{R}_j^T(\tau_R)$  for the opposite endfire case ( $\cos \zeta = -1$ ) to the case in Fig. 79. Here the largest value of  $|\mathbf{R}_j^T(\tau_R)|$  occurs for  $\tau_R > 0$  whereas, in Fig. 79 it was for  $\tau_R < 0$ . Synchronization times  $(\tau_R)$  to be considered in subsequent figures are shown.

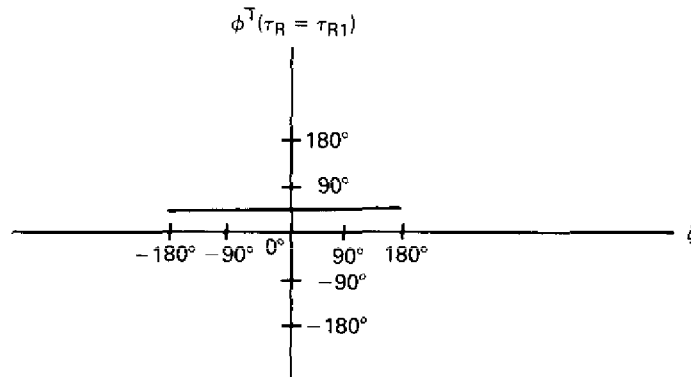


Fig. 81 —  $\phi_i^T(\tau_{R1})$  as the angle of turn  $\zeta$  of an inclined antenna changes from  $-180^\circ$  to  $+180^\circ$  for the synchronization time  $\tau_{R1}$ . This phase is constant because the contribution of the vertical antenna component always exceeds that of the horizontal component for this synchronization time.

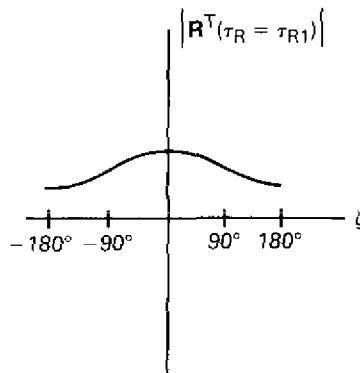


Fig. 82 —  $\{R_i^T(\tau_{R1})\}$  as  $\zeta$  varies from  $-180^\circ$  to  $+180^\circ$ . The relatively gentle variation of  $\{R_i^T(\tau_{R1})\}$  occurs because  $\{R_i^{ve}(\tau_{R1})\} > \{R_i^{he}(\tau_{R1})\}$ .

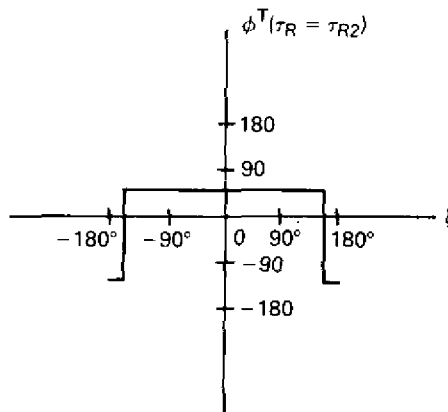


Fig. 83 —  $\phi_i^T(\tau_{R2})$  vs orbit angle  $\zeta$ . For this lock-on time there are two rapid and large phase changes near  $\zeta = 180^\circ$ .

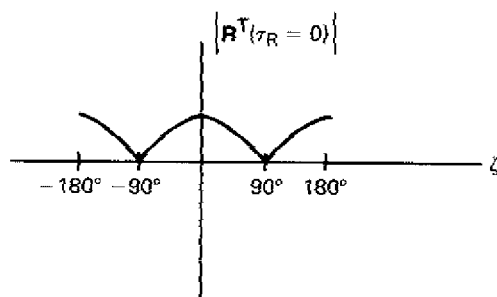


Fig. 84 —  $|R^T(\tau_R)|$  vs orbit angle  $\zeta$ , showing how this function goes to zero when  $\phi^T(\tau_R)$  is making the abrupt phase transition

neighborhood of  $\zeta = 180^\circ$ , and the amplitude goes through two successive nulls. Figures 85 and 86 give  $R^T(0)$ . This vector varies cosinusoidally, because there is no contribution from the vertical electric antenna component. Figures 87 and 88 show the behavior of  $R^T(\tau_{R3})$ , which is similar to the behavior of  $R^T(\tau_{R2})$  except that the nulls occur near  $\zeta = 0^\circ$  rather than  $\zeta = 180^\circ$ . Figures 89 and 90 show the behavior of  $R^T(\tau_{R4})$ , which is similar to  $R^T(\tau_{R1})$  except for a shift in orbit angle  $\zeta$  of  $180^\circ$ .

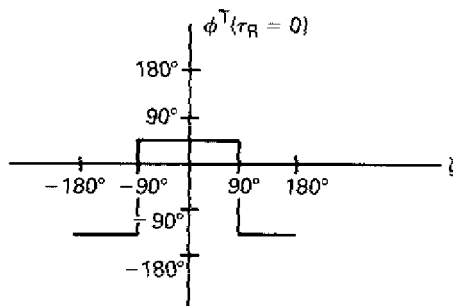


Fig. 85 —  $\phi^T(\tau_R = 0)$  vs angle  $\zeta$ . There is essentially no contribution from the vertical component for this value of  $\tau_R$ , so the phase is controlled by the horizontal component of the transmitting antenna.

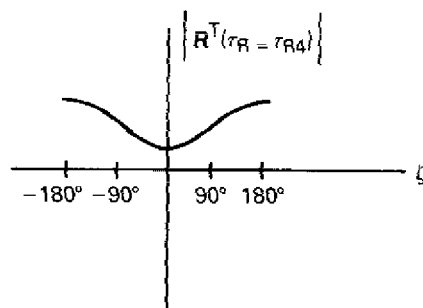


Fig. 86 —  $|R^T(\tau_R = 0)|$  vs orbit angle  $\zeta$ . The cosinusoidal variation is caused by the  $\cos \zeta$  modulation of the horizontal component. The vertical component contributes essentially zero.

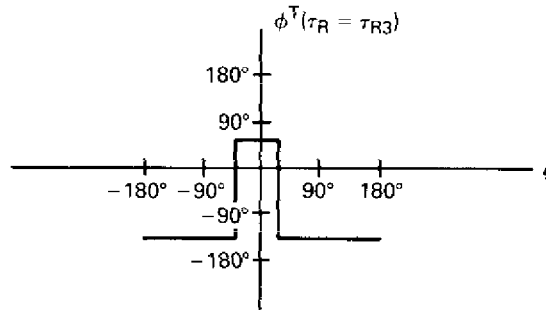


Fig. 87 —  $\phi_I^T(\tau_{R3})$  vs orbit angle  $\zeta$ . For this synchronization time the abrupt changes in phase occur around the  $\zeta = 0^\circ$  point rather than around the  $\zeta = 180^\circ$  for the  $\tau_{R2}$  case illustrated in Fig. 83.

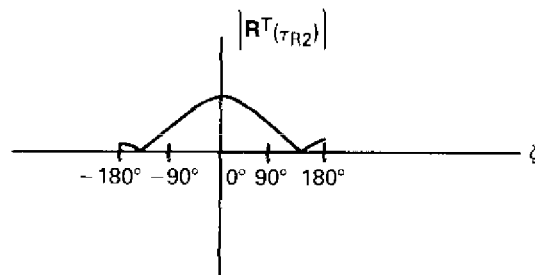


Fig. 88 —  $|R_I^T(\tau_{R2})|$  vs orbit angle  $\zeta$ . The smallest values of  $|R_I^T(\tau_{R2})|$  occur for orbit angles near  $0^\circ$  rather than near  $180^\circ$  as was the case for  $|R_I^T(\tau_{R2})|$  as shown in Fig. 78.

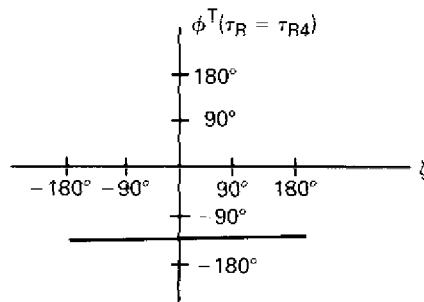


Fig. 89 —  $\phi_I^T(\tau_{R4})$  vs orbit angle  $\zeta$ . For this receiver time the vertically generated correlation vector dominates; that is  $|R_{Ive}^T(\tau_{R4})| > |R_{Ihe}^T(\tau_{R4})|$ . No change of phase can occur, since  $R_{Ive}^T(\tau_{R4})$  and  $R_{Ihe}^T(\tau_{R4})$  are parallel.

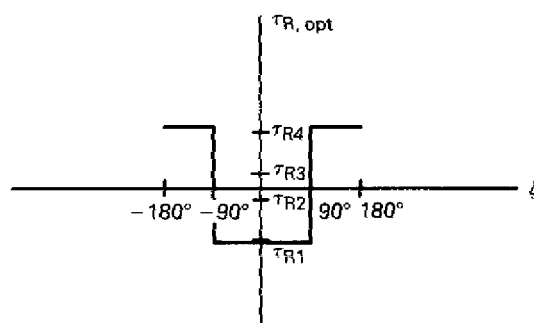


Fig. 90 —  $|R_I^T(\tau_{R4})|$  vs orbit angle  $\zeta$ . For this receiver time the maximum correlation vector occurs for  $\zeta = 180^\circ$ , whereas for  $\tau_{R1}$  the maximum correlation-vector magnitude occurred at  $\tau = 0^\circ$ .

Finally, Fig. 91 shows an estimate of  $\tau_{Ropt}$ , the optimum value of receiver correlation time for different values of orbit angle  $\zeta$ . This graph shows that  $\tau_{R1}$  and  $\tau_{R4}$  are preferable when  $|R_I(\tau_{R1})|$  and  $|R_I(\tau_{R4})|$  are largest. The phase is constant, and the amplitude varies gently. Relatively mild amplitude behavior occurs for this correlation time because  $|R_I^{ve}(\tau_{R1})| > |R_I^{he}(\tau_{R1})|$ . The phase is constant because  $R_I^{ve}(\tau_{R1})$  is parallel to  $R_I^{he}(\tau_{R1})$ . Although  $R_I^{he}(\tau_{R1})$  can change the magnitude of  $R_I^T(\tau_{R1})$ , it does not change the phase.

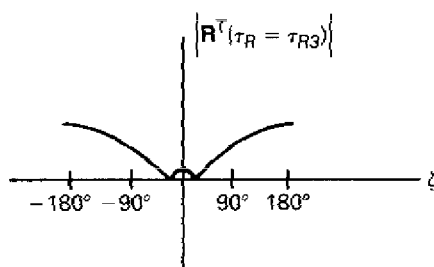


Fig. 91 — Values of  $\tau_R$  that should be chosen for various orbit angles  $\zeta$  for the case illustrated in Figs. 75 through 90

In the preceding example there was minimum correlation near the middle of the correlation envelope, and the correlation maximum was greatly displaced from the maximum point of the correlation of either individual multipath signal. Thus the rather small difference in arrival times  $\tau_{p1} - \tau_{p2}$  changes the optimum chip synchronization time  $\tau_R$  by a major amount. This effect is fairly easy to explain. The condition described by our equations is a severe case of multipath interference. Two signals come to the receiver antenna offset in time by  $\tau_{p1} - \tau_{p2}$ . The first and second signals travel independently of each other, so when the first signal pulse arrives, the signal begins to build up. Then the second signal arrives out of phase and cancels out the first signal for a long interval of time while both are strong. Then the first signal goes to zero because its waveform has passed by, while the second signal remains to give an excitation of the antenna again. Thus the strongest portions of each signaling element in this case of interference occur at the beginning and the end of each signaling element. In the middle of the element, the two signals arriving from different paths interfere, and a reduction of the field present appears.

When a receiver tries to synchronize with the signal at its strongest point, it must search for synchronization either at the beginning of the chip or at the end of it but not in the middle. Thus, if a system were presynchronized with an optimum  $\tau_R$  for either of the individual mode delays or for an average of the two mode delays, it would actually be poorly synchronized for optimum operation! For better operation three correlators might be used—one adjusted at the central expected time of arrival of the wave, and one at each end of the chip. If the two waveforms reinforce each other to give the maximum in the middle, the central correlation peak will be large and the two side peaks will be small. If, however, an interference condition is present, the middle correlator will be weak and the two side correlators will be strong.

## Numerical Calculations

### Procedures

Calculations will follow of some values of  $\mathbf{R}_i^T$  for cases that are inspired by realistic mode-theory calculations of the phase and amplitude of VLF waves. For the calculated fields shown in Fig. 6, the waveguide mode constants are given in Table 5.

These constants were used in the following equations to generate the field-strength values shown in Fig. 69:

$$E_r^{ve}(r, \theta) = i(\mu_0/\epsilon_0)^{1/2} I \, ds^{ve} \sum_n S_n^{1.5} F_n \quad (112)$$

and

$$E_r^{he}(r, \theta) = i(\mu_0/\epsilon)^{1/2} I \, ds^{he} \cos \phi \sum_n \Delta_n(z_s) S_n^{0.5} F_n, \quad (113)$$

where

$$F_n = \frac{1}{(D\lambda h)^{1/2}} \left( \frac{D/a}{\sin(D/a)} \right)^{1/2} G_n(z) G_n(z_s) \Lambda_n \exp(i\pi/4 + ik_0 DS_n). \quad (114)$$

These equations are simplified versions, since they contain only TM-mode constants of an isotropic ionosphere. We calculate  $\mathbf{R}_i^{(i)ve}$  for each mode according to

$$X_i^{(i)ve}(\tau_R, \zeta) = N |A_i^{ve}| \cos[\omega_0 \tau_i^{p,ve}(\zeta)] C(\tau_i^{g,ve}(\zeta) - \tau_R) \quad (115)$$

and

$$Y_i^{(i)ve}(\tau_R, \zeta) = N |A_i^{ve}| \sin[\omega_0 \tau_i^{p,ve}(\zeta)] C(\tau_i^{g,ve}(\zeta) - \tau_R), \quad (116)$$

where

- $N$  is a normalizing constant,
- $A_i^{ve}$  is the amplitude of the  $i$ th TM mode generated by the vertical component of the transmitting antenna,
- $\omega_0$  is the angular frequency of the wave,
- $\tau_i^{p,ve}(\zeta)$  is the delay time of the phase of the wave when the aircraft is at angle  $\zeta$  of its orbit for the  $i$ th waveguide mode, and
- $\tau_i^{g,ve}(\zeta)$  is the group delay time of the wave when the aircraft is at angle  $\zeta$  of its orbit for the  $i$ th waveguide mode.



The amplitude is given by

$$A_i^{ve} = S_i^{1.5} G_i(z) G_i(z_s) \Lambda_i \exp(i\pi/r + i k_0 D S_i). \quad (117)$$

The phase delay time  $\tau_i^{p,ve}(\zeta)$  is obtained by evaluating the phase of  $A_i$ :

$$\omega_0 \tau_i^{p,ve}(\zeta) = \arg(A_i^{ve}). \quad (118)$$

The group delay time  $\tau_i^{g,ve}(\zeta)$  is obtained by evaluating the derivative of the phase of  $A_i$ :

$$\tau_i^{g,ve}(\zeta) = \frac{\partial}{\partial \omega} [\arg(A_i^{ve})]. \quad (119)$$

The path length  $D$  from the transmitting antenna to the receiver location is a function of the orbit angle  $\zeta$  and the orbit radius  $r$  according to the approximation

$$D = D_0 + r \sin \zeta, \quad (120)$$

where  $D_0$  is the distance from the receiver to the center of the orbit. To calculate  $\mathbf{R}_i^{ve}(\zeta, \tau_R)$ , we performed summations as indicated in Eqs. (108) through (110).

We calculate the horizontally electrically generated fields in an analogous manner:

$$X_i^{(i)he}(\tau_R, \zeta) = N |A_i^{he}| \cos [\omega_0 \tau_i^{p,he}(\zeta)] C_0 (\tau_i^{g,he}(\zeta) - \tau_R) \quad (121)$$

and

$$Y_i^{(i)he}(\tau_R, \zeta) = N |A_i^{he}| \sin [\omega_0 \tau_i^{p,he}(\zeta)] C_0 (\tau_i^{g,he}(\zeta) - \tau_R). \quad (122)$$

The amplitude of the  $i$ th mode is given as follows:

$$A_i^{he} = G_i(z) G_i(z_s) \Lambda_i \exp(i\pi/4 + i k_0 D S_i) S_i^{1.5} \Delta_i(z_s) = A_i^{ve} S_i \Delta_i(z_0). \quad (123)$$

The phase and group delay times are given in the same manner as for the vertically generated modes:

$$\omega_0 \tau_i^{p,he}(\zeta) = \arg(A_i^{he}) \quad (124)$$

and

$$\tau_i^{g,he}(\zeta) = \frac{\partial}{\partial \omega} [\arg(A_i^{he})]. \quad (125)$$

Tables 6 and 7 give the numerical values used in making the correlation calculations.

## Results

Figures 92 through 97 show  $\mathbf{R}_i^T(\tau_R)$  and  $\phi_i^T(\tau_R)$  contours for  $\gamma$  values of  $90^\circ$ ,  $85^\circ$ ,  $80^\circ$ ,  $60^\circ$ ,  $45^\circ$ , and  $0^\circ$  with the propagation parameters shown in Table 6. Figure 98 shows  $\mathbf{R}_i^{(1)ve}(\tau_R)$ , the correlation vector of the first-order mode. Figures 99 through 104 show the correlation vector for propagation parameters of Table 7 for  $\gamma$  values of  $90^\circ$ ,  $85^\circ$ ,  $80^\circ$ ,  $60^\circ$ ,  $45^\circ$ , and  $0^\circ$ . The "average" chip duration for each of these calculations was  $\tau_c = 1$  ms. The total length of each chip is  $T = 2\tau_c = 2$  ms. The radius of the orbit is 3 km; the distance from the center of the orbit to the receiver is 4000 km.

## Discussion

Figure 92 shows the correlator performance for the case of a completely horizontal antenna. For this case  $|\mathbf{R}_i(\tau_R)|$  goes to zero at  $\zeta = 90^\circ$  and  $270^\circ$ , and there are sudden  $180^\circ$  phase flips at these angles. The best correlation time appears to be at  $\tau_R = 13.5$  ms, which is the middle of the correlation peak.

Table 6 — Set of Quantities Used in Calculating Correlation Vectors

Mode	Quantity	Value
1	$ A_1^{ve} $	$1.26500262 \times 10^{-1}$
	$\tau_1^{p,ve}$	$1.33658211 \times 10^{-2}$
	$\tau_1^{g,ve}$	$1.34400 \times 10^{-2}$
	$ A_1^{he} $	$2.52495471 \times 10^{-3}$
	$\tau_1^{p,he}$	$1.33533157 \times 10^{-2}$
	$\tau_1^{g,he}$	$1.34400 \times 10^{-2}$
2	$ A_2^{ve} $	$1.11773228 \times 10^{-1}$
	$\tau_2^{p,ve}$	$1.32437617 \times 10^{-2}$
	$\tau_2^{g,ve}$	$1.356666 \times 10^{-2}$
	$ A_2^{he} $	$5.62805237 \times 10^{-3}$
	$\tau_2^{p,he}$	$1.32562578 \times 10^{-2}$
	$\tau_2^{g,he}$	$1.356666 \times 10^{-2}$

Table 7 — Second Set of Quantities Used in Calculating Correlation Vectors

Mode	Quantity	Value
1	$ A_1^{ve} $	$1.26500262 \times 10^{-1}$
	$\tau_1^{p,ve}$	$1.33658211 \times 10^{-2}$
	$\tau_1^{g,ve}$	$1.34400 \times 10^{-2}$
	$ A_1^{he} $	$2.52495471 \times 10^{-3}$
	$\tau_1^{p,he}$	$1.3315820 \times 10^{-2}$
	$\tau_1^{g,he}$	$1.34400 \times 10^{-2}$
2	$ A_2^{ve} $	$1.26500262 \times 10^{-1}$
	$\tau_2^{p,ve}$	$1.33908211 \times 10^{-2}$
	$\tau_2^{g,ve}$	$1.356666 \times 10^{-2}$
	$ A_2^{he} $	$5.62805237 \times 10^{-3}$
	$\tau_2^{p,he}$	$1.3365820 \times 10^{-2}$
	$\tau_2^{g,he}$	$1.356666 \times 10^{-2}$

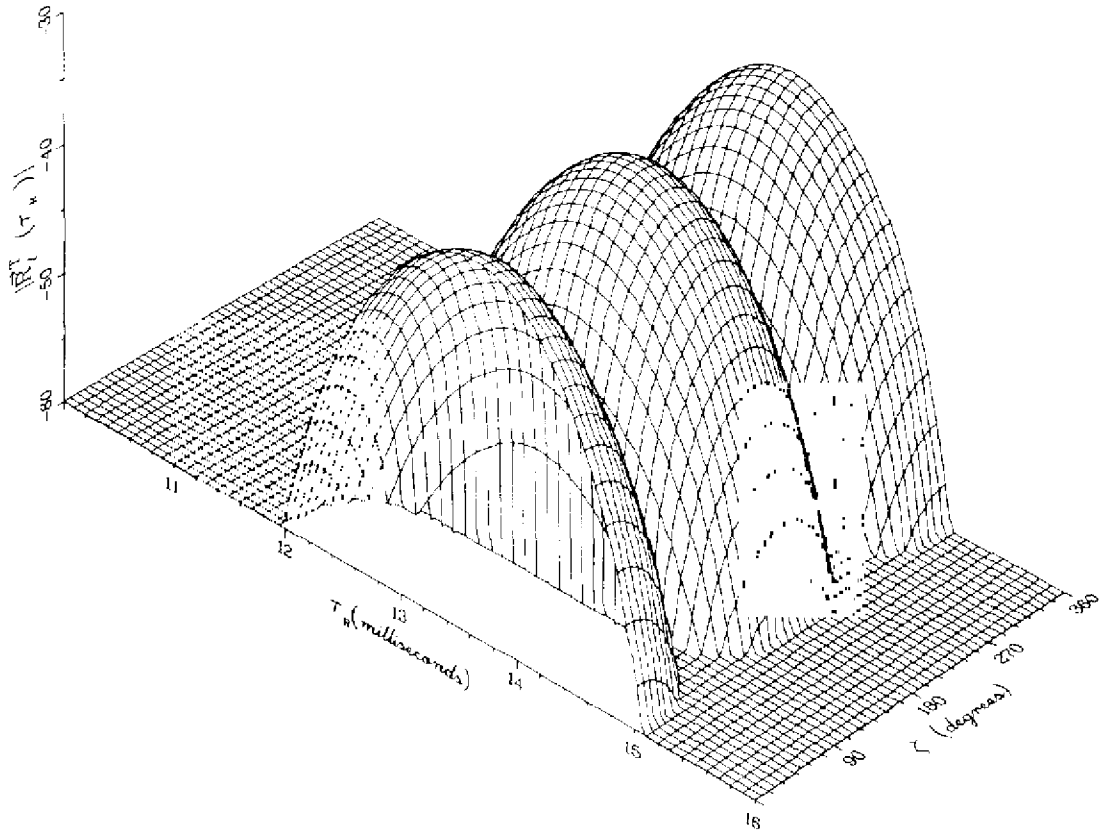


Fig. 92(a) — Amplitude behavior of  $R_l^j(\tau_R)$  for  $\zeta = 90^\circ$ , calculated with the parameters of Table 6

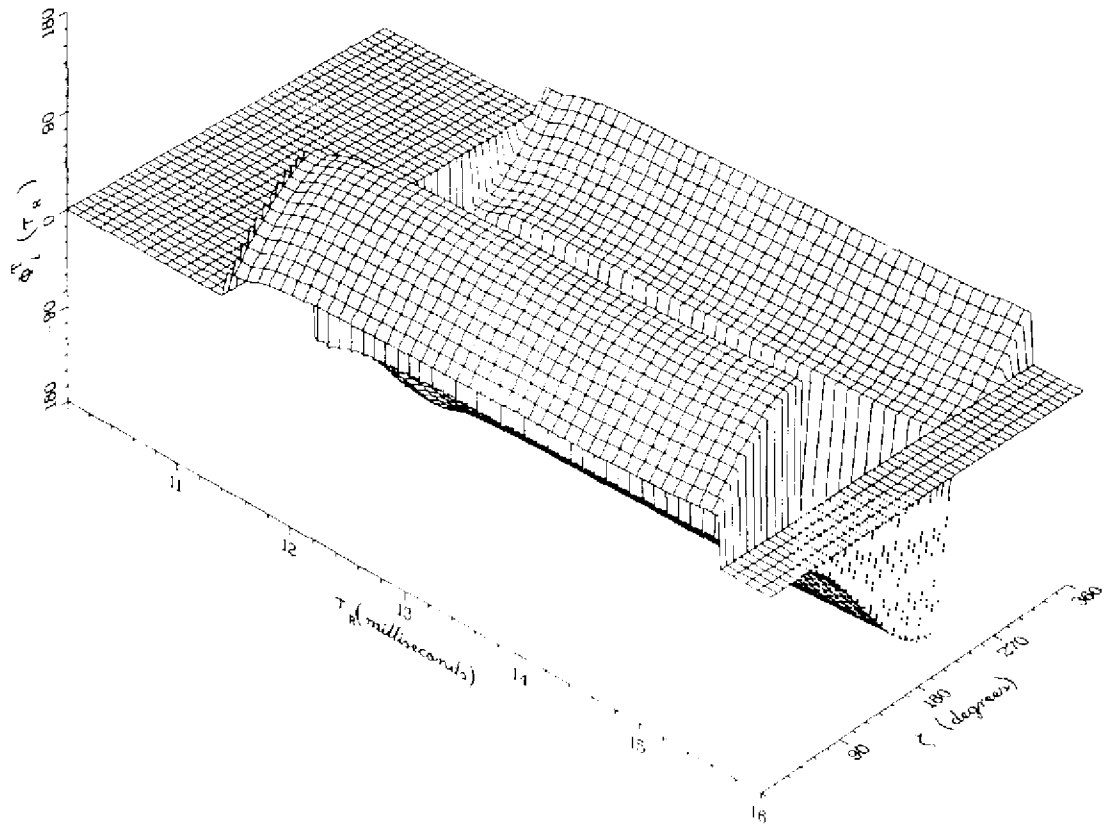


Fig. 92(b) — Phase behavior of  $R_l^j(\tau_R)$  for  $\gamma = 90^\circ$ , calculated with the parameters of Table 6

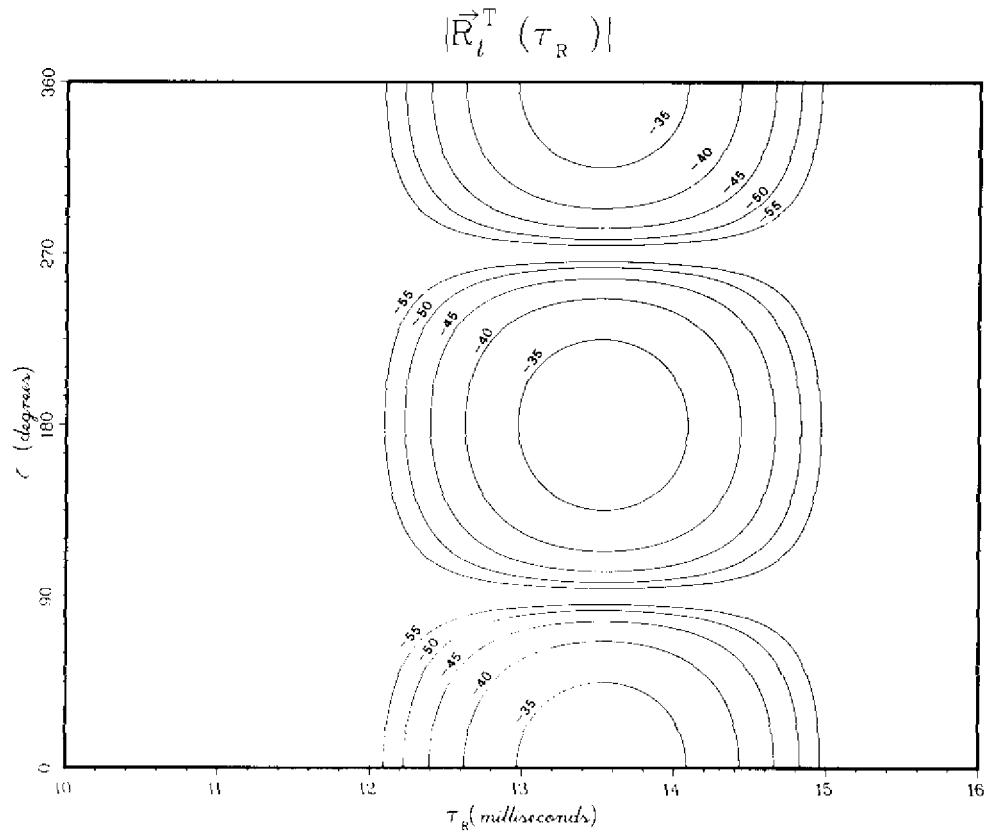


Fig. 92(c) — Amplitude contours corresponding to those in Fig. 92(a)

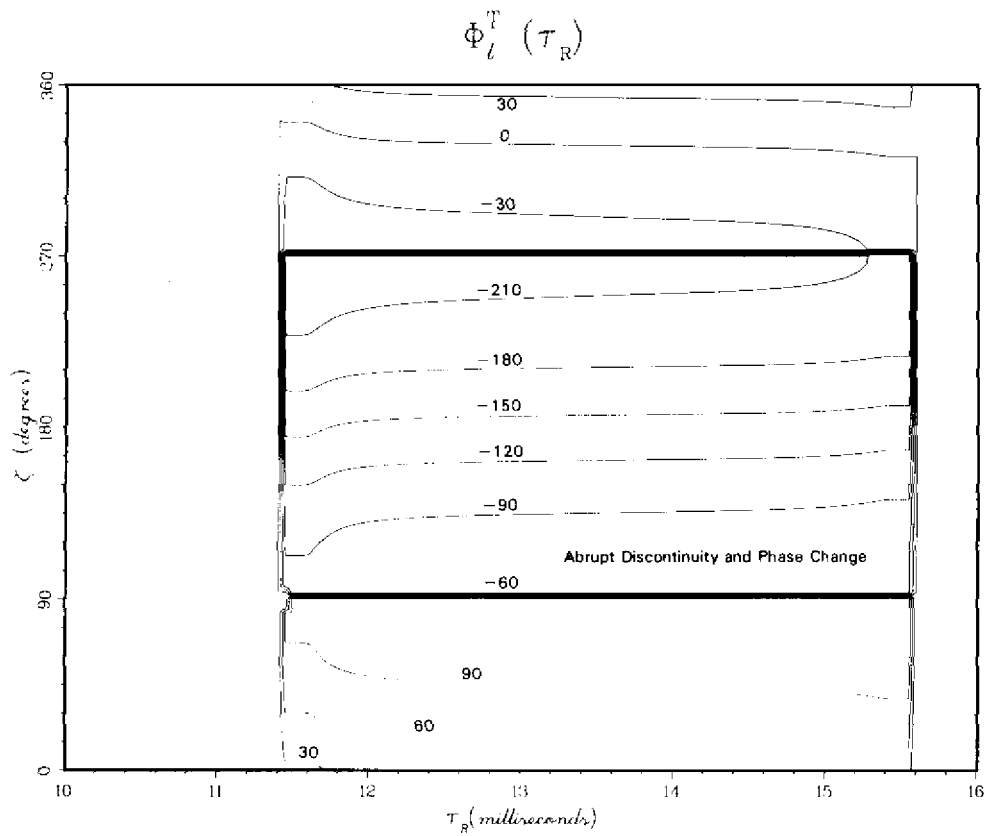


Fig. 92(d) — Phase behavior corresponding to that in Fig. 92(b)

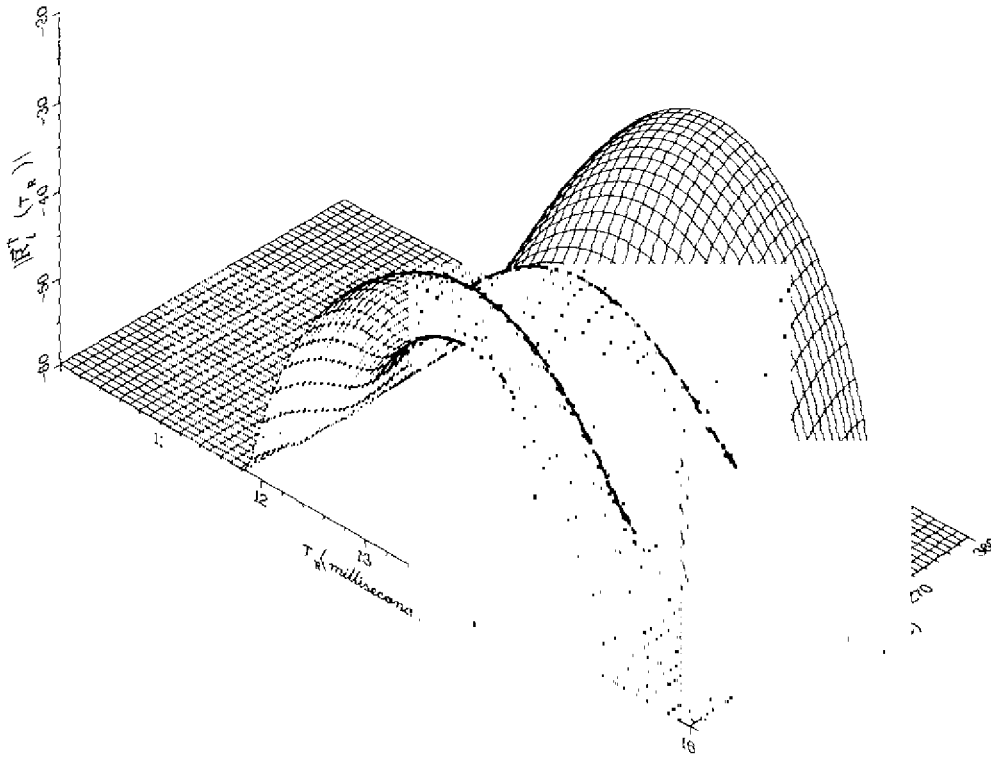


Fig. 93(a) — Amplitude behavior of  $R_l^T(\tau_R)$  for  $\gamma = 85^\circ$ ,  
calculated with the parameters of Table 6

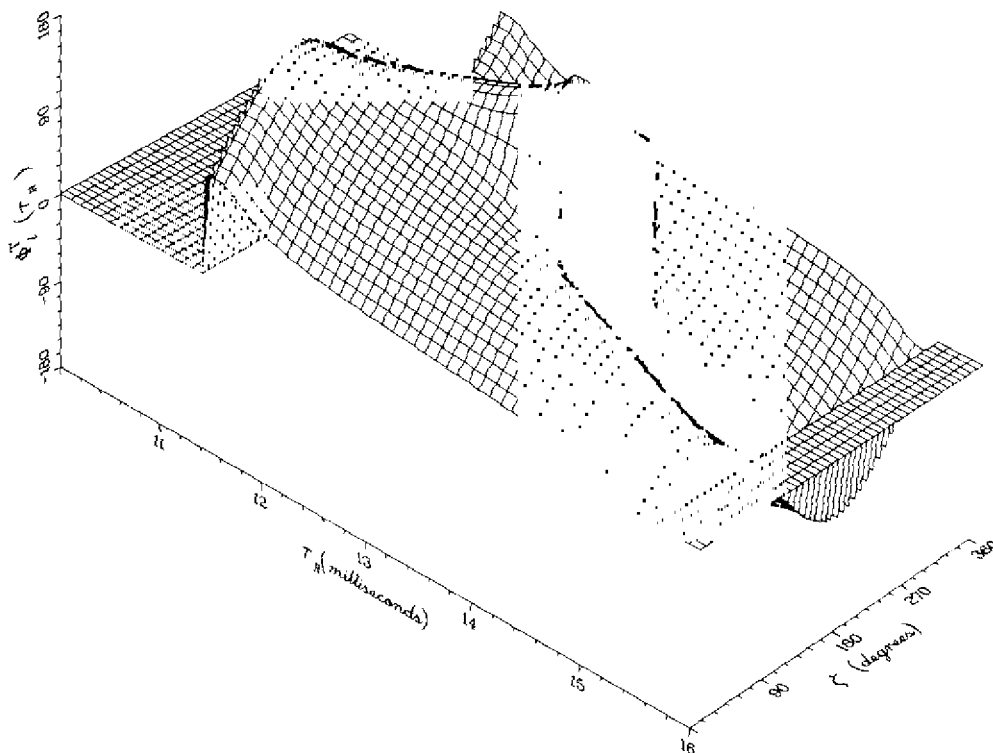


Fig. 93(b) — Phase behavior of  $R_l^T(\tau_R)$  for  $\gamma = 85^\circ$ ,  
calculated with the parameters of Table 6

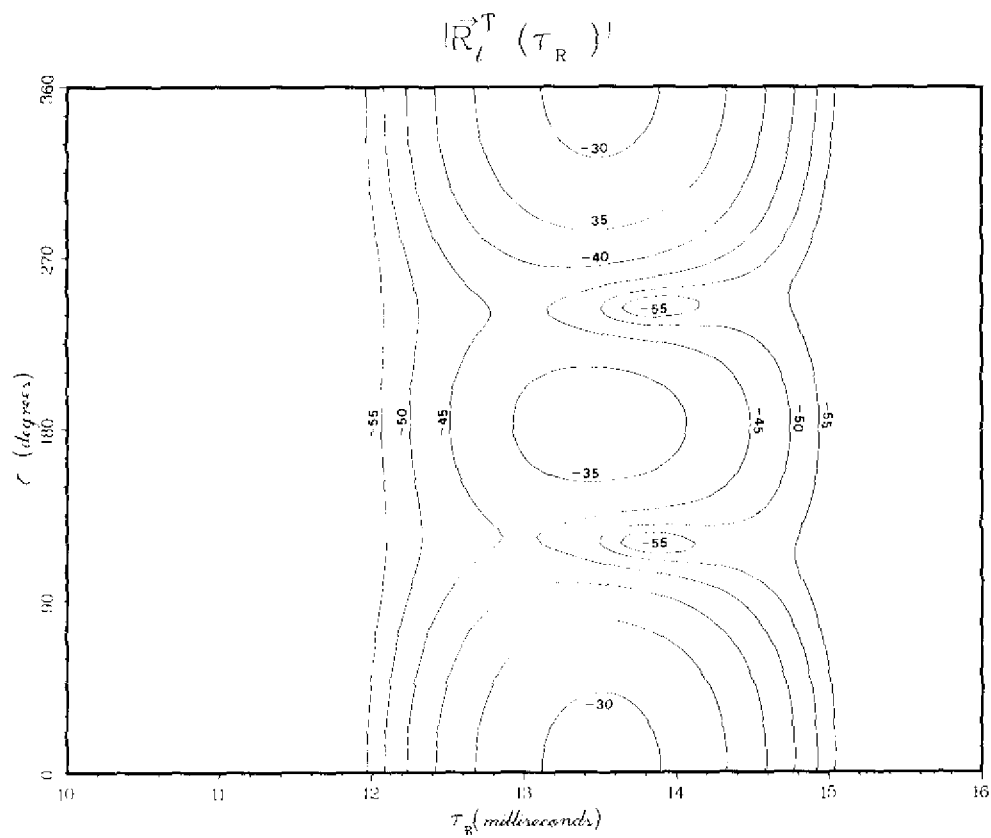


Fig. 93(c) — Amplitude contours corresponding to that in Fig. 93(a)

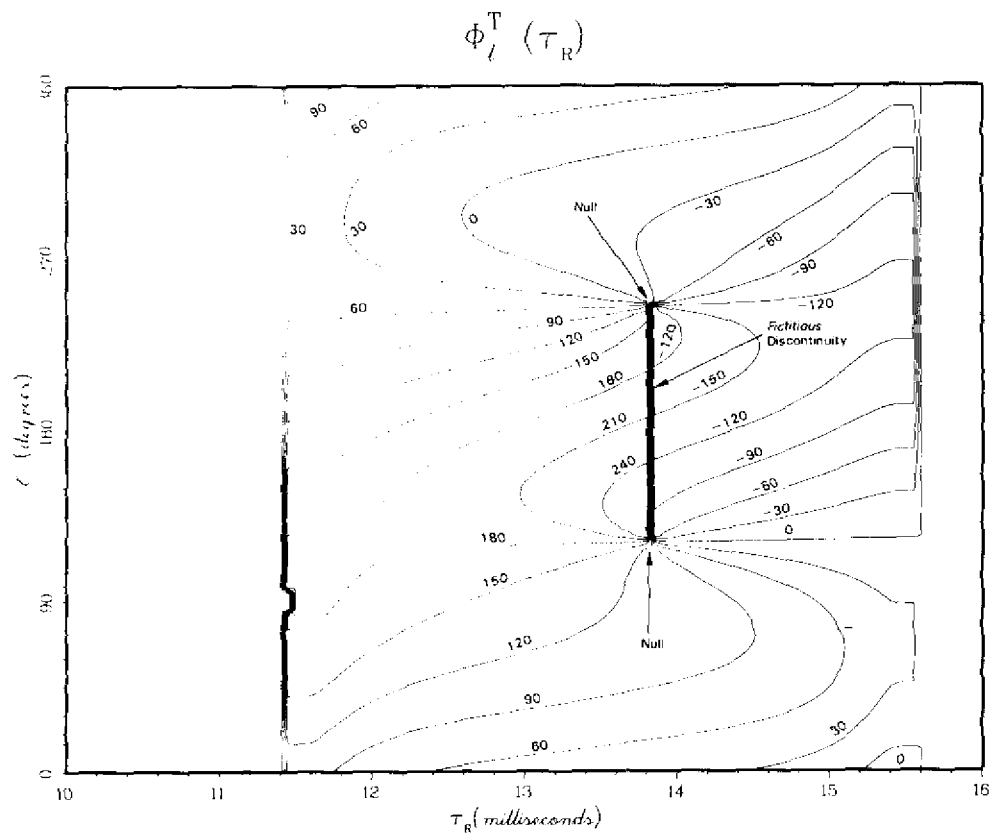


Fig. 93(d) — Phase behavior corresponding to that in Fig. 93(b)

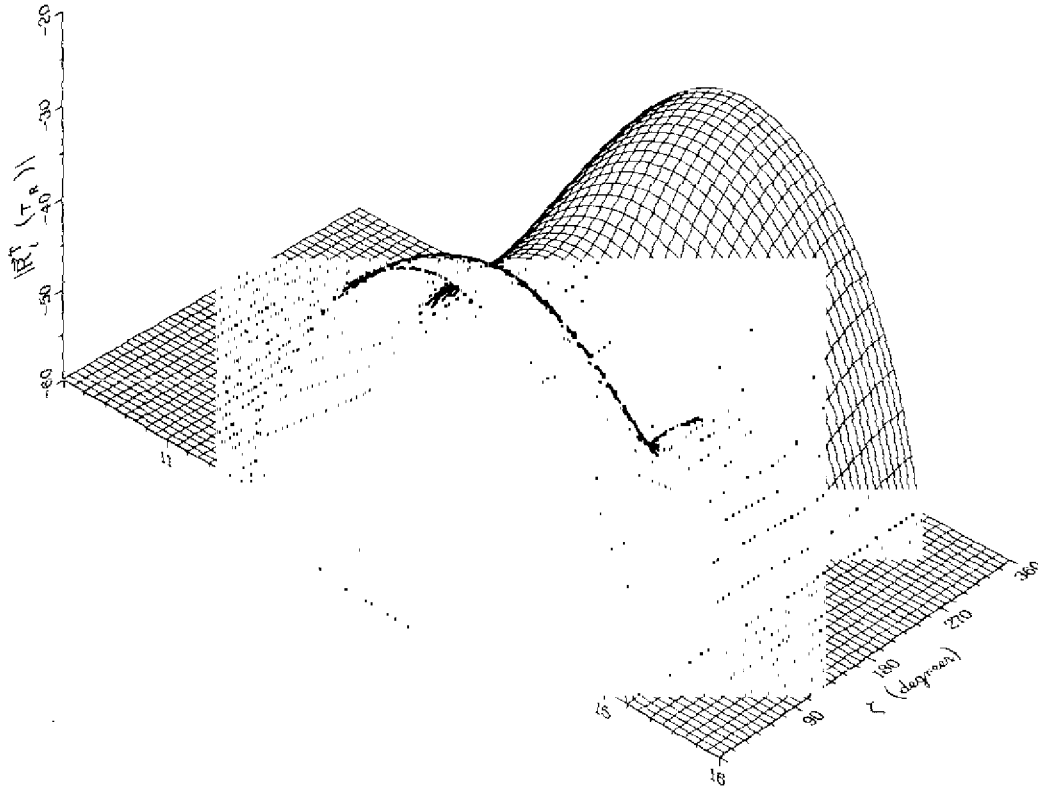


Fig. 94(a) — Amplitude behavior of  $R_I^T(\tau_R)$  for  $\gamma = 80^\circ$ ,  
calculated with the parameters of Table 6

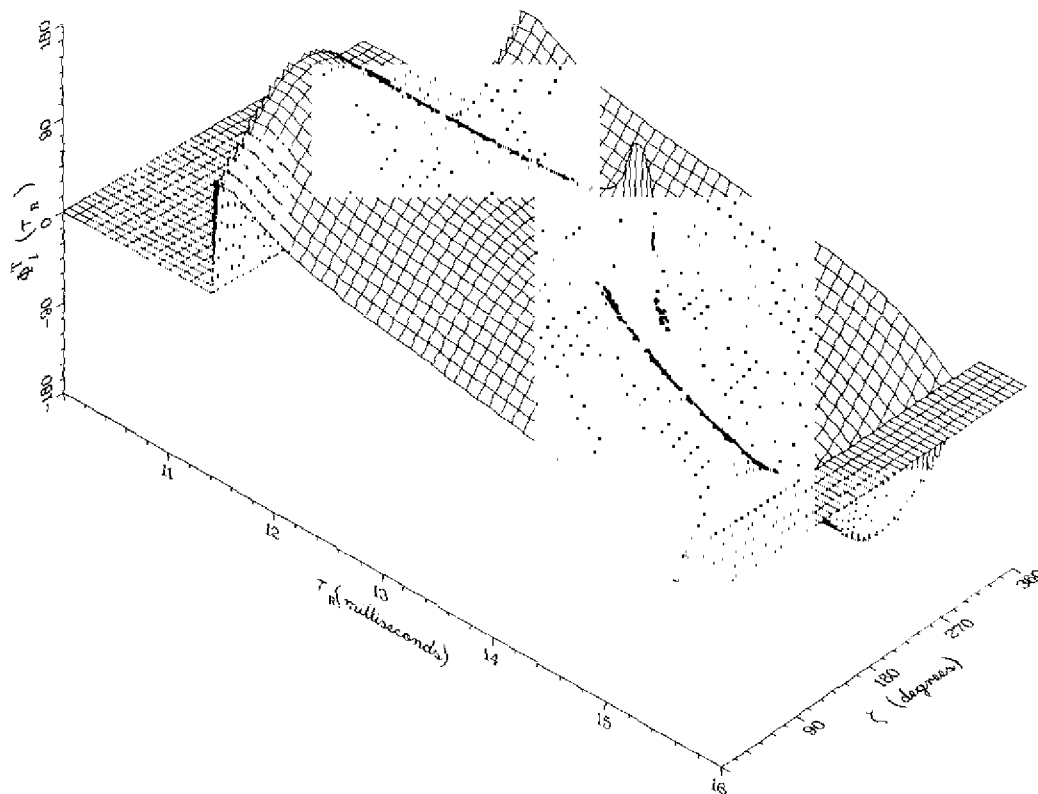


Fig. 94(b) — Phase behavior of  $R_I^T(\tau_R)$  for  $\gamma = 80^\circ$ ,  
calculated with the parameters of Table 6

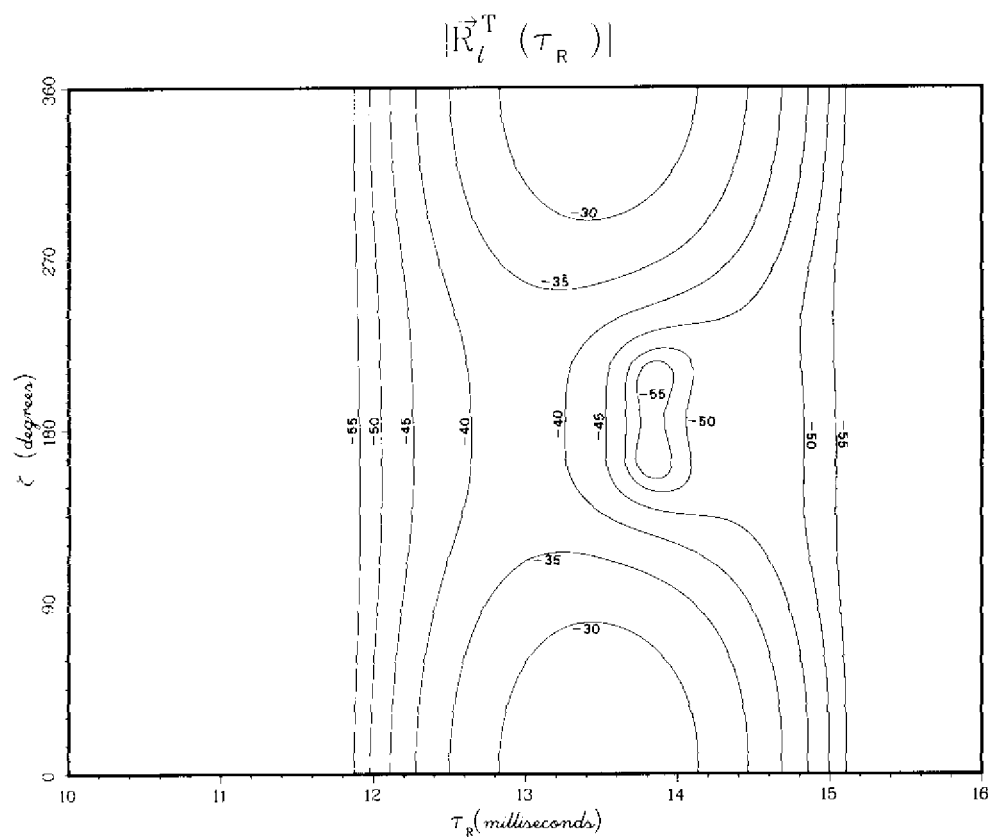


Fig. 94(c) — Amplitude contours corresponding to those in Fig. 94(a)

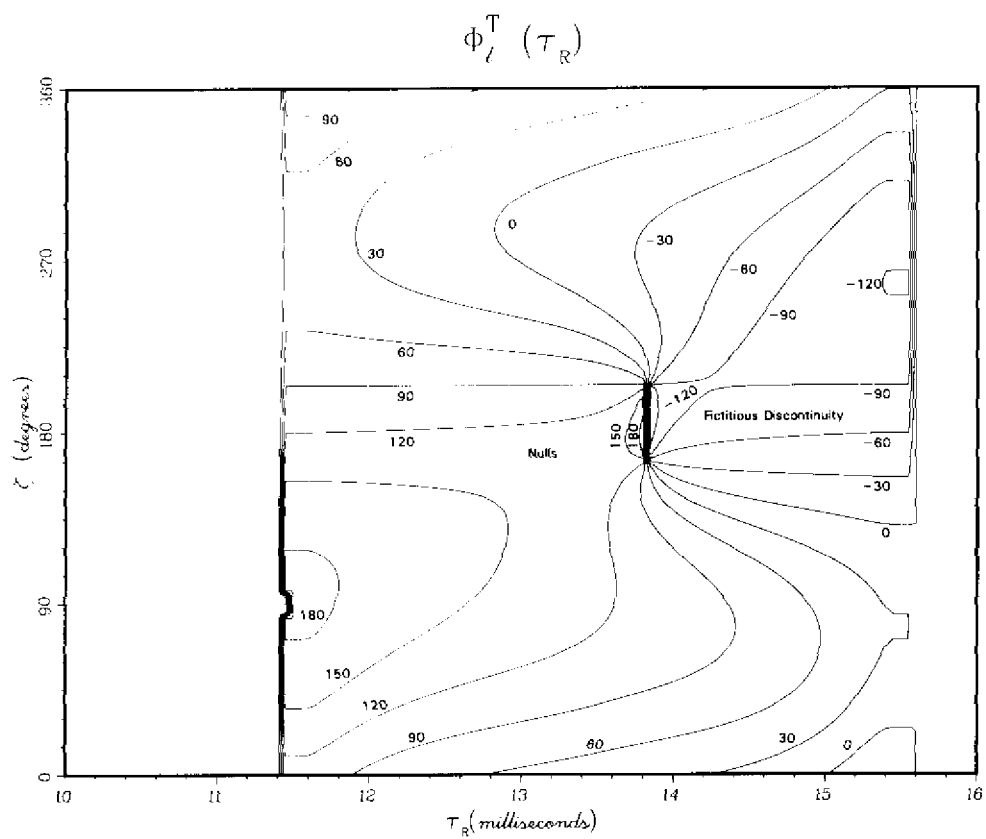


Fig. 94(d) — Phase behavior corresponding to that in Fig. 94(b)



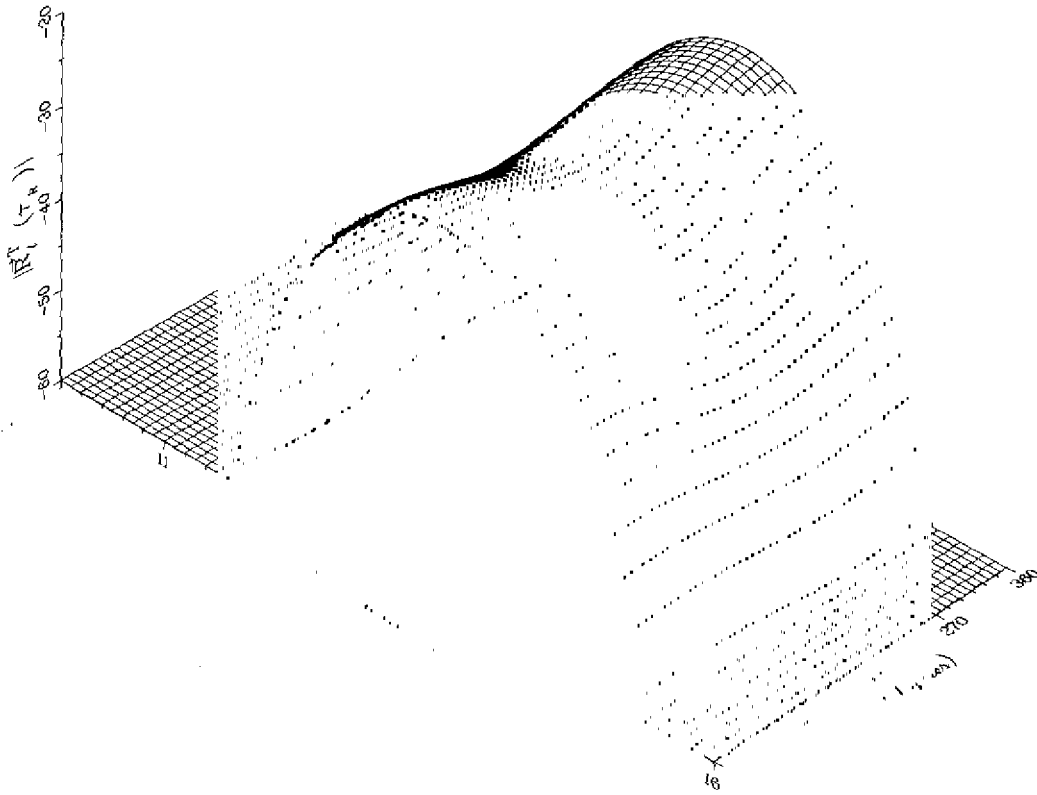


Fig. 95(a) — Amplitude behavior of  $R_r^T(\tau_R)$  for  $\gamma = 60^\circ$ ,  
calculated with the parameters of Table 6

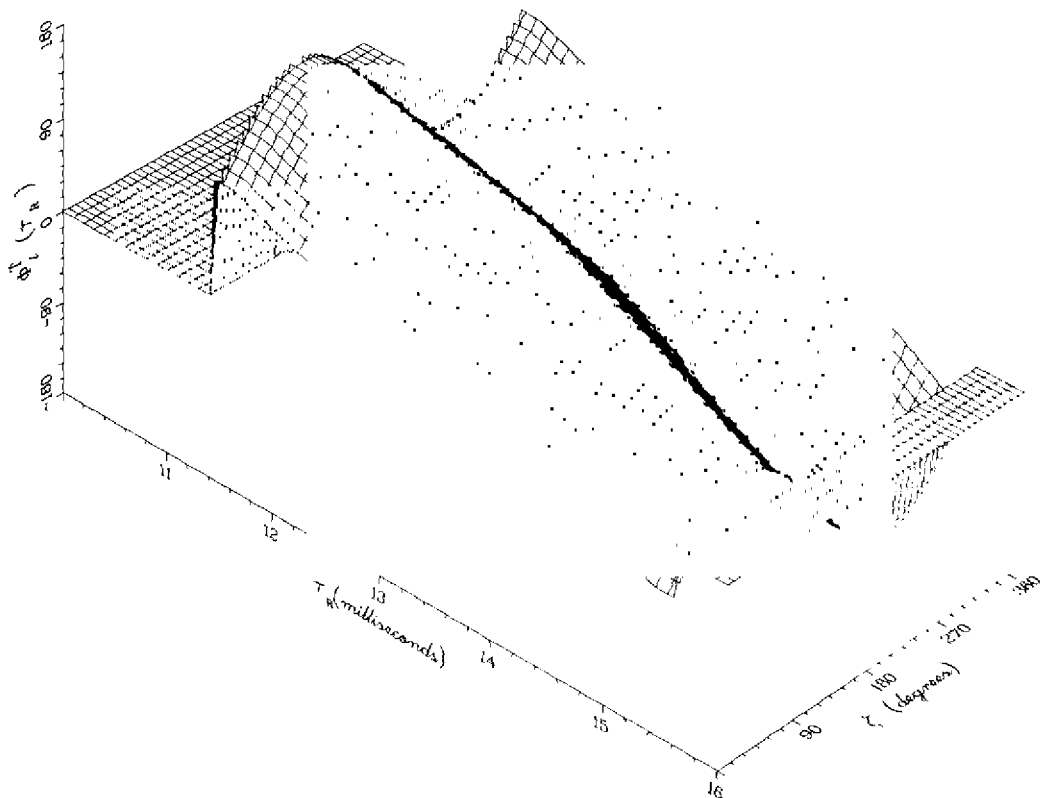


Fig. 95(b) — Phase behavior of  $R_r^T(\tau_R)$  for  $\gamma = 60^\circ$ ,  
calculated with the parameters of Table 6

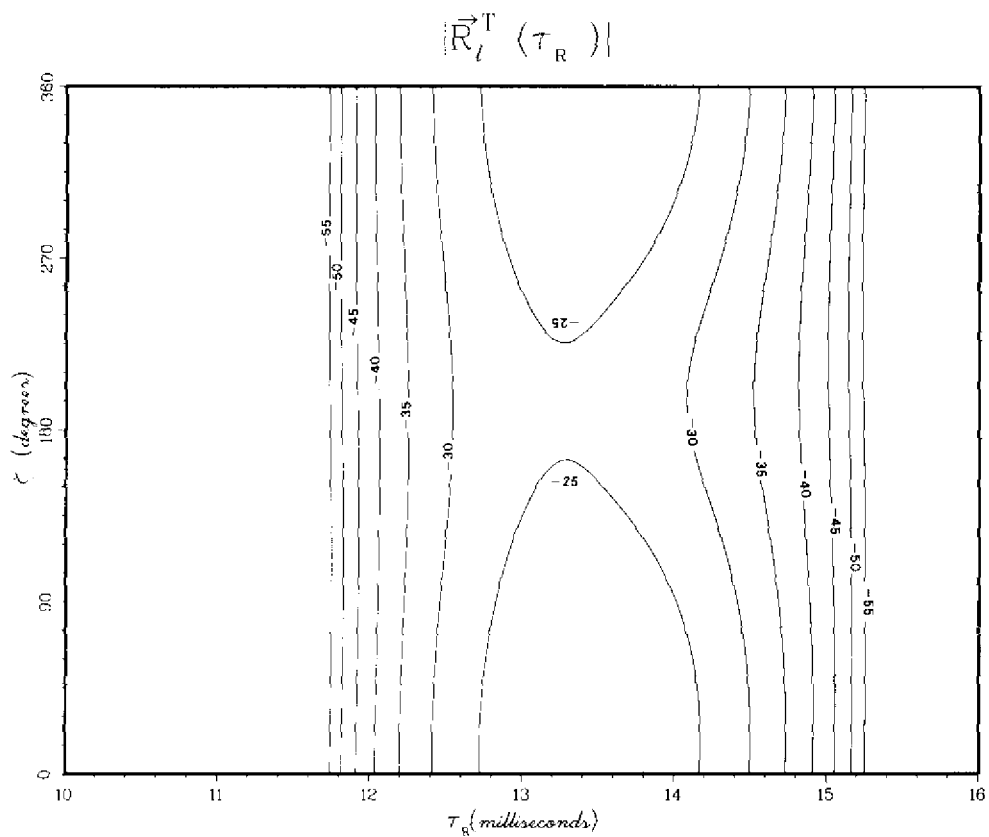


Fig. 95(c) — Amplitude contours corresponding to those in Fig. 95(a)

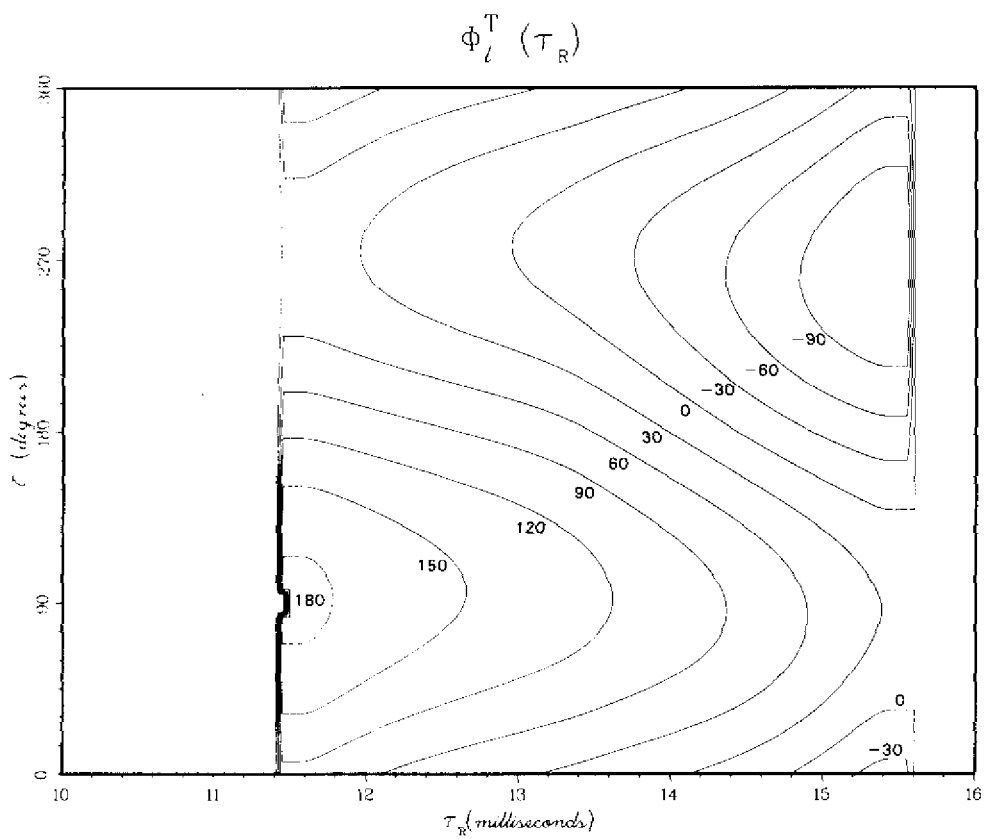


Fig. 95(d) — Phase behavior corresponding to that in Fig. 95(b)

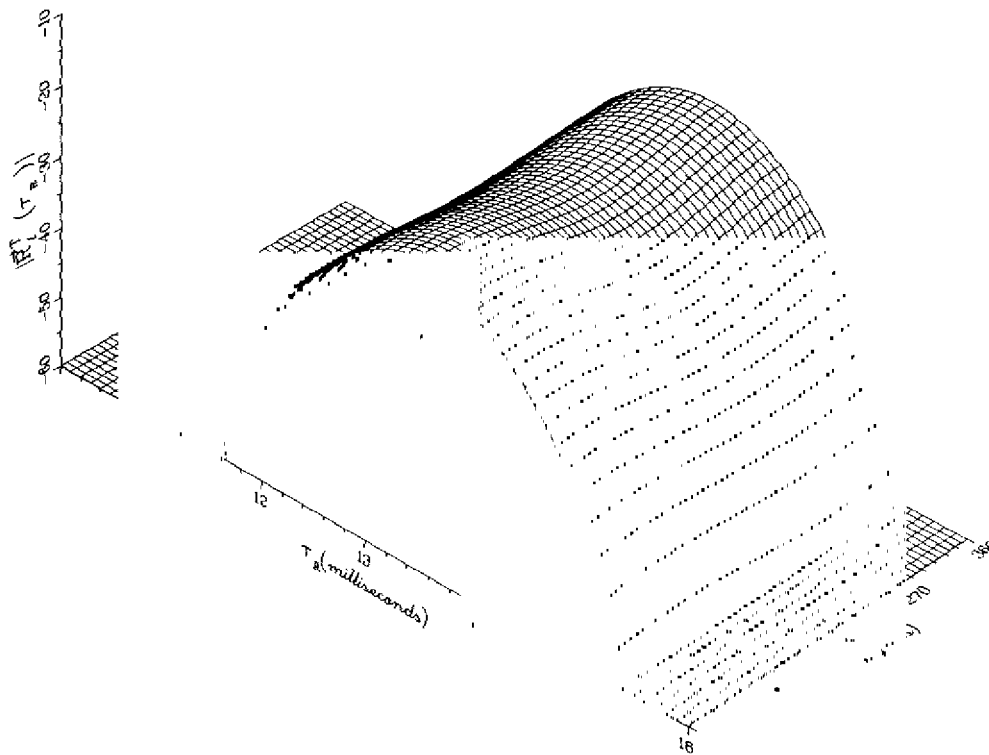


Fig. 96(a) — Amplitude behavior of  $R_I^T(\tau_R)$  for  $\gamma = 45^\circ$ ,  
calculated with the parameters of Table 6

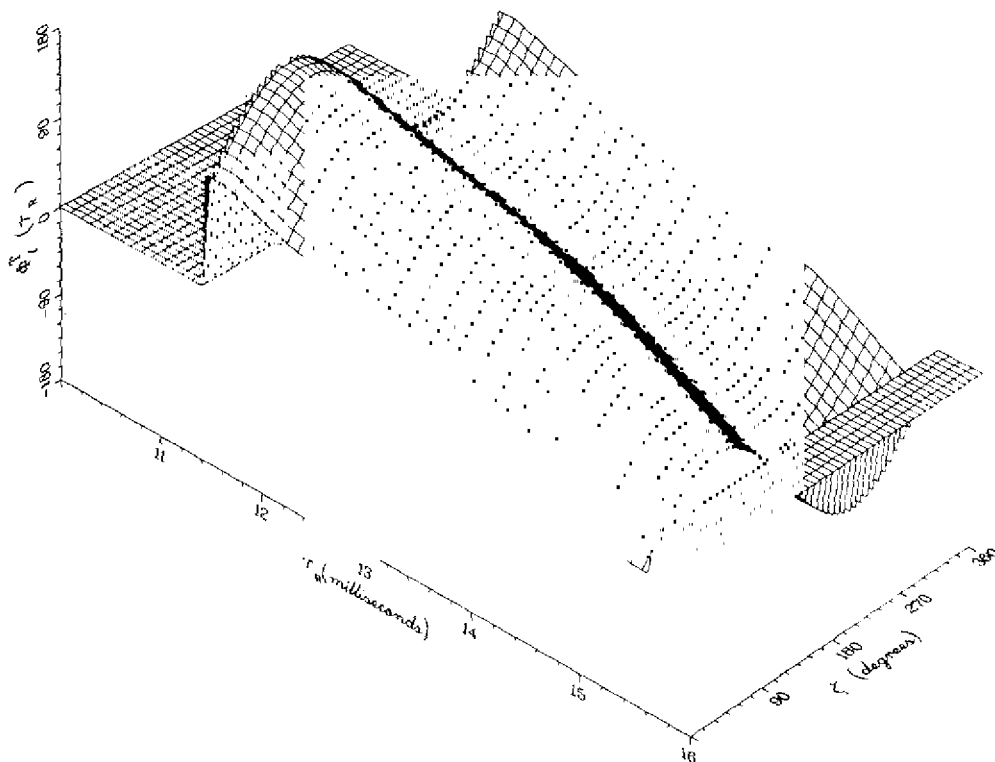


Fig. 96(b) — Phase behavior of  $R_I^T(\tau_R)$  for  $\gamma = 45^\circ$ ,  
calculated with the parameters of Table 6

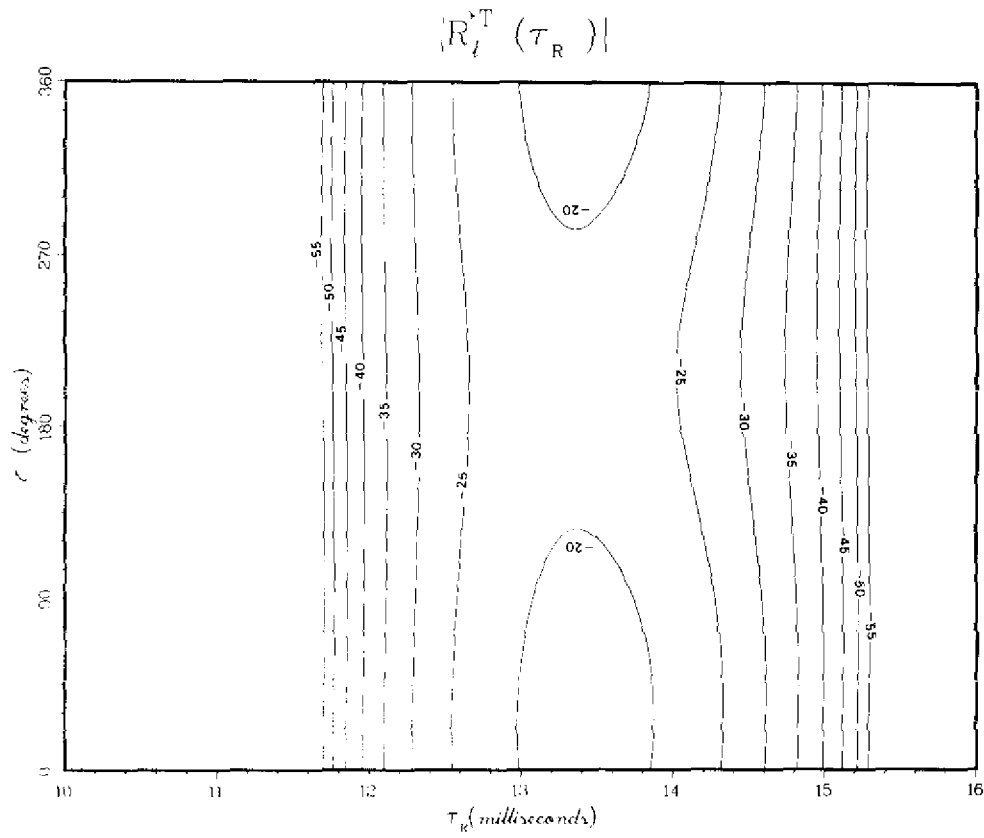


Fig. 96(c) — Amplitude contours corresponding to those in Fig. 96(a)

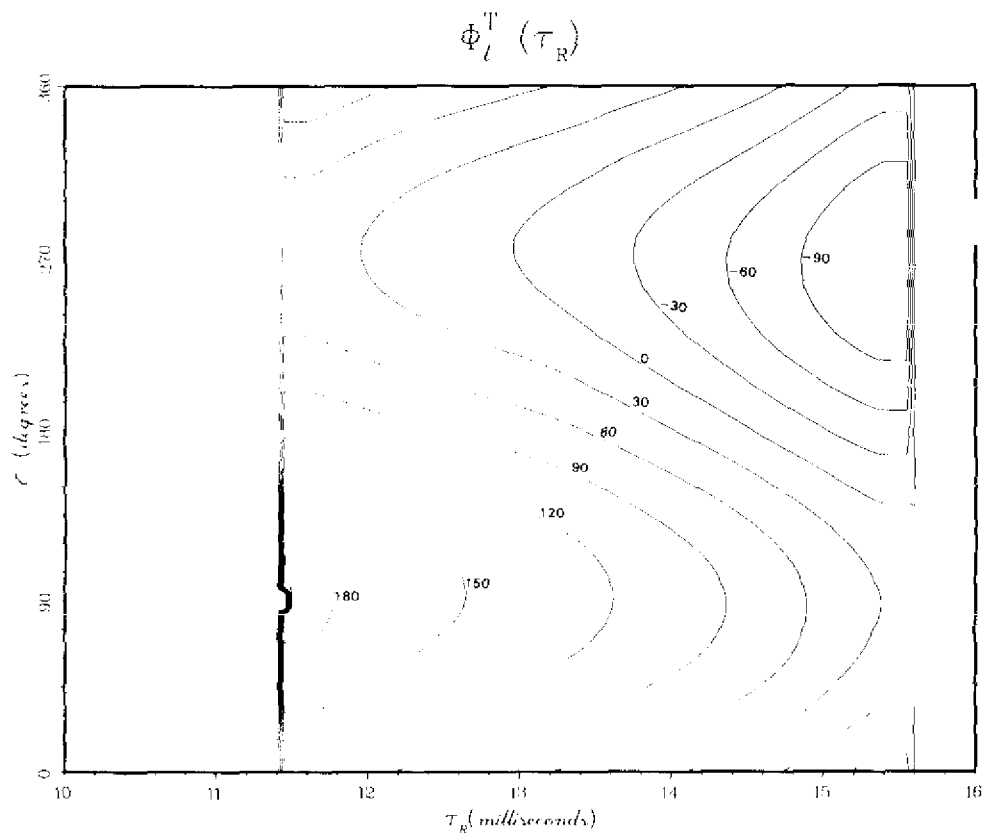


Fig. 96(d) — Phase behavior corresponding to that in Fig. 96(b)

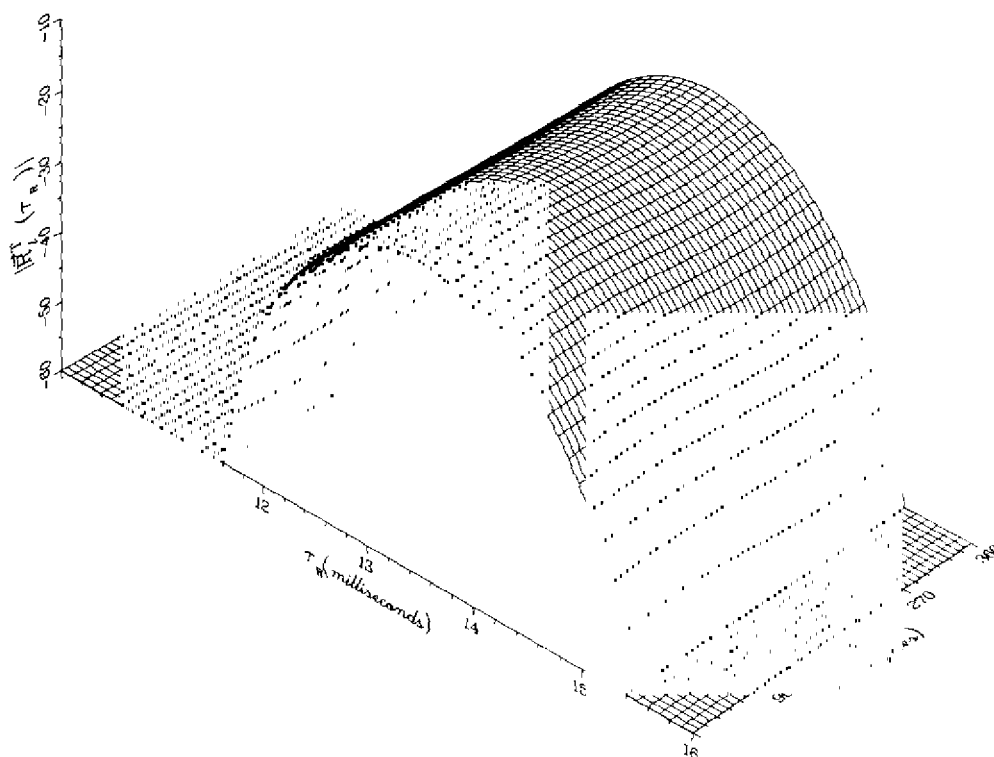


Fig. 97(a) — Amplitude behavior of  $R_I^T(\tau_R)$  for  $\gamma = 0^\circ$ ,  
calculated with the parameters of Table 6

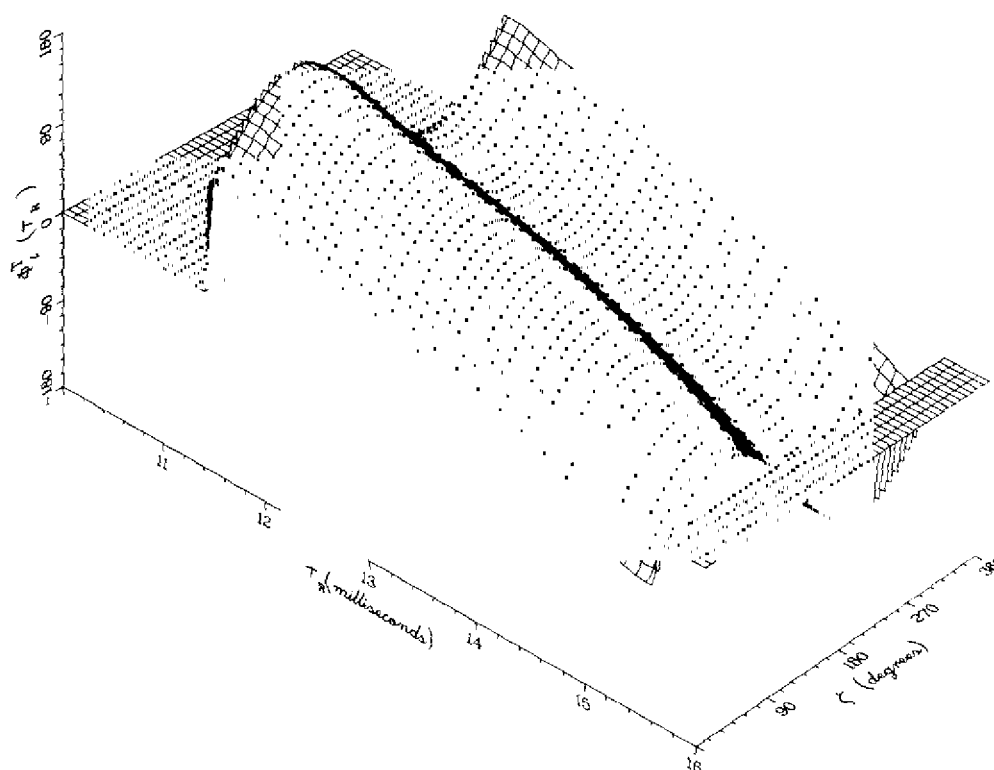


Fig. 97(b) — Phase behavior of  $R_I^T(\tau_R)$  for  $\gamma = 0^\circ$ ,  
calculated with the parameters of Table 6

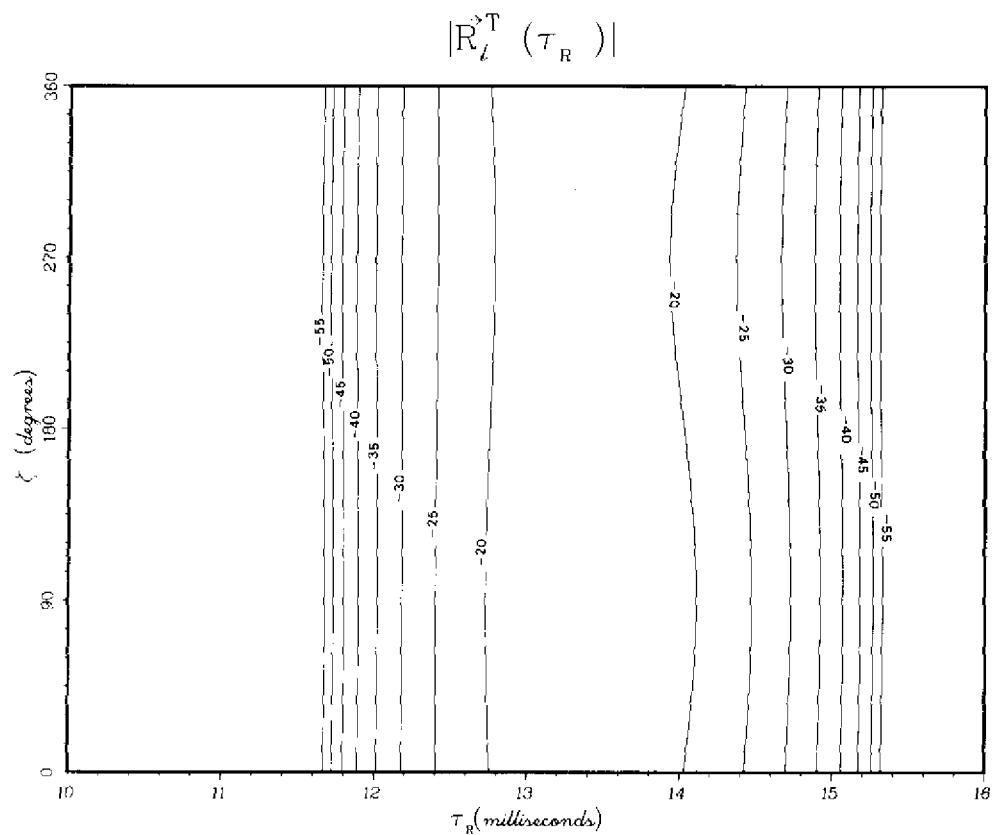


Fig. 97(c) — Amplitude contours corresponding to those in Fig. 97(a)

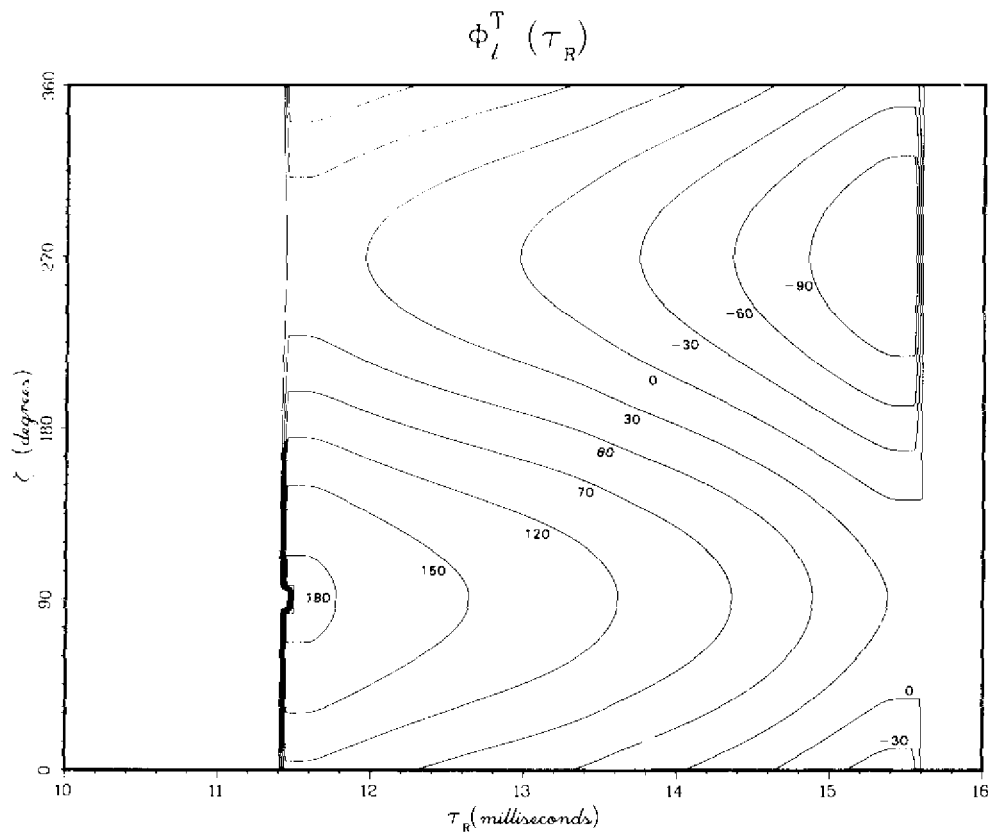


Fig. 97(d) — Phase behavior corresponding to that in Fig. 97(b)

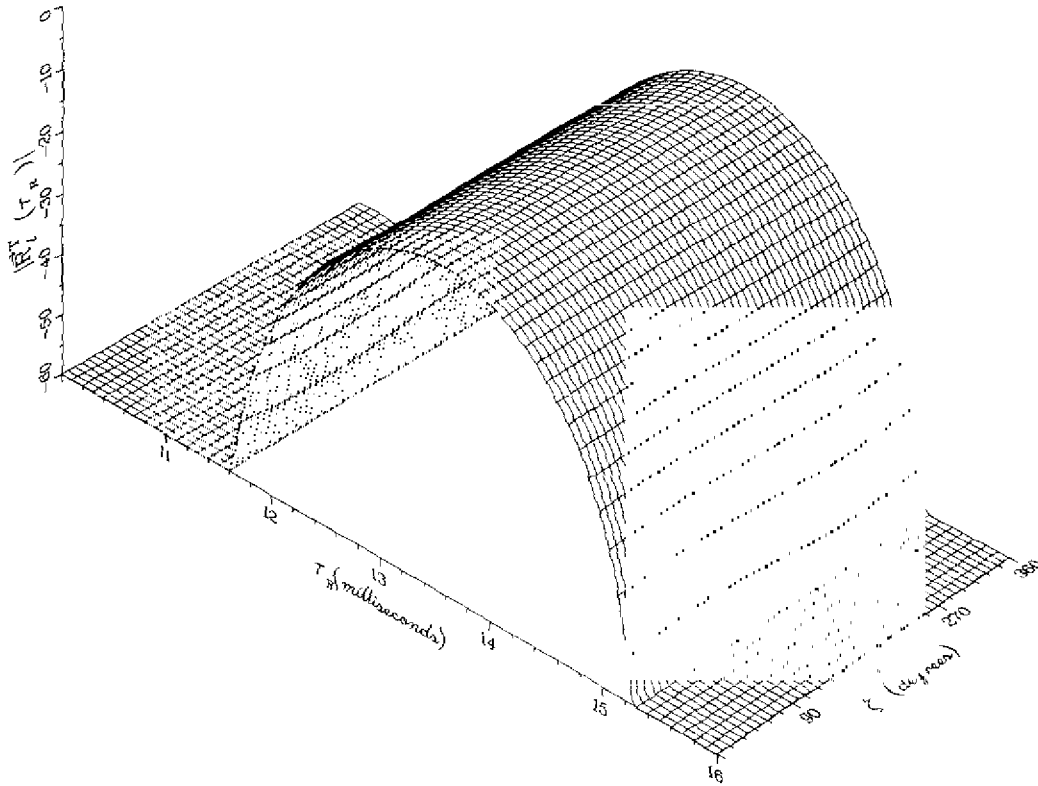


Fig. 98(a) — Amplitude behavior of  $R_l^{(1)}(\tau_R)$  for  $\gamma = 0^\circ$ ,  
calculated with the parameters of Table 6

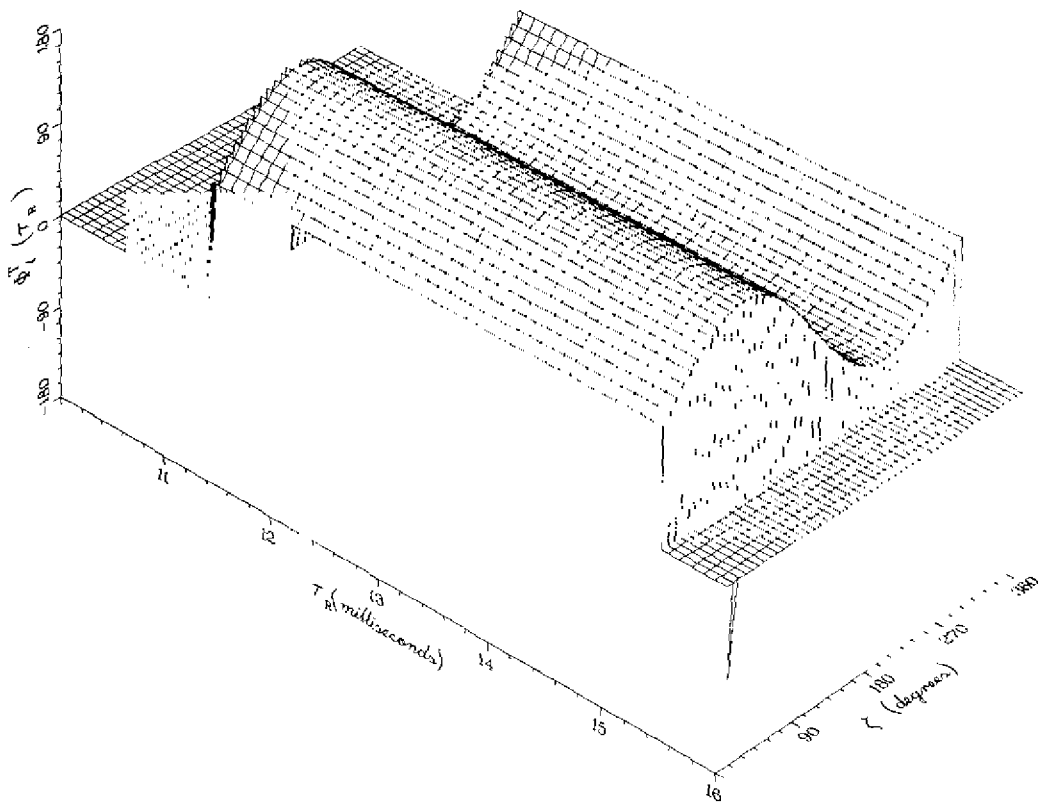


Fig. 98(b) — Phase behavior of  $R_l^{(1)}(\tau_R)$  for  $\gamma = 0^\circ$ ,  
calculated with the parameters of Table 6

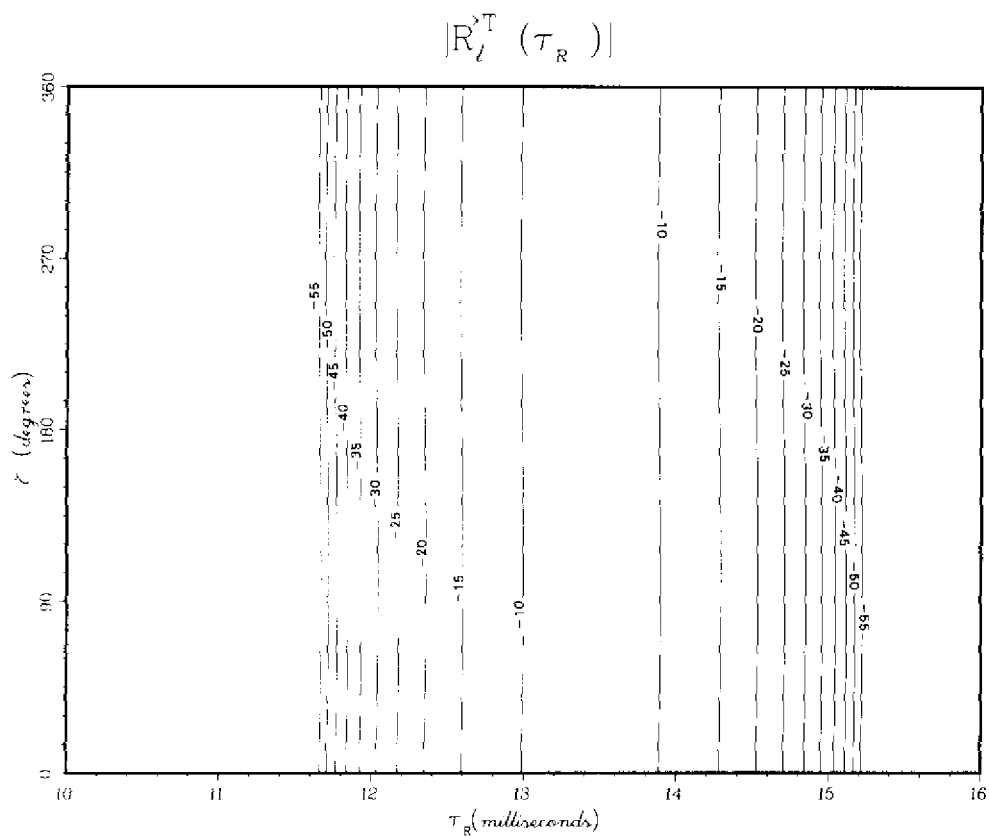


Fig. 98(c) — Amplitude contours corresponding to those in Fig. 98(a)

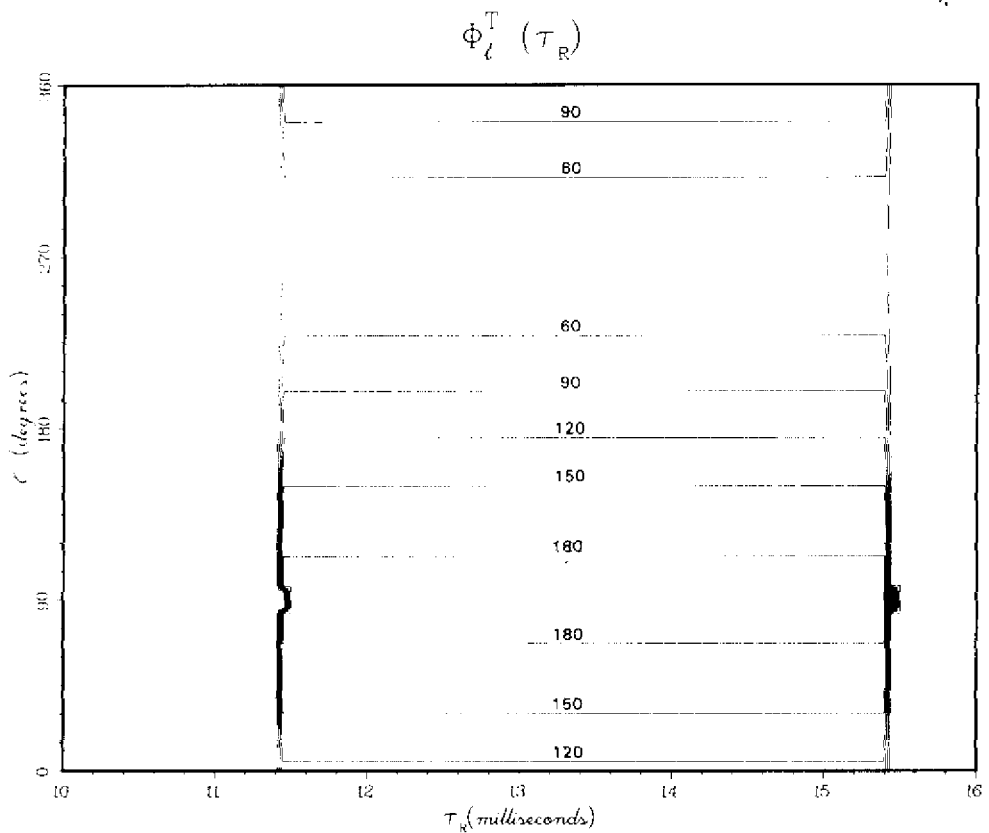


Fig. 98(d) — Phase behavior corresponding to that in Fig. 98(b)



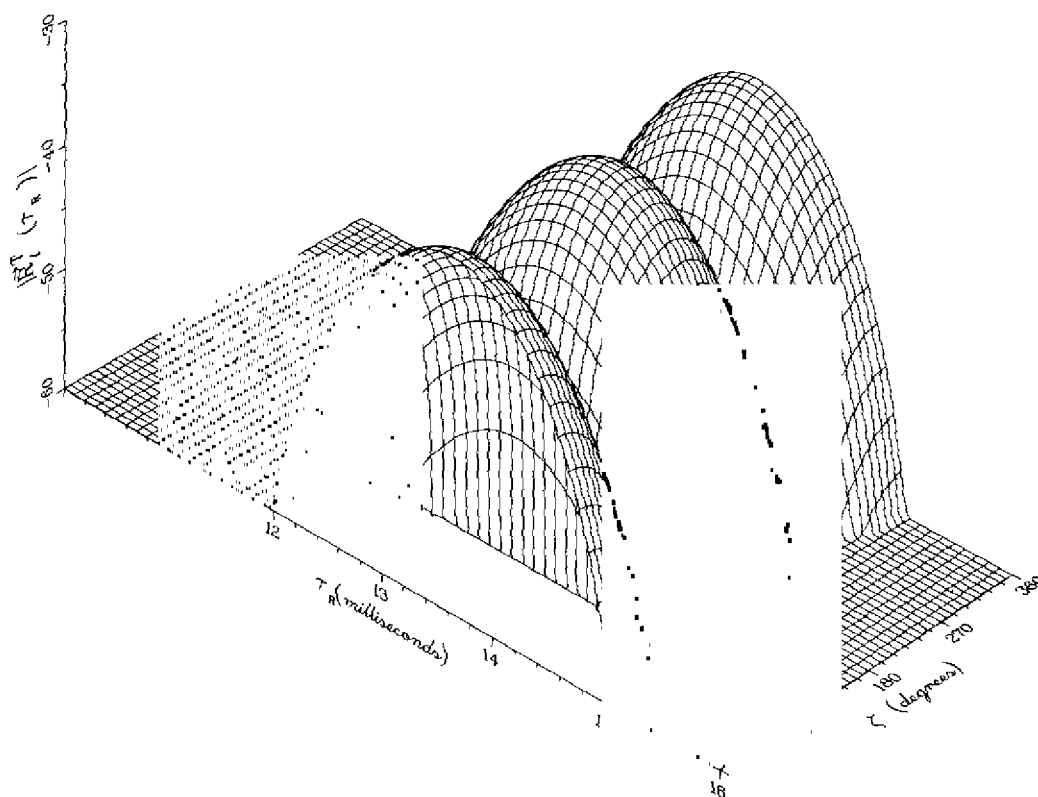


Fig. 99(a) — Amplitude behavior of  $R_I^{\gamma}(\tau_R)$  for  $\gamma = 90^\circ$ ,  
calculated with the parameters of Table 7

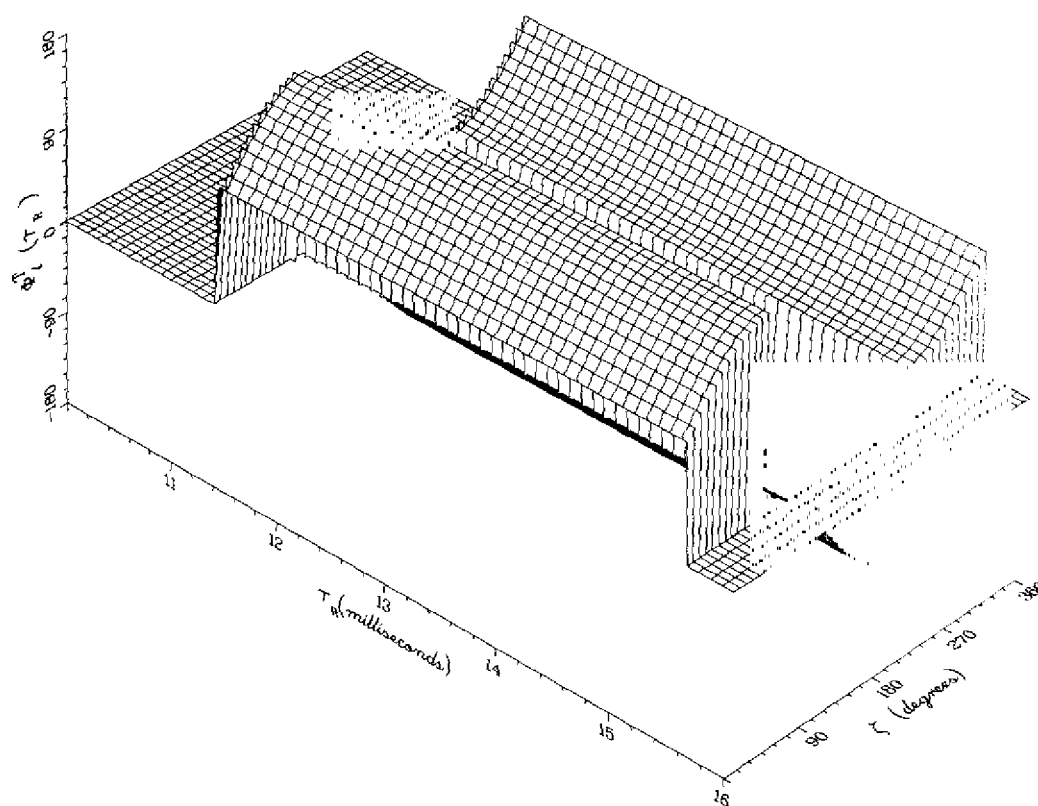


Fig. 99(b) — Phase behavior of  $R_I^{\gamma}(\tau_R)$   $\gamma = 90^\circ$ ,  
calculated with the parameters of Table 7

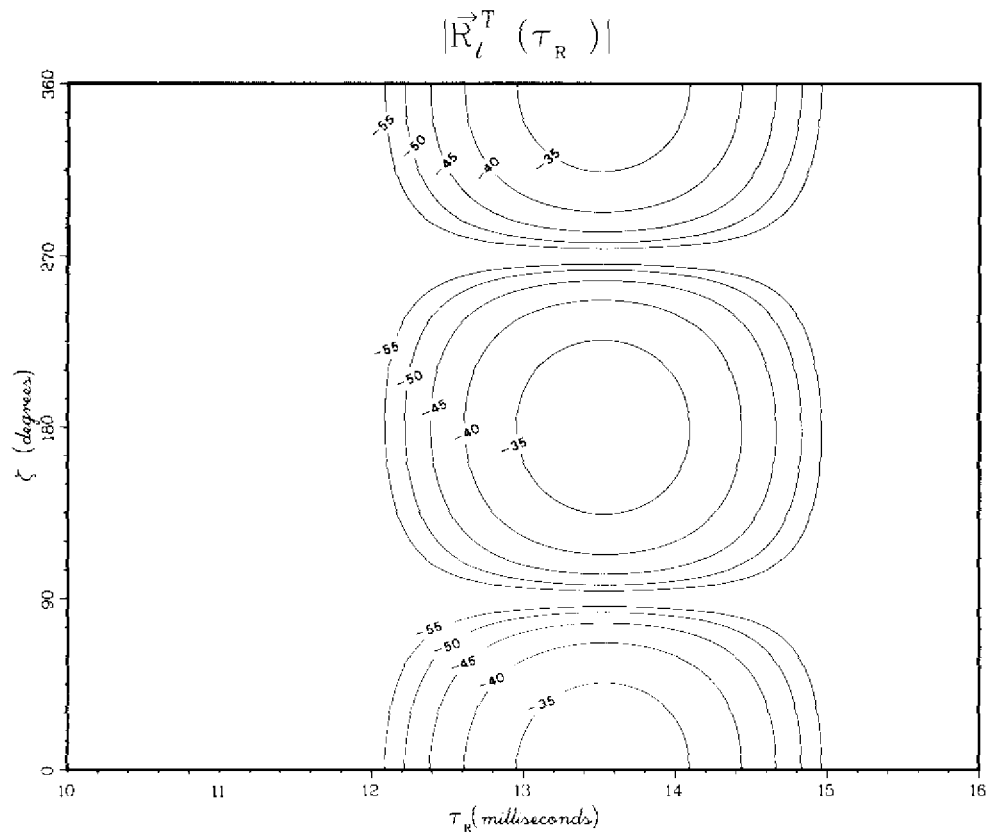


Fig. 99(c) — Amplitude contours corresponding to those in Fig. 99(a)

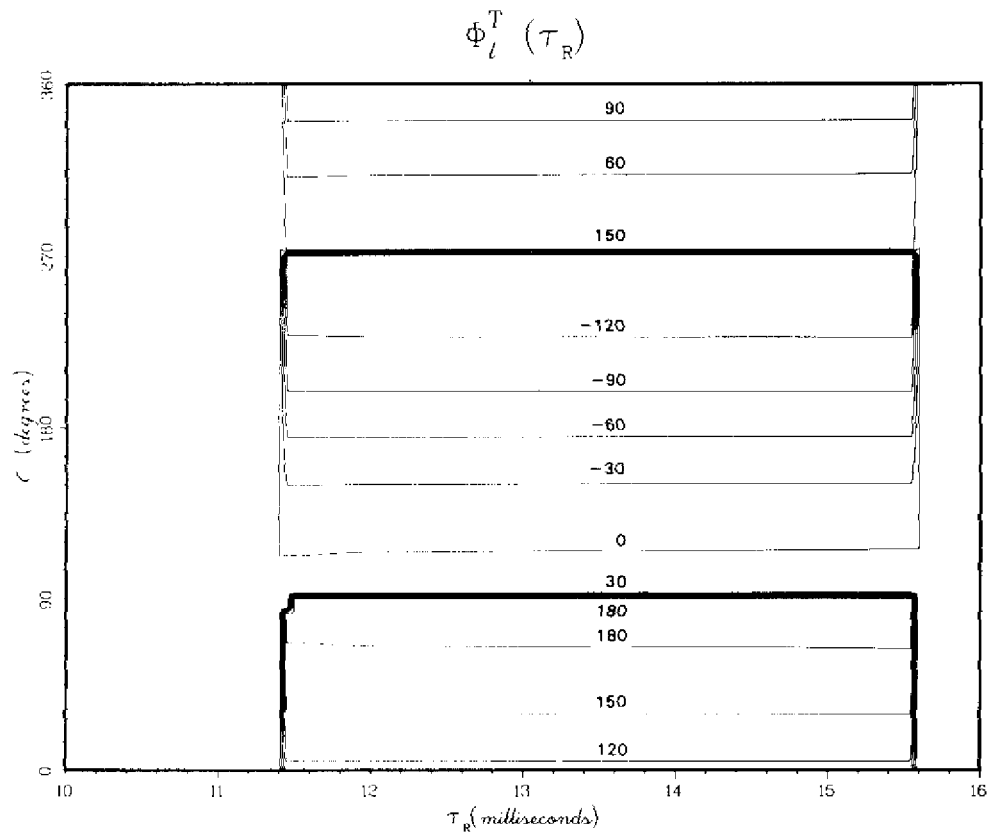


Fig. 99(d) — Phase behavior corresponding to that in Fig. 99(b)

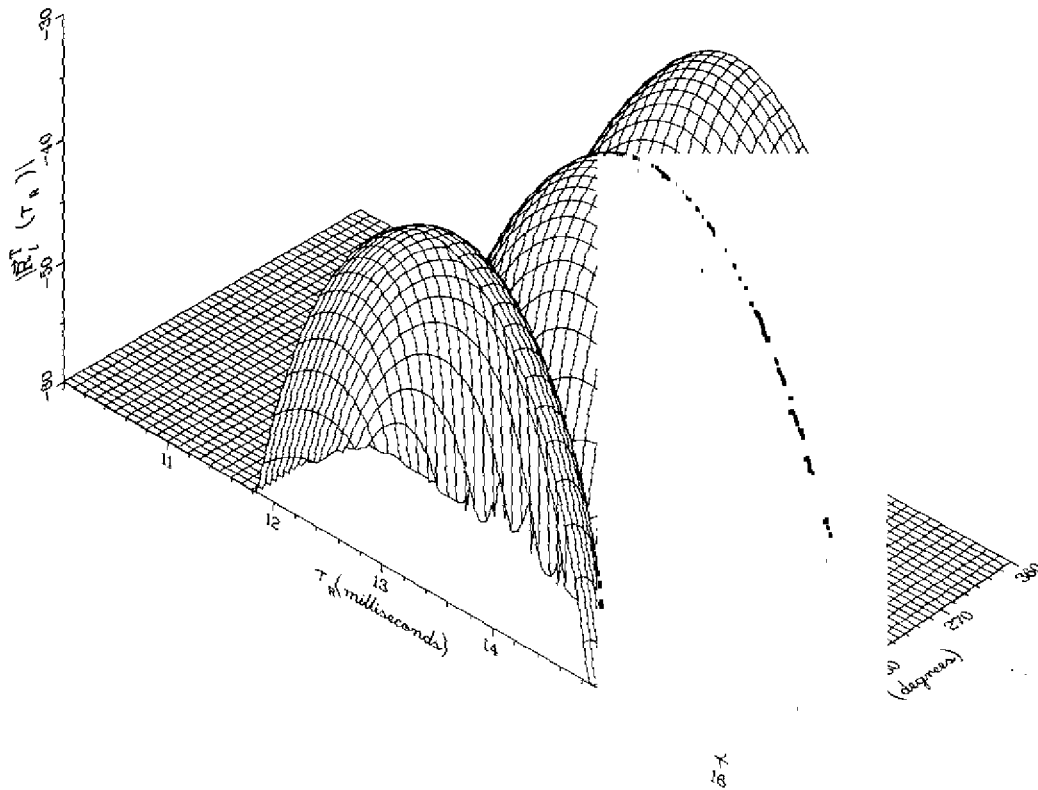


Fig. 100(a) — Amplitude behavior of  $R_l^T(\tau_R)$  for  $\gamma = 85^\circ$ ,  
calculated with the parameters of Table 7

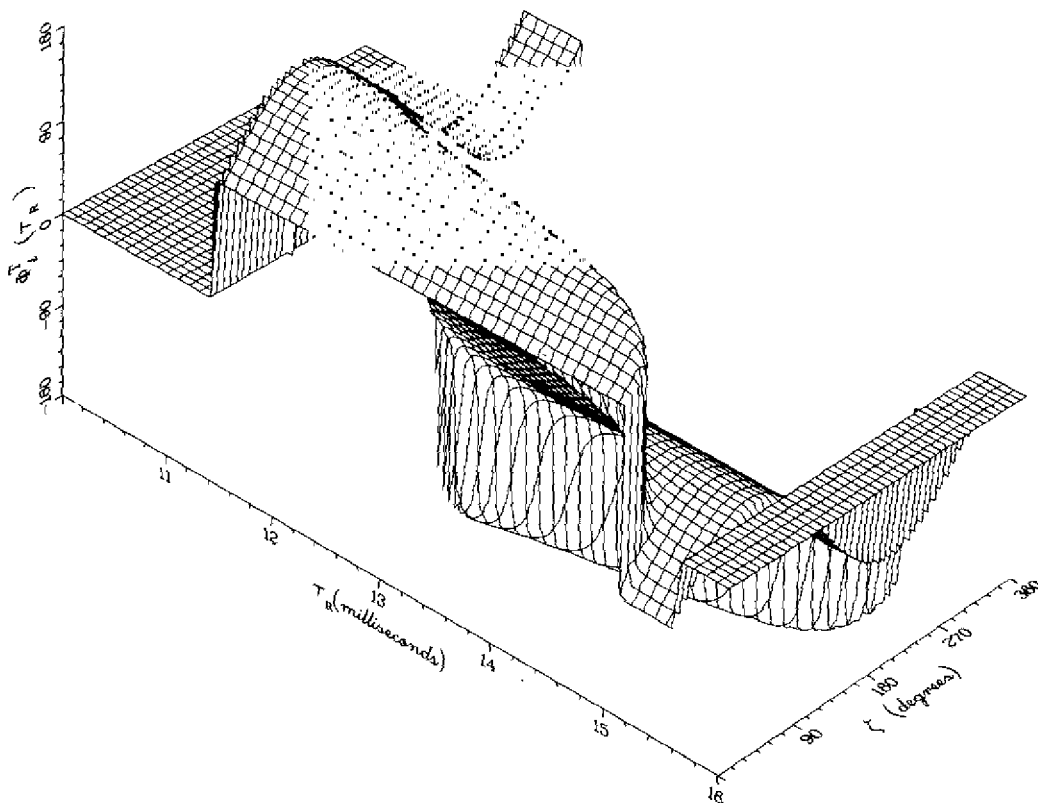


Fig. 100(b) — Phase behavior of  $R_l^T(\tau_R)$  for  $\gamma = 85^\circ$ ,  
calculated with the parameters of Table 7

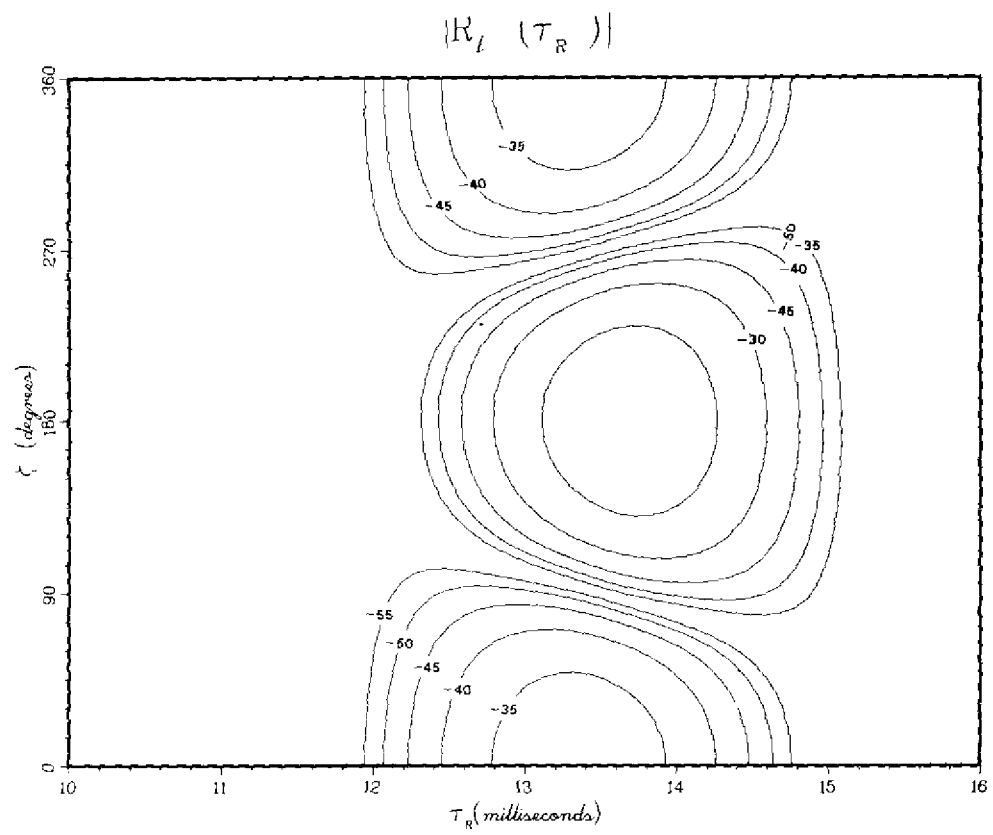


Fig. 100(c) — Amplitude contours corresponding to those in 100(a)

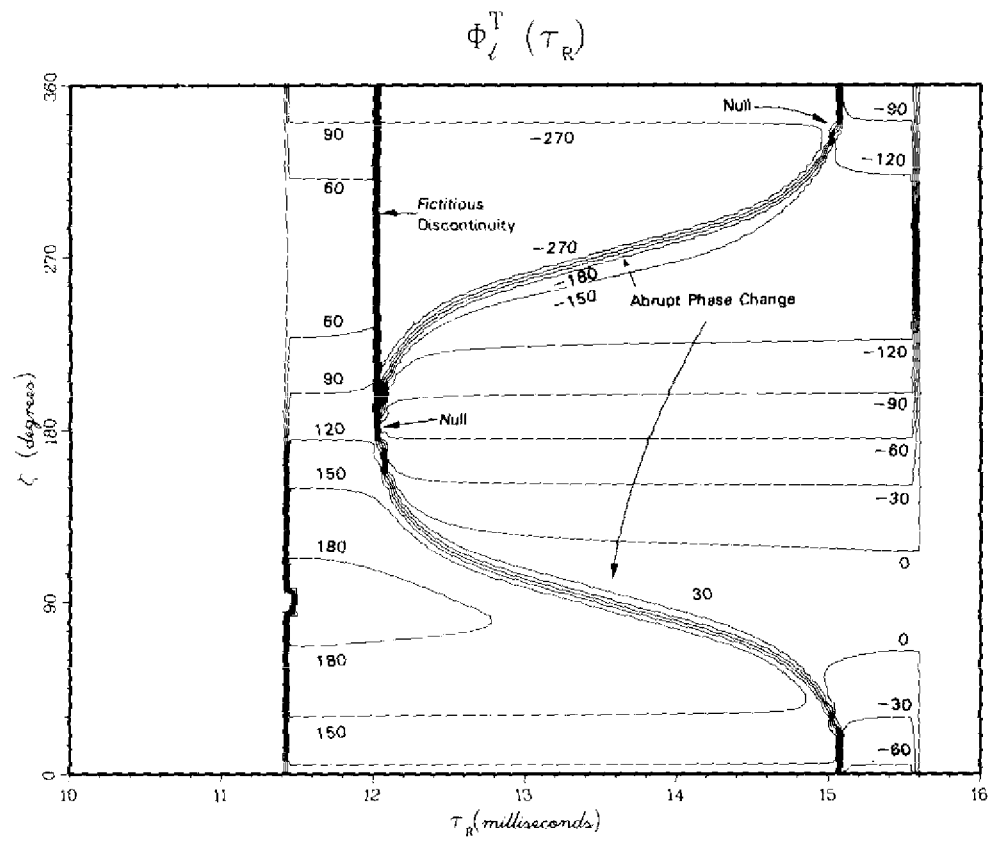


Fig. 100(d) — Phase behavior corresponding to that in Fig. 100(b)

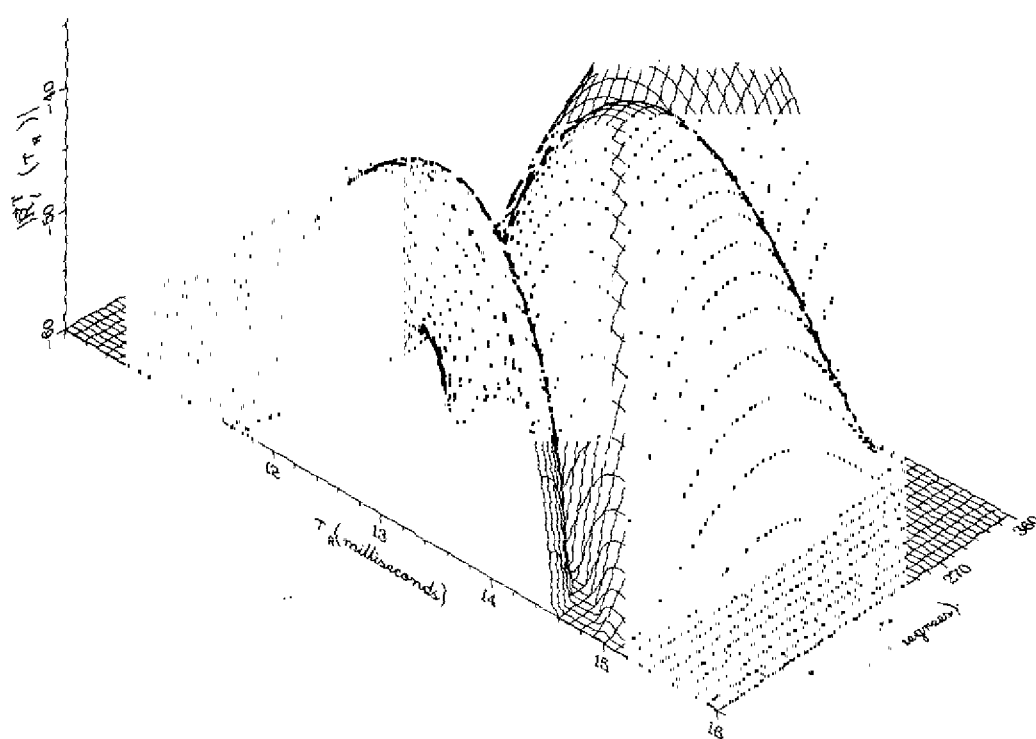


Fig. 101(a) — Amplitude behavior of  $R_I^T(\tau_R)$  for  $\gamma = 80^\circ$ ,  
calculated with the parameters of Table 7

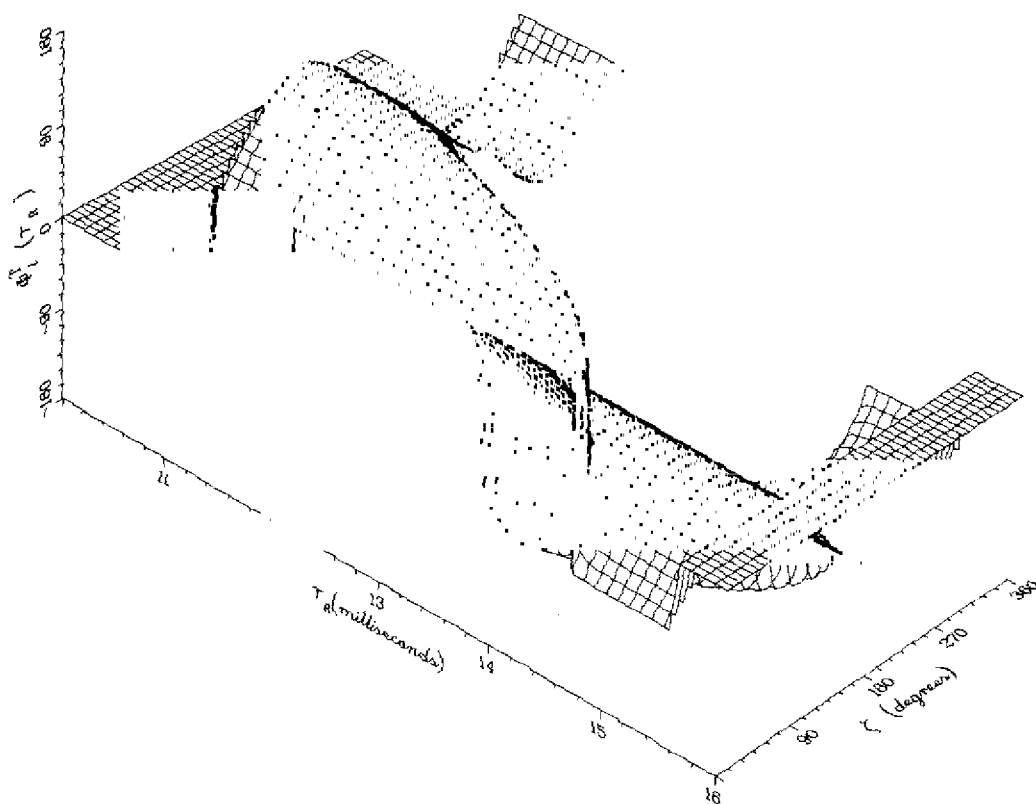


Fig. 101(b) — Phase behavior of  $R_I^T(\tau_R)$  for  $\gamma = 80^\circ$ ,  
calculated with the parameters of Table 7

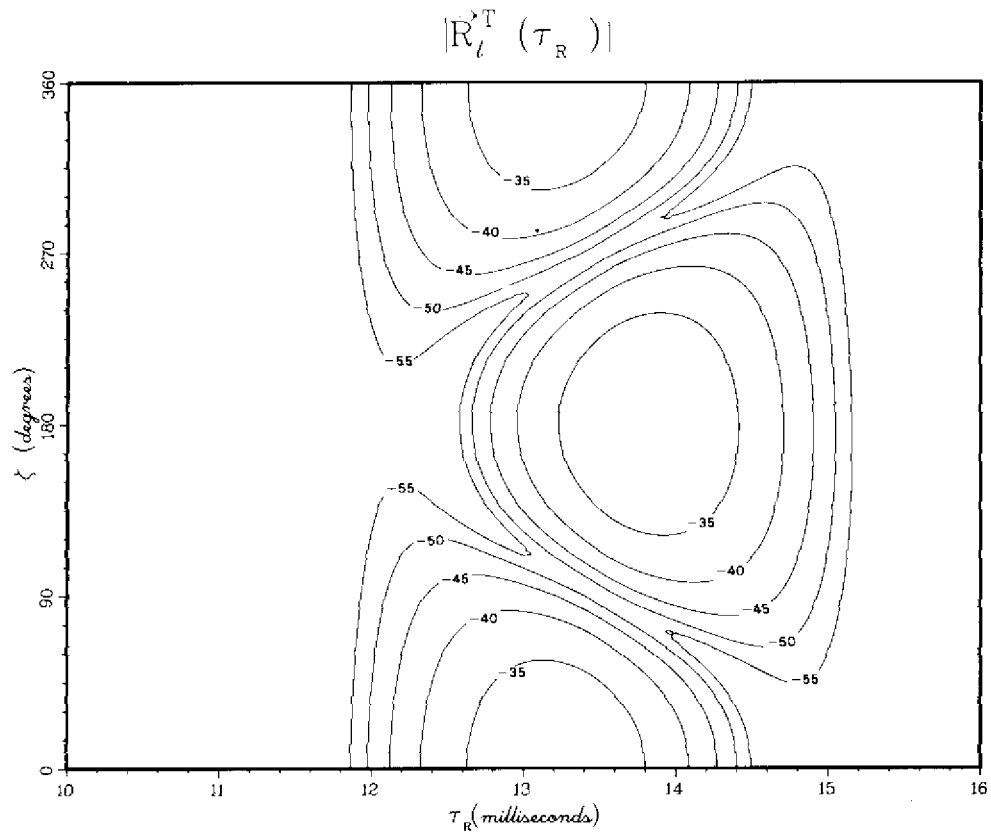


Fig. 101(c) — Amplitude contours corresponding to those in Fig. 101(a)

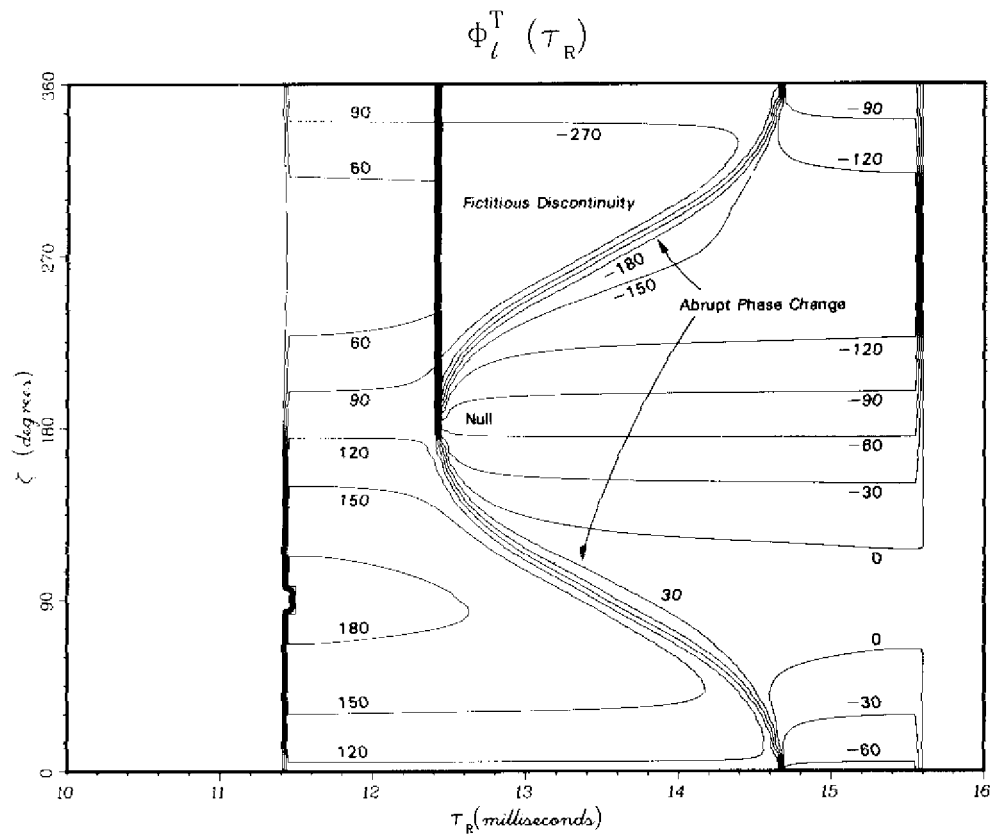


Fig. 101(d) — Phase behavior corresponding to that in Fig. 101(b)

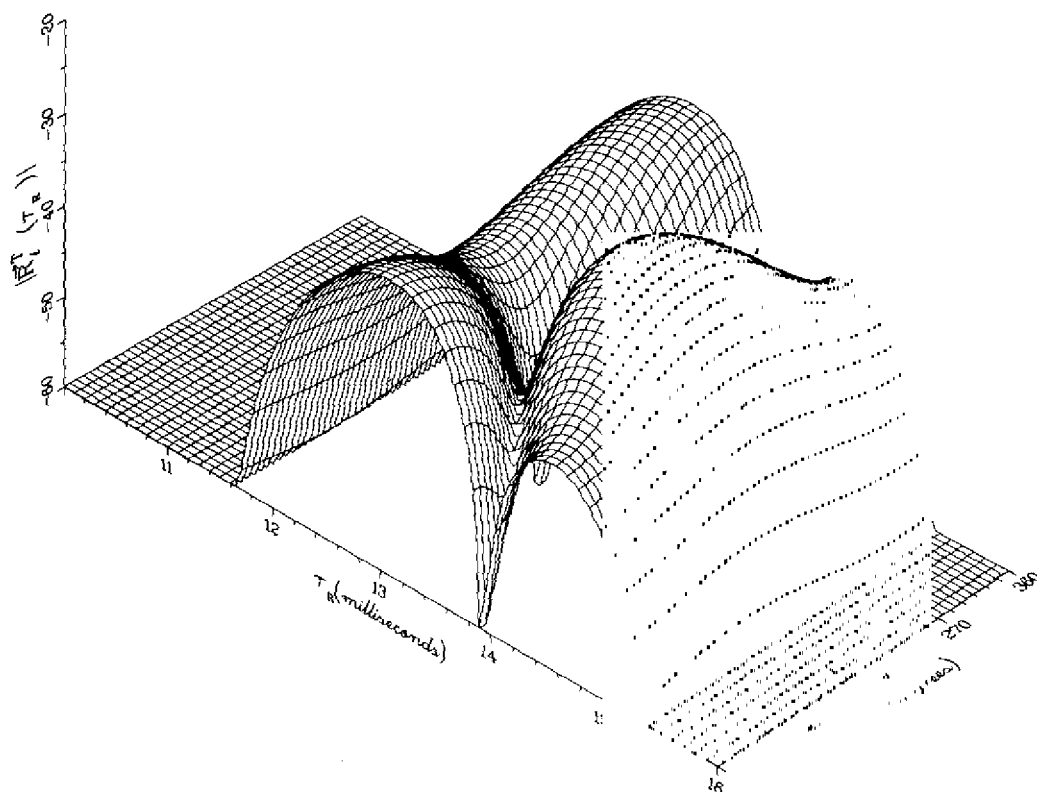


Fig. 102(a) — Amplitude behavior of  $R_l^T(\tau_R)$  for  $\gamma = 60^\circ$ ,  
calculated with the parameters of Table 7

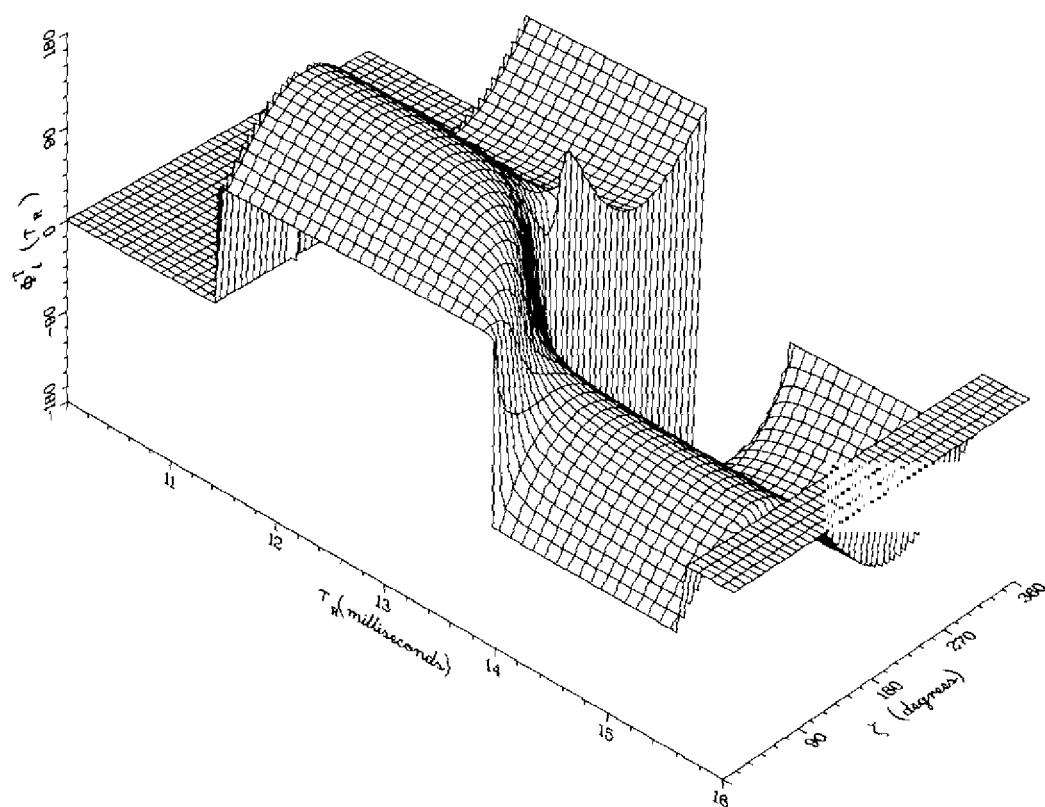


Fig. 102(b) — Phase behavior of  $R_l^T(\tau_R)$  for  $\gamma = 60^\circ$ ,  
calculated with the parameters of Table 7

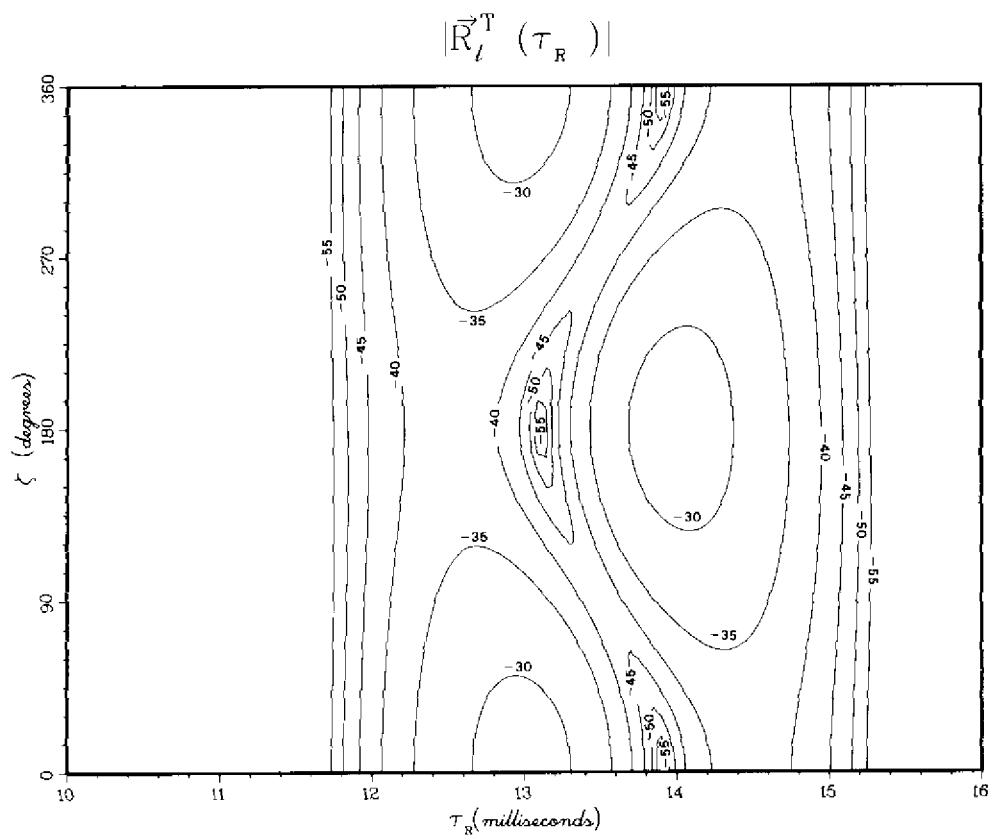


Fig. 102(c) — Amplitude contours corresponding to those in Fig. 102(a)

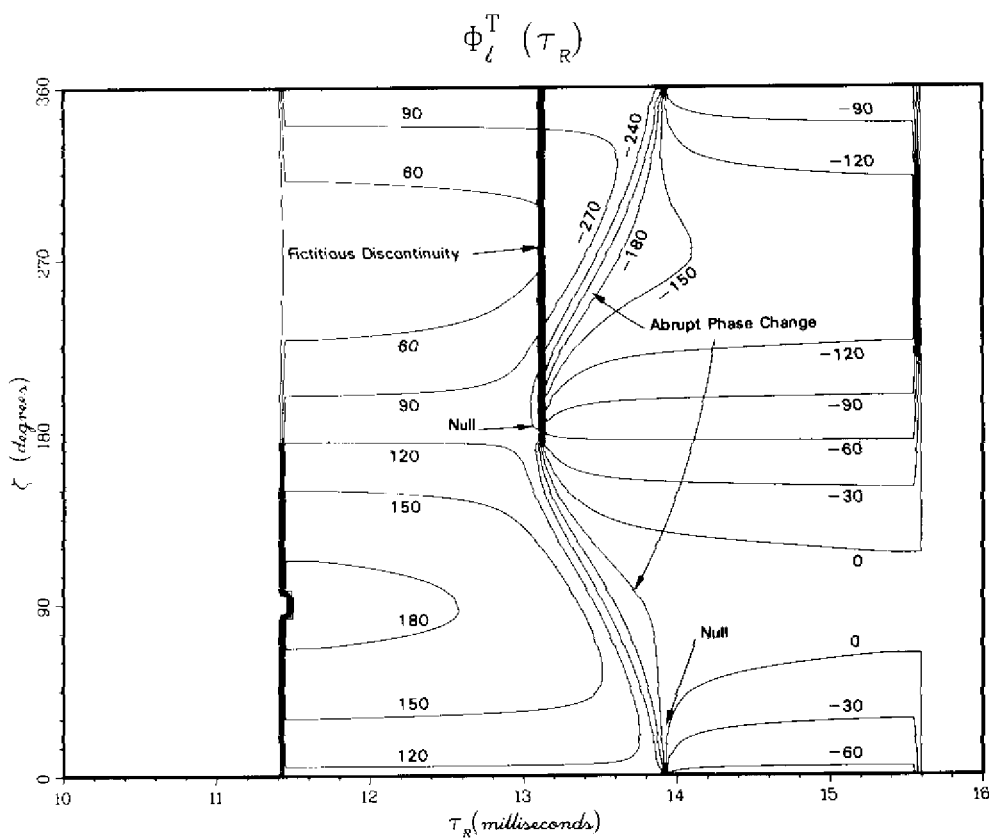


Fig. 102(d) — Phase behavior corresponding to that in Fig. 102(b)



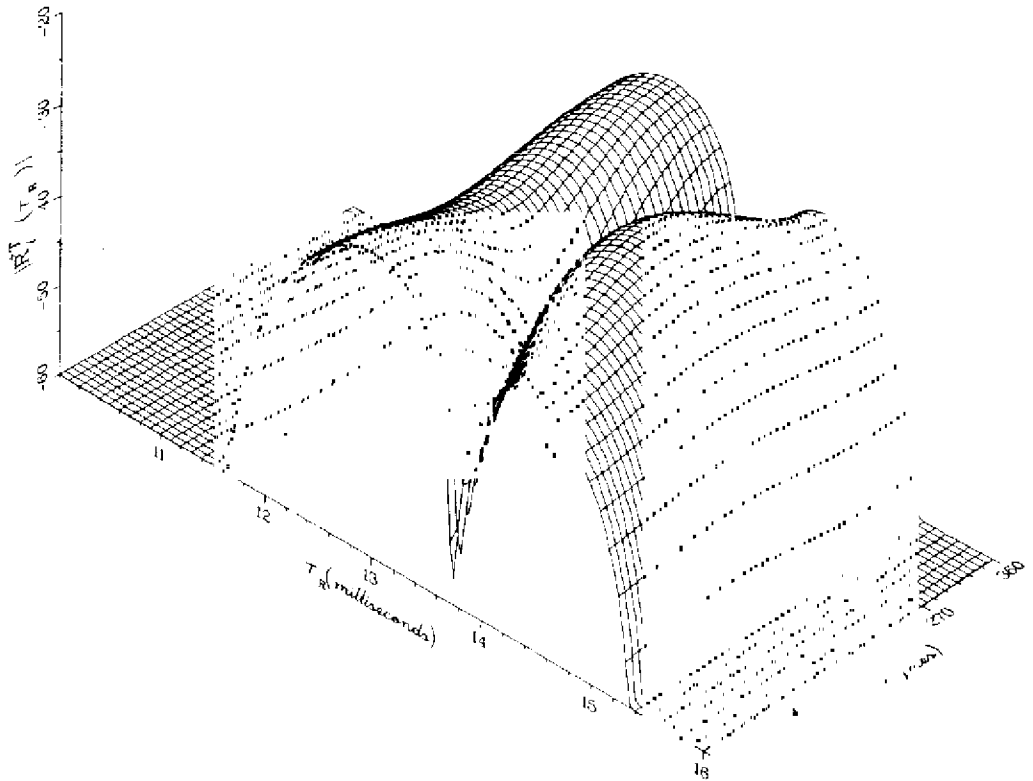


Fig. 103(a) — Amplitude behavior of  $R_I^7(\tau_R)$  for  $\gamma = 45^\circ$ , calculated with the parameters of Table 7

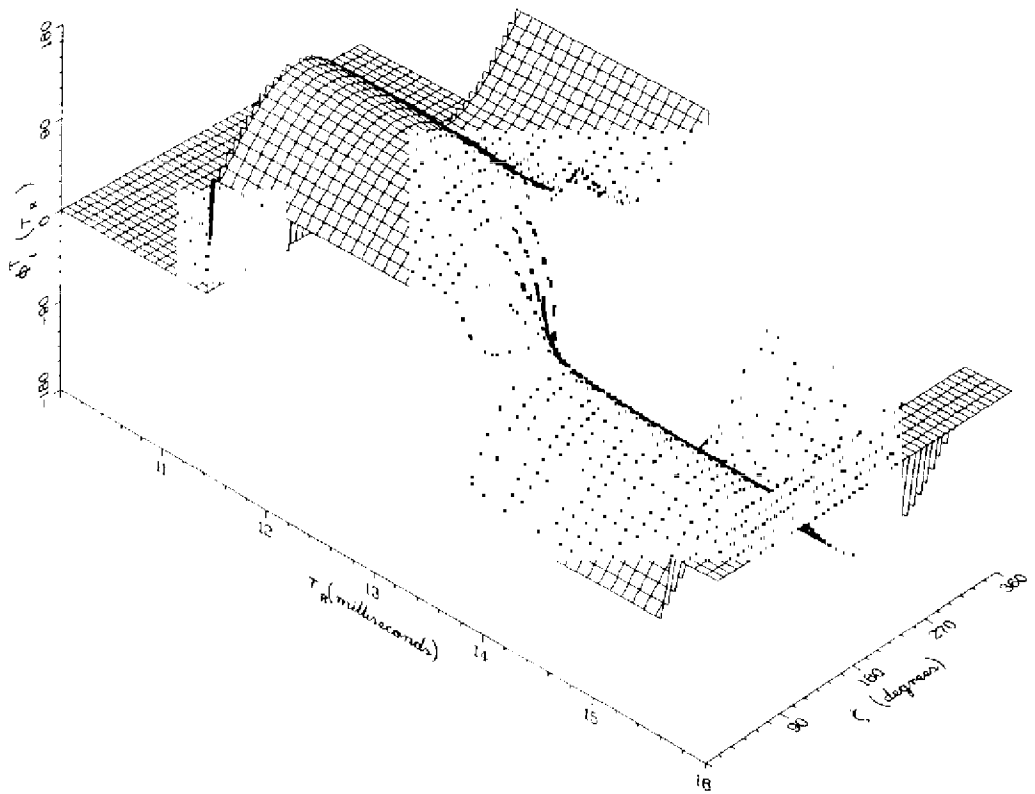


Fig. 103(b) — Phase behavior of  $R_I^7(\tau_R)$  for  $\gamma = 45^\circ$ , calculated with the parameters of Table 7

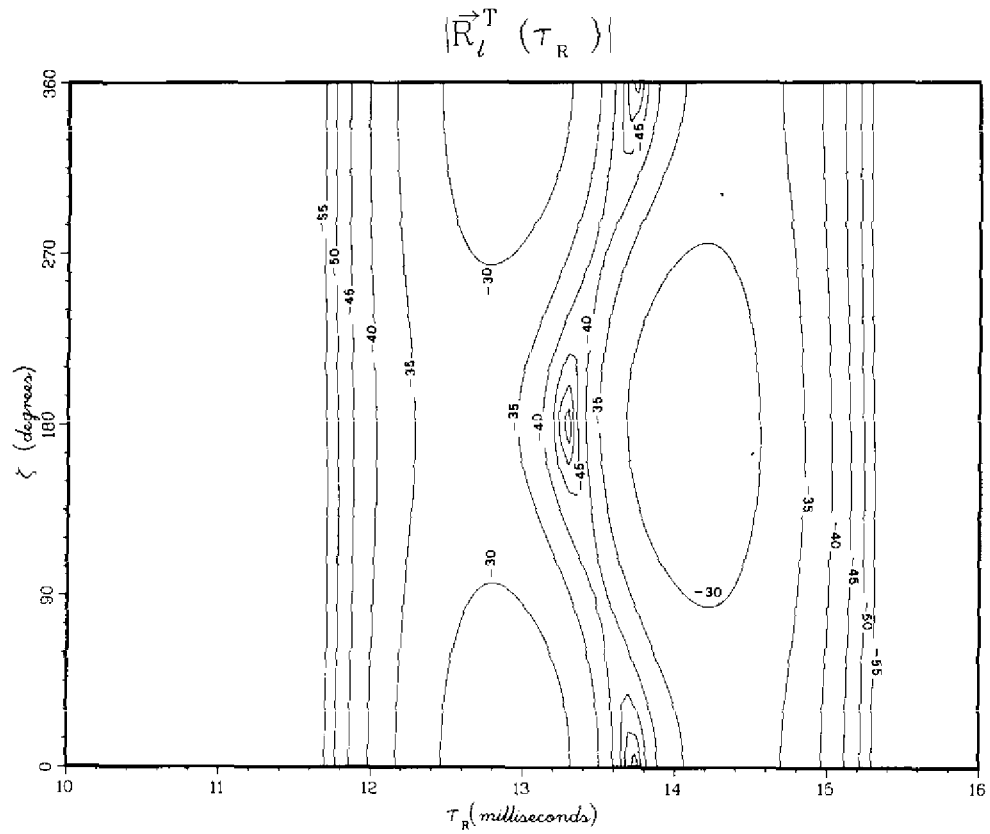


Fig. 103(c) — Amplitude contours corresponding to those in Fig. 103(a)

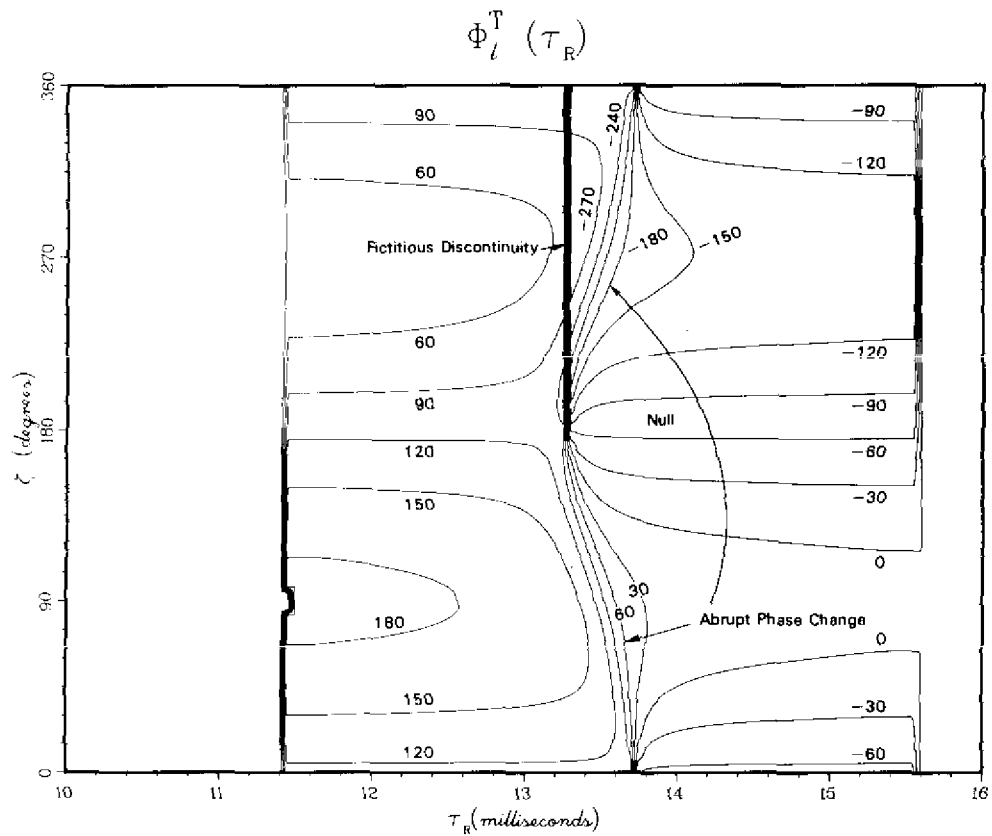


Fig. 103(d) — Phase behavior corresponding to that in Fig. 103(b)

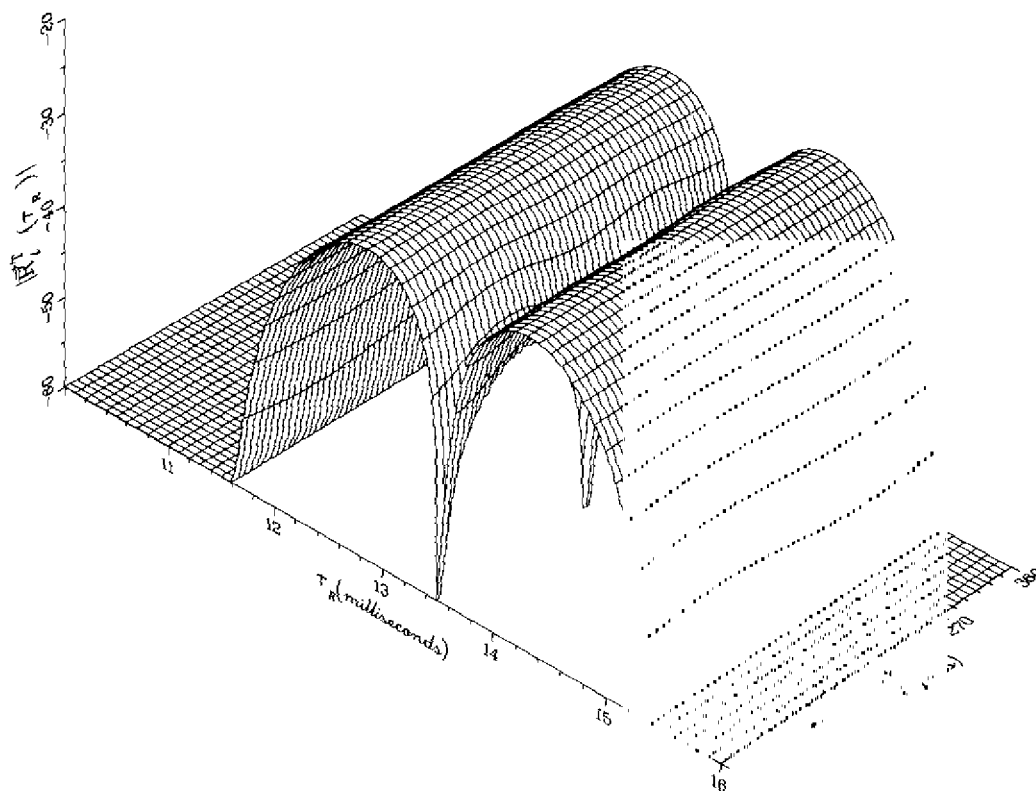


Fig. 104(a) — Amplitude behavior of  $R_l^T(\tau_R)$  for  $\gamma = 0^\circ$ ,  
calculated with the parameters of Table 7

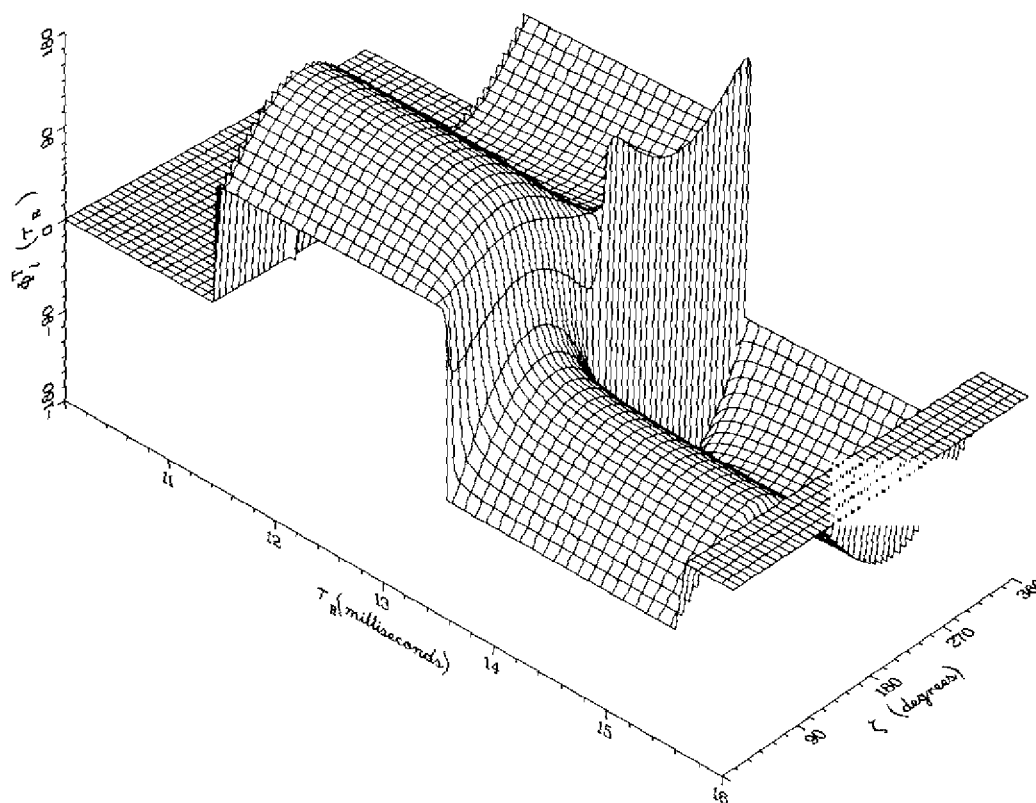


Fig. 104(b) — Phase behavior of  $R_l^T(\tau_R)$  for  $\gamma = 0^\circ$ ,  
calculated with the parameters of Table 7

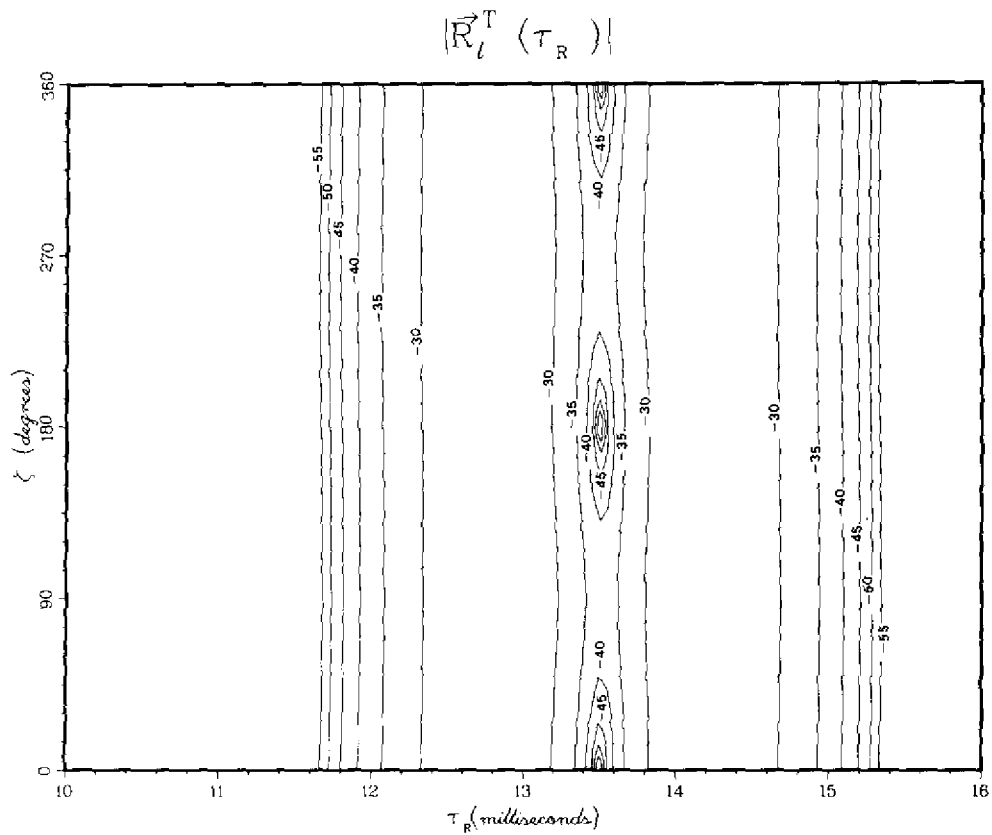


Fig. 104(c) — Amplitude contours corresponding to those in Fig. 104(a)

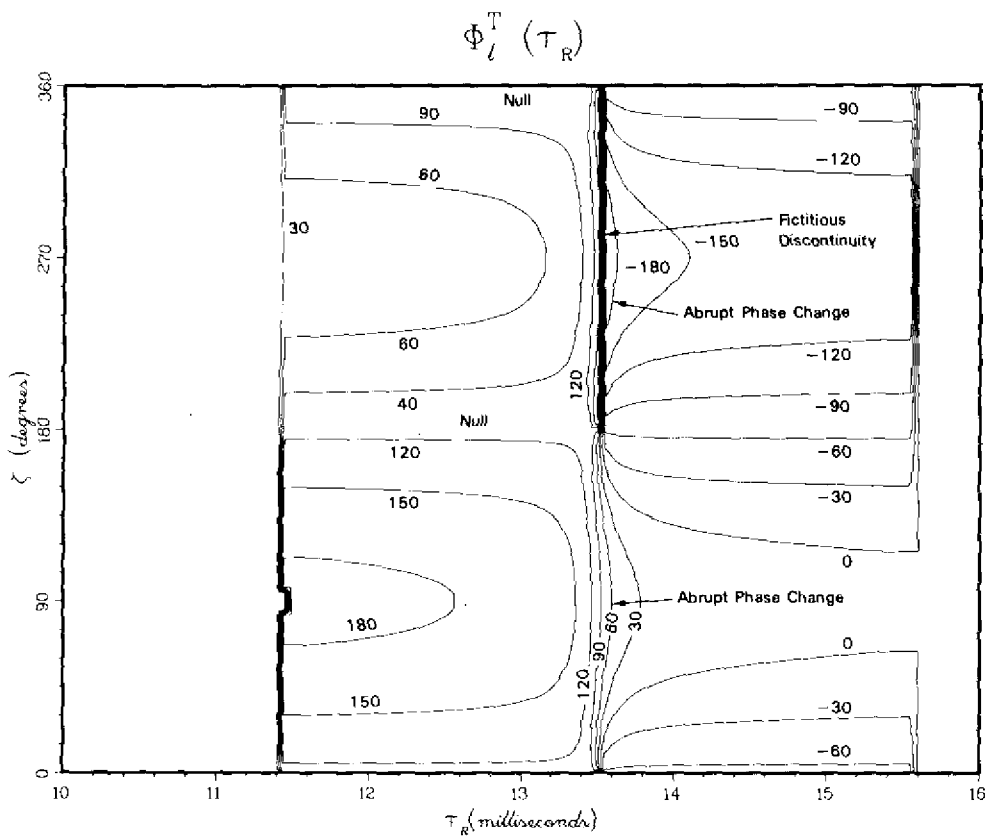


Fig. 104(d) — Phase behavior corresponding to that in Fig. 104(h)

Figure 93 shows the correlator performance for the case of an antenna with inclination  $\gamma = 85^\circ$  from the vertical. For this case it is difficult to say if there is a single best receiver synchronization time  $\tau_R$ . During most of the orbit it appears that the time  $\tau_R = 13.5$  ms would be the best. However, this value of  $\tau_R$  appears to give a value of  $|\mathbf{R}_I^T(\tau_R)|$  that is severely reduced at  $\zeta = 90^\circ$  and  $\zeta = 270^\circ$ . For this case a system of selection of three values of  $\tau_R$  separated by 1-ms intervals (12.5, 13.5, and 14.5 ms) would give a more stable average performance in the evaluation of  $\mathbf{R}_I^T(\tau_R)$ . The discontinuity in Fig. 93d at  $\tau_R = 13.8$  ms, signified by the heavy vertical line, is due to a  $360^\circ$  ambiguity that has no real significance except at the nulls ( $\zeta = 120^\circ$  and  $\zeta = 240^\circ$ ), where  $|\mathbf{R}_I^T(\tau_R)| \rightarrow 0$ . Comparison of Figs. 93(c) and 93(d) illustrate this feature clearly.

Figure 94 shows the correlation performance of an antenna with  $\gamma = 80^\circ$ . Near  $\tau_R = 14.0$  ms and  $\zeta = 180^\circ$  there is an abrupt drop of signal and jump in phase. Otherwise the  $|\mathbf{R}_I(\tau_R)|$  function seems fairly well behaved.

Figure 95 shows the behavior of  $\mathbf{R}_I^T(\tau_R)$  for an antenna with  $\gamma = 60^\circ$ . The amplitude and phase variation of the correlation are much milder than for the cases with smaller values of  $\gamma$ , since the vertical electric-field components exceed the horizontal components by at least one order of magnitude at this droop angle. This trend is continued as  $\gamma$  is decreased to  $45^\circ$  and then to  $0^\circ$  as in Figs. 96 and 97.

Figure 98 shows the value of  $\mathbf{R}_I^{(1ve)}(\tau_R)$ . It illustrates the case of pure first-order-mode propagation from a vertical electric-dipole source.

The values of the propagation quantities in Table 7 are similar to those of Table 6 except for an adjustment to produce maximum mode cancellation and interference effects. We have made the first-order and second-order vertically generated modes have opposite phase and equal magnitude. We have modified the phase of the horizontally generated modes so they are in the same phase plane with the vertically generated modes to produce maximum field-strength variation. Hence both severe effects appear in Figs. 99 through 104.

Figure 99 gives the behavior of  $\mathbf{R}_I^T(\tau_R)$  for the propagation parameters of Table 3. The results are almost identical to those of Fig. 92, since  $\gamma = 90^\circ$  and the only changes made in the parameters of the horizontally generated modes are to the phase delay times  $\tau_{I^{he}}$  and  $\tau_{I^{he}}$ .

Figure 100 shows the behavior of  $\mathbf{R}_I^T(\tau_R)$  for the case of  $\gamma = 85^\circ$ . The influence of the splitting of the vertically generated function is more evident on the phase plot than on the amplitude plot.

Figure 101 shows the behavior of  $\mathbf{R}_I^T(\tau_R)$  for the case of  $\gamma = 80^\circ$ . Here, the influence of the correlation-peak splitting of the vertically generated function is quite evident as the notch in the correlation peak makes its way from side to side through the values of  $\tau_R$  and  $\zeta$ . This is illustrated further in Figs. 102 and 103, which give the graphs for  $\gamma = 60^\circ$  and  $45^\circ$ .

Finally, Fig. 104 shows the split correlation peak for a purely vertical antenna being carried around an orbit. Here we find a nearly constant variation of  $|\mathbf{R}_I^T(\tau_R)|$  versus  $\zeta$ , and the phase of the correlation function  $\phi_I^T(\tau_R)$  varies only moderately with  $\zeta$ . As a function of  $\tau_R$ , these variables show the expected splitting.

## DISTURBANCES

As mentioned previously, long wavelength waves require an ionospheric reflection medium to provide for their world ranging capabilities. This reflecting ionospheric medium is caused by the natural interaction of the sun and the stars with the earth's atmosphere, mediated by the interplanetary medium and by the geomagnetic field of the earth. In total this constitutes an extremely complex system that is poorly understood and monitored. An additional complication arises in the consideration of the ground—the lower boundary of the waveguide. The effective conductivity of the ground surface can vary over great ranges. The conductivity is controlled by the composition and layering of the earth,

by the water content of the soil and rocks, by their roughness, and by their temperatures. One may consider the variation of ground conductivity with location as a disturbance from the placid intellectual picture of a homogeneous propagation path. Also, the seasonal wetting and warming of vast areas of earth should be of consequence to radio propagation forecasts. Further, the lower atmosphere contains elements that slightly retard the propagation of radio waves, form ducting layers and account for the famous "four thirds earth radius" law that becomes applicable even at low frequencies. Therefore, the weather is an additional complicating factor.

Many things can disturb radio waves, but to what degree and how deleterious the various disturbances are is not completely known. There are some answers, however, and a great deal of investigation is still required.

### **Solar Flares—Sudden Ionospheric Disturbances**

Long-wavelength waves have always been thought of as more reliable than high-frequency waves, since the solar flares and magnetic storms, which tend to completely obliterate long-haul high-frequency communications circuits, were not able to shut down communications on long waves. Figuratively, the very low frequency waves effectively "ducked under" the enhanced ionization layer of the lower ionosphere that cause the severe high-frequency signal degradation. The solar flares are noticeable on long-wavelength circuits, but they are normally seen as a change of signal level and not as a complete loss of signal. Sometimes the signal will increase, sometimes it will decrease. The precise behavior is currently unpredictable without making exacting predictions of the locations of interference nulls under normal and disturbed conditions. On the whole I believe that the VLF signal is more likely to be enhanced than depressed during a solar flare for an all-daytime path at temperate latitudes [59].

### **Polar Cap Absorption Events**

Polar cap absorption (PCA) events are natural disturbances that affect VLF propagation for paths crossing the polar regions. PCAs are caused by a flux of charged particles (protons) emitted from the sun during a solar flare. The particles follow the lines of the magnetic field and effectively lower the height of the ionosphere in the polar regions because of the enhanced ionization. The onset of a PCA effect on VLF is more gradual than that of a sudden ionospheric disturbance, however the effects are more long-lasting. PCA events lasting 5 days are not uncommon, and they occur fairly frequently. There were 11 PCAs between March 24, 1966 and June 6, 1967.

Papers by Westerlund et al. [60] and by Dalland et al. [61] contain detailed discussions of PCA events and their effects on VLF signals. A brief summary of the material of these references that seems relevant to a communications channel model follows.

During a PCA the phase of a VLF signal normally advances to some maximum amount and later returns to its pre-PCA value. Phase advances of as much as 50  $\mu$ s have been observed. The behavior of the amplitude of a VLF signal during a PCA is not completely predictable. For paths over water in the polar regions the amplitude variations are generally less severe and unpredictable in sign. However, for paths that involve a good deal of extremely low conductivity soil, Greenland or Antarctica, the amplitude consistently shows strong signal losses (10 to 20 dB) when a PCA occurs. Figure 105 shows the effects of three PCA events on the VLF signal over three Arctic paths. Note that the paths NPG-Stockholm and WWVL-Stockholm show severe attenuation during the PCAs. Both of these paths pass over the low conductivity ground of Greenland. The path from NPM-Stockholm does not pass over Greenland, and relatively small changes in amplitude are observed.

The behavior of the VLF channel during PCA event is very significant for communications over some high-latitude paths. A very low data rate modulation scheme could compensate for the very severe long duration attenuation that occurs. At the same time the phase variation is fairly slow over a message time and should not pose a severe obstacle to communication.

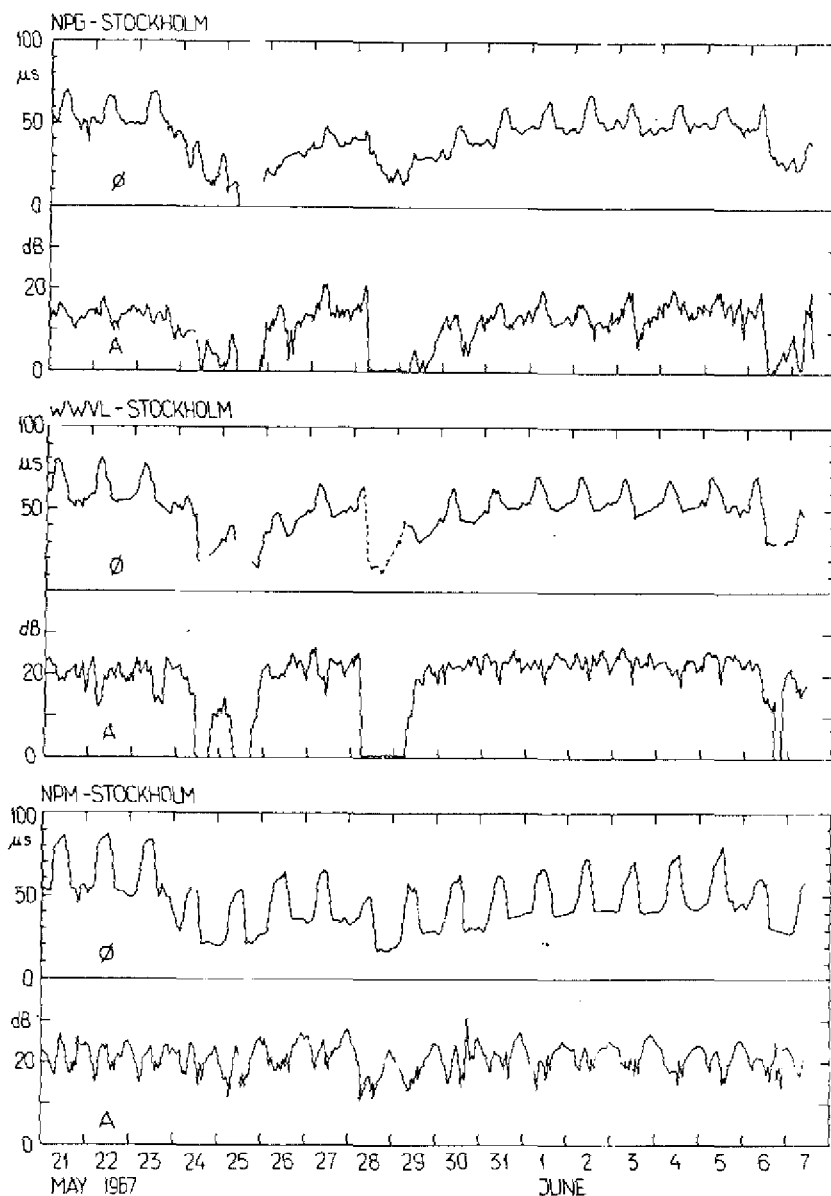


Fig. 105 — VLF phase and amplitude data for the transmissions monitored during PCAs occurring on May 23, 1967, May 28, 1967 and June 6, 1967

### Transition Fading

Transition fading refers to signal fades that occur when the sunrise or sunset line (the terminator) crosses the propagation path between the transmitter and the receiver. This phenomenon has been studied by Crombie [62-64] and others [65,66]. We summarize here the material from these references.

In Crombie's model, the difference in ionospheric heights on either side of the terminator causes modal conversion in the waveguide. The resultant interference on the side of the terminator away from the transmitter gives rise to the transition fading. The principal effect of the fading is to introduce multimode complications similar to those already observed at nighttime. During these times the amount of the multimode interference is determined by the relative amplitudes of the modes and the group and phase delays involved. The effect should be comparable to that observed during normal nighttime conditions when multimode effects are also important.

The transition fading is a dynamic phenomenon because the terminator moves along the path length. Therefore, the rates of change of phase and amplitude are important. Crombie [62] gives an observed maximum  $d\phi/dt$  of  $\sim 70 \pm 2^\circ/\text{min}$ . However, such phase rates could become very large for very short times, and a step function jump of phase is possible if a very sharp and severe modal interference null occurs [67]. The rate of change of amplitude with time is approximately 0.3 dB/min during a fade. Faster rates of change are, of course, possible for very deep fades. Typical fade depth is approximately 10 dB; however, greater fades have been observed, and, of course, even perfect cancellation of modes is theoretically possible.

Schneider and Carlston [66] performed a statistical analysis of transition fading depths and durations. They have applied the statistics of extreme values [68] to data of Rhoads and Garner [69] for the path from Haiku to Washington, DC, that occurred in May and June 1965. They found a good fit to a probability distribution for depth of fade and outage times given by type I and type III distributions of the statistical theory of extreme values.

The cumulative probability distributions for the depths of fade and the times of signal strength, 10 dB below the normal daytime level, are shown in Figs. 106 and 107. Experimental examples of the diurnal variation of received signal from Haiku to Washington, DC [69], are shown in Figs. 108 and 109.

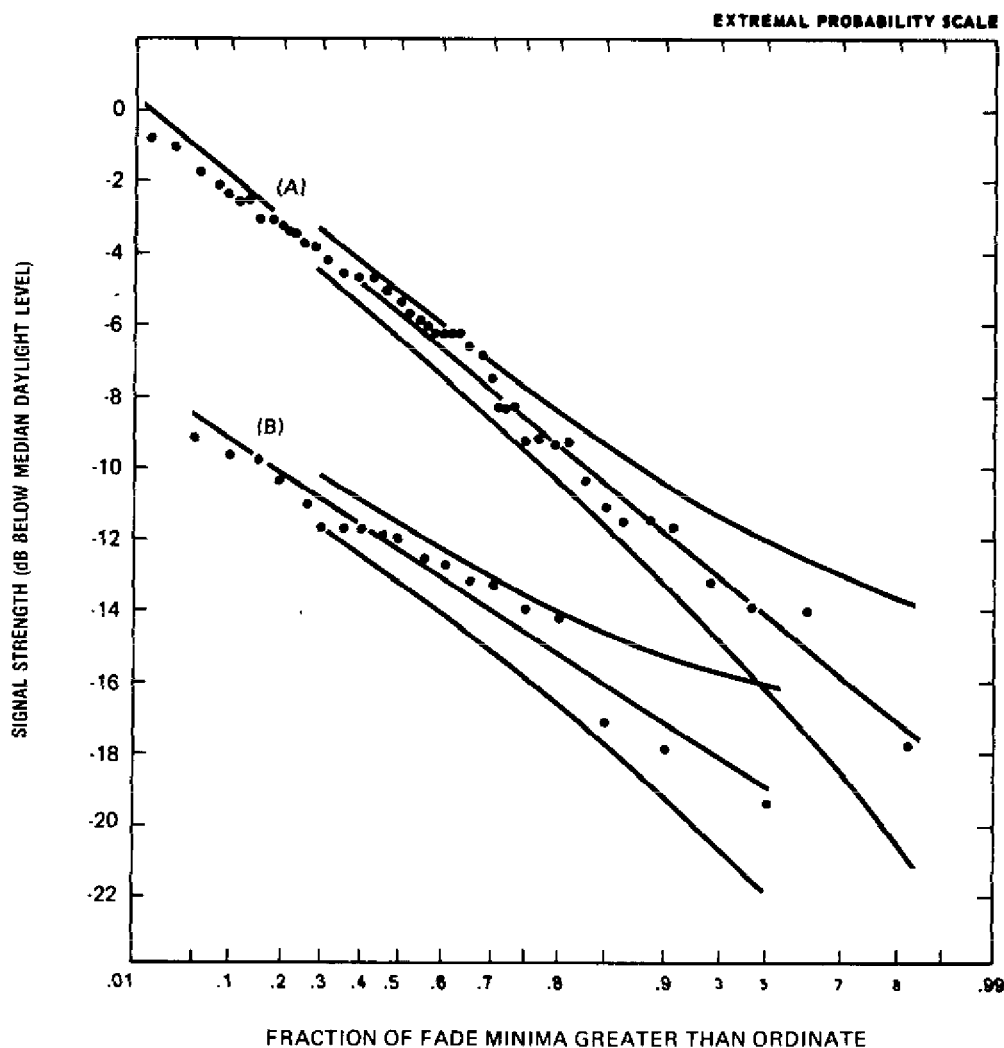


Fig. 106 — Distribution of transition fades for 10 consecutive days; distribution of the third sunrise fade for 19 consecutive days.



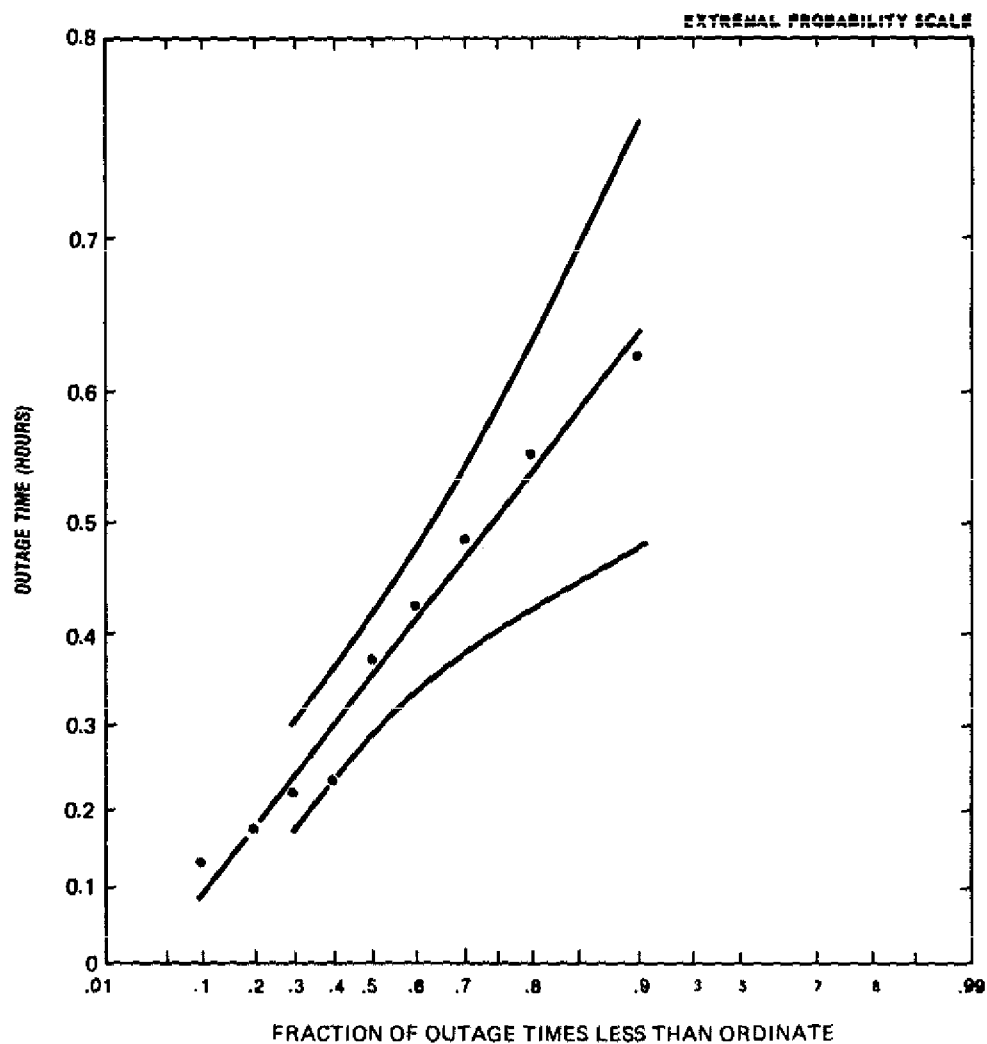


Fig. 107 ~ Distribution of outage time at 10 dB below median daylight threshold level for 10 consecutive days. See Fig. 106 (a).

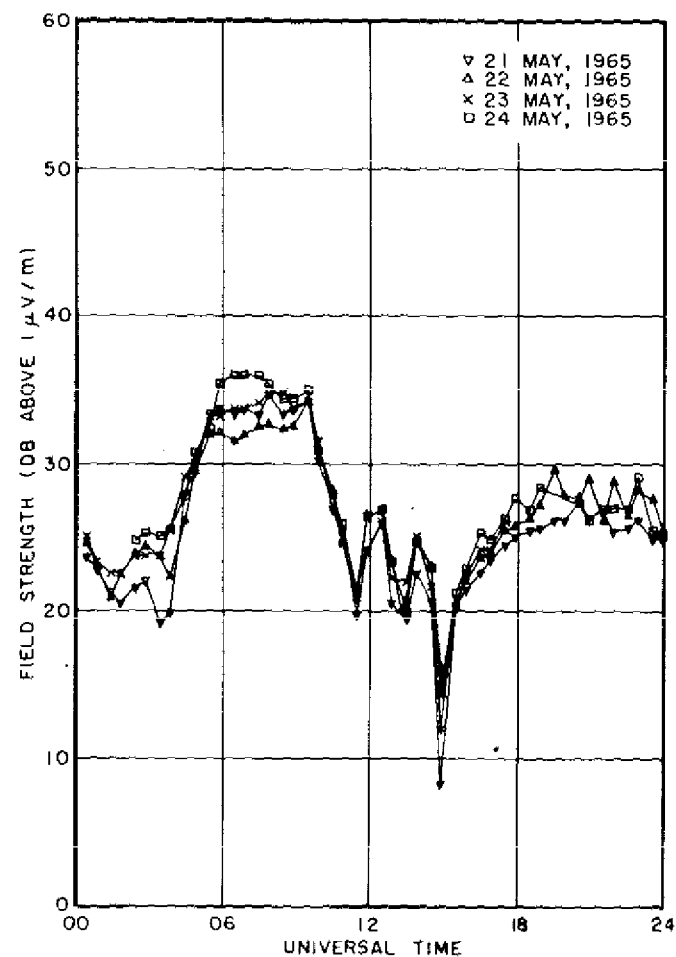


Fig. 108 ~ Haiku (19.8 kc/s) data recorded on May 21, 22, 23, 24, near Washington, DC

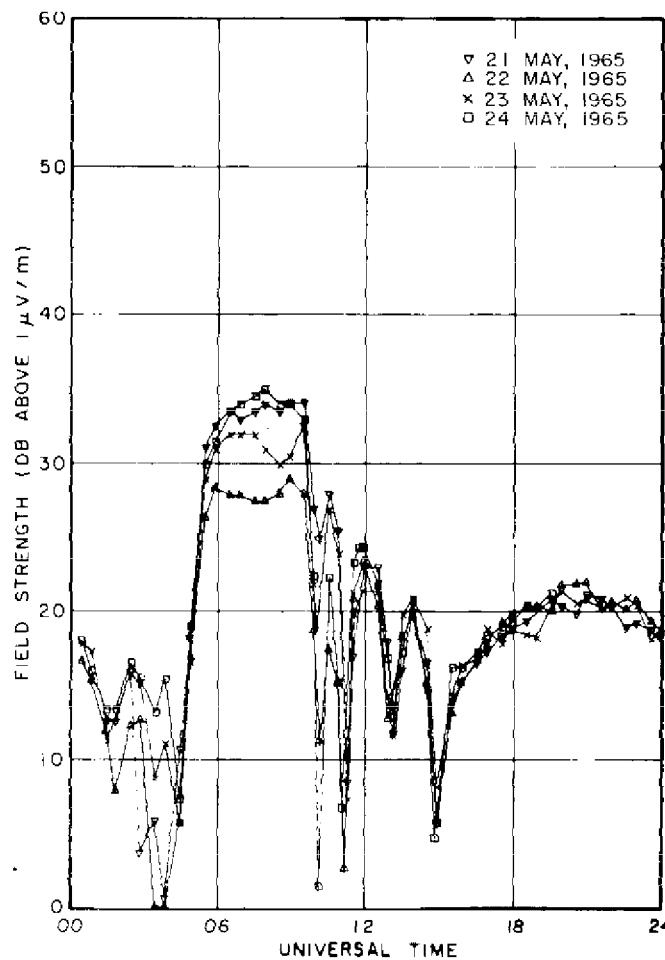


Fig. 109 — NPM (26.1 kc/s) data recorded on May 21, 22, 23, 24, near Washington, DC

### Electron Precipitation-Induced Perturbations

Anyone who has recorded longwave field strengths will note that the nighttime traces are more irregular and "shakey" than the daytime ones—even though the fields are usually stronger and less affected by ambient noise [70].

The picture that is emerging to explain this feature [71] of propagation behavior is curious. It appears that the earth's magnetosphere is filled with energetic particles in the famous Van Allen belts. These belts are continually filling up with particles. The equilibrium reached depends on the plasma density in the magnetosphere and the intensity of lightning generated whistler waves that enter the magnetosphere from the earth ionosphere waveguide [72,73]. The propagation of whistler waves through the magnetosphere can shake or scatter the trapped electrons into their "loss cone," and they precipitate from the Van Allen Belts. When they fall from the magnetosphere, they strike the lower atmosphere and produce electrons in the nighttime D-layer. This sudden electron production causes a quick change in the ionospheric reflection height and thereby perturbs the waves propagating in the earth-ionosphere waveguide causing the abrupt events noted in nighttime recordings.

The reader is invited to learn more about this "strange but (probably) true" mechanism by studying Refs. 74 through 79.

The auroral zone is a region where the electron precipitation is greatly intensified over midlatitudes. It should be expected that these electrons will produce disturbance also [70,80-83].

## ELF Nighttime and PCA Disturbances

The ELF longwave communications system has an interesting disturbance mode that has not been exhibited by the VLF waves. Because of the huge wavelength of ELF (5-3000 Hz) waves, their reflection coefficient matrix (Eq. (1)) at nighttime depends strongly on the electron density distribution up to the F-layer! This means that the ELF nighttime wave will be subject to the vagaries that HF exhibits [84,85] — except the ELF will be averaged over a larger Fresnel zone. This possibility was pointed out early by J. Galejs [86-88]. Now in recent years, it is being treated in greater detail and with greater respect [89-91].

Reference 92 treats the interesting possibility that the change in ELF propagation velocity under a strong PCA could bend the ELF waves so as to cause weakening and reinforcements of the waves in unpredicted ways.

## C-Layer Disturbance

Under some circumstances during daytime, cosmic rays can produce a significant ionization layer beneath the D-layer. This is known as a C-layer [93,94]. The formation and disappearance of this layer is somewhat mysterious (but so is the D-layer). Obviously, with the right intensity this layer will cause its own assembly of effects. The most notable effect is a predicted extra attenuation for waves that go twice through this layer before reflecting at the D-layer. Cosmic rays are known to vary in intensity with the 11-year solar cycle and with solar eruptions [95].

## Ground Conductivity and Weather Effects in Low-Frequency Radio Propagation

In the low-frequency propagation research community awareness is growing of the need for a better propagation model that accounts for ground conductivity, terrain, and atmospheric conditions [96-102]. For example, Fig. 110 from Ref. 99 shows the strong relationship between the time of arrival of a Loran-C groundwave signal transmitted from Carolina Beach, NC, to Fort Wayne, IN, and the atmospheric temperature recorded at Roanoke, VA, very close to this propagation path. Reference 96 puts forth theoretical ideas to explain the weather related propagation delay in terms of changes in the gradient of atmospheric index of refraction. The disturbance of radio wavefields caused by irregular terrain and ground conductivity variations is often observed. For example, Fig. 111 from Ref. 103 shows data illustrating the "recovery effect" observed in passage over ground segments that have dissimilar conductivities. Figure 111(a) shows the flight path of a receiving aircraft over Great Britain. Figure 111(b) shows the dramatic "recovery effect" as the groundwave passes over a river and over a land/sea boundary. The experimental path was chosen because of the flatness and homogeneity of the terrain, otherwise even greater irregularities would be evident in the portion of the flight over land.

Figure 112 [104] illustrates the variation of atmospheric index of refraction vs height which can produce ducting at radar frequencies. Such atmospheric changes should produce measurable effects at the edge of the effective coverage range of a groundwave communications or navigation system. Indeed the 100 kHz, Loran-C community has noticed this effect [105].

## NOISE

The prediction of atmospheric noise is a very important portion of the overall prediction of long wavelength system performance. The basic source of most long wavelength system noise is lightning in thunderstorms. During the 1960s, the National Bureau of Standards conducted a long series of atmospheric noise measurements at stations around the world that led to the CCIR 322 publication [106,107].

Maxwell and others of the Westinghouse Georesearch Corporation utilized NBS data along with propagation models and the statistical records of thunderstorm occurrence to make a more realistic model of noise for the frequency range from 10 to 30 kHz [108]. This model was further improved and extended to predict atmospheric noise at any altitude and polarization within the earth-ionosphere waveguide and also up to nearly 60 kHz [109-112].

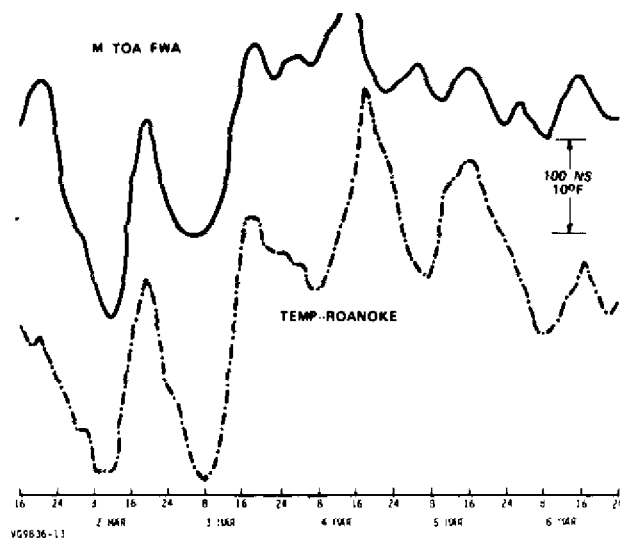


Fig. 110 — Loran C time of arrival at Fort Wayne and temperature at Roanoke

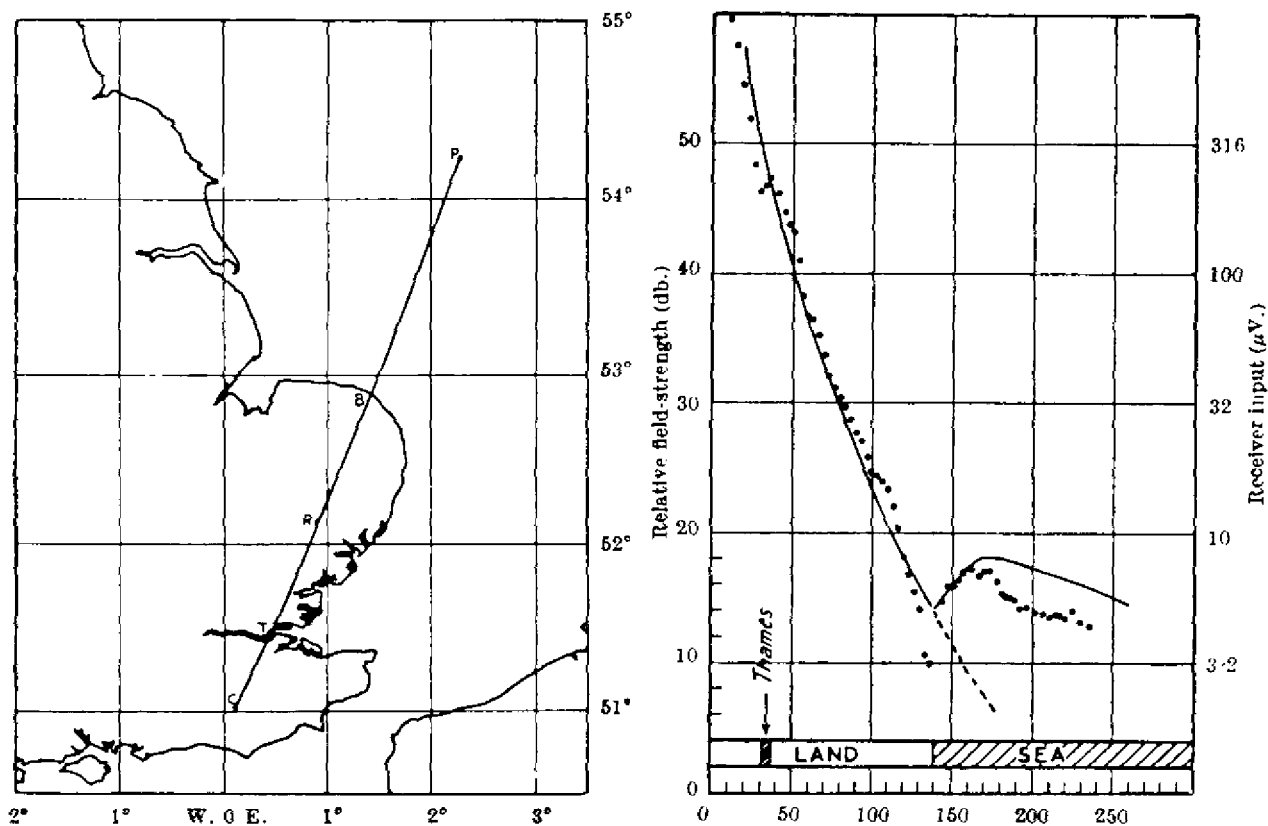
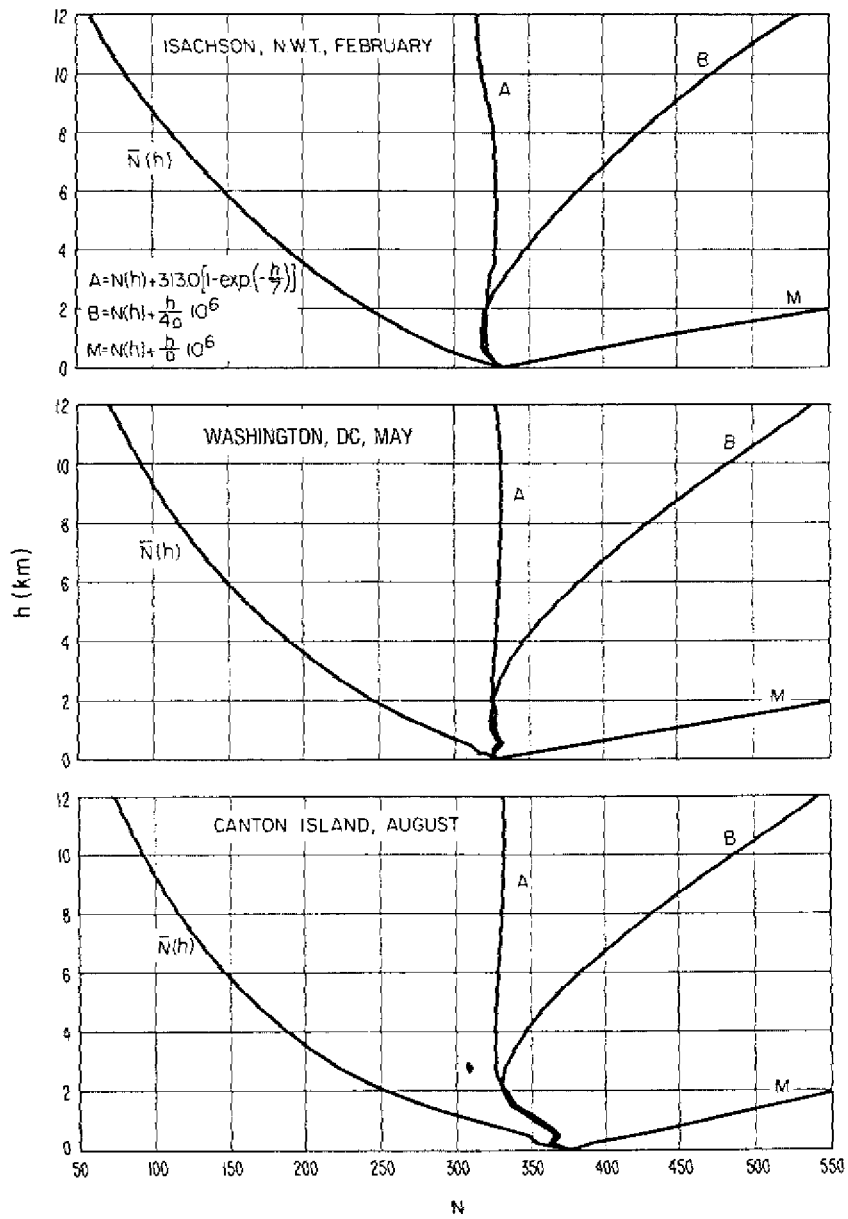


Fig. 111 — Data showing "recovery" effect on groundwave propagation on 1.1 MHz waves (Figure 1, page 115 entitled "Ground-Wave Propagation across a Land/Sea Boundary," by G. Millington from Nature, No. 4157, Vol. 164, July 2, 1949, published by MacMillan and Co. LTD, used by permission.)

## RADIO REFRACTIVE INDEX OF AIR

Fig. 112 — Index of refraction data.  $N = (n-1)10^6$

The NBS noise data [106] was taken through the LF and medium frequencies up to the HF range.

At ELF frequencies, similar studies have been made [114-119] on a sporadic basis. No official group has released worldwide maps of ELF noise and/or powerline interference. It would seem appropriate to extend the model of Ref. 112 down to ELF and up through MF to HF frequencies.

Some proportion of the noise is generated by currents flowing in the ionosphere and magnetospheres [120]. These noise sources are believed to be more important at polar receiver sites throughout the longwave band, but a clear understanding of precisely when, where, and how much noise comes from extraterrestrial sources is not known [113].

### Noise Mitigation

Because the highest noise pulses generated by lightning are strongly nonthermal in amplitude probability distribution various methods have been used to reject the energy contained in these pulses so as to reduce the "effective" root-mean-square (RMS) noise in a receiver much below that which would be seen by a "true" RMS noise meter. It is believed that Shannon's Theorem on Communication Channel Capacity is valid for gaussian noise statistics but that for non-Gaussian noise receiver can do better than look at the RMS noise. Noise theorists have defined a parameter called  $V_d$  that is the ratio of the RMS noise envelope to the average noise envelope. It is believed that an effective noise clipper circuit can reduce the noise level down to about the average levels. (This belief is always being sorely tested by the untractable performance of real systems in the real noise world.) Caution is advised for anyone who thinks that a few simple measurements will suffice to characterize a receiver's performance in noise for all time. Noise is noisy! It is variable in time and place, and a good amount of experience with any nonlinear receiver must be obtained before its performance can be relied on. It is even questionable how to characterize a receiver's performance in noise. Noise has an amplitude probability distribution and a time probability distribution; but these distributions may not be enough to characterize noise to permit a receiver's performance to be specified.

### SYSTEM PERFORMANCE CALCULATION

At ELF, Ref. 121 gives a good example of a longrange communication system performance calculation. At VLF and LF, the system performance calculation is facilitated by computer programs [38,46,47] that can be used to produce coverage maps such as those illustrated in Figs. 56 and 57 and in Figs. 113 through 116. One merely decides what signal to noise ratio (S/N) is needed for reliable communication for a given keying rate receiver and antenna. One then selects the appropriate contours that describe this coverage.

### ACKNOWLEDGMENTS

I want to express my gratitude to my many colleagues at the Naval Research Laboratory, who have guided and helped me, especially W.E. Garner, F.J. Rhoads, D. Baker, J.R. Davis, H. Beck, S. Knowles, J. Goodman, J.A. Murray, J. Brogden, J.P. Hauser, E.S. Byrd and A.J. Martin. I want to thank the engineers at the Defense Communication Agency (R. Heidig, A. Blankfield, G. Jones, Y.S. Fu, P. Bird and P. Sumptor) and at the Department of the Navy (T. Giadrone, R. Savarese, L. Woznak, J. Don Carlos, L. Hice, M. Deeble, and R. Boebel) who have sponsored propagation research. Also I want to express my appreciation to Boyd Burgess of RAE, Farnborough for recommending me as lecturer for the NATO Advisory Group for Aerospace Research and Development Electromagnetic Propagation Panel course for which these notes were originally compiled.

LONG WAVE PROPAGATION CENTER NCPP 74 C3ER016 &gt;

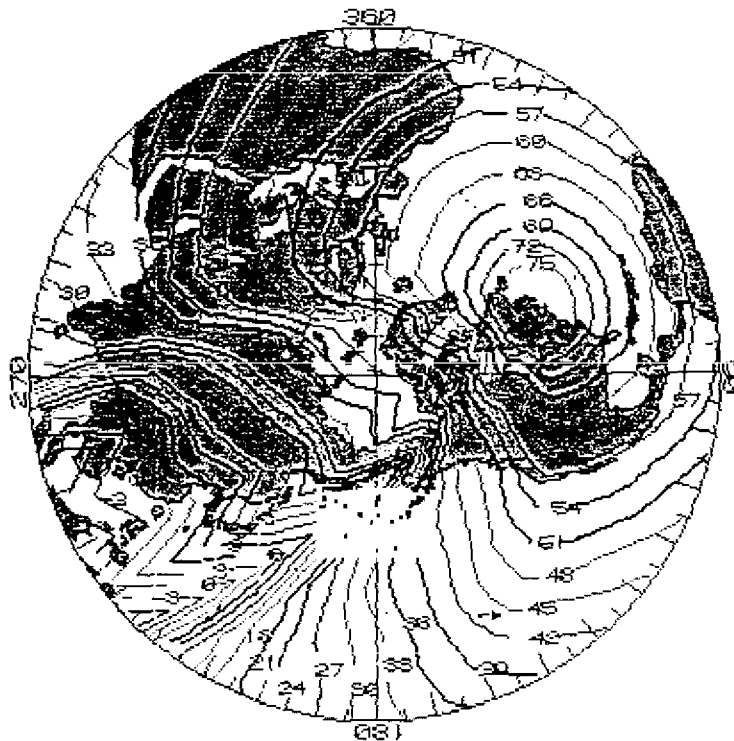


Fig. 113 — Signal level contours in dB above 1  $\mu\text{V}/\text{m}$  for the NAA transmitter in Cutler, ME (Lat 44.60°, Long -67.20°) for 1 MW radiated power during July at 24.0 kHz and 90% time availability

LONG WAVE PROPAGATION CENTER NCPP 74 C3ER016 &gt;

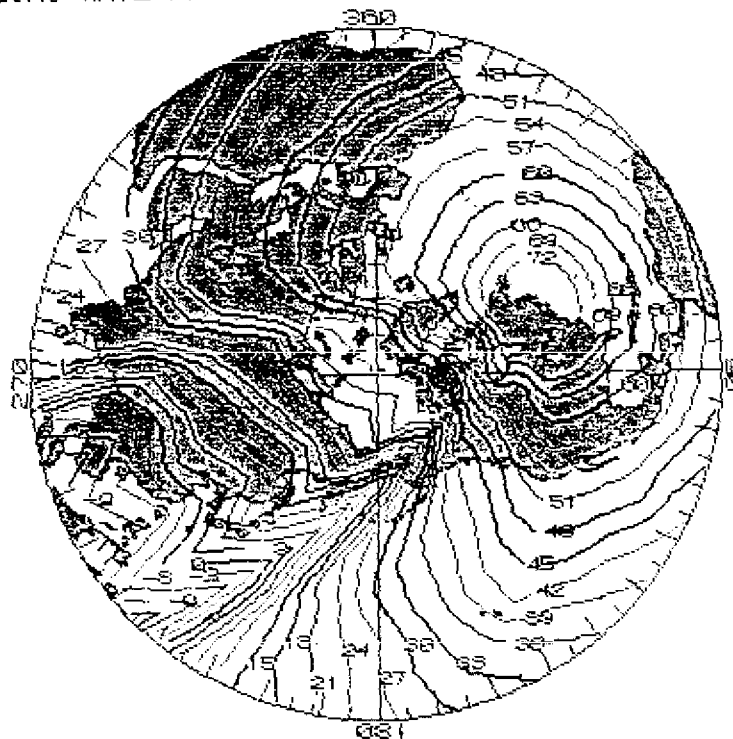


Fig. 114 — Signal level contours in dB above 1  $\mu\text{V}/\text{m}$  for the NAA transmitter in Cutler, ME (Lat 44.60°, Long -67.20°) for 1 MW radiated power during July at 24.0 kHz and 99% time availability

LONG WAVE PROPAGATION CENTER NCPP 74 (SER016 )

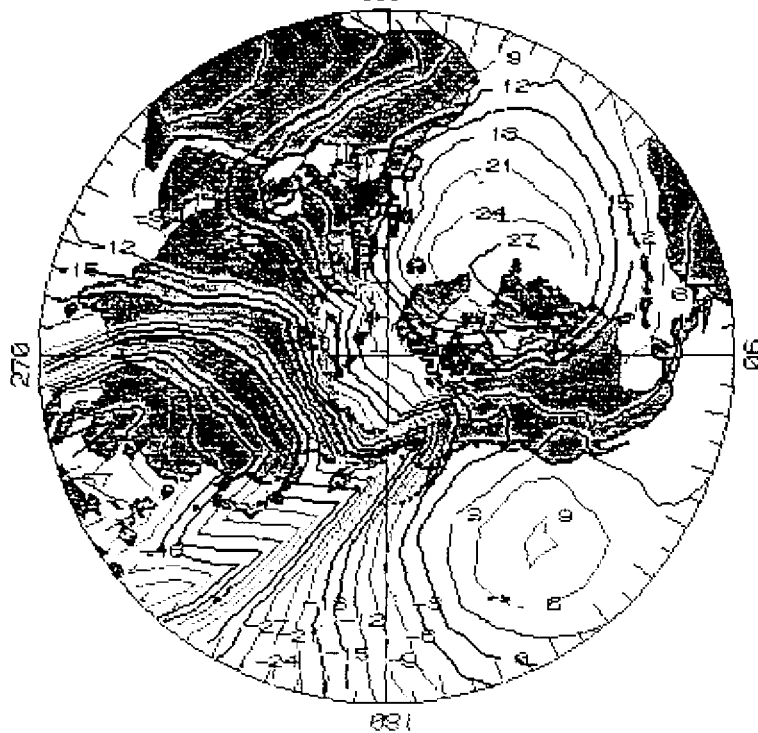


Fig. 115 — Signal-to-noise level contours in dB for a 1 kHz bandwidth for the NAA transmitter in Cutler, ME (Lat 44.60°, Long -67.20°) for 1 MW radiated power during July at 24.0 kHz and 90% time availability

LONG WAVE PROPAGATION CENTER NCPP 74 (SER016 )

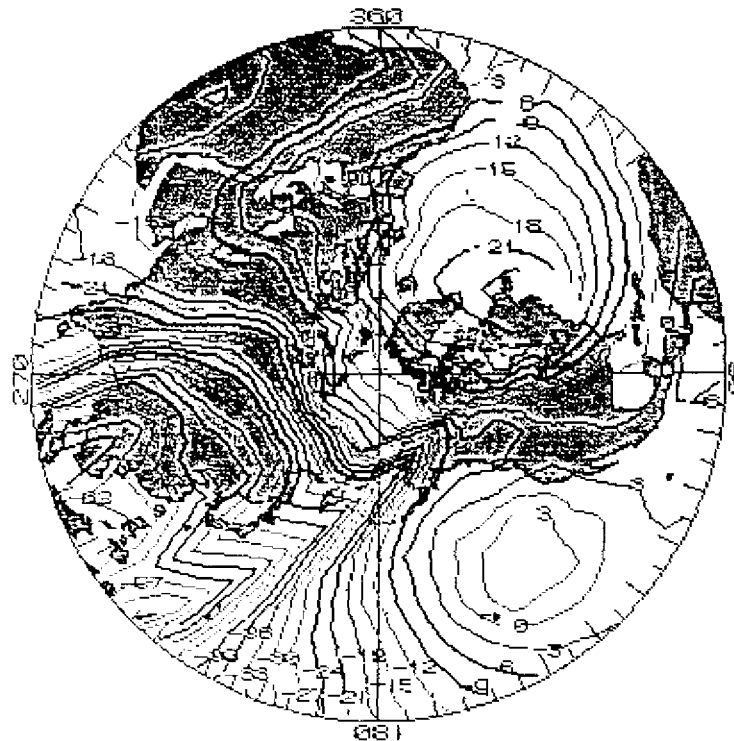


Fig. 116 — Signal-to-noise level contours in dB for a 1 kHz bandwidth for the NAA transmitter in Cutler, ME (Lat 44.60°, Long -67.20°) for 1 MW radiated power during July at 24.0 kHz and 99% time availability



## REFERENCES

1. D.C. Latham, "The  $C^3$  Budget in Perspective," *Signal*, **40**, (9), 107-120, (1986).
2. A.D. Watt, "VLF Radio Engineering, International Series of Monographs on Electromagnetic Waves", (Pergamon, 1967), Vol. 14.
3. H.A. Wheeler, "Fundamental relations in the Design of a VLF Transmitting Antenna," *IRE Trans. Antennas Propagat.*, **AP-6**, 120-122, (1958).
4. NAVELEX Report 101, 113: "VLF, LF and MF Communication Systems," (Sup. of Doc., U.S. GPO).
5. B.G. Blair, "Strategic Command and Control and National Security," *Signal* **39**, (7), 23-32 (1985).
6. K.M. Black, et al., "TACAMO," *Signal* **33**, (1) 6-13 (1978).
7. A. Bystrom, "The Evolution of TACAMO," *Signal* **40**, (3) 33-40 (1986).
8. *IEEE Trans Commun.*, **Com-22** (4) (1974).
9. M. Burrows, "ELF Communications Antennas," in *IEE Electromagnetic Waves, Series 5* Peter Peregrinus Ltd, Herts, England, (1978).
10. M.D. Grossi, "New Technology for ELF Radiators: A Review of Airborne, Rocket-Borne and Space Borne Antennas," in AGARD Conference Proceedings No. 305, "Medium, Long and Very Long Wave Propagation (at frequencies less than 3000 kHz)" J.S. Belrose, ed. (1982).
11. K. Davies, "Ionosphere Radio Propagation," *NBS Monograph* **80** (1965) U.S. GPO, Wash., DC.
12. R.N. DeWitt, F.J. Kelly and G.A. Chayt, "Lower Ionosphere Effects on the Propagation of Waves from an ELF/VLF Source in the Magnetosphere," *Radio Sci.*, **11**, (3), 189-197 (1976).
13. F.J. Kelly and D.N.M. Rao, "Ionosphere Heating Effects on LF Propagation" in *Effect of the Ionosphere on Radiowave Systems* J.M. Goodman, F.D. Clarke, and J. Aarons eds. (Sup. of Doc., U.S. GPO, Wash., DC.) based on Ionosphere Effects Symposium Alexandria, VA (1981).
14. J.S. Belrose "The Oblique Reflection of Low Frequency Radio Waves from the Ionosphere," in *Propagation of Radio Waves at Frequencies Below 300 Kc/s*, W.T. Blackband, ed., (Macmillan Co., New York, pp. 149-168, 1964).
15. M.L.V. Pitteway, "The Numerical Calculation of Wave-Fields, Reflection Coefficients and Polarizations for Long Radio Waves in the Lower Ionosphere," *Phil. Trans. R. Soc.* **A257**, 219, (1965), and G.H. Smith and M.L.V. Pitteway, *Fortran Program for Obtaining Wavefields of Penetrating, Nonpenetrating, and Whistler Modes of Radio Waves in the Ionosphere*, in *ELF-VLF Radio Wave Propagation*, J. Holtet, ed., (D. Reidel Publishing Co. Dordrecht, Holland, 1974).
16. J. Galejs, *Terrestrial Propagation of Long Electromagnetic Waves* (Pergamon Press, New York, 1972).
17. R.A. Pappert, W.F. Moler, and L.R. Schockey, "A Fortran Program for Waveguide Propagation Which Allows for Both Vertical and Horizontal Dipole Excitation," NELC Interim Report 702 (1970).

18. C.H. Shetty, R. Pappert, Y. Gough, and W. Moler, "A Fortran Program for Mode constants in an Earth-Ionosphere Waveguide," NELC Interim Report 683 (1968).
19. R.A. Pappert and L.R. Shockey, "A Program for Computing Earth Ionosphere ELF/VLF Excitation Factors for Satellite-borne Antennas," NELC Interim Report 741 (1974).
20. R.A. Pappert, "Effects of Elevation and Ground Conductivity on Horizontal Dipole Excitation of the Earth-Ionosphere Waveguide," *Radio Sci.* 5 (3), 579-590 (1970).
21. F.J. Kelly, G.A. Chayt, and D.J. Baker, "Waveguide-Mode Power Budget for an ELF/VLF Transmitting Satellite," NRL Report 8032, Sept. 1976.
22. F.J. Kelly, J.P. Hauser, and F.J. Rhoads, "Computer-Program Model for Predicting Horizontally and Vertically Polarized VLF Atmospheric Radio Noise at Elevated Receivers," NRL Report 8479, Dec. 1981.
23. J.R. Wait and K.P. Spies, "Characteristics of the Earth-Ionosphere Waveguide for VLF Radio Waves," NBS Tech. Note 300 (1964).
24. C.M. Brookes, J. McCabe, and F.J. Rhoads, "Theoretical VLF Multimode Propagation Predictions," NRL Report 6663 (1967).
25. F.J. Kelly, F.J. Rhoads, and I.P. Hansen, "On Statistical VLF Multimode Field Strength Prediction," NRL Report 7239 (1971).
26. F.J. Kelly, F.J. Rhoads, and I.P. Hansen, "Statistical Multimode VLF Field Strength Predictions," NRL Memorandum Report 2202 (1971).
27. R.S. Gardiner, "Comparison of Predicted VLF/LF Signal Levels with Propagation Data," Defense Communications Agency, 960-TP-74-5, Jan. 1974.
28. W.G. Reed, "Determination of Effective Ionosphere Electron Density Profiles for VLF/LF Propagation," Defense Communications Agency, C650-TP-76-4, Jan. 1976.
29. R.R. Morgan, "World-Wide VLF Effective-Conductivity Map," Westinghouse Electric Corporation Report 80133 F-1, Jan. 1968.
30. J.P. Hauser, W.E. Garner, and F.J. Rhoads, "A VLF Effective Ground Conductivity Map of Canada and Greenland with Revisions Derived from Propagation Data," NRL Report 6893, Mar. 1969.
31. H.M. Swarm, D.K. Reynolds, and A.W. Biggs, "Analytical Study of ELF and VLF Radiation Fields from a Horizontal Dipole in Antarctica," University of Washington College of Engineering, Dept. of Electrical Engineering, Tech. Report No. 87, Jan. 1964.
32. J.R. Wait, "An analysis of VLF Mode Propagation for a Variable Ionosphere height," *J. Res. NBS* 66D (4), 453-461 (1962).
33. J.R. Wait, "Mode Conversion in the Earth-Ionosphere Waveguide," NBS Tech. Note No. 151 (1962).
34. R.A. Pappert and L.R. Shockey, "Effects of Strong Local Sporadic E on ELF Propagation," NOSC Tech. Report 282, Aug. 1978.
35. R.A. Pappert and R.R. Smith, "Mode Conversion Program for an Inhomogeneous Isotropic Ionosphere," NELC Interim Report 701, Apr. 1970.

36. R.A. Pappert and L.P. Shockey, "WKB Fields Program for Lower ELF," NELC Interim Report 731, Jan. 1973.
37. R.A. Pappert and L.R. Shockey, "A Simplified Mode Conversion Program for VLF Propagation in the Earth Ionosphere Waveguide," NELC Interim Report 751, Oct. 1974.
38. J.P. Hauser, F.J. Rhoads, and F.J. Kelly, "VLFACM Program Description and Operational Manual," NRL Report 8530, Nov. 1981.
39. J.P. Hauser and F.J. Rhoads, "Coverage Predictions for the Navy's Fixed VLF Transmitters," NRL Memorandum Report 2884, Sept. 1974.
40. J.R. Wait, "A Diffraction Theory of LF Sky-Wave Propagation," *J. Geophys. Res.*, **66**(6), 1713 (1961).
41. C.N. Watson, *Proc. Roy. Soc. London*, **A95**, 83 and 546.
42. J. Hollingworth, "The Propagation of Radio Waves," *J. IEEE* **64**, 579-589 (1962).
43. H. Bremmer, *Terrestrial Radio Waves* (New York, Elsevier Publishing Co., Inc., 1949).
44. J.R. Wait and A.M. Conda, "A Diffraction Theory for LF Sky-Wave Propagation—An Additional Note," *J. Geophys.* **66**, 1725-1729 (1961) (see also pp. 1713-1724).
45. L.A. Berry, G. Gonzalez, and J.L. Lloyd, "Wave Hop Series for an Anisotropic Ionosphere," *Radio Sci.* **4**, 1025-1027 (1969).
46. L.A. Berry, and J.E. Herman, "A Wave Hop Propagation Program for an Anisotropic Ionosphere," OT/ITS Research Report 11, Apr. 1971.
47. L.A. Berry, and J.E. Herman, "Fortran Program for Estimating LF-VLF Radio System Performance," OT TM 63, Office of Telecommunications, Institute for Telecommunications Sciences, Boulder, CO, Oct. 1971.
48. J.R. Jöhler, "Spherical Wave Theory for MF, LF and VLF Propagation," *Radio Sci.* **5**, 1429 (1970).
49. L.A. Berry, G. Gonzalez, and J.L. Lloyd, "Wave Hop Series for an Anisotropic Ionosphere," *Radio Sci.* **4**, (11), 1025-1027.
50. T.B. Jones, and K. Mowforth, "A Review of the Analytical Techniques for Determining the Phase and Amplitude of a VLF Radio Wave Propagation in the Earth-Ionosphere Waveguide," AGARD Conf. Proc. **305**, "Medium, Long and Very Long Wave Propagation (At Frequencies Less Than 3000 kHz)," J.S. Belrose, ed., Feb. 1982.
51. D.F. Morfitt, and R.F. Halley, "Comparison of Waveguide and Wave Hop Techniques for VLF Propagation Modeling," NWC Tech. Publication 4952, Naval Weapons Center, China Lake, CA (1970).
52. J.C. Huffman, Lauaber, F.J. LeBlanc, and C.I. Meng, "Ultraviolet Remote Sensing of the Aurora and Ionosphere," paper 4-4, in *Effect of the Ionosphere on C<sup>3</sup>I Systems*, J.M. Goodman, F.D. Clarke, J.A. Klobucher and H. Soicher, eds. based on Ionospheric Effects Symposium, Alexandria, VA, May 1984.

53. J.R. Wait, "Propagation of Very-Low-Frequency Pulses to Great Distances," *J. Res. NBS* **61**(3), 187-203 (1958).
54. J.R. Wait, "Propagation of Pulses in Dispersive Media," *J. Res. NBS (Radio Sci.)* **69D**(1), 1387-1401 (1965).
55. F.J. Kelly, "Multimode and Dispersive Distortion in the Very-Low-Frequency Channel," *Radio Sci.* **5** (3) 569-573 (1970).
56. J.D. Jackson, *Classical Electrodynamics*, 1st ed. (John Wiley and Sons, Inc., New York, 1962).
57. F.J. Kelly, "VLF Field Strength Variations from an Airborne Trailing-Wire Antenna," *Radio Sci.* **5** (5), 785-791 (1970).
58. F.J. Kelly, J.P. Hauser, H.M. Beck, and F.J. Rhoads, "Multipath VLF Propagation Effects on Correlation Receivers," AGARD Conf. Proc. 305, Medium, Long, and Very Long Wave Propagation (at Frequencies less than 3000 kHz), J.S. Belrose, ed.
59. B. Wingate, "The Very Low Frequency Experimenter's Newsletter," 121 Chesapeake Avenue, Lake Hiawatha, NJ 07034.
60. S. Westerlund, F.H. Reder, and C. Abom, "Effects of Polar Cap Absorption Events on VLF Transmissions," *Planet and Space Sci.* **17**, 1329-1374.
61. J. Dalland, K.W. Eriksen, B. Landmark, and H.J. Weedon, "The Influence of Polar Blackouts on VLF Circuits," NDRE Report 36, Apr. 1961.
62. D.D. Crombie, "Periodic Fading of VLF Signals Received Over Long Paths at Sunrise and Sunset," *Radio Sci. J. Res. NBS* **68D** (1), 27-34 (1964).
63. D.D. Crombie, *Radio Sci.* **1**, 47 (1966).
64. D.D. Crombie, "The Waveguide Mode Propagation of VLF Radio Waves to Great Distances," *Conference on MF, LF and VHF Radio Propagation*, Nov. 1967, pp. 138-150.
65. J.R. Wait, "Mode Conversion and Refraction Effects in the Earth Ionosphere Waveguide for VLF Radio Waves," *J. Geophys. Res.* **73**, 3537 (1968).
66. A. Schneider and P.K. Carlston, *Radio Sci.* **4**, 377-380 (1969).
67. J. Bickel, (private communication).
68. W.C. Hoffman, "Some Statistical Methods of Potential Value in Radio Wave Propagation Investigations," in *Statistical Methods in Radio Wave Propagation*, W.C. Hoffman, ed. (Pergamon Press, New York, 1960), pp. 117-135.
69. F.J. Rhoads and W.E. Garner, "An Investigation of the Modal Interference of Very-Low-Frequency Radio Waves," NRL Report 6359, Oct. 1965.
70. P.R. Bannister, et al., "Scientific and Engineering Studies: Extremely Low Frequency (ELF) Propagation," Naval Underwater Systems Center, Newport Laboratory, Newport, RI.
71. R.A. Helliwell, (private communication).

72. C.F. Kennel and H.E. Petschek, "Limit on Stably Trapped Particle Fluxes," *J. Geophys. Res.* **71** (1) (1966).
73. N. Brice, "Harnessing the Energy of the Radiation Belts," *J. Geophys. Res.* **76** (19), 4698 (1971).
74. A. Tolstoy and T. Rosenberg, (private communication).
75. T.A. Potemra and A.J. Zmuda, "Precipitating Energetic Electrons as an Ionization Source in the Midlatitude Nighttime D Region," *J. Geophys. Res.* **75**, (34), 7161 (1970).
76. T.R. Larsen, T.A. Potemra, W.L. Imhof, and J.B. Reagan, "Energetic Electron Precipitation and VLF Phase Disturbances at Middle Latitudes Following the Magnetic Storm of December 16, 1971," *J. Geophys. Res.* **82** (10), 1519 (1977).
77. T.R. Larsen, J.B. Reagan, W.L. Imhof, L.E. Montriand, and J. Belrose, "A Coordinated Study of Energetic Electron Precipitation and Region Electron Concentrations Over Ottawa during Disturbed Conditions," *J. Geophys. Res.* **81**, (13), 2200 (1976).
78. L.E. Montbriand, and J.S. Belrose, "Changes in Electron Precipitation Inferred from Spectra Deduced from D Region Electron Densities During a Post-Magnetic Storm Effect," *J. Geophys. Res.* **81**(13), 2213 (1976).
79. W.L. Imhof, R.R. Anderson, J.B. Reagan, and E.E. Gaines, "The Significance of VLF Transmitters in the Precipitation of Inner Belt Electrons," *J. of Geophys. Res.*, 11225-11234 (1981).
80. L. Harang, *The Aurorae* (John Wiley and Sons, Inc., New York, 1951).
81. R.C. Whitten and I.G. Poppoff, *Physics of the Lower Ionosphere* (Prentice-Hall, Inc., Englewood Cliffs, NJ, 1965).
82. C.I. Meng, "Electron Precipitation in the Midday Auroral Oval," *J. Geophys. Res.* **86**(A4), 2149-2174 (1981).
83. C.I. Meng, "The Auroral Electron Precipitation During Extremely Quiet Geomagnetic Conditions," *J. Geophys. Res.* **86**(A6), 4607-4627 (1981).
84. J.M. Goodman and D.R. Uffelman, "The Role of the Propagation Environment in HF Electronic Warfare," NRL Memorandum Report 4953, Nov. 1982.
85. J.M. Goodman "A Survey of Ionospheric Models—A Preliminary Report on the Development of an Ionospheric Model Thesaurus and Users Guide," NRL Memorandum Report 4830, July 1982.
86. J. Galejs, "F Layer Reflections and Ion Effects in the Propagation of Terrestrial ELF Waves," *J. Geophys. Res.* **75**, 2529-2539 (1970).
87. J. Galejs *Terrestrial Propagation of Long Electro-magnetic Waves* (New York, Pergamon, 1972).
88. J.R. Davis, E.L. Althouse, and D.R. Uffelman, "Some Possible Propagation-Associated Constraints on ELF Communications," NRL Report 7269, July 1971.
89. R.A. Pappert, "Effects of a Large Patch of Sporadic E on Night-Time Propagation at Lower ELF," *J. of Atmospheric and Terrestrial Phys.*, **42**, 417-425 (1980).
90. J.R. Davis, "ELF Propagation on Northern and Mid-Latitude Paths," in *ELF-VLF Radio Wave Propagation*, J.A. Holtel ed. (D. Reidel Publishing Co., Dordrecht, Holland, 1974), pp. 263-277.

91. R.A. Pappert, "Broadside Excitation of ELF by a Horizontal Dipole Beneath a Sporadic E Environment: Theory" *Radio Sci.* **21**, 106-116 (1986).
92. E.C. Field, C.R. Warber, and R.G. Joiner, "Focusing and Shadowing of ELF Signals," *Radio Sci.*, **21**, 511-517 (1986).
93. W.C. Bain, "The Use of VLF Propagation Results in Ionospheric Modelling," in *ELF-VLF Radio Wave Propagation*, J.A. Holtel, ed. (D. Reidel Publishing Co., Dordrecht-Holland, 1974), pp. 151-163.
94. J.E. Rasmussen, P.A. Kossey, and E.A. Lewis, "Evidence of an Ionospheric Reflecting Layer Below the Classical Region" *J. of Geophys. Res.* **85**(A6), 3037-3044 (1980).
95. V.P. Okhlopkov, L.S. Okhlopkova, and T.N. Charakhch'yan, Two-Year Cosmic-Ray Variations, *Geomagnetism and Aeronomy* **19**(3), 287 (1979).
96. S.N. Samaddar, "Weather Effects on Loran-C Propagation," *Navigation: J. Institute of Navigation* **27**, 39-53 (1980).
97. R.H. Ott, L.W. Vogler, and G.A. Hufford, "Ground Wave Propagation over Irregular, Inhomogeneous Terrain: Comparisons of Calculations and Measurements," NTIA Report 79-20.
98. R.H. Doherty and J.R. Johler, "Meteorological Influences on Loran-C Groundwave Propagation," *J. Atmos. Terr. Phys.* **37**, 1117-1124 (1975).
99. W.N. Dean, "Diurnal Variations in Loran-C Groundwave Propagation," Proc. Ninth Annual Precise Time and Time Interval Applications and Planning Meeting, NASA - Goddard Space Flight Center, Greenbelt, MD, 1977.
100. W.N. Dean, "Study of Temporal Behavior of Loran-C to A Data," Feb. 15, 1979.
101. S. Horowitz and J.R. Johler, "Loran C/D Coordinate Prediction Dependence on Ground Electrical Properties," AGARD Conf No. 209 on Limitations of Navigation and Positioning Systems, Istanbul, Turkey, Oct. 20-22, 1976.
102. J.R. Johler, "Prediction of Ground Wave Propagation Time Anomalies in the Loran-C Signal Transmissions over Land," AGARD Conference No. 209 on Limitations of Navigation and Positioning Systems, Istanbul, Turkey, Oct. 20-22, 1976.
103. G. Millington and N. Elson, "Ground-wave Propagation Across a Land/Sea Boundary," *Nature* **164**, 114-116 (1949).
104. B.R. Bean and E.J. Dutton, "Radio Meteorology," *National Bureau of Standards Monograph* 92, (U.S. GPO, 1966), p. 18.
105. S. Samaddar, private communication.
106. W.Q. Crichtlow, C.A. Samson, R.F. Disney, and M.A. Jenkins, "Quarterly Radio Noise Data," NBS Tech. Note 18 series (1960).
107. "World Distribution and Characteristics of Atmospheric Radio Noise," Proc. CCIR Xth Plenary Assembly, Geneva, 1963, Report 322, International Telecommunications Union, Geneva, 1964.
108. E.L. Maxwell, D.L. Stone, R.D. Croghan, L. Ball, and A.D. Watt, "Development of a VLF Atmospheric Noise Prediction Model," Westinghouse Georesearch Laboratory Report 70-1H2-VLF NO-R1 (1970).

109. J.P. Hauser and F.J. Rhoads, "Analysis of a VLF Atmospheric Noise Prediction Model," paper presented at USNC/URSI Mtg., Commission VIII, Session 1, Aug. 1973.
110. J.P. Hauser, "Further Analysis of a VLF Atmospheric Noise Model," paper presented at USNC/URSI Mtg., Commission VIII, Session 2, Oct. 1974.
111. F.J. Kelly, J.P. Hauser, and F.J. Rhoads, "Atmospheric VLF Radio Noise at Elevated Receivers: Horizontal and Vertical Polarization," AGARD Conf. Proc., Brussels, Sept. 1981.
112. F.J. Kelly, J.P. Hauser, and F.J. Rhoads, "Computer-Program Model for Predicting Horizontally and Vertically Polarized VLF Atmospheric Radio Noise at Elevated Receivers," NRL Report 8479, Dec. 1981.
113. J.P. Hauser, F.J. Kelly, and F.J. Rhoads, *Atmospheric Radio Noise Modelling at NRL*, in *Effect of the Ionosphere on C<sup>3</sup>I Systems*, J.M. Goodman, F.D. Clarke, J.A. Klobucher and H. Soicher, eds., based on Ionospheric Effects Symposium, Alexandria, VA. (1984), pp. 375-386.
114. L.H. Ginsberg, "Extremely Low Frequency (ELF) Atmospheric Noise Level Statistics for Project Sanguine," *IEEE Trans. Comm. Com-22* (4), 555-561 (1974).
115. J.E. Evans and A.S. Griffiths, "Design of a Sanguine Noise Processor Based upon World Wide Extremely Low Frequency (ELF) Recordings," *IEEE Trans. Comm. COM-22* (4), 528-539 (1974).
116. J.R. Davis and W.D. Meyers, "Observations of ELF Signal and Noise Variability on Northern Latitude Paths," NRL Report 7923, Nov. 1975.
117. W.D. Meyers and J.R. Davis, "ELF Nonlinear Noise Processing Experimental Measurements: Part 1—Preliminary Results in July and October 1975," NRL Memorandum Report 3226, Mar. 1976.
118. J.R. Davis and W.D. Meyers, "ELF Nonlinear Noise Processing Experimental Measurements, Part 2—Synoptic Sample and Seasonal Noise Variation in Norway," NRL Report 8039, Oct. 1976.
119. J.A. Goldstein, W.D. Meyers, and J.R. Davis, "ELF Nonlinear Noise Processing Experimental Measurements: Part 3—Synoptic Sample of Diurnal and Seasonal Noise Variation in Italy," NRL Memorandum Report 3543, July 1977.
120. J.K. Alexander and M.L. Kaiser, "Terrestrial Kilometric Radiation .....", *J. Geophys. Research* **81**, 5948-5956 (1976); **82**, 98-104 (1977).
121. S.L. Bernstein, M.L. Burrows, J.B. Evans, A.S. Griffiths, D.A. McNeill, C.W. Niessen, I. Richer, D.P. White, and D.K. Williams, "Long Range Communications at Extremely Low Frequencies," *Proc. IEEE*, **62**, 292-312 (1974).

## Appendix

### THE IMPORTANCE OF THE ELF/VLF/LF BAND

The Ground Wave Emergency Network (GWEN) will provide a nuclear hardened terrestrial communications system to carry warning data and emergency action messages and force direction orders to U.S. forces. When the first phase is operational, in FY 1987, GWEN will be a unique, low-cost, hardened communications system serving both national and nuclear CINC requirements. The second phase of the program will have additional transmitters and receivers, and will provide a hardened link to the intercontinental ballistics missile force and other strategic elements. We expect to procure about 50 more nodes for the network in FY 1987 and to complete the system by the end of the decade.

To improve communications connectivity with strategic bombers in flight, we plan to equip them with Miniature Receive Terminals (MRTs) for receiving low-frequency (LF) and very low frequency (VLF) communications. Although slower than transmissions in higher frequency bands, LF/VLF communications can be transmitted over much greater distances than can line-of-sight communications, and they are much less susceptible to nuclear effects and jamming than the existing satellite and high-frequency (HF) communications are. Flight tests of the terminals are planned to be completed in FY 1987; production should be completed in early FY 1988.

To communicate with ballistic missile submarines, the Navy maintains special radio relay aircraft continuously airborne over the Atlantic and Pacific oceans. These planes, called Take Charge and Move Out (TACAMO), transmit relayed messages to the submarines by a variety of communications media. In FY 1989, we will begin replacing the EC-130s (modified C-130 transports) now flying the TACAMO mission with the faster, more survivable, more endurable and longer range E-6A (a derivative of the Boeing 707 airborne warning and control system [AWACS] airframe). At the same time, the SSBN force will be outfitted with improved VLF receivers. The E-6 A's ability to operate over vast expanses of the ocean will permit SSBNs and nuclear cruise missile equipped submarines to expand their operating areas and still receive messages from the President. Building toward a fleet of 15 E-6As, we are requesting funds to procure the third, fourth, and fifth production aircraft in FY 1987. Although the planes will be outfitted initially with communications equipment transferred from EC-130s, they eventually will carry a vastly improved VLF communications system.

Submerged submarines now must deploy an antenna at or close to the ocean's surface to receive messages, thus potentially increasing their susceptibility to detection. The use of extremely low frequency (ELF) communications, which can penetrate to great depths, will alleviate this constraint. The ELF Communications System consists of two transmitter sites (in Wisconsin and northern Michigan), operating in electrical synchronization with receivers aboard submarines. The ELF system's high reliability and continuous transmissions significantly will upgrade peacetime communications to deployed submarines and will support the transition to wartime operations. Receivers are being installed in some submarines this year so that the full system can be tested in FY 1987. We are requesting funds for FY 1987 to procure receivers for other submarines. The system should be fully operational by the end of FY 1988.

---

From "The C<sup>3</sup> Budget in Perspective" by Donald C. Latham, Assistant Secretary of Defense for Command, Control, Communications and Intelligence.